# Characterising disturbance in tropical peat swamp forest using satellite imaging radar

Thesis submitted for the degree of

Doctor of Philosophy

at the University of Leicester

by

Matthew Scott Waldram

Department of Geography

University of Leicester

February 2013

**Characterising disturbance in tropical peat swamp forest using satellite imaging radar**

Matthew Scott Waldram

# Abstract

Satellite radar imaging is a promising technique for biomass mapping and the monitoring of deforestation in tropical forests and reducing the uncertainty in the quantification of forest biomass in tropical regions. The present paradigm in radar imaging is the fitting of empirical relationships between the radar signal and biomass for diverse forest ecosystems, especially in the humid tropics. Therefore, there is a great need to generate knowledge about how to monitor and characterise the biomass of intact and disturbed tropical forest biomass. This research presents the analysis of data from four years of L-band radar imagery from ALOS PALSAR within a carbon dense, tropical peat swamp forest ecosystem in Central Kalimantan (Indonesia).

The results showed that the temporal behaviour of the radar signal varied across a gradient of forest biomass, being highly variable at low biomass levels. Critically a large amount of signal change was unrelated to biomass change. Changes in the radar signal were related in a complex non-linear manner to changes in the peatland water table. This allowed, for the first time, the estimation of water table depth at high spatial resolutions from radar images. It was found that the radar signal related to loss of primary forest biomass after fire were in the opposite direction to that expected according to fitted radar-biomass equations. Burnt areas showed highly variable temporal radar with variability linked to rainfall indicating a possible interaction between the water table and remaining (dead) aboveground biomass.

The implications of these results are that, at least in tropical peatlands, estimates of biomass based on single date radar images are likely to be highly misleading; multitemporal radar data sets are required to both interpret disturbance histories and to produce accurate classifications of above ground biomass.

# Acknowledgements

I would like to thank Prof. Sue Page for her unrivalled knowledge of and contacts in the world of tropical peatlands. Dr. Kevin Tansey for taking the time to introduce me to the dark arts of radar remote sensing, radar processing and scripting. You were both patient and understanding supervisors, thank you for all your support.

Thanks are also due to:

Dr Suwido Limin and his staff at CIMTROP, the University of PalangkaRaya for their assistance in the field. The Indonesian Australian Forest Carbon Partnership staff for further field assistance and the free sharing of project data. Also Laura Graham for taking the time to explain the IAFCP field protocols, Al Hooijer and Ronald Vernimmen who shared their bias corrected TRMM data and their expertise concerning peatland hydrology and the OUTrop project in the Sebangau forest who provided assistance and accommodation when the degraded peatlands got too much.

To my fellow graduate students, particularly Ross Morrison for many a discussion and to Bashar Dahdal for sharing those first small steps of peatland exploration. Tetsuo Shimamura, Agata Hoscilo helped to introduce me to tropical peatlands and for sharing their knowledge of peat swamp forest and peatland fire regimes respectively. Also the University of Leicester HPC team particularly Liam Gretton for help with cluster computing. To the NCEO who provided a fantastic training network, thank you also to Shaun Quegan for radar advice and Martin Whittle for sharing computer codes and radar images. This research was funded by the National Environment Research Council, through the National Centre for Earth Observation; Carbon Cycle theme.

And finally but most importantly, to Emma for her patience and for keeping an eye on the important things.....

# Table of Contents

## List of Figures

## List of Tables

# Glossary

| | | |
|---|---|---|
| ex-MRP | - | The ex-Mega Rice Project in Central Kalimantan, Indonesia |
| EOF | - | Empirical Orthogonal Function |
| Gt | - | Gigatonnes= $1*10^9$kg = petagram = $*10^{15}$g |
| GCC | - | Global Carbon Cycle |
| IAFCP | - | Indonesia/Australia Forest Carbon Partnership |
| LULUCF | - | Land use, Land use change, Forestry |
| MODIS | - | Moderate-Resolution Imaging Spectroradiometer |
| PCA | - | Principal component analysis |
| PSF | - | Peat Swamp Forest |
| REDD | - | Reducing Emissions from Deforestation and forest Degradation |
| SAR | - | Synthetic Aperture Radar |
| tMean | - | Temporal mean |
| tSD | - | Temporal standard deviation |
| TRMM | - | Tropical Rainfall Measuring Mission |
| t $CO_{2e}$ $ha^{-1}$ $year^{-1}$ | - | Area based carbon flux: reported as tonnes of carbon dioxide equivalents per hectare per year |
| Gt $CO_{2e}$ $year^{-1}$ | - | Total carbon flux |
| radar signal | - | Change in the radar variable between $t_1$ and $t_2$ |

# 1. Introduction

## 1.1 Research Aim

The overall aim of this research is to contribute knowledge towards a robust remote sensing system that is able to reduce the uncertainty in the estimation of carbon stocks in tropical forests through the use of remote sensing and to hence more accurately and consistently resolve the carbon fluxes that result from land use change processes operating in these environments.

Although there is a long history of using various remote sensing techniques, in conjunction with field mensuration, to estimate forest properties (such as area, stem density, canopy height, biomass, etc) this has been largely confined to experimental work and has been limited in both temporal and spatial domains. There is a need, driven by and the emerging carbon economy and international forest negotiations aimed at reducing carbon emissions, to move beyond the experimental to wide area, frequent, operational monitoring of forest resources. Such systems are likely to require multi-sensor, semi automated approaches to monitoring rather than simply mapping tropical forests.

This thesis aims to contribute to such a system by examining the temporal change signatures captured within four years of L-band radar images obtained over tropical peat swamp forest and relating these to land use change processes occurring on the ground.

## 1.2 Tropical forests and the global carbon cycle

The global carbon cycle (GCC) is composed of an interlinked network of carbon pools (carbon in its various chemical states) connected together by fluxes; reactions which alter or move the carbon from one chemical state to another (Figure 1.1). Our need to understand the processes governing these pools and fluxes has increased over the last ~30 years in conjunction with our need to control the increase of atmospheric $CO_2$ in order to prevent harmful global warming (IPCC, 2007). A complete understanding of the GCC is difficult as it requires the integration of processes occurring at different spatial scales (from individual leaves to interactions between ecosystems) and temporal scales (from daily photosynthetic fluxes to multi-decadal accumulations of carbon in old growth forests). These processes require the use of a variety of research techniques and integration of these into single yet accurate estimates. In addition to these scaling issues we do not have adequate knowledge of many aspects of the GCC, particularly of those processes operating over very large spatial scales (Meir et al., 2006) and this leads to large uncertainties in estimates of the pools and fluxes controlling the GCC.

Terrestrial ecosystems convert atmospheric $CO_2$ into organic carbon via photosynthesis and large pools of carbon accumulate in vegetation and

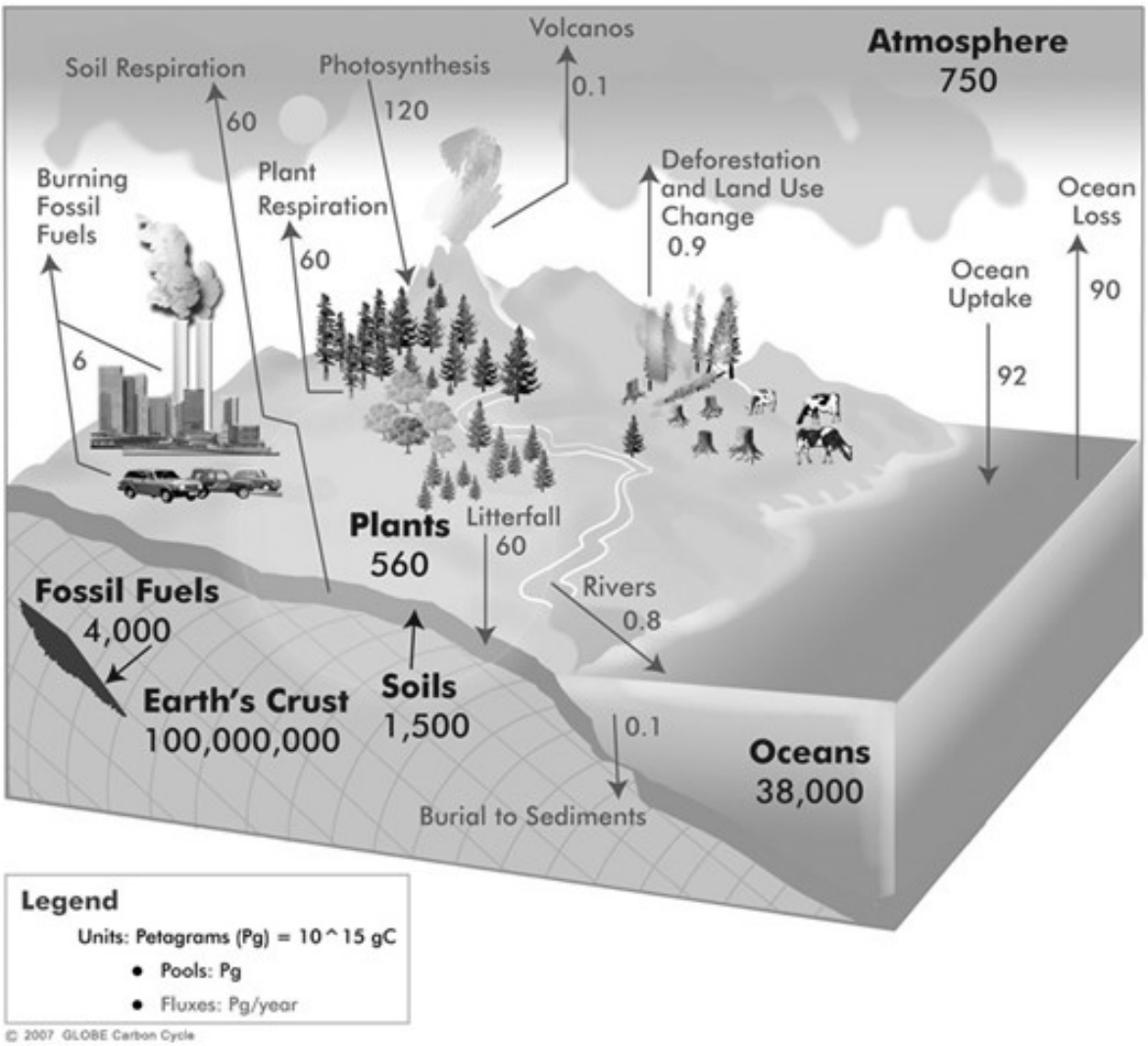


Figure 1.1. Pools and fluxes of carbon within the GCC. (figure taken, with permission, from http://www.globe.gov/image/image_gallery?img_id=2595661&fileName=Global_Carbon_Cycle_diagram-2009.jpg&t=1357917736330)

subsequently in the soil. The amount of carbon stored in terrestrial systems is related to climatic constraints, ecological conditions and disturbances events. Tropical forests contain large amounts of carbon as vegetation, making tropical forests particularly important pools of carbon. As ecosystems reach maturity they achieve a dynamic equilibrium whereby the carbon gained by photosynthesis equals that lost by net ecosystem respiration and biomass accumulation through growth is balanced by that lost by decomposition (though in some circumstances carbon can continue to

accumulate in soil). Disturbances to this equilibrium result in changes to the carbon balance that operate over time scales varying from daily (e.g. the balance between photosynthesis and respiration in a leaf) to millennial (e.g. the shifting range of biomes between ice ages). Anthropogenic disturbances to terrestrial vegetation, such as the clearance of forests for agriculture (also known as land use change), result in fluxes of carbon to the atmosphere. Since the industrial revolution 7-11*$10^6$$km^2$ of forest has been cleared (Foley et al., 2005), largely from the developed nations in the northern hemisphere. The sum of emissions due to changes in land management and land use along with the response of forest to disturbance are summed to give the land atmosphere flux. Since the 1960s, land use change has contributed ~20% of annual $CO_2$ emissions, with the source of emissions changing from extra tropical nations to being almost exclusively tropical (Canadell et al., 2007).

## 1.3 Difficulties in calculating forest carbon pools and fluxes.

When calculating forest carbon pools a number of compounding uncertainties result in very large uncertainties in the final estimates. Firstly estimates of tropical forest cover vary from 1116*$10^4$ $km^2$ (Achard et al. 2002) to 1768*$10^4$ $km^2$ (Grainger 2008). Uncertainties in the amount and distribution of forest biomass further enlarge these errors. For example, values given for the biomass content of the Amazonian rainforest vary from 39-93 Gt (Houghton & Lawrence, 2001), 86 +/-20 Gt (Saatchi et al. 2007) when including dead and below ground biomass to 93+/-23 Gt excluding roots and dead biomass (Malhi et al., 2006). Figure 1.1 illustrates the spatial distribution of uncertainties when producing a biomass estimate using a single methodology from remote sensing data (from Saatchi et al., 2011). Uncertainties are much larger when contrasting

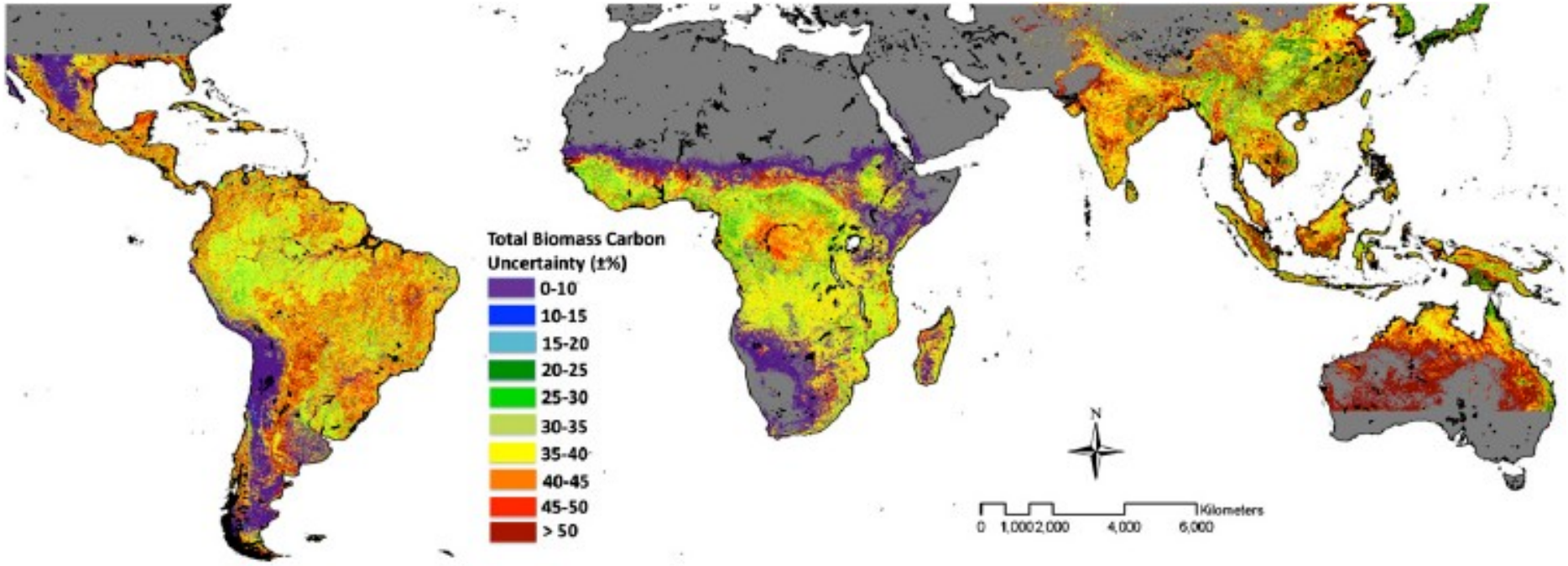


Figure 1.2. Uncertainty in the amount of estimated tropical biomass. Note high values of uncertainty located in south east Asia, figure taken from and © (Saatchi et al., 2011).

estimates produced by different methodologies for biomass estimation (e.g. Mitchard et al., 2011). Calculating the $CO_2$ flux produced by land use changes such as deforestation involves calculating the area of forest lost over a certain time period and multiplying this by estimates of the amount of carbon contained in these forests. As there are compounding errors particularly in the estimation of forest biomass there is often a high degree of uncertainty related to these values (see examples given in Figure 1.3). Achard et al. (2002) give an estimate of the global deforestation rate of $5.8*10^4$ $km^2$ (+/- 1.4) from the monitoring of global hotspots of deforestation between 1990 and 1997. A useful overview of estimates of the resultant carbon fluxes is given by Cramer (2004). Yearly carbon emission rates vary from 1.9 Gt of carbon per year (Houghton 1999) whereas DeFries et al (2002) quote lower figures of 0.65 and 0.97 Gt per year for the 1980s and 1990s, respectively. It is for these reasons that terrestrial carbon fluxes are currently the least well constrained component of the GCC with largest uncertainties in tropical regions as can be seen in Figure 1.3. A further complication is that the terrestrial portion of the GCC also shows interannual variability.

## 1.4 Requirements for future forest monitoring capabilities.

The requirement for more detailed information on tropical forest cover and biomass is driven by a need to reduce the uncertainties associated with estimates of the forest carbon pool and related fluxes in order to better understand the role played by tropical forests within the GCC. Reducing emissions from tropical land use change has been identified as the most cost effective method of lessening the increase of atmospheric $CO_2$ (Eliasch, 2008),

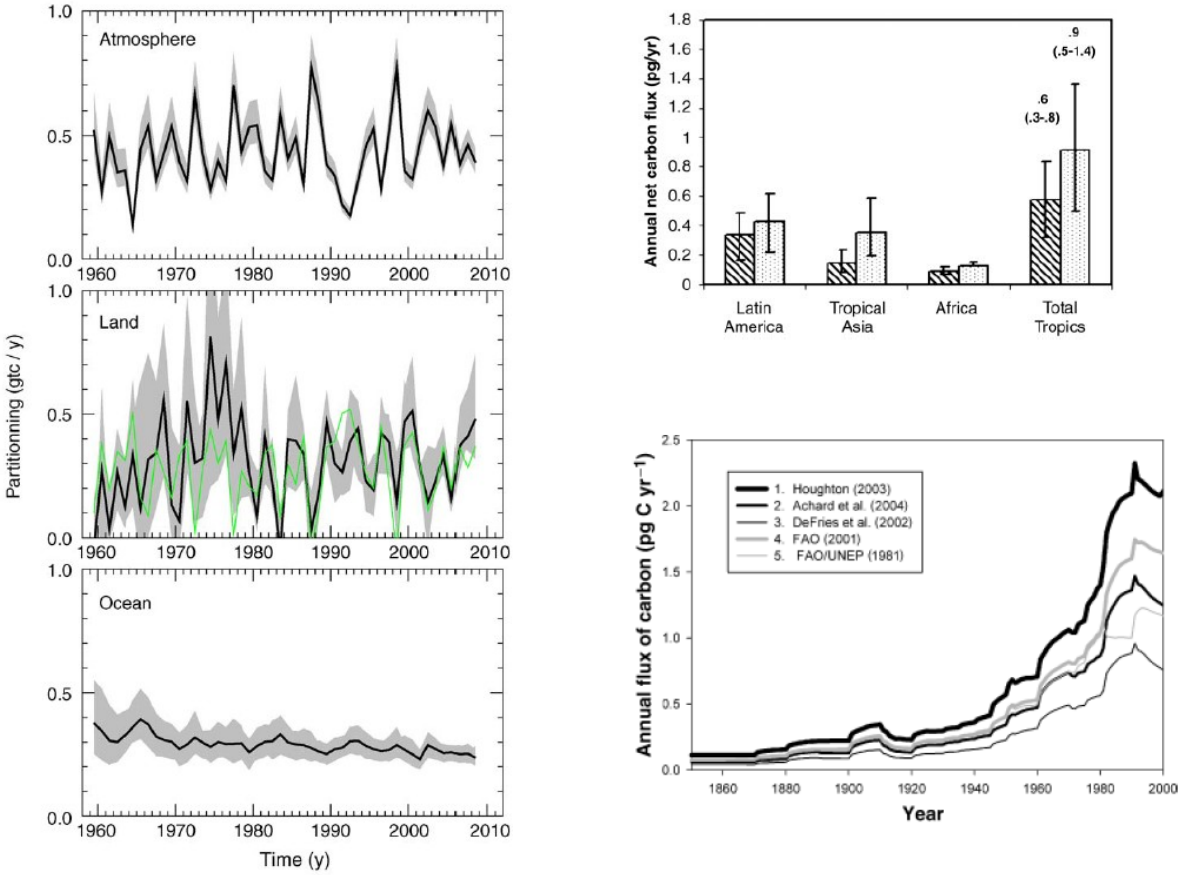


Figure 1.3 Examples of uncertainties in terrestrial carbon fluxes. Left; partitioning of anthropogenic carbon emissions. Note high variability and uncertainty surrounding the land component, middle compared to atmosphere and ocean (from Le Quéré, 2010, ©Elsevier). Top right; carbon fluxes as a result of tropical deforestation. Note large error bars in relation to size of estimates (from and © DeFries, 2002). Bottom right; changes in the annual carbon emissions from land use change in the tropics as calculated using different methods (from and © Houghton, 2005, © Wiley)

while further motivation for the development of forest monitoring tools is the framework agreement to reduce emissions from deforestation and forest degradation (known as REDD) which was agreed at the UNFCCC COP13 in Bali, 2005. REDD+ goes beyond deforestation and forest degradation to include sustainable forest management and other enhancements of forest carbon. Although to date no REDD( or REDD+) agreement has been formally signed, significant progress has been made on several key aspects which are likely to be included should any agreement come to fruition. These include information on baseline historical rates of deforestation that are likely to be sourced from the Landsat data archive, and the requirement for up to date spatial information on areas affected by forest loss and degradation and on forest carbon stocks. Any agreement to reduce tropical deforestation would also have substantial co-benefits with efforts to reduce biodiversity loss (e.g. Venter et al., 2009), thus forest monitoring techniques are likely to have significant importance for forest reserve design and management. The work presented in this thesis is likely to prove beneficial to the monitoring, reporting and validation (aka MRV) activities of REDD and could also be of use in REDD+ where management enhancements reduce the occurrence of forest disturbance.

## 1.5 Thesis structure

Chapter 2: Literature review. Remote sensing technologies and techniques for monitoring tropical forests are introduced as well as the advantages and limitations of specific techniques and the role they can play in providing data towards a monitoring system for tropical forests. The characteristics of tropical

peatlands and peat swamp forest are presented; their distribution, high carbon density and impact on global carbon fluxes are discussed. Finally research gaps are identified and knowledge requirements are summarised and research questions are specified.

Chapter 3: Methodology. This chapter gives details on the study area and the processes used to produce the temporal radar stacks and the vegetation sampling field methods used to create the forest biomass dataset. Both of these datasets are used throughout this thesis. Data sets and methodologies specific to individual analyses are discussed in the relevant chapters.

Chapter 4. In this chapter the spatio-temporal patterns of radar backscatter change in the study area are analysed and related to above ground forest biomass levels and land surface processes occurring in the study area. This chapter lays the foundation for the succeeding two chapters which look in detail at the different aspects of temporal backscatter change.

Chapter 5. In this chapter the portion of the radar change unrelated to vegetation disturbance is examined in detail. Radar backscatter and interferometric coherence are shown to be related to variations in the peatland water table and this relationship is then used inversely to provide high resolution maps of estimated peatland water table depth from the radar data.

Chapter 6. The temporal backscatter change associated with vegetation change (peat swamp forest through fire) is examined in more detail in this

chapter. Fire occurrences within our dataset were limited so an independently derived fire history dataset is used to construct long term estimates of backscatter variation associated with historical fires. The effects of fire frequency and the period since fire are examined. Variation in the radar signal is linked to monthly rainfall estimates.

Chapter 7 summarises the results from the individual chapters and synthesises them into conclusions for monitoring peat swamp forest with radar data. Implications for the use of radar in monitoring other forest ecosystems and the role to be played by radar in global forest monitoring systems and possibilities for future research are discussed.

# 2. Literature Review

The first section in this chapter the reviews literature relating to tropical peat swamp forests and their role as a globally important carbon pool. Methods for monitoring changes in tropical forests are then examined with a particular emphasis on the use of remotely sensed data and the role that these can play in a system for the monitoring of tropical forests. Subsequently current knowledge gaps are identified and used to frame the research objectives to be pursued in this thesis.

This thesis focuses on one tropical forest ecosystem, namely tropical peat swamp forest. Located mostly in Southeast Asia, this ecosystem has a high carbon density but is vulnerable to destabilisation through human and climate induced changes.

## 2.1 Tropical peatlands and peat swamp forests

Peatlands form where anaerobic soil conditions in waterlogged soils impede the decomposition of organic inputs to the soil (dead plant matter). The resultant build up of organic matter into layers of peat forms a significant pool of carbon within the GCC (Vasander & Kettunen, 2006). Disturbances to these peatlands can lead to significant fluxes of $CO_2$ and $CH_4$ to the atmosphere (e.g. Macdonald et al., 2006) as stored carbon becomes accessible for decomposition. Large areas of peatland occur in boreal areas, however, peatlands also occur in poorly drained areas of the tropics. Tropical peatlands

have been estimated to comprise 11% of global peatlands by area (Page et al., 2011) although accurate estimates of the extent of tropical peatlands are difficult due to their remoteness and inaccessibility. Current best estimates suggest that tropical peatlands are concentrated in South East Asia; this region contains 56% of the total tropical peatlands by area, located in Malaysia, Indonesia and to a lesser extent in Papua New Guinea (Page et al., 2011) and covering an area of 24.8 to $27.1*10^4$ $km^2$ (Aljosja Hooijer et al., 2010; Page et al., 2011).

In order to calculate the size of the tropical peatland carbon pool, data on the thickness of peatland deposits are required in order to estimate peat volume. Tropical peatlands can reach depths of up to 20m (Page et al., 1999) much deeper than boreal peatlands which typically have depths of only a few meters. Accurate characterisation of the topography of peatlands is difficult due to the arduous fieldwork techniques required and data on both surface and subsurface topography are severely lacking. Remote sensing, especially radar and LiDAR can provide some topographical information (Ballhorn et al., 2011; Jaenicke et al. 2008) useful for peat volume estimation but ground measurements are still required to give information on peat depth that is necessary for accurate peat volume estimation. Outside the South East Asian region, tropical peatlands have also been found in the Congo basin of Africa and in the neotropics (Lähteenoja et al., 2012; Wright et al., 2011) although knowledge of the extent, depth and carbon content of these peatlands is particularly lacking.

Due to various data uncertainties, estimates of the size of the South East Asian peatland carbon pool vary widely and have large error margins. A conservative estimate of 55Gt +/- 10Gt is given by Jaenicke et al (2008). A larger value of 65.2Gt is reported by Page et al. (2011) with a global tropical peat carbon pool of 88.6Gt. This latter value represents 15-20% of the total global peatland carbon pool making tropical peatlands, especially those in South East Asia, globally significant.

Tropical peatlands in South East Asia typically form dome shaped structures between watercourses with peat maximum depth situated at greatest distance from the rivers and reducing peat depth closer to rivers. In South East Asia intact peatlands are covered by a type of tropical forest called Peat Swamp Forest (PSF). PSF differs from tropical forests growing on mineral soils in that the trees are generally shorter, have smaller diameters, higher stem densities and adaptations to coping with waterlogged soils such as breathing roots (pneumatophores). There is a zonation of forest communities within a PSF largely distinguished by tree height and linked to the structure of the peat dome by the hydrological conditions. Riverine forest is found on shallow peat soils closest to watercourses, followed by shorter statured mixed swamp forest (Page et al., 1999). Towards the centre of the peat dome and almost permanently flooded is low pole forest where tree height rarely exceeds 15m. Some peat domes also have areas of open water in or close to the highest part of the dome, although these are not always present and are often the first features to disappear once peatlands are disturbed. PSFs support high levels of biodiversity including endangered species such as Gibbon (*Hylobates sp*.)

and Orangutans (*Pongo pygmaus pygmaeus )* along with habitat endemics (Yule 2008) and perform useful ecosystem services such as water regulation and storage (Page et al., 2009).

Intact peatlands the capillary action of the peat maintains the water table close to the surface of the peatland and usually within 30cm of the peat surface. The stagnant water table maintains anaerobic conditions which impede the decomposition of organic inputs (leaf and branch fall of the forest trees) and lead to the accumulation of large and, if left intact, stable stocks of peat. The hydrological balance that maintains tropical peatlands is delicate and can be disturbed both by a combination of climatic changes (i.e. periods of low rainfall) and anthropogenic interference. South East Asian PSFs are threatened by logging for timber, plywood and chipboard manufacture and clearing for silvicultural plantations (mainly of *Elaeis guineensis* for palm oil and *Acacia* sp. for wood pulp and paper manufacture) and drainage for agriculture. All of these anthropogenic processes involve drainage of the peatlands through the construction of networks of ditches and canals which have the effect of lowering the peatland water table leading to exposure (see Figure 2.1) of the peat to atmospheric oxygen and decomposition (Hirano et al., 2008). As the peat dries there is also an increased risk of fire (Hoscilo, 2009). Fires lead to a rapid loss of forest cover, accumulation of dead wood and an increased likelihood of further fires (Page et al., 2009). Both drainage and fire result in the loss of large amounts of carbon (largely in the form of $CO_2$) to the atmosphere from the peatland as well as increased rates of carbon loss through the waterways (Moore et al., 2011). The degradation

pathway of PSF varies according to the length of the dry season in that area. In areas with a relatively short  dry season drainage leads to peat oxidation and compaction (Hooijer et al., 2012; Jauhiainen et al., 2012) even at distances of 2 km from the drainage canal. In areas where the dry season is more severe as in Central Kalimantan there the fires that occur are particularly linked to periods of low rainfall associated with El Nino events (Field et al., 2009; Siegert et al., 2001) leading to an accelerated degradation pathway as primary forest is lost to subsurface peat fires. Once-burnt primary forest is vulnerable to further fires due to the high surface fuel load of dead wood and further lowering of the water table as the peat is exposed to the sun. Although forest regeneration is possible after a single fire, due to the residual seed bank and proximity of undisturbed forest, further fires are almost inevitable and forest regeneration potential is then greatly reduced. The heightened fire risk is exacerbated by the colonisation of the peat surface by ferns, which provide a flammable fine fuel load.

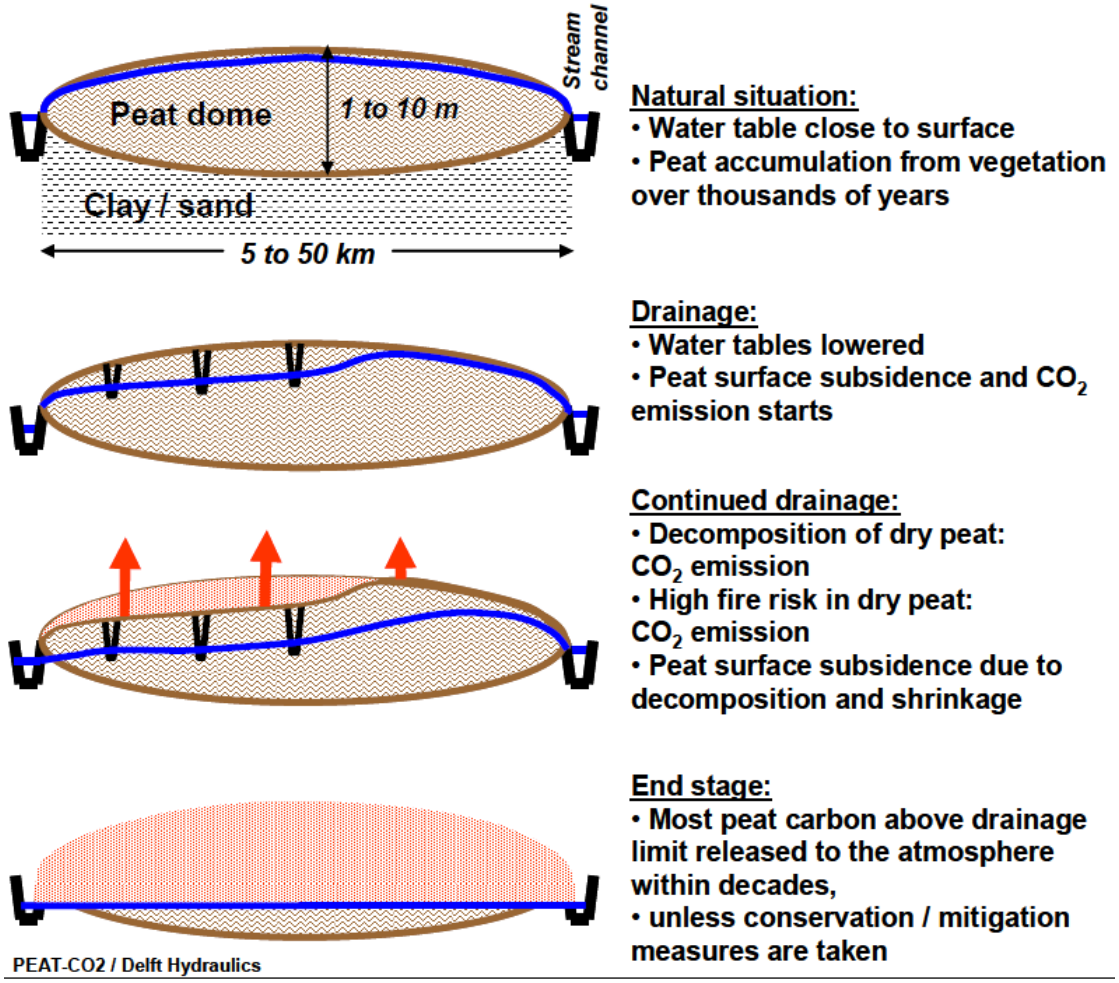


Figure 2.1. Mechanism of peatland degradation. Figure taken from and © Hooijer et al., 2010. Red arrows indicate fluxes of carbon from the peatland to the atmosphere.

Prior to the 1960s, although there had been large scale degradation of peatlands in peninsular Malaysia due to colonial timber plantations, the insular peatlands in Borneo and Sumatra had remained relatively intact. As undisturbed forests are resistant to degradation fires occurred only rarely in the 1960's despite periods of low rainfall (Miettinen et al., 2012). As a result of changes in land use policies, particularly in Indonesia, which promoted development in forested areas (Dennis & Colfer, 2006) by the 1980's fires had

become more frequent during periods of low rainfall (Field et al., 2009) due to encroachments into the forest. Extensive fires occurred in South East Asia in 1997 during a severe El Nino period resulting in estimated carbon emissions of 0.81-2.75 Gt from the peat to the atmosphere; equivalent to 13-40% of total global fossil fuel emissions in the same year (Page et al., 2002). The 1997 fires also had significant effects on the health of local populations and lowered surrounding sea surface temperatures by intercepting solar radiation (Rajeev et al., 2008). Satellite studies indicate that by 2010 20% ($3.1*10^4$ $km^2$) of South East Asian peatlands had been converted into plantations, resulting in emissions of between annual carbon emissions 0.230 and 0.310 Gt $CO_{2e}$ $y^{-1}$ to the atmosphere as a result of peat oxidation (Miettinen et al., 2012). Once plantations are established on peat soils the peat continues to decompose because the water table is maintained in a drained state in order to promote tree growth (for example, oil palm requires a water table that is at least 60 cm below the peat surface, but in practice is often much lower), leading to fluxes estimated at 86 t $CO_{2e}$ $ha^{-1}$ $year^{-1}$ (Jauhiainen et al., 2012; Page et al., 2011). In 2010, Hooijer et al. (2010) estimated that almost half of the total peatland area ($12.9*10^4$ $km^2$, Hooijer et al., 2010) with total carbon fluxes due to peatland drainage and degradation estimated at between 0.355 and 0.855 Gt per year. These emission estimates put carbon fluxes from tropical peatlands as contributing between 1.3 and 3.1% of total current global carbon emissions.

These large pools and fluxes of carbon from tropical peatlands in South East Asia make them attractive areas for forest restoration particularly if any future

REDD mechanism is extended to include soil carbon, since potential carbon payments would be substantial (Busch et al., 2012). A forest carbon funding partnership has been instigated between Norway and Indonesia and a moratorium on the issuing of forest concession licenses in primary forest and peatlands has been put in place (Presidential Instruction No. 10/2011),although doubts remain over its scope and efficacy (Clements et al., 2010; Murdiyarso et al., 2011). Current peatland restoration techniques concentrate on damming drainage channels in order to restore the hydrology of the peatland and raise the level of the water table alongside assisted regeneration of the forest by planting and fire control (Page et al., 2009). Although tropical PSF are globally an uncommon vegetation type it is clear from the review above that due to the size and vulnerability of the sub-surface carbon pool, the rapid rates of conversion to other land uses and their degradation by fire that they are a globally relevant source of carbon fluxes to the atmosphere. Tropical peatlands globally contain 50-70 Gt carbon (3% global soil carbon, Page et al. 2011) but land use changes and fire are reducing this carbon store and contributing to greenhouse gas emissions to the atmosphere. Information on the sizes of these emissions is urgently required as a failure to account for these emissions could lead to underestimates of future rates of increase in atmospheric GHGs and the extent of human induced climate change. Improved understanding of tropical peat swamp forest carbon dynamics has implications for and relevance to a range of national and international policies and obligations dealing with climate change, including REDD.

## 2.2 Remote sensing of tropical forests

The United Nations Food and Agriculture Organization (FAO) has produced Forest Resource Assessments (FRAs) since 1948 every 5-10 years and this series of reports provides the longest international dataset on changes in forest cover. The methodology for the reports was initially based on data produced by participating countries, however missing data, differing methodologies (both between countries and between assessments) and variations in the definition of forest in different countries have limited the utility of the data for the accurate reporting of changes in forest cover or for calculating carbon emissions from LULUCF (land use, land use change and forestry). Estimates of forest loss derived from remote sensing are typically higher than those from the FAO statistics (e.g. Shearman et al., 2009), meaning that the FAO forest estimates can detect relative changes in forest cover but do not give accurate estimates of absolute forest cover (Grainger, 2008). With the advent of remote sensing it became possible for scientists to make more direct observations of tropical forests and the most recent FAO report (Lindquist et al., 2012) has evolved to include remotely sensed data. There are three remote sensing methodologies of use for monitoring changes in tropical forests. These are optical remote sensing, LiDAR and radar remote sensing. Of these, optical remote sensing has the longest history and is the most developed. Both radar and LiDAR are newer techniques and have been less widely adopted than optical remote sensing. Remote sensing studies of changing global tropical forest cover have mostly used optical data and take one of two approaches; wall to wall coverage or sub sampling. In the first

instance tropical areas are completely mapped at continental or global scales. Because of the amounts of data to be processed when using this approach the majority of studies have been performed at a decadal scale using composite images from low resolution optical satellites (e.g. AVHRR 8km$^2$ DeFries, 2002, SPOT 1km$^2$ Stibig et al., 2009). The second approach to estimating forest cover and forest cover change is to sub sample. In this case each sample unit (i.e. country or continent) is sub-sampled by a number of remote sensing images. These can be randomly distributed (Achard et al., 2002) or in a regular sample grid (Lindquist et al., 2012). These samples are then used to calculate statistical deforestation rates. A related approach is to use a global coverage at coarse resolution (e.g. from the MODIS satellite) to identify deforestation hotspots that can be further examined with higher spatial resolution data such as LANDSAT (Hansen et al., 2008; Hansen et al., 2010) Although coarse remote sensing resolutions (greater than 100m$^2$) allow the processing of large global forest datasets and allow the detection of long term forest trends, they are much larger than the scale of deforestation and degradation processes happening on the ground. Low resolution remote sensing data sets are therefore of little use for near real time monitoring of forest processes and higher resolutions, in the order of tens of meters, are required to adequately describe forest loss processes.

Higher resolution optical satellites (e.g. Landsat with a spatial resolution of 30m$^2$) have not in the past been used for wide area tropical forest monitoring due to the size of the datasets and computer processing limitations. However, such datasets have been used in limited spatial contexts for detection of small

scale disturbances, such as logging (Asner et al., 2002; Asner et al., 2004; Peres et al., 2006) which is not visible at lower resolutions. Recent advances in cluster computing have alleviated these constraints and considerable progress has been made in the last few years in the analysis of the historical optical satellite data archive, particularly of Landsat data, in order to provide data to calculate historical deforestation rates for use as baseline data (Huang et al., 2010; Roy et al., 2010). This has required the development of automatic spectral correction, cloud masking algorithms (Zhu & Woodcock, 2012), temporal stacks (Kennedy et al., 2010; Zhu et al., 2012) and automatic detection of disturbances (Cohen et al., 2010). The recent launch of the Landsat data continuity mission satellite will no doubt see these techniques applied to more temporally current datasets. The great limitation of optical systems is that the sensors are frequently obscured by persistent cloud cover and smoke haze; they are also effected by variations in the angle of illumination by the sun. Despite work to overcome these limitations the use of optical satellite data for high frequency monitoring of tropical forests is still limited.

LIDAR is an alternate remote sensing technology of use for forest monitoring which works by calculating the return time of laser pulses fired vertically from the sensor, thus providing information on the height distribution of vegetation within a forest and hence giving information on forest biomass. LiDAR measurements have been used extensively for aerial surveys of forest structure and biomass (e.g. Kronseder et al., 2012). One orbital LiDAR instrument has been flown onboard the ICESAT satellite. This has been used

to produce a biomass map of tropical regions (Saatchi et al., 2011). The limitations of LIDAR are that it currently produces discrete point measurements (in the case of the orbital sensors) or thin strips of data (for aerial sensors) rather than a full coverage. This means that other data sources must be used to interpolate a full coverage between LIDAR samples (Mitchard et al., 2012).

It is likely that future orbital LIDAR missions will be flown and lead to further developments for orbital biomass mapping. However LIDAR suffers from the same issue as optical remote sensing in that clouds and smoke haze prevent collection of data, a problem which requires careful filtering of the LiDAR dataset. LiDAR derived biomass data (Saatchi et al., 2011) have been combined with coarse deforestation data (Hansen et al., 2010) to give spatial estimates of carbon loss due to deforestation (Harris et al., 2012), However the resolution of these maps is still very coarse (18.5km$^2$) in comparison to deforestation and degradation processes. Nevertheless, the techniques used do point the way for multisensor data fusion techniques that will be needed to monitor carbon stocks at the resolution required to detect forest degradation. Currently such mapping has only been performed at a sub-national scale (e.g. Asner et al., 2010; Sheldon et al., 2012).

Radar remote sensing is not hampered by cloud cover since water vapour does not absorb at the microwave frequencies used and has hence been described as an all weather imaging system. Being an active system it is also able to gather information both day and night with no complications caused by differences in solar illumination angle that can complicate multidate optical

imaging. The other major advantage of radar remote sensing is that the radar waves penetrate into forest canopies rather simply reflecting from the top allowing radar remote sensing to measure structural variables of forests.

The location of scattering within the various structural elements of the forest is important to understand the nature of the returned radar signal and can vary depending on both the wavelength and polarisation of the incident radar signal. Canopy scattering occurs when the dominant scatterers are randomly orientated twigs, branches and leaves and results in a moderate amount of radar energy being returned to the sensor. Longer radar wavelengths interact less with the fine leaves and branches and tend to scatter from the larger trunks and boughs within the canopy (volume scattering). Dihedral (or double bounce) occurs when the radar signal is reflected from two surfaces at or near right angles to each other often from the ground and walls or tree trunks. This scattering mechanism produces strong radar signal returns in the co-polarised bands (HH & VV), less so in the cross-polarised bands (HV, VH). Surface (ground) scattering is generally low but is related to the roughness of the surface with increased roughness producing  increased returns, particularly in the co-polarised signal. Finally specular (mirror like) scattering occurs from smooth surfaces such as rivers and standing water and results in no returning radar energy to the sensor in any polarisation. These areas hence look black in radar images.

Coherence can be used to further discriminate the properties of surfaces. Similar phase information collected from on different dates represents a stable arrangement of scattering elements such as is found in hard structures and

open ground, whereas low coherence indicates that elements have shifted slightly such as in forest canopies. For more details on radar scattering mechanisms see Ulaby & Dobson (1989).

Most studies calculate the empirical relationship between ground measured biomass and the power of the backscattered radar signal, fit a suitable curve to the data and then use this curve in order that the relationship may be inverted to produce estimates of biomass directly from the radar data. Examples of this include (Austin, 2003; Carreiras et al., 2012; Luckman et al., 1997; Mitchard et al., 2009; Saatchi et al., 2007; Sandberg et al., 2011; Smith-Jonforsen et al., 2007; Le Toan et al., 2004; Wang et al., 1995) and many others. An example, taken from Englhart et al., (2011) is shown in Figure 2.2. Quantifying this radar:biomass calibration for various radar systems and in various ecosystems has become the dominant paradigm within radar remote sensing. A limitation of these relationships is that they give the impression of a stable relationship between radar backscatter and above ground biomass. However no indication is given of how stable the relationship is from a temporal perspective or how the relationship is likely to vary seasonally or across different vegetation types.

Detecting the biomass of tropical forests directly is, however, made difficult by the tendency of the radar returns to saturate at relatively low biomass levels compared to mature forest (Le Toan et al. 2004). Radar imaging can make use of a range of microwave frequencies, although due to design limitations only one frequency can be built into a satellite. Longer wavelengths

designated as L-band (23cm ) and P-band (69cm) give more direct information on forest biomass as they penetrate further into the forest structure and because the signal saturates at higher biomass levels (Le Toan et al., 2011; Rignot et al., 1995; Sandberg et al., 2011). Radar data can be collected at different polarisations of transmission and reception is in both the horizontal and the vertical direction giving four detection modes each of which gives different information about the area being imaged. Radar energy can also be electronically pointed giving rise to a number of different observation modes (e.g. strip mapping and spotlight mode) which utilise different polarisation combinations. A final application is radar interferometry whereby radar signals collected from different orbital positions can be compared to produce accurate maps of vertical displacement. The drawbacks of radar remote sensing are the complex and user intensive image processing chain and difficulties of image interpretation.

Radar waves, being electromagnetic, can be affected by the varying properties of the ionosphere and these can complicate radar remote sensing from orbiting satellites, particularly at longer wavelengths. Specifically the magnitude of scintillation (seemingly random increase or decrease in radar signal) and faraday rotation (rotation of polarised radar waves) vary according to solar activity (Rogers et al., 2013 ). However as this study was conducted during a period of low solar activity the effects were deemed to be negligible.

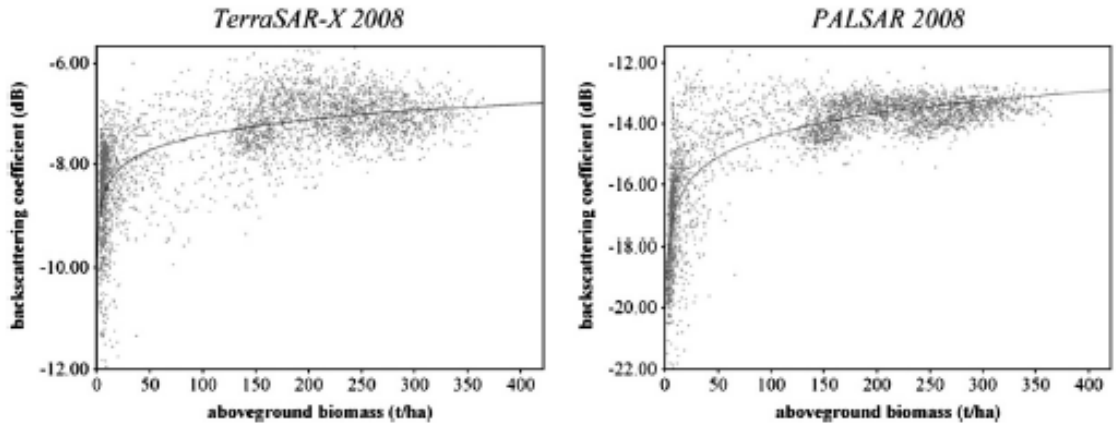


Figure 2.2 One example of an empirically fitted radar:biomass relationship (taken from Englhart et al., 2011, © Elsevier).

The properties make radar remote sensing systems particularly suitable for large scale mapping of forest cover and biomass. Radar mosaics of forests in tropical areas have previously been published from data collected by the JERS1 satellite (Rosenqvist et al., 2000) and from the PALSAR instrument (De Grandi et al., 2011), although no attempt has been made to interpret these mosaics. One issue that has to be dealt with when processing these mosaics is that because the image is made of strips of images collected on different orbits and hence dates, moisture conditions of the scenes can vary, thus changing the overall image brightness of the strips and causing sharp contrasts at strip edges (De Grandi et al., 2011).

Radar remote sensing has been used for biomass mapping via backscatter (Carreiras et al., 2012) as part of a forest cover mapping system for the Amazon (Sheldon et al., 2012) and for fire mapping in Mediterranean ecosystems (Tanase et al., 2010; Tanase et al , 2010a). Radar remote sensing has the potential for obtaining regular mapping of both forest area

and structure without the complications of cloud masking. The ability to create cloud free mosaics makes it an area of growing interest for the forest monitoring community. However few radar remote sensing studies have investigated the potential for forest monitoring in a similar manner to the advances recently made for optical remote sensing, with most studies using only single or bi-temporal sets of radar images for mapping rather than examining multi-temporal dynamics of the radar signal.

## 2.3 Summary

There is clearly a need for more detailed observations of tropical land use change processes in order to reduce the large uncertainties related to the terrestrial portion of the global carbon cycle. This need will only become more pressing should REDD or a similar scheme for preserving forest carbon become a reality. A forest monitoring system that can provide timely and accurate data concerning forest cover, biomass and disturbance detections is urgently required. Remote sensing will be key to such a system and the different techniques outlined above are suited to providing different aspects of this system.

Optical remote sensing has seen large advances in the analysis of the historical optical remote sensing archive in order to provide baseline data on forest area and deforestation rates. Although with high temporal frequency near-real time monitoring of forest cover is possible with optical remote sensing, it is not possible with current systems to do this at spatial resolutions below that of MODIS ($250m^2$) because of the need for multiple dates in order

to allow for cloud masking and compositing. Despite these limitations most of the current literature concerning the implementation of REDD suggests the use of optical systems for monitoring purposes (Gibbs et al., 2007; Herold & Johns, 2007; Herold & Skutsch, 2011).

Global LiDAR data are limited but recent studies (Mitchard et al., 2012; Saatchi et al., 2011) and work with aerial LiDAR (Asner et al., 2010) have shown the potential of LiDAR for producing accurate estimates of spatial estimates of forest biomass. The ability of radar to provide data on biomass has dominated research for a number of years, but radar remote sensing can also play an important role in prompt detection of forest disturbance. Although the processing of radar data is not straightforward the lack of clouds allows for the ready accumulation of images and thus the easy development of temporal data stacks for tracking forest change.

Any forest monitoring system is likely to consist of historical deforestation (and coarse spatial/temporal) data from optical remote sensing, location of forest carbon from LiDAR data and high frequency spatial/temporal data from radar remote sensing for disturbance detection.

## 2.4 Current knowledge gaps and research needs

The following research gaps have been identified:

- The literature on monitoring (i.e. multi-temporal datasets) of tropical forests with radar is lacking, particularly when it comes to detecting and characterising disturbances.

- Knowledge about the temporal radar signal generated by forest disturbance has not been reported in tropical peat swamp forests and rarely in other types of tropical forest.
- It is not known if the forest disturbance signal seen in the radar dataset is distinct from other temporal signals.
- There is no information on how applicable radar:biomass calibrations are in a forest monitoring context.

This thesis sets out to address these knowledge gaps through an examination of the use of long wavelength (L-band) radar remote sensing and its potential application for monitoring forest loss in a carbon-dense tropical forest ecosystem: peat swamp forest in Southeast Asia. The problem of understanding temporal changes in the radar signal is approached from the 'bottom up', seeking to understand the behaviour of the radar signal in small areas rather than using a 'top down' approach of constructing global radar mosaics.

## 2.5 Research Objectives

Specifically:

1. To observe the temporal pattern of the radar signal change across a four year dataset and examine how these patterns are related to landscape processes such as deforestation (Chapter 4).
2. To examine the effect that ecosystem processes other than changes in above ground biomass have on the radar dataset (Chapter 5).
3. To examine the radar signal occurring as a result of loss of peat swamp forest through fire (Chapter 6).

# 3. Study area, data collection & data processing

This chapter begins with an introduction to the study area, its climate and recent history, before moving on to the methodology for collection of above ground biomass data in the field. Finally a detailed account of the radar processing methodology is given.

## 3.1 Study Area

The province of Central Kalimantan, Indonesia is located in the southern half of the island of Borneo. PalangkaRaya is the provincial capital and is located on the banks of the Kahayan River and is surrounded by extensive peatlands occupying the low lying coastal plains. This area was chosen as the study site (Figure 3.1) because of the range of intact and degraded peatlands occurring across the landscape and because previous research projects have provided detailed information about the history and mechanisms of forest loss. There were also pre-existing collaborative partnerships built up with local institutions, giving access to and pre-existing data sets and field teams. The study area covered an area of 28,500km$^2$ or approximately 3.7% of the land area of Borneo.

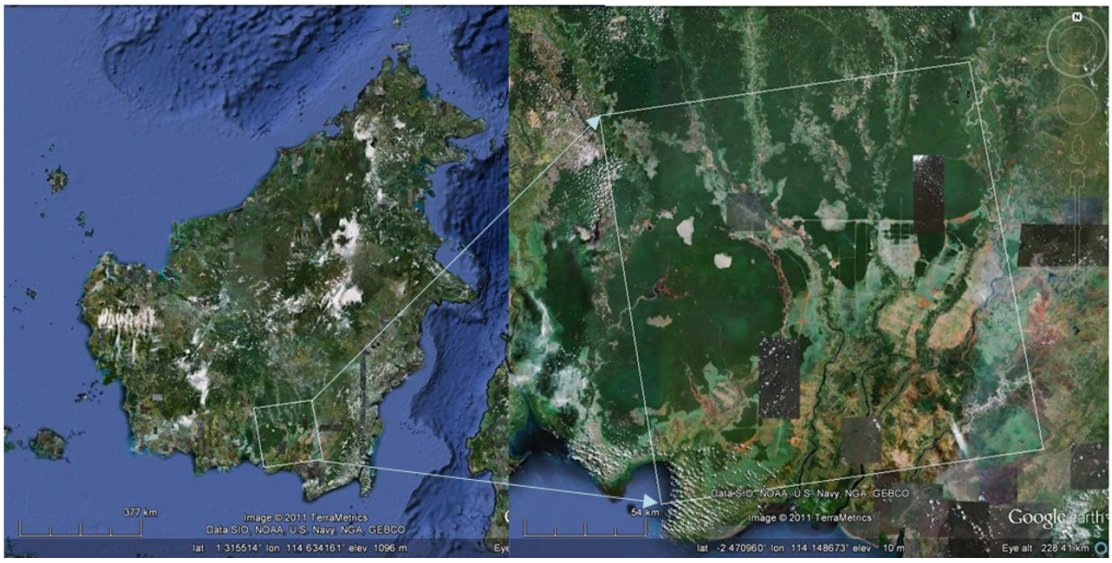


Figure 3.1. Map showing the location of the study area (right square outline) in Central Kalimantan on the island of Borneo (left). Images from and © Google Earth.

### 3.1.1 Climate

The area experiences a monsoonal climate with annual rainfall averaging 2700 cm a year (Hooijer et al., 2008). Rainfall is greatest in the 9 month period between October and June. The 'dry' season months, between July and September typically see rainfall reduced to less 5 cm per month (Hooijer et al., 2008) shown in Figure 3.2. However the length and severity of the dry season is highly variable and is strongly influenced by El Nino, becoming longer and more severe when El Nino episodes occur (Wooster et al., 2011). The relatively long duration and unpredictability of the dry season in Central Kalimantan in comparison to other peatland areas in South East Asia makes the area prone to wild fires. Air temperature is relatively constant throughout the year and is in the range of 25-27$^{o}$C (Moore et al., 2011).

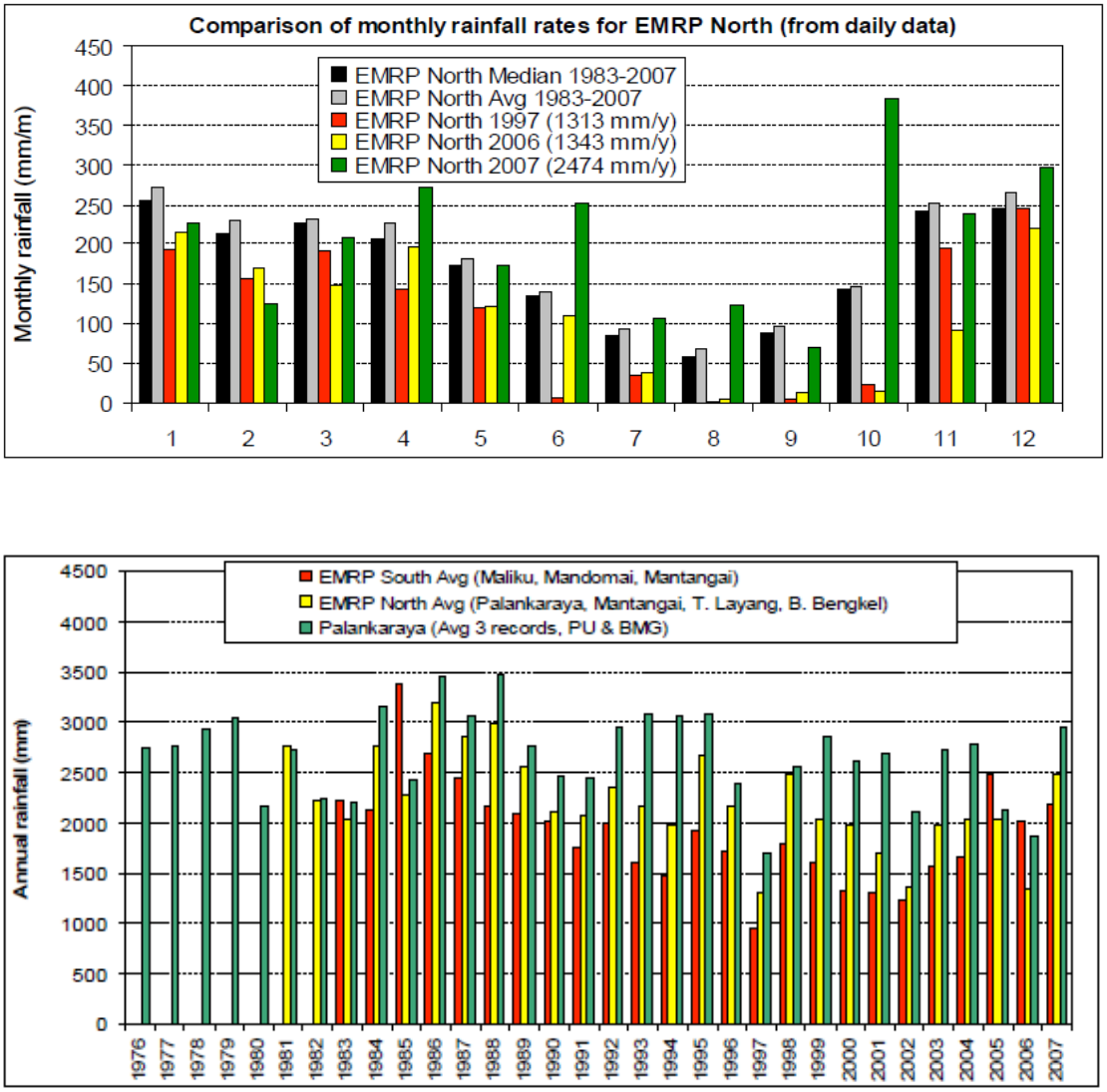


Figure 3.2. Top: average long term monthly rainfall (grey) in the study area, in low rainfall period (red and yellow) an in high rainfall years (green). Bottom: annual rainfall in the study area. Taken from Hooijer et al (2008).

### 3.1.2 Recent history of forest loss, fire and development

Prior to the 1970s most of the local population were indigenous to Central Kalimantan and resided along the major rivers, living by fishing and small scale subsistence agriculture. In the late 1970s and 1980s this population was boosted by the Indonesian government's transmigration programme which moved people from the heavily populated islands of Java and Sumatra and

moved them to less densely populated and 'less developed' regions such as Kalimantan (Abdoellah, 1987). Within the study area, transmigrant communities settled on peat and alluvial in the southern part of the study area close to the River Kahayan and a limited number of drainage canals were dug to facilitate agriculture. Fire is used as a land management tool by local people and in years of average rainfall the fires are easily controlled and cause few problems.

The next major change to affect the area was the initiation in 1996 of the Mega Rice Project (MRP) which aimed to convert 10,000 $km^2$ of PSF into paddy fields for the cultivation of rice. In order to facilitate this, a network of canals were dug across the peatland domes to provide irrigation/drainage (shown in Figure 3.7). These canals had the effect of lowering the peatland water table and exposing previously wet, anoxic peat to the atmosphere, thereby facilitating the loss of the peat through aerobic decomposition and an increased incidence of fire. The acidic, nutrient-poor peat soils proved unsuitable for rice production and the project was soon abandoned (Muhamad & Rieley, 2002). The area is now referred to as the ex-Mega Rice Project (exMRP; the block names used in the project are still used to refer to the four large land parcels of land, see Figure 3.3). The MRP left behind a legacy of peat fires, forest loss and environmental degradation.

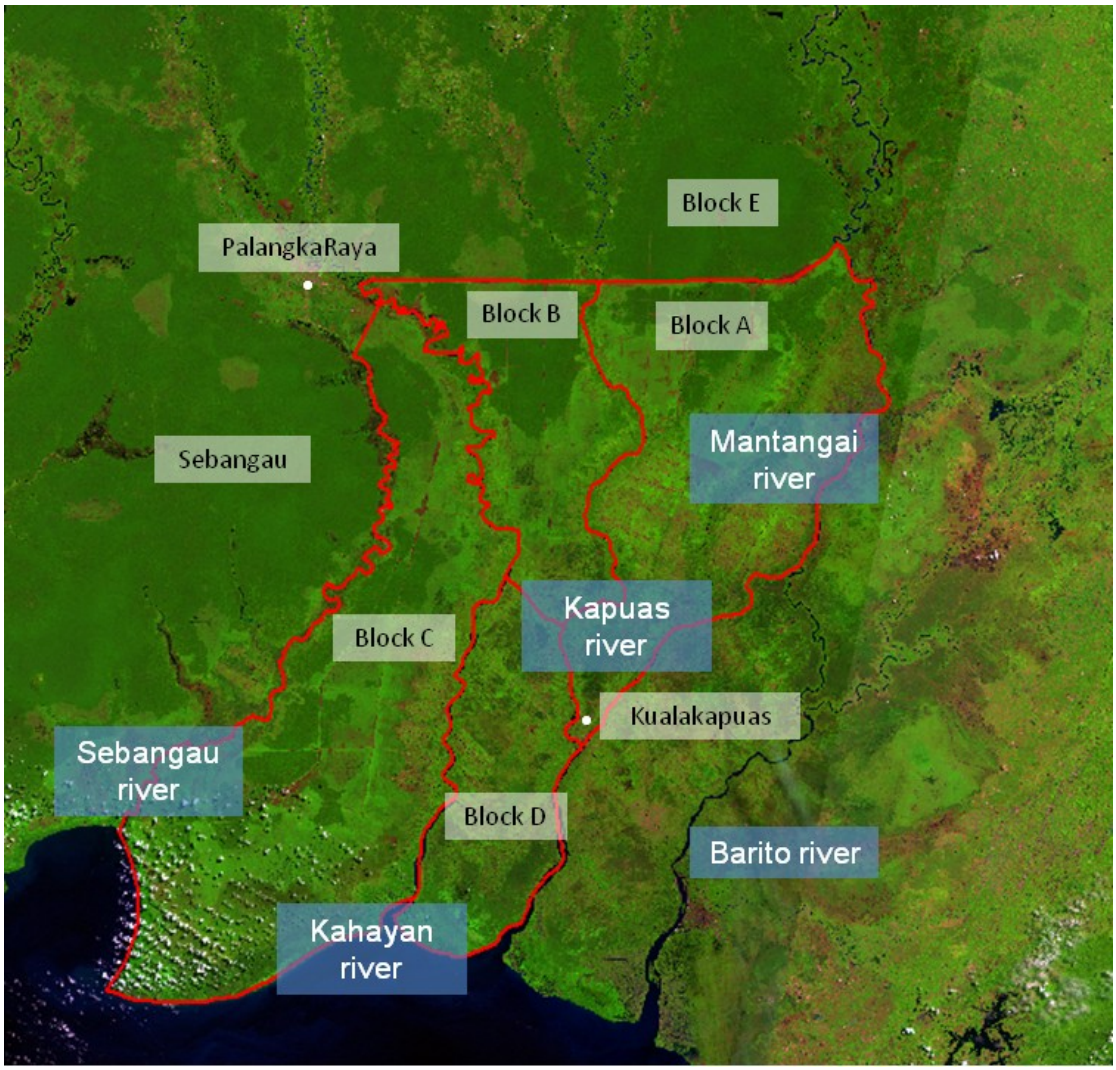


Figure 3.3 Location of the blocks of ex-Mega Rice Project (red outline) and the Sebangau forest in Central Kalimantan, Indonesia. Also shown are the towns of PalangkaRaya and Kualakapuas and the local rivers in blue. Remaining areas of forest show as dark green. Background image is from the Global Landcover 2000 collection, USGS/NASA Landsat.

Hoscilo et al (2011) provide a history of the land cover in the study area based on a time series of remote sensed images. In the early 1970s, the land cover consisted largely of intact peat swamp and riverine forests, with some transmigration settlements at the southern end of Block C (see Figure 3.4). Over the next 30 years the area of peat swamp forest was reduced by 72% to

be replaced by mosaics of trees and non-woody vegetation (grasses and ferns). This change in vegetation cover was a result of an increase in fire frequency (Figure 3.5) with fires spreading away from the vicinity of the drainage channels and roads. Prior to the establishment of the MRP fire return intervals were in the order of 10 years. After the initiation of the MRP and in conjunction with the intense El Nino episode of 1997-98, large areas of peat swamp forest were lost to fires with the carbon emissions from this one event having impacts at both local and global scales (Page et al., 2002). Since then periodic fires have become much more frequent with return periods of 2-5 years, with the most recent fires occurring in October 2009. A result of the fire history is that the landscape presents a range of biomass and disturbance histories over which to study the changes in the radar signal and also the opportunity for direct observation of disturbance events within a multitemporal radar data set.

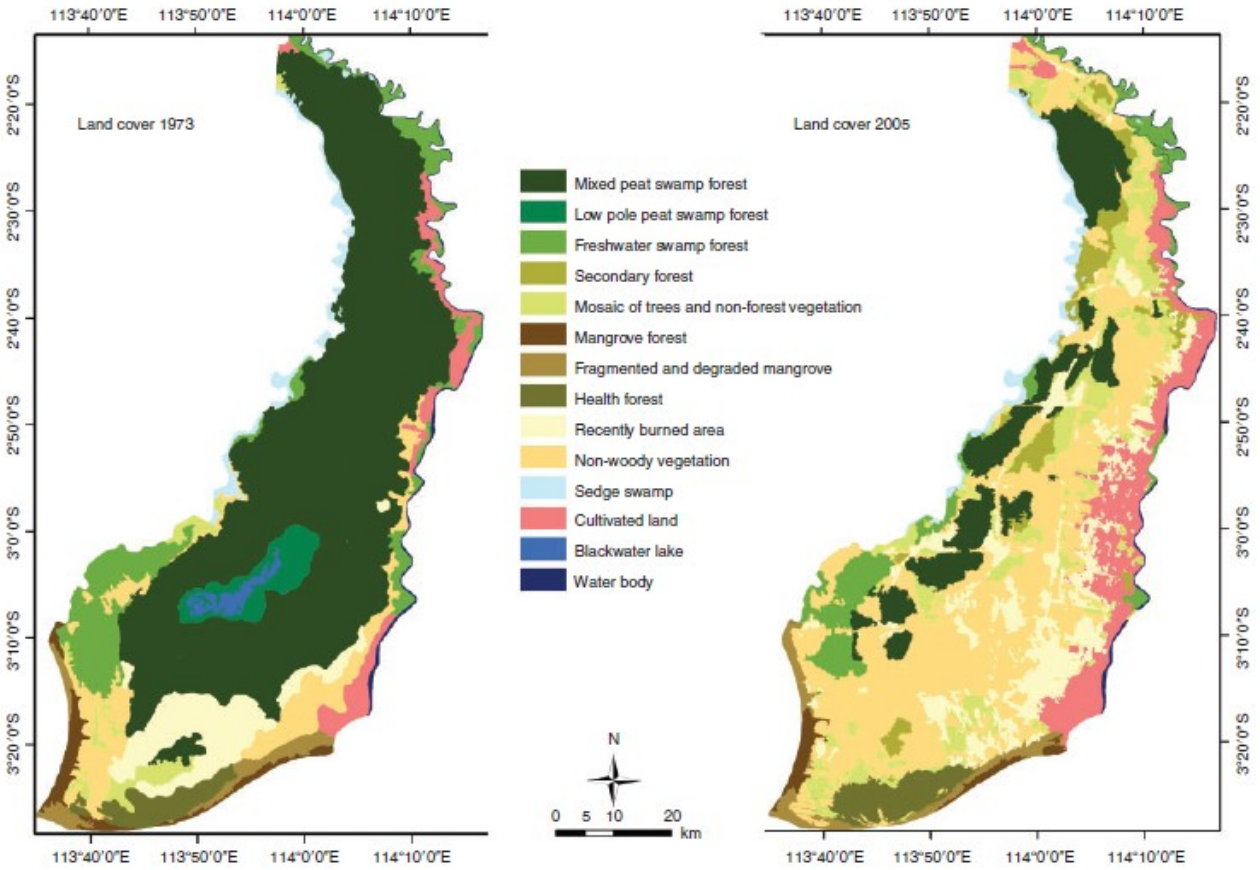


Figure 3.4.Land cover change in block C of the exMRP 1973 (left) and 2005 (right, figure taken from Hoscilo 2009 PhD thesis).

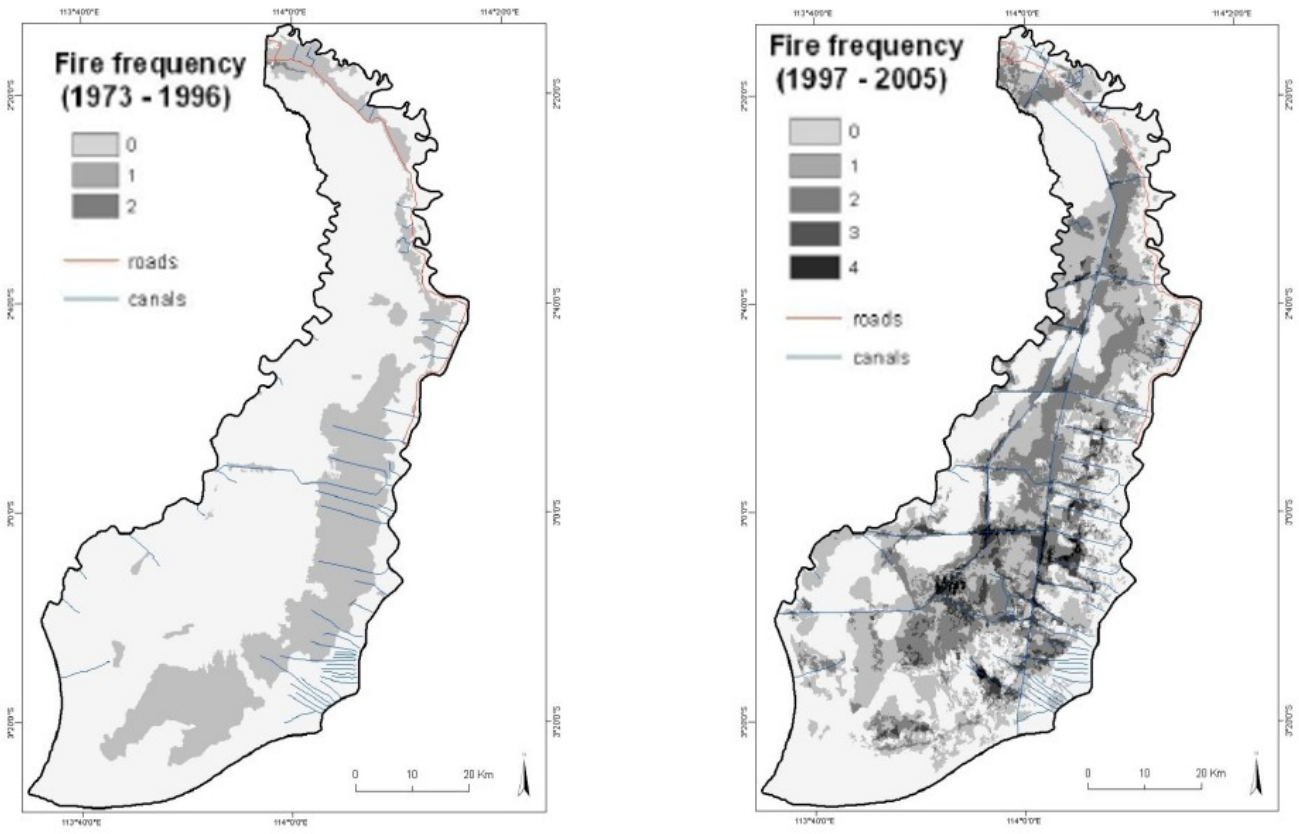


Figure 3.5 Fire frequency in Block C, (left) 1973-1996 and (right) 1997-2005, (figure taken from Hoscilo, 2009 PhD thesis)

### 3.1.3 Field data collection

Above ground biomass data for peat swamp forest (PSF) and secondary vegetation derivatives were collected along a gradient of increasing forest degradation from intact forest to areas that had been burnt multiple times and which contained no woody vegetation at all. As the period of data collection was limited to a period of three years, long term monitoring of plots in order to quantify growth/regrowth of vegetation following disturbance was not possible. Instead plots were located across a biomass gradient from relatively intact peat swamp forest in the Sebangau forest to the west of the Sebangau river and outside the exMRP area. This forest has a history of selective logging which ceased some ten years ago and is referred to subsequently as the Sebangau peatland. In contrast, further plots were located in heavily degraded areas of PSF within the exMRP where the land cover was dominated by non-woody vegetation (these locations are referred to subsequently by the Block names, i.e. Blocks A, C and E). These plots provided data across a gradient of disturbance frequency/intensity (Hoscilo et al., 2013). Plots were only revisited if, in the time since the last visit, there had been a disturbance, as occurred in 2009 when fires burnt some of the previously measured plots.

Forest biomass data were collected using two different methodologies: the first created for the purposed of this thesis and referred to below as the methodology one. The second method was developed for long term monitoring by the Indonesia Australia Forest Carbon Partnership (IAFCP). It is referred to as method two below. Although it would have been ideal if all data

had been collected using the same methodology, the inclusion of primary and secondary data collected according to the IAFCP methodology not only greatly increased the amount of available biomass data, but also gave valuable additional information at the higher end of the biomass scale. Despite the different data collection methodologies data derived from both datasets are comparable using the method described below. Some degree of bias was inevitably introduced by the inclusion of two different sampling schema, however this was difficult to quantify as the two datasets sampled vegetation at different ends of the biomass range. For a small number of plots in the dataset there were estimates of both biomass from both methods. These showed no significant bias at high biomass (>50 tonnes per hectare). At lower biomass levels the IAFCP method two showed either lower or higher biomass estimates as the smaller plot sizes (primarily designed for sampling high biomass areas) were affected by the inclusion or exclusion of larger trees compared to the larger plots used in method 1.

Plot data were collected at the study sites in the dry seasons of 2009, 2010 and 2011. The first two trips involved data collection from in and around Block C and the Sebangau peatland as well as some plots to the north of PalangkaRaya; all data collection on these trips used the University of Leicester methodology. The 2011 trip collected data from the IAFCP study area in Block A, largely along the banks of the Mantangai River. The data from this latter trip were collected in conjunction with IAFCP and according to their field protocols. In total, 30 plots were sampled in Block A and 25 in and

around Block C and the Sebangau forest (including 6 plots that were sampled in both 2009 and again after they burnt in 2010). Access to the IAFCP database provided data for another 84 plots in Block A and Block E giving a total number of 139 plot based biomass estimates. The locations of all plots are shown in Figure 3.7.

Field biomass estimation: method 1.

As in the emphasis of this study was on assessment of forest biomass rather than floristic composition, no tree species identification was undertaken. Species identification is an often time consuming process and time saved by omitting tree IDs could be spent measuring further plots. A sampling methodology utilising two plot sizes was used; three small sub plots of 20m by 20m in which trees were measured were nested within a 100m by 100m (1 ha) plot. The reason for choosing this sampling schema was to try and account for the spatial heterogeneity that is found, particularly in degraded areas. This heterogeneity took the form of isolated clumps of trees often centred around surviving intact large forest trees. The high biomass of these clumps in comparison to the surrounding areas of fern dominated peatlands could lead to significantly skewed biomass estimates if not accounted for in the experimental design of the sampling plots. The scale at which these clumps occurred is of a scale too large to be sampled within the nested plots but is of a scale that can be captured within the overall 1 ha plots. An average biomass value was calculated from the three nested plots that was less likely to be affected by stochastic spatial variation in biomass (i.e. clumps of trees)

and hence provided an estimate of biomass representative of the sampled area less effected by the random inclusion of tree clumps. The difference in the biomass between the nested plots also provided an indication of the spatial heterogeneity of biomass at the sample locations. The size of the 1ha plots was also chosen so that they would contain >5 pixels of medium resolution satellite data (e.g. Landsat, ALOS PALSAR, etc). This allowed some spatial averaging of information extracted from the remote sensing data and reduced the effect of pixel variation, a phenomenon that is particularly prevalent in radar imagery where it is referred to as speckle (Lee, 1986) and to take into account slant effects of the incident radar sensor, whereby trees located outside plots may contribute to scattering apparently from within the plot.

In the field the four corners of the 1ha plots were marked using GPS waypoints. The locations of the three sub-plots within the 1 ha plot were chosen from a pre-prepared list of random co-ordinates on a 5*5 grid (with a possible 20*20m plot locations within the 1 ha plot). Once located the sub-plots were laid out with the aid of a compass and delineated using 40m measurement tapes. The percentage cover of bare earth and non woody vegetation within each subplot was noted. The diameter at breast height (dbh, standardised as 1.3m above ground level) of all trees in the plots was measured using a diameter tape. The height of all trees in the plot >1.5m in height was measured in meters using a 2m pole marked in 10cm increments. Where tree height was greater than 4m the height was calculated using a clinometer at a known horizontal distance from the tree (measured using the

height pole) to measure the angle to the top of canopy in relation to the horizontal. Tree height was then calculated using equation 3.1. Trees were recorded as alive or dead, as judged by the presence or absence of green leaves. Where trees had a multi-stemmed growth form with multiple braches sprouting from ground level, measurements were taken from each stem.

Calculation of forest biomass

Biomass was calculated using the global allometric equations for wet forests as published by Chave (2005, see equation 2) as there is a lack of any specific allometric equations produced specifically for PSF trees. Input variables for the equation were tree height and dbh (both measured in the field). The third input variable is wood density. Average values of wood density were calculated for degraded areas and forested areas as it was thought likely that tree species found in degraded areas would be faster growing and therefore likely to have less dense wood. In order to calculate these average values 16 tree cores were collected using an increment borer. Ten cores were taken from trees in a forested area and six from trees in degraded areas (tree species were not ascertained as values were used to give average wood density for degraded and forested areas). Cores were stored and labelled in drinking straws until they could be returned to the lab at the University of PalangkaRaya. Wet weight in grams was measured to two decimal places using laboratory scales and samples were then dried in an oven and weighed daily until their weight was no longer decreasing. Dry weight was then recorded and sample volume was calculated using the water

displacement method (volume increase after immersion of samples in a water filled measuring cylinder). Wood density was calculated according to equation 3 (Chave, 2005) and the results are shown in Figure 3.6. It is however likely that the wood density value for degraded areas is an overestimate as the most common species of tree (*Cratoxylum arborescens*) had wood so light that the corer would not bite and wood cores were unobtainable. Once the biomass of each tree had been calculated using the allometric equation and the appropriate wood density for the sample areas (forest or degraded), biomass values were summed per sub-plot and then converted to values in tonnes per hectare.

$$H = d * tan\theta + h \qquad (3.1)$$

Clinometer formula for the calculation of tree height in meters (H) where d is the distance from base of tree (m) to the measuring position, $\theta$ is the angle from horizontal of tree top as measured with a clinometer and h is the the eye height of the person using the clinometer.

$$AGB \equiv \exp(-2.577 + 0.940 * \ln(\rho D^2 H)) \qquad (3.2)$$
$$\equiv 0.776 * (\rho D^2 H)^{0.940}$$

Chave's formula for calculating biomass from tree height in meters(H), where D is the diameter of the tree at breast, and *p* is wood density. (Chave et al., 2005).

$$WD = w/v \qquad (3.3)$$

Calculation of wood density (after Chave, 2005), where WD is wood density (g/cm$^3$), w is dry sample weight (g) and v is sample volume (cm$^3$).

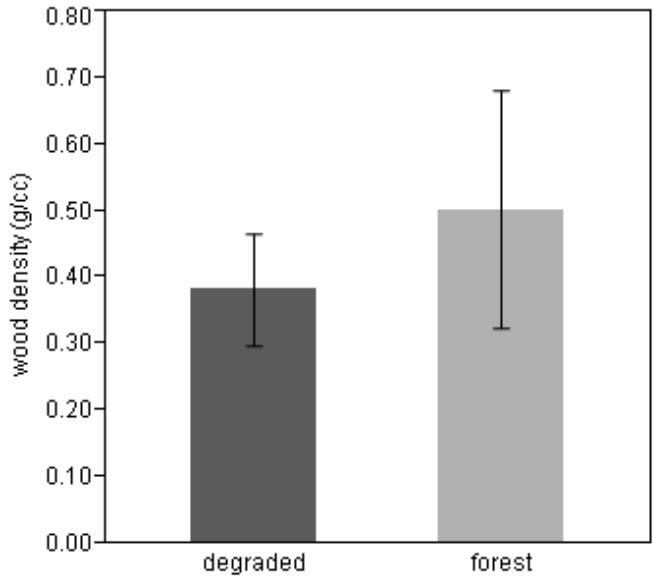


Figure 3.6. Average wood density for each landscape type (degraded = 0.38 g cc-1, forested = 0.50 g cc-1). Bars are +/- standard error.

Field biomass estimation method 2

The IAFCP data collection methodology was designed to enable long term monitoring of forest carbon stocks and as such had subtly different aims to the University of Leicester methodology described above. Degraded areas were under represented in the existing IAFCP biomass database, thus fieldwork was undertaken in the dry season of 2011 using the IAFCP methodology to sample plots in burnt areas of Block A (i.e. in order to increase the representation of plots with low biomass within the database).

IAFCP plots were 32*32m, however as they were designed to be used in areas of high stem density (i.e. intact forest) the trees sampled within the plot were stratified by tree size and sampled from within nested plots as follows: Trees with dbh >20cm were sampled in the full 32*32m plot, trees with a dbh of between 10 and 20cm were sampled within a 16*16m sub-plot, trees with a

dbh <10cm and >1.5m in sub-height were sampled within an 8*8m sub-plot and trees <1.5m in height within a 2*2m plot. The final class of trees (<1.5m in height) were not included in the biomass estimate as no height values were attached to them and because they had not been sampled under the University of Leicester methodology.

As for the University of Leicester methodology the volume of each tree was calculated using Chave's equation and converted to biomass using the wood density value for degraded areas. Biomass values for each tree class/nested plot were then summed and converted to biomass values in tonnes per hectare. The location of biomass plots throughout the study area is shown in Figure 3.7.

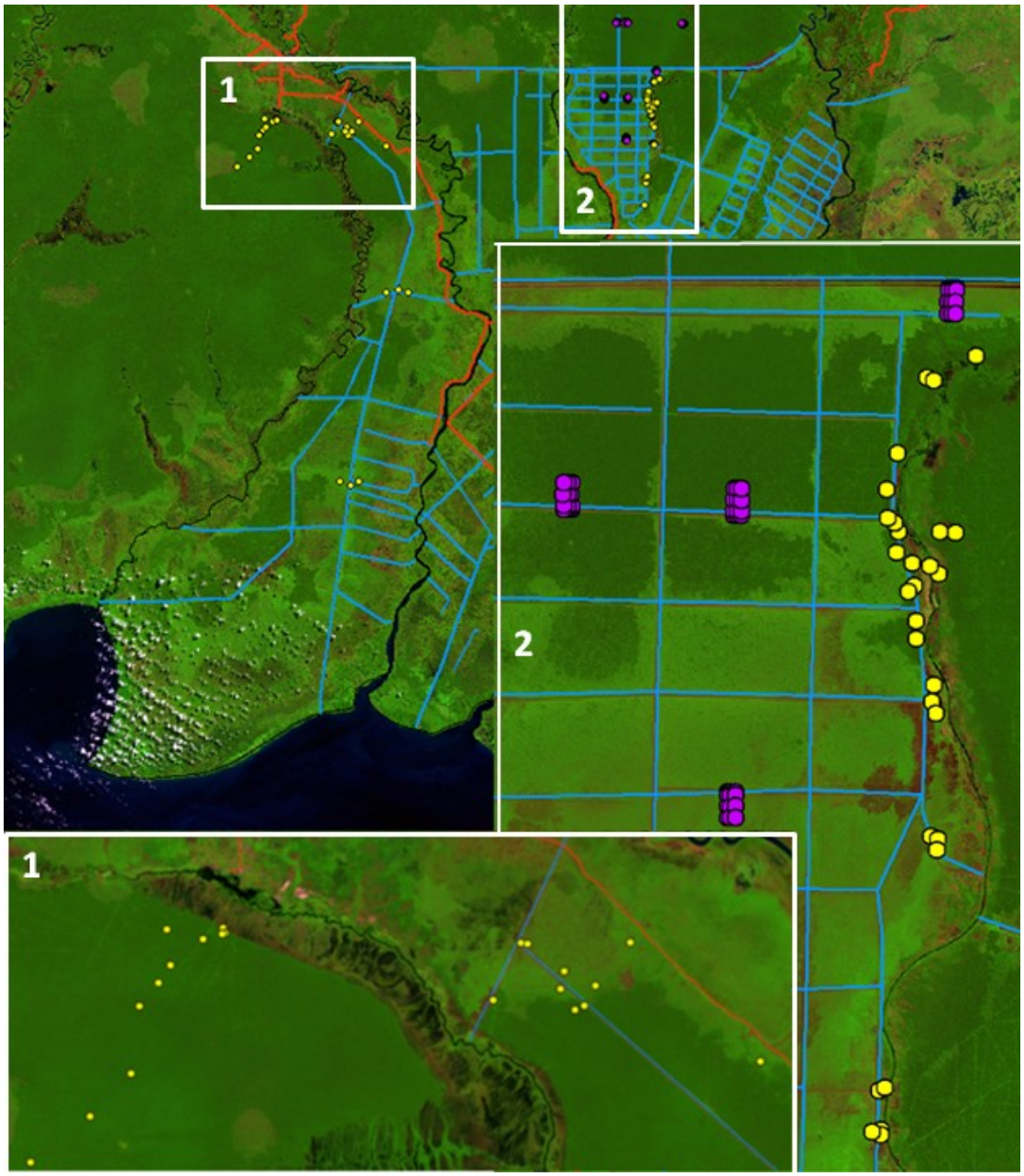


Figure 3.7. The location of biomass sample plots. Yellow dots indicate plots sampled by the University of Leicester, Purple dots indicate biomass data collected by the AusAID project. Insets show details of two areas where plots were concentrated. Also shown are canals (blue) and roads (red). The background Landsat image is as used in Figure 3.3.

## 3.2 Radar image processing

The following section describes the processing chain used to generate the radar dataset; scripts are given in Appendix 8.1.

### 3.2.1 Image mode selection

PALSAR images were obtained via the ALOS user interface gateway (https://auig.eoc.jaxa.jp/auigs/top/TOP1000Init.do; shown in Figure 3.8) which allows searching and ordering of the radar image catalogue. Images were obtained in Fine Beam Dual Polarisation (FBD) mode because of the regular acquisition schedule compared to the fully polarimetric (quad-polar, PLR) mode, which allowed the collection of a denser time series of images and because the extra channel increased the information content compared to the single polarimetric mode (FBS). FBD images were utilised in favour of the ScanSAR product which produces monthly images covering a wide area. It was felt that the extra spatial resolution (100$m^2$ in the ScanSAR mode as opposed to 12.5$m^2$ in FBD) was more suited to the scale at which forest degradation was occurring in Kalimantan. The FBD products were collected at a consistent incidence angle of 34.3$^o$ which simplified image interpretation. The PALSAR data were downloaded in the ungeocoded level 1.1 format as this provided an opportunity to investigate the use of multidate interferometric coherence as an extra channel of image information.


Figure 3.8. Screenshot from the ALOS user gateway showing location of PALSAR radar footprints. Boxes 1-3 strip 423, 6-8 strip 422 and 4 & 5 strip 421. Inset shows location of area within the Borneo, © JAXA.

### 3.2.2 Radar backscatter

Once image files have been downloaded from JAXA and were decompressed the basic radar processing was done using the GAMMA radar processing package with commands being structured into bash scripts running under a Linux platform. PALSAR images were extracted to single-look complexes (SLC) and calibrated using a calibration factor of -115db as published on the JAXA website (https://auig.eoc.jaxa.jp/auigs/en/doc/an/20090109en_3.html). Multilooking was then performed using 2 looks in the range direction and 9 looks in the azimuth direction. This number of looks was chosen based on the effect that they would have on the output pixel size with the selected number of looks producing an output pixel of 25m$^2$ identifier by Asner et al.,(2005) as

the minimum at which forest degradation could be detected whilst also providing a suitable levels of reduction speckle noise.

### 3.2.3 Interferometric coherence

Coherence images show the phase similarity of a pair of images obtained from different locations and/or times. Coherence images were calculated based on image pairs acquired 46 days apart (the return time of the ALOS satellite). In order to generate coherence images the spatial offset between images was calculated using the intensity cross correlation technique and the image pair was resampled so that they were precisely co-located and the interferogram was calculated. The perpendicular baseline (spatial separation between the locations where images were obtained) was calculated from the orbital parameters of the satellite and the image was then flattened to compensate for the curvature of the earth. The coherence was then generated from the interferogram and the results filtered using adaptive interferogram filtering.

### 3.2.4 Geocoding

The next task was to convert the calibrated and multilooked images into a geocoded product. To do this required an already geocoded reference image against which to geocode the processed radar image. A number of reference images covering the study area were tested including SRTM tiles and a mosaic of Landsat panchromatic bands. However best geocoding results were obtained using a combination of the SRTM scene for rough preliminary geocoding and a mosaic of PALSAR L1.5 scenes (which were supplied geocoded by JAXA) for the final precision geocoding. The process involved

creating a map parameter file (dem_par) for the SRTM and PALSAR L1.5 images and then projecting them both into the final map projection (UTM zone 50 South). Look up tables for the cross correlation of the reference images and the radar images were then produced. The initial values in the look up tables was derived from the orbital parameters of the satellite at the time of image aquisition and transformed in to the output geometry. The image was converted at this stage from slant range to ground range viewing geometries. Fine geocoding between the two images was performed using intensity cross-correlation in a number of sample windows. Once a rough solution to the geocoding had been produced it was stored in the parameter file. Further precision geocoding was then performed against the L1.5 PALSAR mosaic with the geocoding solution being refined using matched search windows in the radar and reference image for intensity cross correlation. This was an iterative procedure with the size of the windows decreasing and the number of windows increasing in order to provide the most accurate final geocoding solution possible. The final solution was then applied to the calibrated multilooked dual polarisation images and to the interferometric coherence images. Images were terrain corrected to account for differences in elevation at this stage. However as the study area has little change in elevation (max height 30m above sea level) the effects of this process were neglible.

### 3.2.5 Mosaicing and Filtering

Subsequent radar processing was carried out using the ENVI 4.7 software package. This was facilitated by converting the GAMMA radar parameter files

into ENVI header files. To simplify further processing, the images were mosaiced into strips obtained on the same date using the georeferenced mosaic tool in ENVI. Same strip mosaics from different dates were then stacked into a single image using the Layer stack option.

In order to further reduce speckle noise and improve radiometric resolution each stack of images was filtered in the temporal domain using the multi-channel filtering algorithm developed by Quegan & Yu (2001). The multi-channel filter was used instead of the more usual spatial filtering in order to preserve spatial resolution and because it is particularly suited to reducing speckle in multi-temporal image stacks (Trouve et al., 2003). This process was implemented in IDL (the script is given appendix 8.2.1) and was performed separately for each image stack and polarisation mode. Coherence data were not filtered as they had already been filtered in the interferometric processing and implementing the MCF filter resulted in overly smoothed image data. In order to check that the filtering technique was not altering the image data the mean and standard deviation (Std Dev) of pixels values collected from regions of interest representing a variety of landscape types and image collection dates were compared before and after the filtering process. Ideally a filter would not change the average pixel values as this could introduce a bias into later analyses, however it would act to 'smooth' the pixel by reducing the variability within the pixels. Figure 3.9 shows that the MCF filter performs this task almost perfectly with the mean (of mean) ROI values remaining virtually unchanged (0.0852 before against 0.0851 after filtering) whilst the mean of StDev of pixel values was reduced from (0.0212

before and 0.0130 after filtering). The range of mean values was also near identical before and after filtering, whilst the range of StDev values was significantly reduced. From this it was concluded that that the MCF filtering did not introduce any bias into the radar data and that there should be no significant effects of the MCF filter on temporal dynamics. The processing chain includes two steps in which averaging takes place, firstly in the multilooking stage were averaging occurs in the spatial domain and secondly in the MCF filtering where the averaging occurs across the temporal domain. Although efforts have been made to ensure that neither of the processes introduces artefacts onto the data and that the two processes work synergistically, it would be preferable if the process could be accomplished with a single algorithm, However no such algorithms are available at the present time. The final step in the processing chain was to convert the radar backscatter from linear units to logarithmic units (decibels). This was done using the band math feature within ENVI and multiplying the pixel values by 10 log10.

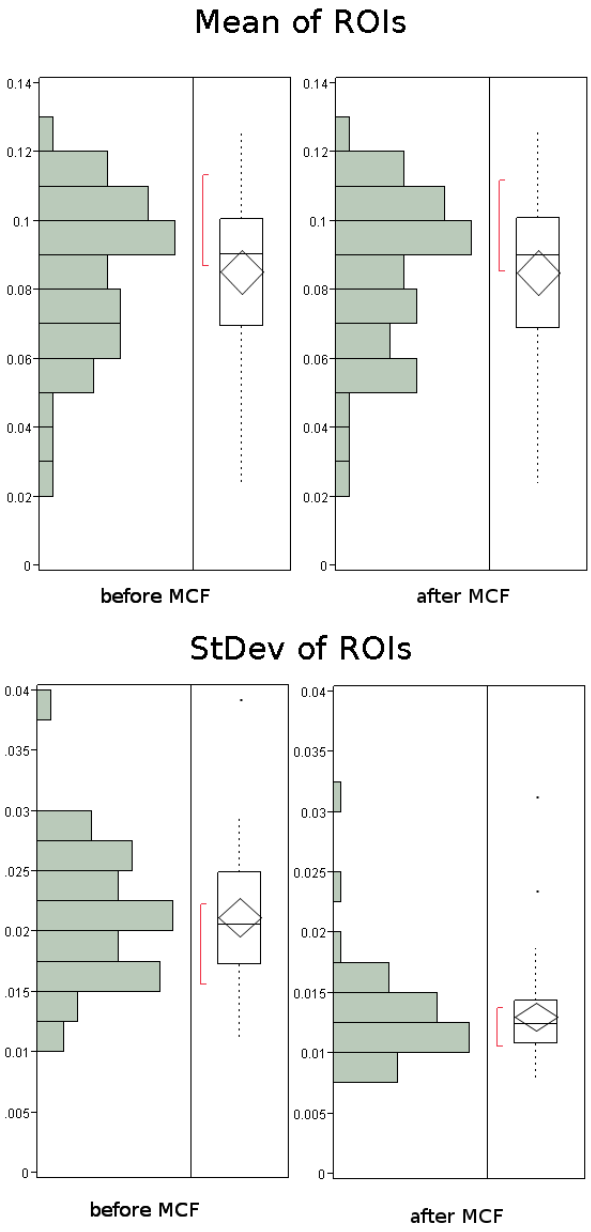


Figure 3.9. Mean (top) and Standard Deviation (bottom) of pixel values collected from ROIs covering a range of landscape types before (left) and after (right) filtering by using the Multi Channel filtering algorithm. Histograms are shown on the left of each inset whilst on the right the boxes show 25th and 75th quartiles whilst whiskers show 95% quantiles and dots are outliers beyond this range . Red bars show the shortest range containing 50% of values.

| Table 3.1a | | Strip: 421 | | | |
|---|---|---|---|---|---|
| **Year** | **Date** | 421_7130 | | 421_7140 | |
| | | **HH** | **HV** | **HH** | **HV** |
| 2007 | 20070622 | ✔ | ✔ | ✔ | ✔ |
| | 20070807 | ✔ | ✔ | ✔ | ✔ |
| | 20070922 | ✔ | ✔ | ✔ | ✔ |
| 2008 | 20080509 | ✔ | ✔ | ✔ | ✔ |
| | 20080809 | ✔ | ✔ | ✔ | ✔ |
| | 20080924 | ✔ | ✔ | ✔ | ✔ |
| 2009 | 20090627 | ✔ | ✔ | ✔ | ✔ |
| | 20090812 | ✔ | ✔ | ✔ | ✔ |
| 2010 | 20100630 | ✔ | ✔ | ✔ | ✔ |
| | 20100815 | ✔ | ✔ | ✔ | ✔ |
| | 20100930 | ✔ | ✔ | ✔ | ✔ |
| | 20101105 | ✔ | ✔ | ✔ | ✔ |

| Table 3.1b | | Strip: 422 | | | | | |
|---|---|---|---|---|---|---|---|
| **Year** | **Date** | 422_7120 | | 422_7130 | | 422_7140 | |
| | | **HH** | **HV** | **HH** | **HV** | **HH** | **HV** |
| 2007 | 20070709 | ✔ | ✔ | ✔ | ✔ | ✔ | ✔ |
| | 20070824 | ✔ | ✔ | ✔ | ✔ | ✔ | ✔ |
| | 20071009 | ✔ | ✔ | ✔ | ✔ | ✔ | ✔ |
| 2008 | 20080526 | ✔ | ✔ | ✔ | ✔ | ✔ | ✔ |
| | 20080711 | ✔ | ✔ | ✔ | ✔ | ✔ | ✔ |
| | 20080826 | ✔ | ✔ | ✔ | ✔ | ✔ | ✔ |
| | 20081011 | ✔ | ✔ | ✔ | ✔ | ✔ | ✔ |
| 2009 | 20090714 | ✔ | ✔ | ✔ | ✔ | ✔ | ✔ |
| | 20090829 | ✔ | ✔ | ✔ | ✔ | ✔ | ✔ |
| | 20091014 | ✔ | ✔ | ✔ | ✔ | ✔ | ✔ |
| 2010 | 20100717 | ✔ | ✔ | ✔ | ✔ | ✔ | ✔ |
| | 20100901 | ✔ | ✔ | ✔ | ✔ | ✔ | ✔ |
| | 20101017 | ✔ | ✔ | ✔ | ✔ | ✔ | ✔ |
| | 20101202 | ✔ | ✔ | ✔ | ✔ | ✔ | ✔ |

| Table 3.1c | | Strip: 423 | | | | | |
|---|---|---|---|---|---|---|---|
| **Year** | **Date** | 423_7120 | | 423_7130 | | 423_7140 | |
| | | **HH** | **HV** | **HH** | **HV** | **HH** | **HV** |
| 2007 | 20070610 | ✔ | ✔ | ✔ | ✔ | ✔ | ✔ |
| | 20070726 | ✔ | ✔ | ✔ | ✔ | ✔ | ✔ |
| | 20070910 | ✔ | ✔ | ✔ | ✔ | ✔ | ✔ |
| 2008 | 20080427 | ✔ | ✔ | ✔ | ✔ | ✔ | ✔ |
| | 20080612 | ✔ | ✔ | ✔ | ✔ | ✔ | ✔ |
| | 20080728 | ✔ | ✔ | ✔ | ✔ | ✔ | ✔ |
| | 20080912 | ✔ | ✔ | ✔ | ✔ | ✔ | ✔ |
| 2009 | 20090615 | ✔ | ✔ | ✔ | ✔ | ✔ | ✔ |
| | 20090731 | ✔ | ✔ | ✔ | ✔ | ✔ | ✔ |
| | 20090915 | ✔ | ✔ | ✔ | ✔ | ✔ | ✔ |
| 2010 | 20100618 | ✔ | ✔ | ✔ | ✔ | **x** | ✔ |
| | 20100803 | ✔ | ✔ | ✔ | ✔ | **x** | ✔ |
| | 20100918 | ✔ | ✔ | ✔ | ✔ | **x** | ✔ |
| | 20101103 | ✔ | ✔ | ✔ | ✔ | **x** | ✔ |

Table 3.1. Dual polarisation radar backscatter processing results. Top Table gives results for strip 421, middle Table gives results for strip 422 and bottom, Table gives results for strip 423. A tick indicates successful processing and georeferencing of the scene. A cross indicates that the scene was not able to be processed.

| Table 3.2a | | | Strip: 421 | | | |
|---|---|---|---|---|---|---|
| **Year** | **Date 1** | **Date 2** | 421_7130 | | 421_7140 | |
| | | | HH | HV | HH | HV |
| 2007 | 20070807 | 20090812 | ✔ | ✔ | ✔ | ✔ |
| | 20070922 | 20080924 | ✔ | ✔ | ✔ | ✔ |
| 2008 | 20080924 | 20070922 | ✔ | ✔ | ✔ | ✔ |
| 2009 | 20090812 | 20070807 | ✔ | ✔ | ✔ | ✔ |

* south east portion largely obscured

| Table 3.2b | | | Strip: 422 | | | | | |
|---|---|---|---|---|---|---|---|---|
| **Year** | **Date 1** | **Date 2** | 422_7120 | | 422_7130 | | 422_7140 | |
| | | | **HH** | **HV** | **HH** | **HV** | **HH** | **HV** |
| 2007 | 20070709 | 20070824 | ✔ | ✔ | ✔ | ✔ | ✔ | ✔ |
| | 20070824 | 20071009 | ✔ | ✔ | ✔ | ✔ | ✔ | ✔ |
| 2008 | 20080526 | 20080711 | ✔ | ✔ | ✔ | ✔ | ✔ | ✔ |
| | 20080711 | 20080826 | ✔ | ✔ | ✔ | ✔ | ✔ | ✔ |
| | 20080826 | 20081011 | ✔ | ✔ | ✔ | ✔ | ✔ | ✔ |
| 2009 | 20090714 | 20090829 | ✔ | ✔ | ✔ | ✔ | ✔ | ✔ |
| | 20090829 | 20091014 | ✔ | ✔ | ✔ | ✔ | ✔ | ✔ |
| 2010 | 20100717 | 20100901 | ✔ | ✔ | ✔ | ✔ | ✔ | ✔ |
| | 20101202 | 20101017 | ✔ | ✔ | ✔ | ✔ | ✔ | ✔ |
| | 20100901 | 20101017 | ✔ | ✔ | ✔ | ✔ | **x** | **x** |

| Table 3.2c | | | Strip: 423 | | | | | |
|---|---|---|---|---|---|---|---|---|
| **Year** | **Date 1** | **Date 2** | 423_7120 | | 423_7130 | | 423_7140 | |
| | | | **HH** | **HV** | **HH** | **HV** | **HH** | **HV** |
| 2007 | 20070610 | 20070726 | ✔ | ✔ | ✔ | ✔ | ✔ | ✔ |
| | 20070726 | 20070910 | ✔ | ✔ | ✔ | ✔ | ✔ | ✔ |
| 2008 | 20080728 | 20080912 | ✔ | ✔ | ✔ | ✔ | ✔ | ✔ |
| 2009 | 20090615 | 20090731 | ✔ | ✔ | ✔ | ✔ | ✔ | ✔ |
| | 20090731 | 20090915 | ✔ | ✔ | ✔ | ✔ | ✔ | ✔ |
| 2010 | 20100618 | 20100803 | ✔ | ✔ | ✔ | ✔ | ✔ | ✔ |
| | 20100803 | 20100918 | ✔ | ✔ | ✔ | ✔ | ✔ | ✔ |

* scene obscured, **some image artefacts (striping) across these scenes

Table 3.2. Coherence processing results. Top Table gives results for strip 421, middle Table gives results for strip 422, bottom Table gives results for strip 423. Date 1 and date 2 give the collection dates for the image pairs. A tick indicates successful interferometric processing of the pair of scenes. A cross indicates that the scene was not able to be processed.

### 3.2.6 Processing environment

All processing was done on the University of Leicester cluster computer. Each scene was processed on a separate core with 2Gb of memory and took approximately 10 minutes. 263 scenes were processed, however it was not possible to process a number of the backscatter scenes due to the geocoding algorithm being unable to match sufficient numbers of intensity cross correlation windows due to high signal noise ratios. Details of processed backscatter scenes are given in Table 3.1

The processing of the coherence scenes from image pairs was much more problematic with many coherence images failing to process correctly due to errors in the processing chain and for this reason there are many fewer coherence images available. Details of the coherence processing dates are given in Table 3.2. Coherence images were calculated from both HH and HV image pairs. However the coherence layers for both polarisations were essentially identical and only HH coherence images were used for the subsequent analyses in this thesis. Figure 3.10 shows a small subset of a false colour composite taken from the final radar data.

## 3.3 Summary

In this chapter the study area has been introduced and its disturbance history described. The method of sampling forest biomass in the field is described as is the processing and production of the temporal stacks of radar data. In the next chapter the spatio-temporal variation of the radar signal in the temporal stacks is examined and in the subsequent chapters this variation is linked to ecological processes occurring in the landscape.

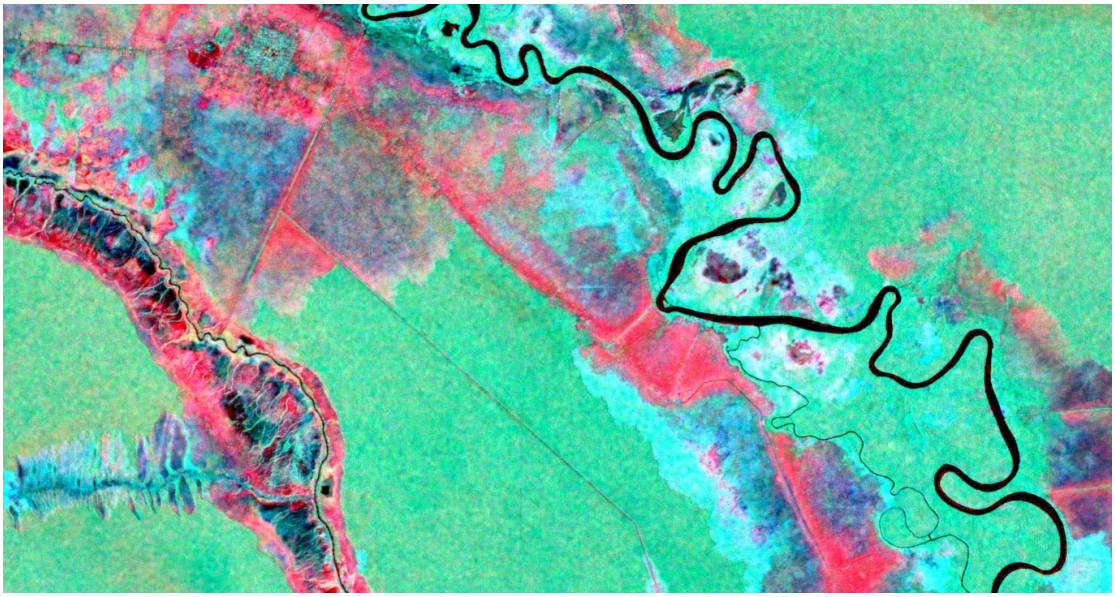

Figure 3.10. Example of false colour composite PALSAR image covering the Kalampangan region at the northern end of Block C. (Red channel = HH coherence, Green channel = HV backscatter, Blue channel = HH backscatter.) Forested areas appear green, floodplains and burnt areas bright turquoise, degraded areas and floodplains red and open water black. Linear features are drainage canals.

# 4. Patterns of backscatter change across a landscape of Peat Swamp Forest

## 4.1 Introduction

Past research has established relationships between the radar backscatter and the amount of above ground biomass measured on the ground (e.g. Le Toan et al., 1992; Cartus et al., 2012; Mitchard et al., 2009; Mitchard et al., 2009). However, the majority of these radar:biomass calibration curves are based on single temporal samples of (approximately) co-located biomass estimates and radar signals and contain no indication of the temporal stability of the radar signal and hence of the calibration curve (e.g. Figure 4.1).

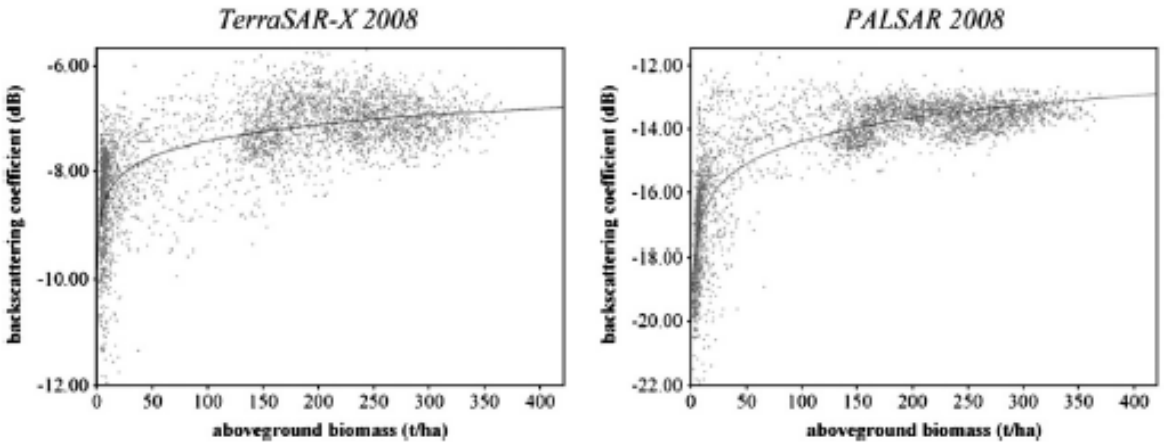


Figure 4.1. Example of radar biomass calibration curves (taken from Englhart et al., 2011, © Elsevier).

Only a few studies provide temporal radar profiles with more than two samples; of those that do, most report high levels of radar backscatter variability. For example, Salas et al (2002) exploited a chronosequence of forest disturbance

that produced a range of biomass values for which the temporal backscatter profiles in a series of 8 JERS over Amazonian forest were generated. Good qualitative relationships were found when JERS backscatter was compared across this chronosequence but it was also observed that quantitative estimates of biomass at the plot scale were not stable due to temporal variability in the radar signal. This was attributed to a combination of moisture effects, calibration errors and system noise. Romshoo (2003), using a time series of 14 JERS-1, L-band radar scenes collected over the ex-MRP in Central Kalimantan, found that undisturbed forest had very low temporal variation (<1dB). He thus used a change detection threshold of >2dB in order to identify areas of biomass change, but noted that riparian and short pole peat swamp forest were likely to be falsely identified using this threshold and that croplands and burnt areas could show >7dB of radar change between wet and dry seasons. In an effort to minimise these temporal variations and overcome false detections his analysis proceeded using only radar images collected from the dry season. Similarly, Siegert (2000) noted that unburnt areas of peat swamp forest in East Kalimantan showed backscatter variation of ~0.5 dB across a collection of 6 ERS images collected over a 9 month period. Martinez (2007) acquired a temporal sample of 21 JERS scenes collected over the Amazonian floodplain and used a multitemporal classifier in order to perform a vegetation classification. This exploited a division of the space described by the mean backscatter and a temporal change estimator to label vegetation types and flooding duration. A more advanced method utilising decision trees was used in the Brazilian Pantanal exploiting both ALOS PALSAR and RADARSAT data to perform a classification of vegetation (Evans et al., 2010). Working with ERS

data, Minchella et al. (2009) used unburnt forest as a control to compare with burnt areas of Mediterranean pine forest. The backscatter from these undisturbed areas showed a temporally consistent backscatter value across a range of 34 dates with variation approximately +/- 1 dB around the long term mean value. Reasons for this temporally stable backscatter are likely related to the biomass signal saturating any moisture signal but could equally be due to the study occurring in a dry Mediterranean climate without much seasonal variability in rainfall.

Some patterns do emerge from the limited literature on temporal radar profiles. Firstly. high biomass areas such as intact forest show more stable (i.e. less variable) temporal radar profiles than low biomass or disturbed areas of vegetation. Secondly. many of the studies showing high temporal variability of the radar signal come from wetland ecosystems or ecosystems that go through periods of inundation, indicating that water or moisture effects may be at least partially responsible for causing some of the temporal variation in the radar signal (e.g. Kasischke, 2003). Moisture effects are further investigated in Chapter 5.

In this chapter the aim is to describe how the radar signal behaves across a gradient of increasing biomass from areas of degraded forest with low biomass to areas of intact peat swamp forest with high biomass. The focus in this chapter is on areas and/or periods where no change in biomass occurred during the period covered by the radar samples. (The radar signal from areas undergoing changes in the amount of biomass is examined in more detail in Chapter 6 of this thesis). One area of potential terminological confusion should be clarified. Although there is some natural variation in the biomass of

undisturbed peat swamp forest (for example between mixed peat swamp forest on the margins of the peat dome to low pole peat swamp forest further up the peat dome) the majority of the biomass gradient examined in this chapter is a product of the past history of disturbance across the landscape, in this case the accumulated effects of multiple fires (Hoscilo et al., 2011). Hence by examining the radar signal across a gradient of peat swamp forest biomass this chapter explores the effect of forest disturbance on the radar signal; it does not address (at least, not within this chapter) the proximate effect of disturbance directly within the time series of radar images.

### 4.1.1 Aims

In this chapter, the following research questions are addressed:

1. What are the patterns of temporal backscatter change across a gradient of increasing biomass from low to high biomass peat swamp forest?
2. How do the levels of temporal backscatter change across the biomass gradient relate to the temporal radar signal across the whole landscape?
3. Does the temporal variation of the radar signal need to be taken into account when producing maps of biomass from radar images?

## 4.2 Methods

In this section the temporal mean and temporal standard deviation (referred to in the following text the as tMean and tSD) of the radar data are investigated.

### 4.2.1 How does the temporal backscatter pattern vary across a biomass gradient?

The radar image stacks and biomass amounts described in Chapter 3 were overlaid and the temporal radar profile for each plot was extracted using a 100m circular buffer around the GPS point for each plot. Temporal mean backscatter for each biomass value was plotted against measured biomass (n= 145) with +/- 1 tSD plotted as error bars around the mean (Figure 4.2) in order to show the temporal variability of the radar signal. In order to reduce the variation between biomass values, the biomass estimates were grouped into classes. Biomass ‘bins’ were smaller when biomass was <100 tonnes per hectare compared to when they were >100 tonnes per hectare because of the skewed distribution of biomass values (the majority of plots contained only small amounts of biomass). The mean, minimum, maximum and 10% and 90% quantiles of HH and HV backscatter temporal variability were calculated and plotted for each biomass class (Figure 4.3) in order to show how the 'envelope' of radar signal variability changed across the biomass gradient. Finally, the mean HH and HV backscatter values and standard deviations for each biomass value were plotted against each other. In order to assist with the interpretation of the plot, however, it was necessary to reduce the size of the error bars so the tSD were multiplied by 0.2 (Figure 4.4).

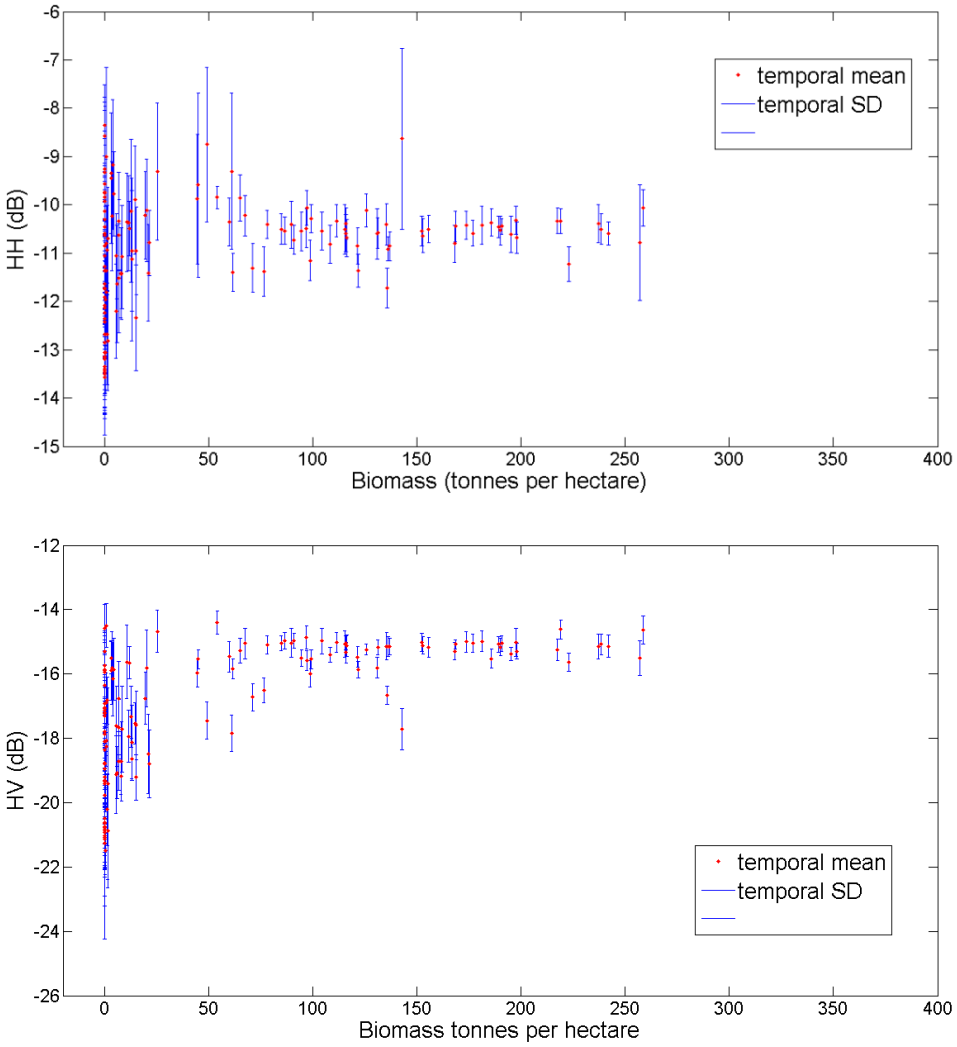


Figure 4.2. The temporal variation of the PALSAR radar signal measured from 2007-2010 across the biomass gradient. Error bars represent +/- 1SD of the temporal variation. Top, HH polarisation and bottom, HV polarisation.

As an alternate means of visualising the variability of the radar signal/biomass dataset an interactive online animation of this dataset is available online: http://mattwaldram.com/biomass_radar.htm.

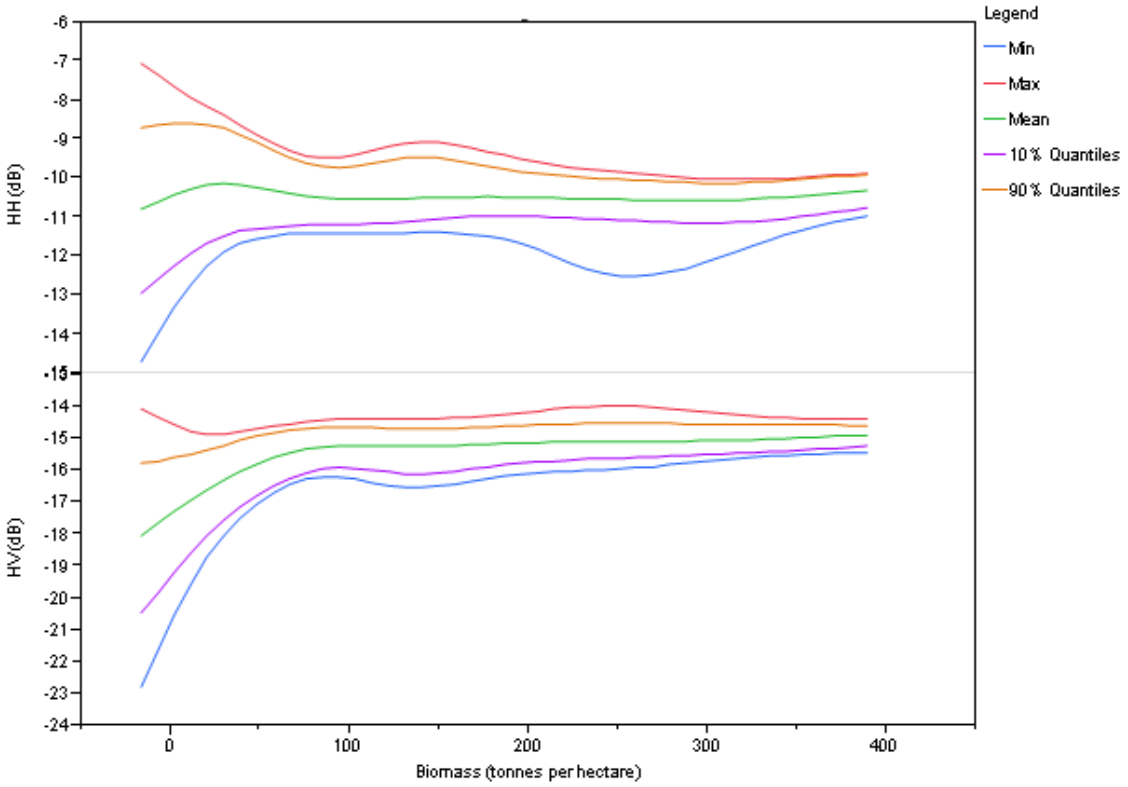


Figure 4.3. Envelopes of temporal variability across the biomass gradient. Biomass plots are binned into groups and lines join the minimum, 10% quantile, mean, 90% quantile and maximum for each group.

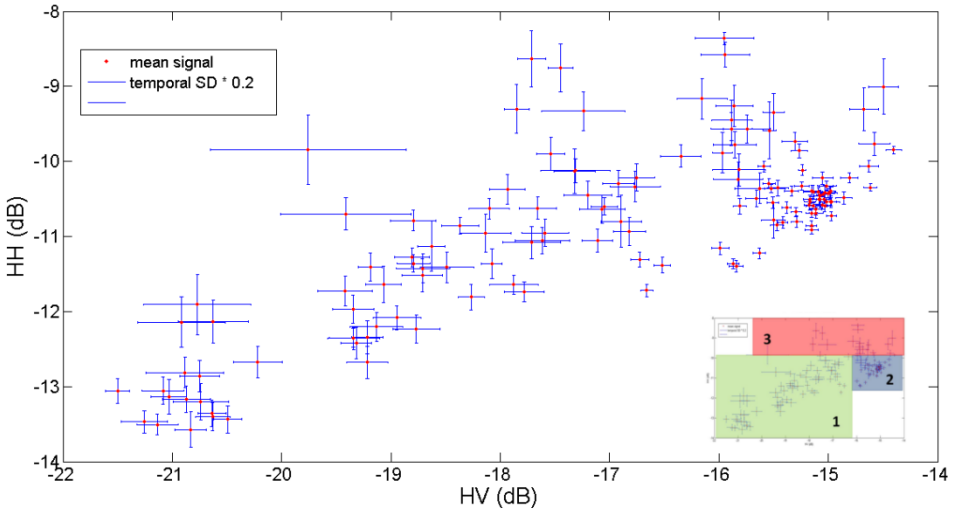


Figure 4.4. The relationship between temporal variability in HH and HV polarisation. NOTE that the error bars are the 0.2 *standard deviation multiplied by in order to make this graph intelligible. Inset shows groups of points as discussed in the text.

### 4.2.2 How does radar backscatter vary over an entire landscape?

Figure 4.3 shows that the variability of the radar signal changes across the biomass gradient. In order to understand how this variability fits with that observed across the entire landscape the temporal mean and temporal standard deviation were calculated on a per pixel basis for each stack of calibrated, multilooked and filtered radar images (see Chapter 3). Image stacks were read into MATLAB using the 'enviread.m' script (Appendix 8.3.1) and the temporal mean and standard deviation for each stack of pixels were calculated ('mean_SD_calc.m' scripts, Appendix 8.3.2). The resulting images were then joined into a mosaic covering the entire study area and displayed using a colour map (ENVI rainbow) in order to provide contrast. This was done separately for both polarisations of radar data. The tMean is shown in Figure 4.5, the tSD is shown in Figure 4.6.

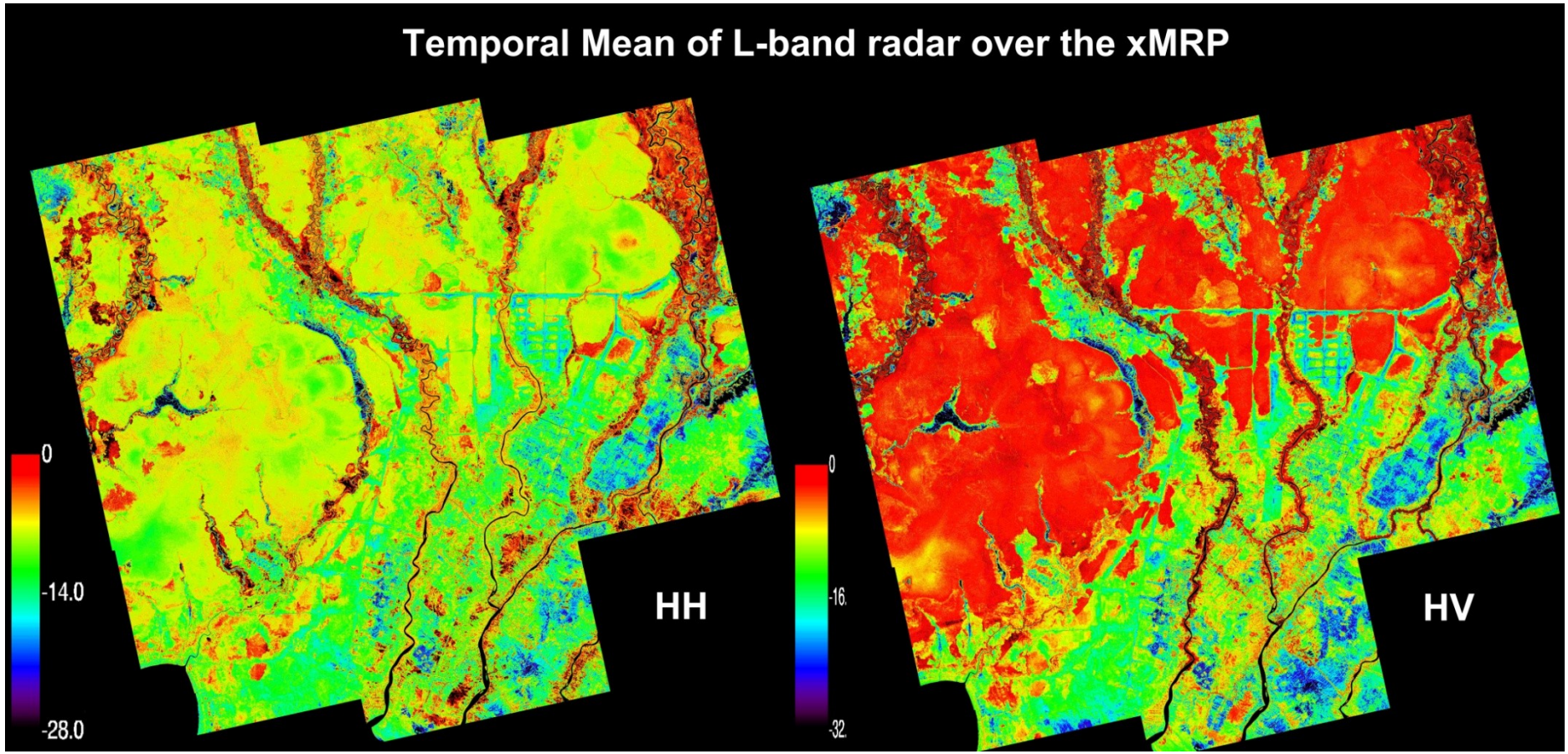


Figure 4.5. A mosaic of 8 PALSAR FBD showing temporal mean (tMean) of the PALSAR backscatter image stack over the period 2007-2010. HH left, HV right. Note different colour scales.

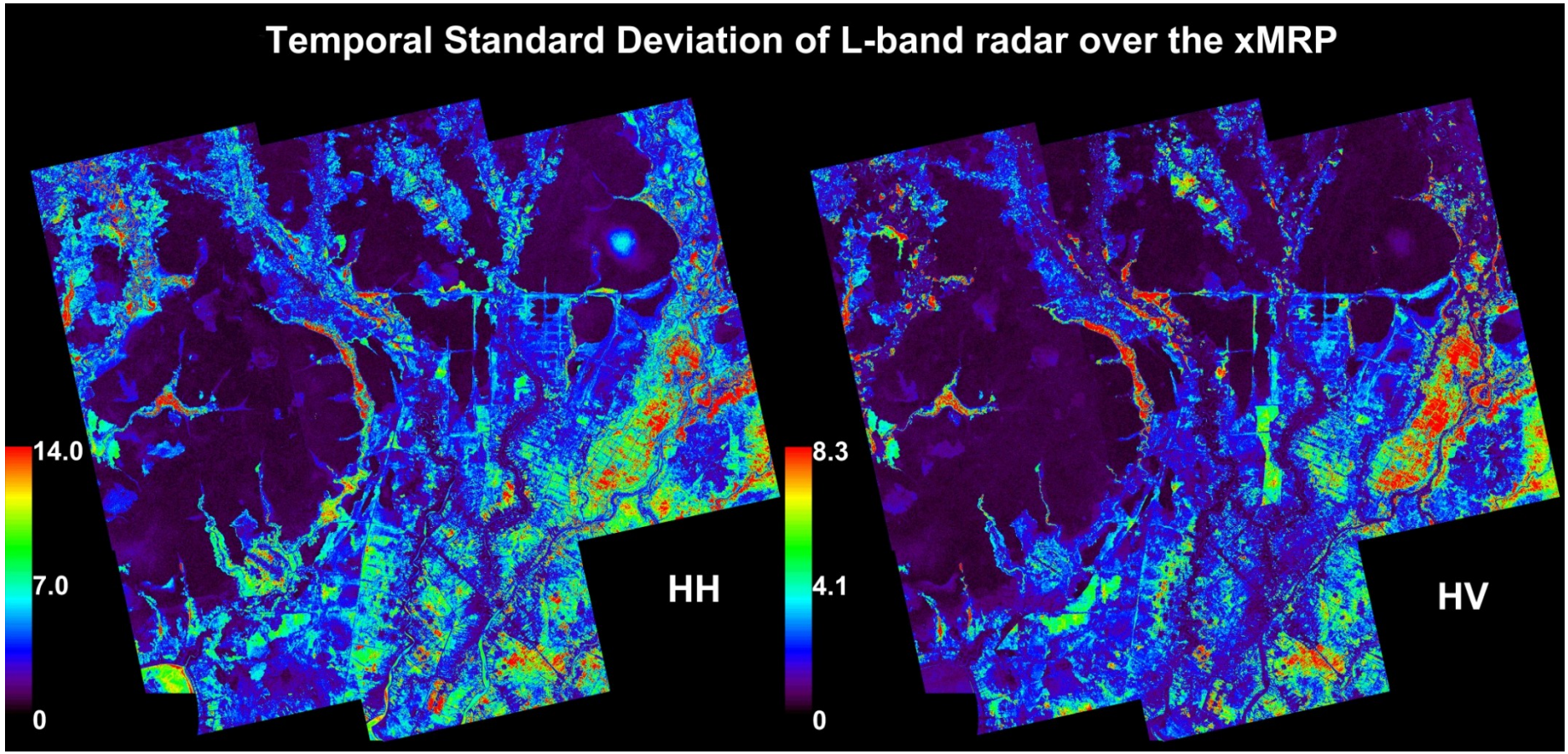


Figure 4.6. A mosaic of 8 PALSAR FBD images showing the temporal Standard Deviation (tSD) over the ex-MRP, Central Kalimantan.

### 4.2.3 How can temporal patterns of landscape backscatter change be interpreted?

Maps of tSD only show the locations where changes in radar backscatter are happening; they say nothing about the relative timing of the changes or how frequently they occur. Empirical Orthogonal Functions (EOFs) were used to separate different patterns of temporal change in the radar backscatter in both the spatial and temporal domains. EOFs belong to a family of eigentechniques that utilise matrix rotations in order to simplify data by reducing dimensionality (Hannachi, 2004). EOFs are computationally very similar to Principal Component Analyses (PCAs) extended into the time domain and have a long history of use in climatology where analysis of datasets varying in both the temporal and spatial modes has been common for some time (Hannachi et al., 2007). As an example to explain the concept imagine a data set consisting of 10 years of daily satellite images (i.e. 3650 image) captured over the same location. Captured in this large high dimensional dataset would likely be a number of processes occurring over daily, seasonal, annual and interannual timescales. When analysed using the EOF methodology the data set would be reduced in size and dimensionality. A number of EOF layers would be produced each accounting for successively less of the variation in the entire dataset. A time profile would indicate the magnitude and frequency of changes and an EOF image would indicate where these modes of variation were occurring. EOFs have been predominantly used for describing spatio-temporal patterns in atmospheric and oceanographic contexts, although they have also been used to describe the changes in patterns of urban development (Small & Elvidge, 2011). In this thesis they have been applied in a terrestrial context with the aim of separating seasonal or quasi-seasonal patterns of backscatter change from more abrupt changes associated with forest loss and degradation. The input dataset for the EOFs are the time stack of

radar images and the outputs are a series of images explaining decreasing percentages of the variation in the original stack. Pixels in the images show how similar a pixel's temporal behaviour is to that described by the individual EOF. Pixel values in the output images indicate how similar that pixel's temporal profile is to that of the output EOF band. Each EOF image has with it an associated graph showing the variation of that band through time.

EOFs were calculated individually for each strip and polarisation of radar data. In order to calculate the EOFs for each time period the stack of radar images were reformatted into a 2 dimensional matrix with one row for each pixel and separate columns for each time period. This was done using the 'map2map.m' script (Appendix 8.3.3). During this process all 0 values around the outside of the image stack were masked. The first 6 EOFs were then computed using the 'caleof.m' script (Appendix 8.3.4) with the memory efficient method 2 selected. Output images files, one for each EOF, were then converted back in to geographic co-ordinates ('mat2map.m' Appendix 8.3.5) and converted into an ENVI format using the script 'enviwrite' (Appendix 8.3.6). If the EOF script would not run a peat depth mask (shown in Figure 4.7) was used to reduce the spatial extent of the input radar dataset. Table 4.1shows which scenes required masking and which mask was used.

Table 4.1. EOF processing success and masking parameters. **Y =** processed successfully, x = process failed.

| Strip | Polarisation | No | peat | peat > 50cm | peat >100cm |
|---|---|---|---|---|---|
| 421 | HH | Y | | | |
| | HV | x | x | Y | |
| 422 | HH | Y | | | |
| | HV | x | x | x | x |
| 423 | HH | x | x | x | x |
| | HV | Y | | | |

Text files containing the temporal variability and amount of variation in the total dataset explained by each EOF were also output and converted into line graphs and tables respectively. EOFs were calculated in MATLAB using a large memory node of the ALICE cluster computer (http://www2.le.ac.uk/offices/ithelp/services/hpc/alice). Due to computer RAM size constraints it was not possible to run the entire dataset as one mosaic as was done for the spatial maps of temporal standard deviation and mean. Instead the analysis was run on individual strips of radar data.

Not all scenes ran successfully with an error produced when the eigenvalues failed to converge, indicating that the program had not been able to separate the dominant modes of variation in the data. In an effort to overcome this, the peat depth map shown in Figure 4.7 was used to spatially subset the input data in an attempt to isolate the temporal variability in peatlands from that observed around rivers. Data were successively clipped to include only areas of peatland (i.e. peat >0cm), areas of peat >50cm deep and areas of peat >100cm. Table 4.1 gives details on which datasets were run with which mask.

## 4.3 Results

### 4.3.1 Temporal variation of radar backscatter across a biomass gradient

Temporal radar profiles were extracted for 145 locations with associated biomass estimates. Figure 4.2 shows the temporal variability of the radar signal (+/- 1 tSD) over a 4-year period for both polarisations of the radar signal for each biomass value across the gradient of measured biomass for peat swamp forest. The general pattern of signal variability change is evident in both radar polarisations, namely that the greatest signal variability occurs at low biomass levels, but with the HH polarisation showing much high variability. There is also a large amount of variability between

biomass values even when the measured biomass is similar. The variability at low biomass in the HH polarisation results in some low biomass values having at some time points greater backscatter than high biomass values. This can be clearly seen in Figure 4.3 which shows the 'envelopes of variation' calculated using binned biomass values for both radar polarisations. Whilst the line representing the maximum variation is flat in the HV polarisation, in the HH polarisation it is higher at low biomass than at higher biomass levels. Figure 4.4 shows how the radar signal variability in the HH polarisation is related to that in the HV polarisation. There is a concentration of plots with small standard deviation on the right side of the graph which consist of biomass plots from high biomass intact forest.

### 4.3.2 Temporal variation of radar backscatter over the landscape

The images of temporal mean backscatter shown in Figure 4.5 and temporal standard deviation (Figure 4.6) provide the landscape context in which to place the biomass information in figures 4.2.1-3. Figure 4.5 shows that in the HH polarisation the highest mean temporal backscatter occurs in the areas surrounding rivers with further isolated patches seen in forests. The lowest mean backscatter is seen along rivers and canals. The HV backscatter is highest in intact peat swamp forest with areas of low backscatter observed along water courses (especially rivers and less so along canals) and in agricultural landscapes to the south and east of the mosaic. Comparing the patterns seen in the two polarisations of temporal mean radar data it appears that areas of high HV tend to relate to values in the middle of the range of HH mean backscatter. Figure 4.6 shows a mosaiced image of tSD in both polarisations of radar. The highest temporal variability occurs along rivers and in areas of agriculture. However some areas of high to moderately high areas of tSD

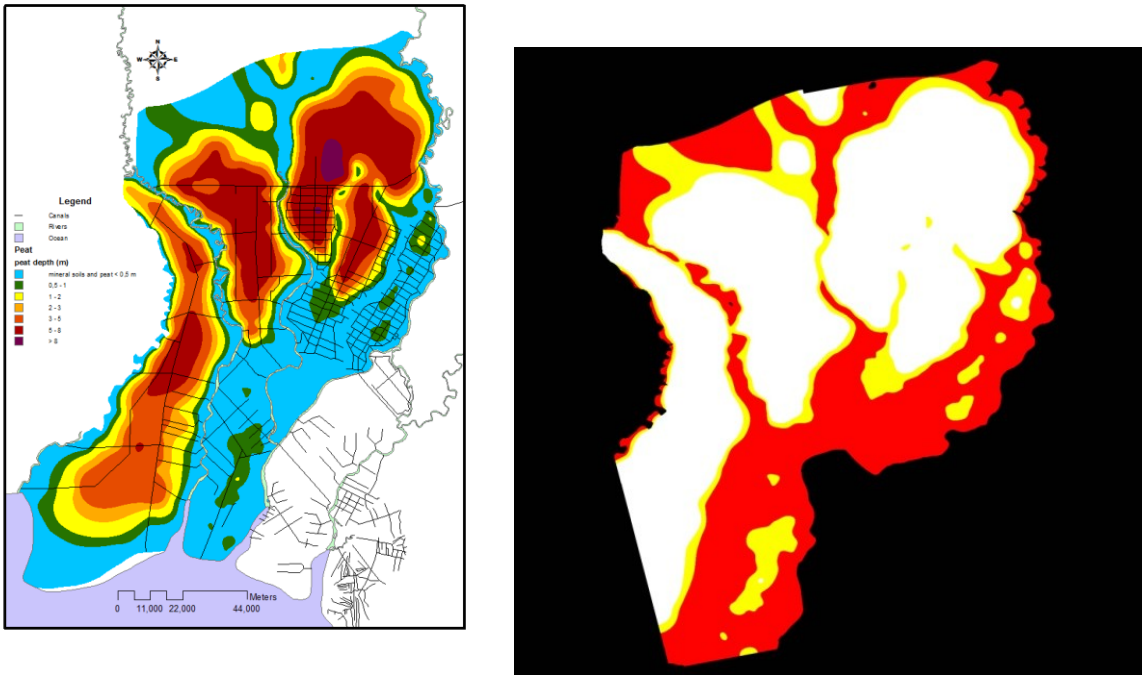


Figure 4.7 Peat depth map courtesy of Delft Hydraulics (left) and peat depth mask (right). Red=peat mask, yellow= peat >50cm deep , white = peat >1m deep

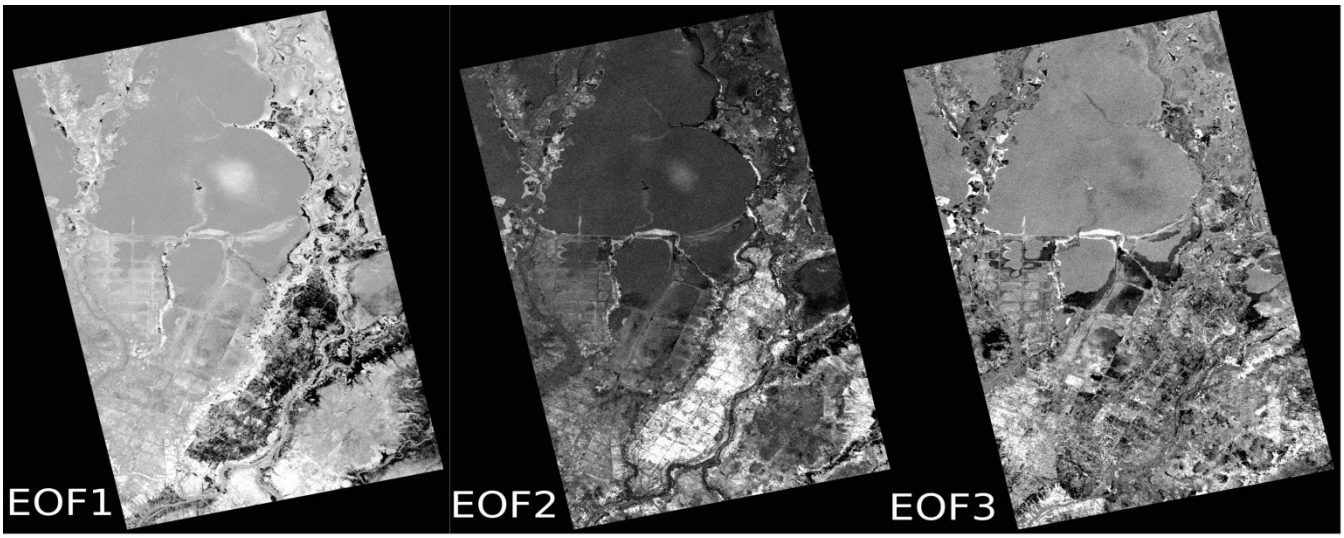


| EOF | 1 | 2 | 3 | 4 | 5 | 6 |
|---|---|---|---|---|---|---|
| Variance explained | 56.3 | 20.6 | 10.6 | 5.2 | 3.6 | 3.3 |
| Cumulative variance | 56.3 | 76.9 | 87.5 | 92.7 | 96.3 | 99.6 |

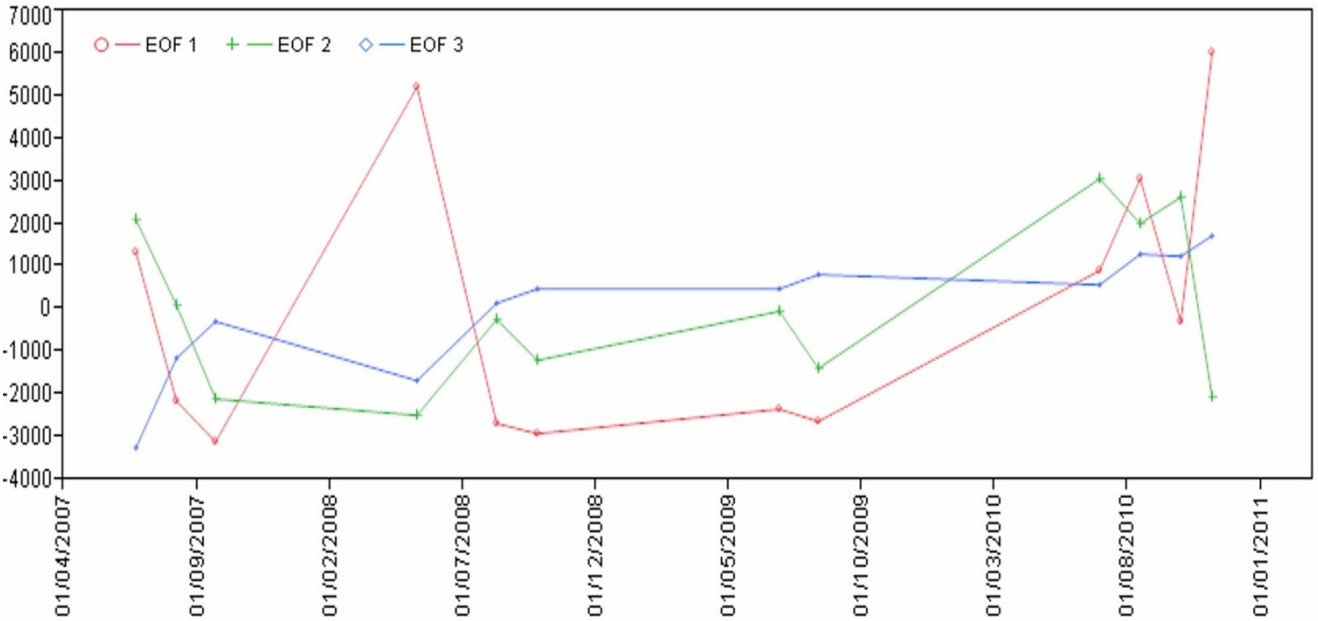


Figure 4.8. Result of the EOF analysis for the 421 (eastern strip), HH polarisation. Top, grayscale images of the first three EOFs. Middle, the percentage variance explained by each EOF. Bottom, the temporal profile of each EOF.

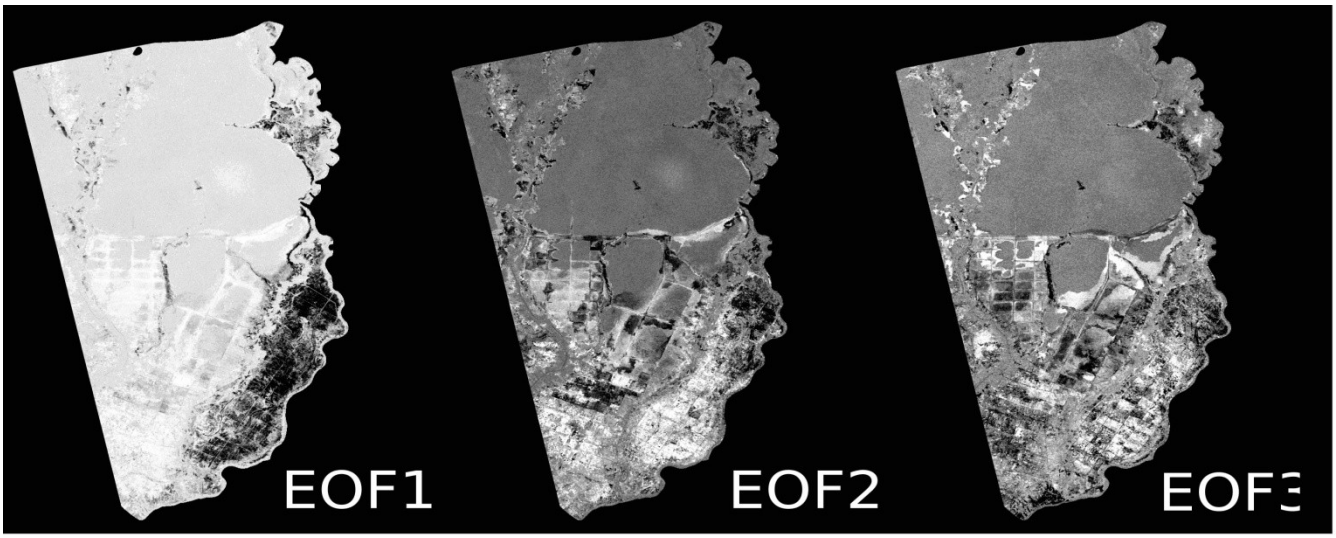


| EOF | 1 | 2 | 3 | 4 | 5 | 6 |
|---|---|---|---|---|---|---|
| Variance explained | 51.3 | 24.8 | 9.8 | 6.9 | 3.5 | 3.4 |
| Cumulative variance | 51.3 | 76.1 | 85.9 | 92.8 | 96.3 | 99.7 |

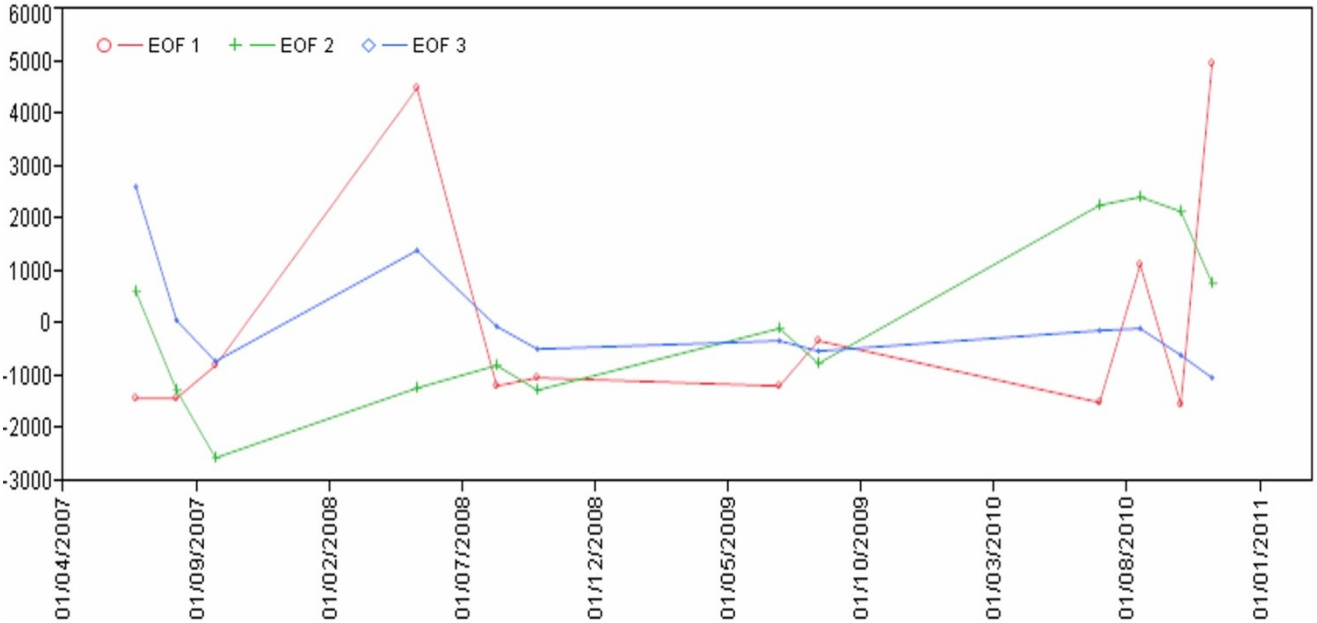


Figure 4.9. Result of the EOF analysis for the 421 (eastern strip), HV polarisation. Top, grayscale images of the first three EOFs. Middle, the percentage variance explained by each EOF. Bottom, the temporal profile of each EOF. This datasets was cropped using the >50cm peat mask.

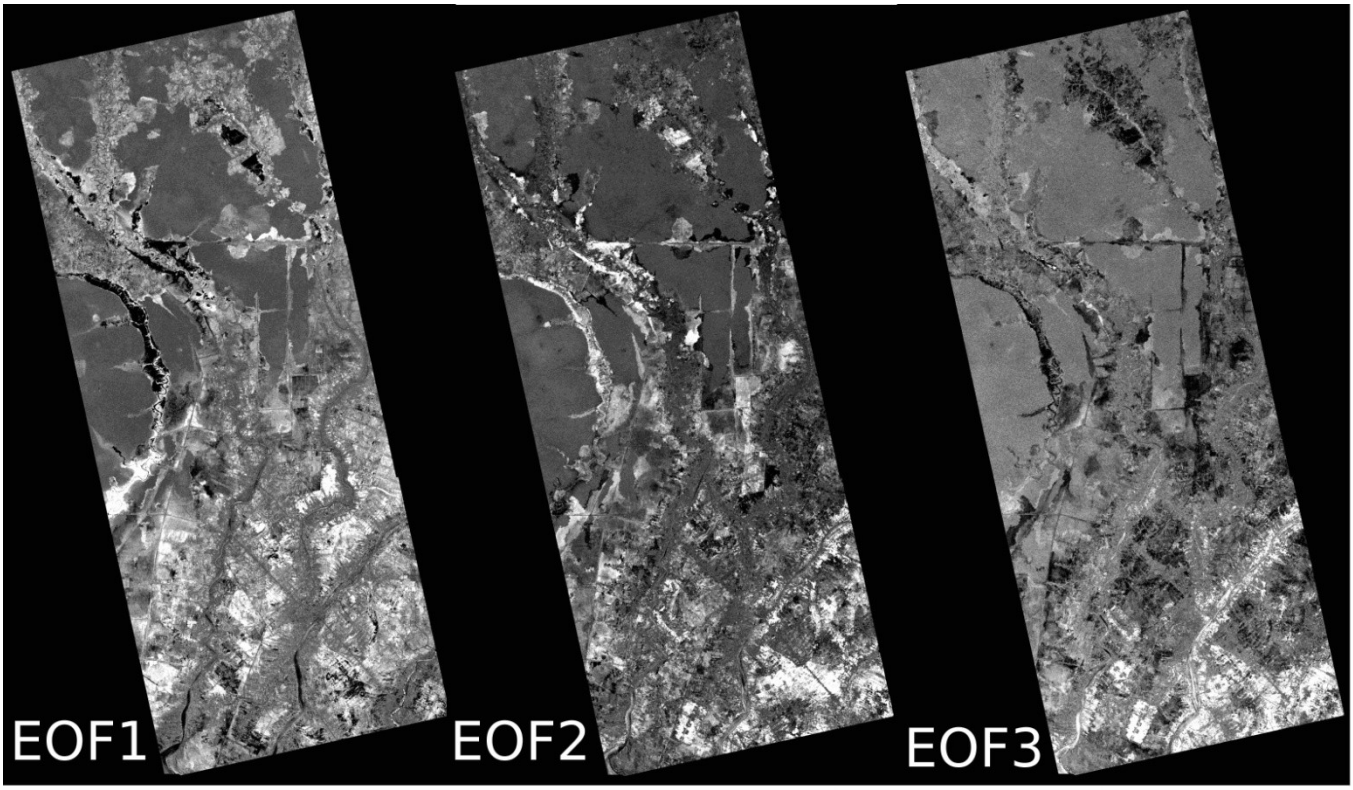


| EOF | 1 | 2 | 3 | 4 | 5 | 6 |
|---|---|---|---|---|---|---|
| Variance explained | 46.8 | 25.0 | 10.2 | 6.6 | 5.7 | 5.4 |
| Cumulative variance | 46.8 | 71.8 | 82 | 88.6 | 94.3 | 99.7 |

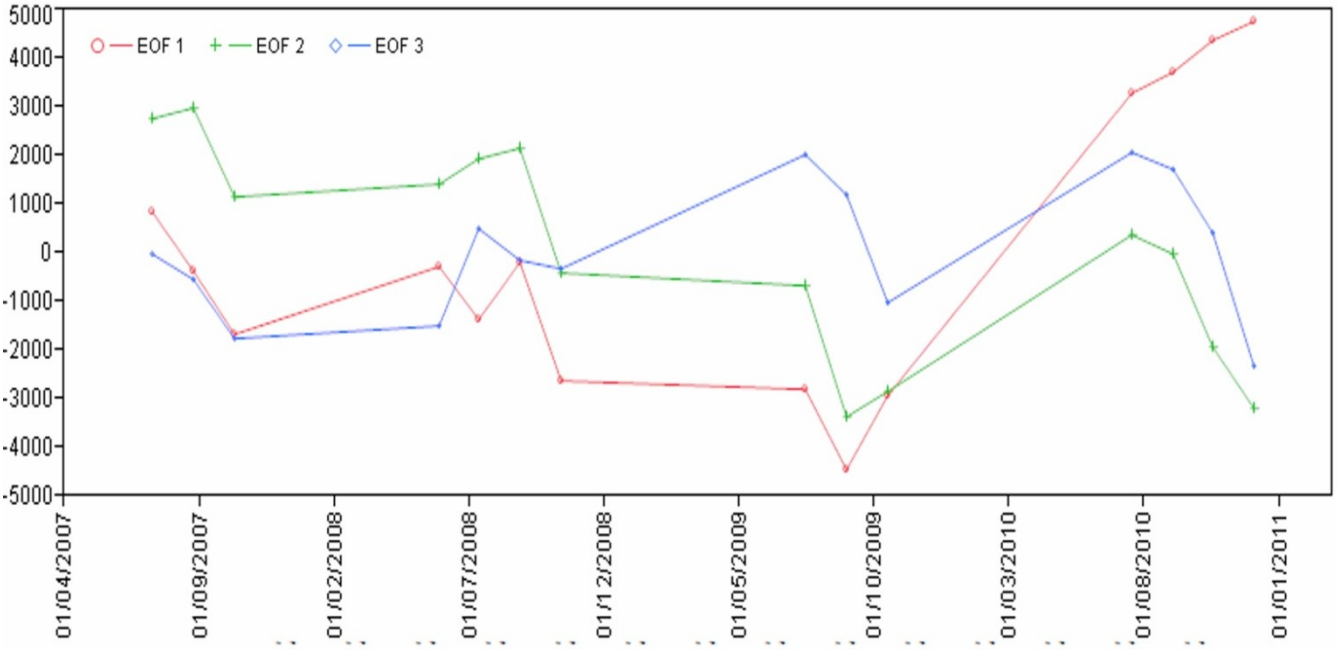


Figure 4.10 Result of the EOF analysis for the 422 (middle strip), HH polarisation. Top the first three EOFs. Middle the percentage variance explained by each EOF. Bottom the temporal profile of each EOF.

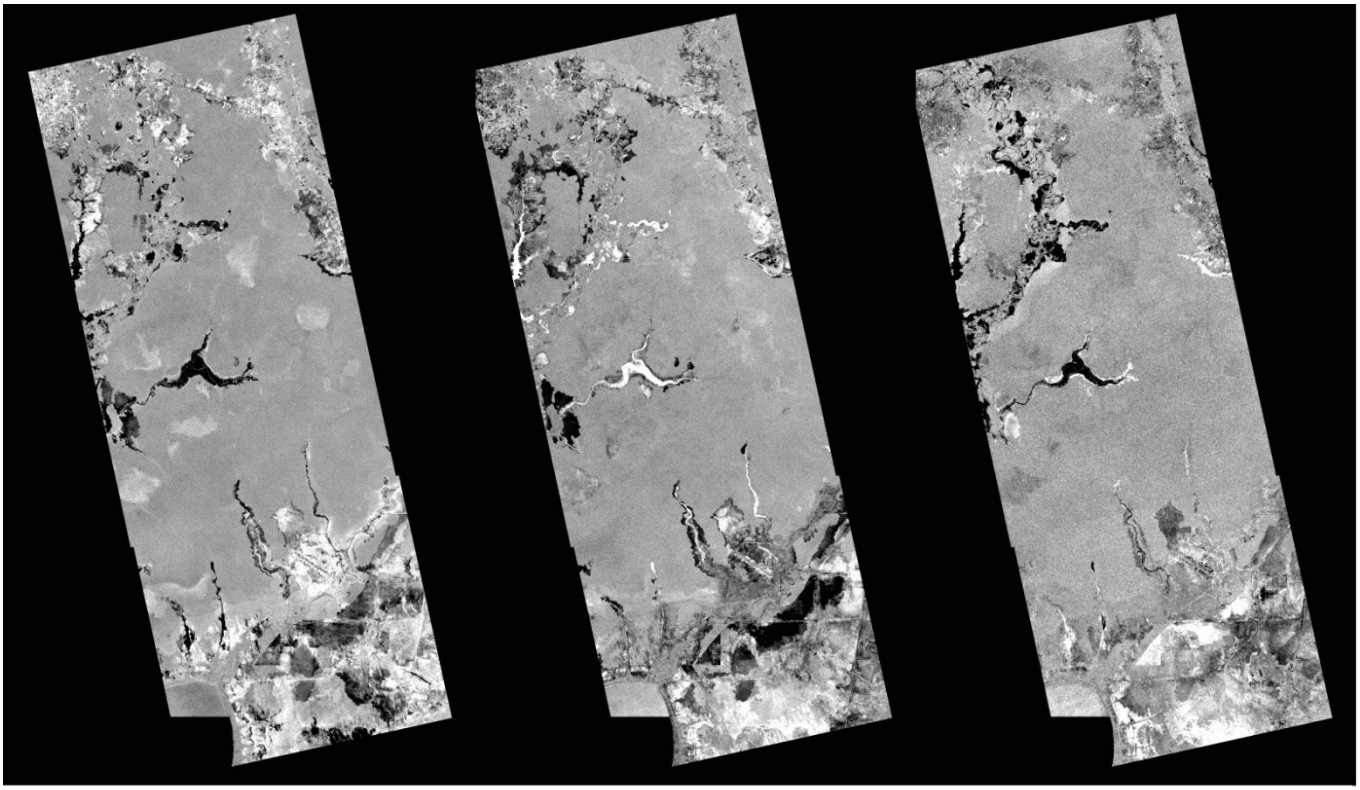

| EOF | 1 | 2 | 3 | 4 | 5 | 6 |
|---|---|---|---|---|---|---|
| Variance explained | 36.3 | 26.7 | 15.8 | 8.6 | 7.2 | 5.2 |
| Cumulative variance | 36.3 | 63 | 78.8 | 87.4 | 94.6 | 99.8 |

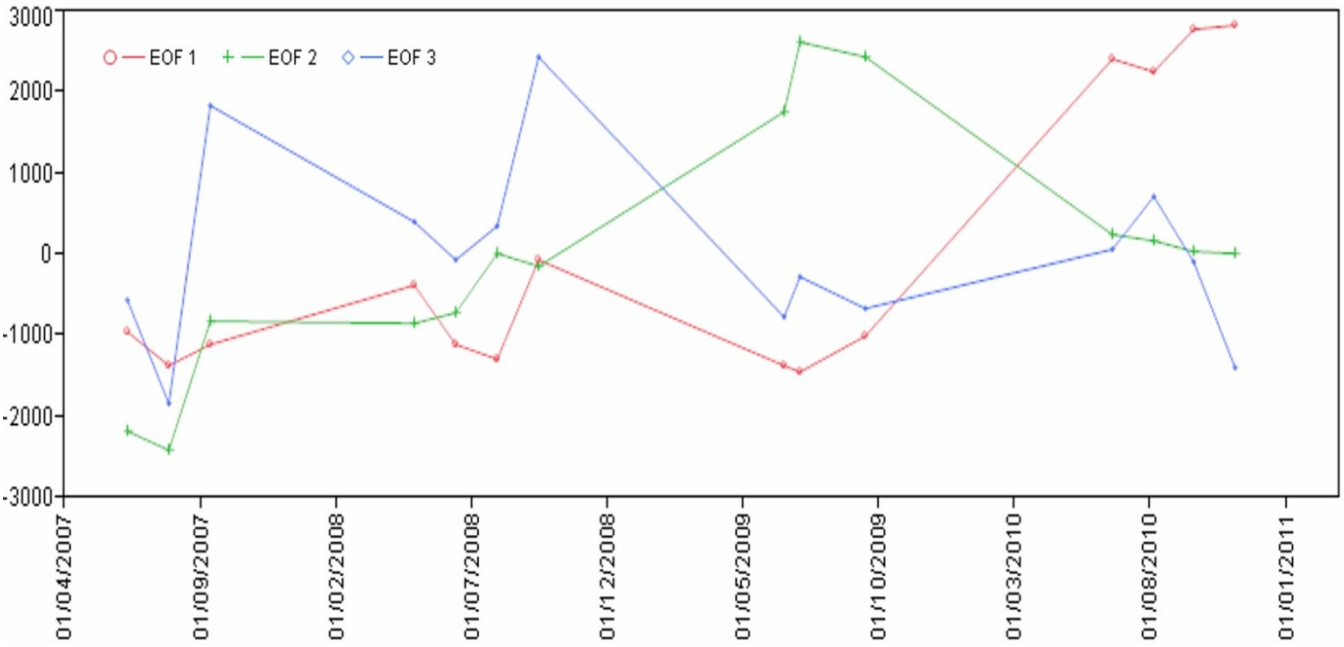


Figure 4.11. Result of the EOF analysis for the 423 (western strip), HV polarisation. Top the first three EOFs. Middle the percentage variance explained by each EOF. Bottom the temporal profile of each EOF

were seen in the HH and to a lesser extent the HV polarisation in areas of forest adjacent to low biomass degraded areas. The HV polarisation also highlighted straight edged areas associated with timber plantations (middle of image) and oil palm plantations (bottom left of image).

### 4.3.3 Mapping patterns of temporal backscatter change

The calculation of EOFs was not possible for all scenes in Table 4.1 even with the use of the various peat masks to reduce the variation of the input data set. The failures were computational errors due to a lack of convergence within the dataset, i.e. failure to sufficiently identify modes of variation within the data to assign as EOF layers. However of the 6 input datasets run (3 strips and 2 polarisations) results were obtained for 4 datasets and the EOF outputs for these datasets are given in Figures 4.8-11. The only strip of images for which both polarisations ran was the eastern most strip (421). In the HH polarisation (Figure 4.8) 56% of the variation in the full image stack was explained by EOF1. This temporal variation associated with the first EOF appears to be quasi-seasonal with a number of peaks occurring on an annual basis, with the exception of 2009. This year, however, was the driest during the study period as demonstrated by it being the only year in which extensive fires occurred. The second EOF appears to be spatially associated with areas of agriculture in the lower left part of the image. The third EOF appears to be associated with areas of forest in close proximity to canals and rivers and shows an increase in late 2009. The first three EOFs together account for 87.5% of the variation in the entire dataset. The first EOF of the HV (Figure 4.9) dataset appears to be similar both spatially and temporally to EOF1 of the HH

dataset. EOF2 was associated with areas of agriculture and degraded peat swamp forest. Finally EOF 3 was strongly associated with recently burnt forest.

It was only possible to obtain an EOF analysis in the HH polarisation for the middle (422, Figure 4.10) strip of images. Here the first EOF accounted for 46% of the overall variation. Spatially this band appears to be associated with forest burnt during the 2009 fires; this is indicated in the time series by a marked increase in backscatter. EOF2 is related largely to water courses but also appears to be associated with degraded areas. EOF3 appears to be associated with agricultural areas in the bottom eastern corner of the image. The first 3 EOFs accounted for 82% of the total variation in the input dataset.

The final EOF analysis (Figure 4.11) was for the western most strip (423) and in the HV polarisation. In this analysis the first EOF explained only 36% of the variation and was spatially associated with areas surrounding the larger rivers. Temporally it was very similar to EOF1 in Figure 4.10. The second EOF appeared to be associated with water courses with their source on the Sebanagu peat dome. The third EOF interestingly appeared to be largely associated with an area of expanding oil palm plantation in the south of the image and temporally showed peaks in both 2007 and 2008 followed by a reduction in backscatter in 2009-10.

## 4.4 Discussion

### 4.4.1 Temporal variation of backscatter across a biomass gradient

Figure 4.2 clearly shows how the temporal variation changes across the biomass gradient with high biomass areas showing much lower temporal variation than low biomass areas in both polarisations, and with HH showing more variation across

the whole biomass gradient than HV. This finding is similar to that described by Romshoo (2003), although his sample of biomass plots did not include any riverine forest plots that were directly affected by riverine flooding. It should also be noted that the temporal variation in the radar signal at low biomass can be larger than the increase due to biomass. In other words the backscatter values from some low biomass points (particularly in HH) can be higher than the backscatter from high biomass plots. This can be seen most clearly in Figure 4.3 which presents 'envelopes of variation' of the radar signal over peat swamp forest. Figure 4.4 shows how the biomass values are grouped within the space described by the two radar axes. Biomass values fall in to several groupings: firstly a dense grouping of plots with low variability at the high end of the HV axes (group 2 in the inset of Figure 4.4); these represent high biomass forest where the radar signal is saturated. Secondly plots lying on the increasing gradient of HH and HV (group1 in the inset). These biomass values generally have high levels of tSD and represent degraded forest with lower biomass than that of intact forest. Finally a third group (group 3 in the inset of Figure 4.4), show a variety of values in HV backscatter and higher mean HH backscatter than intact forest. Despite the high levels of tSD for biomass value in both the HH and HV polarisations, the tSD shown in Figures 4.2.1-3, is much less than that observed in the mosaic images of tSD (Figure 4.6).

### 4.4.2 Mapping of temporal backscatter variation over the PSF landscape

Levels of HH tSD seen over the biomass gradient are dwarfed by those observed in the radar mosaic which are seven times as great. In the HV polarisation the

difference in tSD is twice as much in the mosaic as that observed over the biomass plots.

These results point to problems when using either of the polarisations or combinations of the two polarisations for biomass estimates as the resulting estimates could vary widely according to the date of the radar acquisition.

The maps of tSD and the EOF analysis highlight that similar spatial locations exhibit high levels of variability within the radar backscatter stacks. The EOFs provide further information on which areas show similar timing and patterns of temporal radar backscatter change, although they give no information on what landscape processes are producing these patterns. It is likely that they identify different processes (e.g. seasonal flooding vs. agricultural land use) and different stages in landscape processes (e.g. immediately post fire or years after fire). One advantage of the use of EOFs is that they are totally automatic: patterns are described with no user input in an unsupervised manner. The challenge to the user is then to correctly identify the temporal patterns of backscatter change as landscape processes. The next two chapters of this thesis investigate the environmental factors causing these patterns of backscatter change.

Despite being useful in an attempt to partition the landscape according to backscatter history the use of EOFs presents a number of challenges. Being based on eigentechniques the memory requirements of the EOF analysis are large, scaling with the square of the number of pixels in an image. Such limitations have not been so problematic in the climatological arena from which the technique originates where pixel sizes are of the order of kilometres (often quarter degree cells). However in analysing land surface processes the required pixel resolution to

adequately describe complex processes such as deforestation and forest degradation is of the order of meters (25m$^2$ in this case) and therefore memory requirements quickly become limiting. In undertaking this analysis, these obstacles were overcome to a limited degree by using memory efficient MATLAB shortcuts, masking out image boundaries and performing the analysis on the large memory nodes of a cluster computer. However, the present regional scale analysis likely represents the approximate maximum spatial scale possible at this pixel resolution under current conditions, which precludes the technique from being used for very large scale national or global analyses.

One possible future method to enable the analysis of larger spatial datasets using EOF, may be to reduce the size of the input dataset by masking out areas of low temporal standard deviation, which are likely to represent landscape units which are not undergoing any significant vegetation change. Since EOFs analysis does not highlight areas of temporally stable backscatter this should not affect the overall outcome of the analysis. Ultimately what is required, however, are memory efficient statistical and analytical techniques able to describe the similarity of the temporal variability of pixels across images. This need is likely to become more acute as satellite data become ever more present and the historical depth of imagery around the globe increases. In the last few years algorithms for analysis of temporal behaviour have begun to emerge, focussed on differentiating natural seasonal variability from disturbances using the Landsat and MODIS datasets (e.g. Coops et al., 2010; Zhu & Woodcock, 2012).

Memory constraints also add an additional complexity to interpreting the resulting maps of spatio-temporal variation. It is not possible to produce single mosaics as

was done for tSD and tMean since the processing must be split into strips. The EOF bands may not be directly comparable between strips as they may capture different components of variability (i.e. a mosaic of EOF1 bands for the different strips could be misleading). For example although EOF1 for strips 422 (Figure 4.10) and 423 (Figure 4.11) appear to have similar temporal profiles and might be thought to be describing comparable landscape processes, EOF1 from strip 421 shows a very different temporal profile and likely represents a different landscape process. This difference may be due to the fact that forest occupies a much larger portion of strip 423 than it does 422. In a similar manner EOF output bands calculated for different time periods may also not be directly comparable.

## 4.5 Summary

In this chapter the spatial temporal patterns of PALSAR backscatter variation in a ~28,500km$^2$ area of peat swamp forest have been examined over a 4 year period.

Aim 1: **What are the patterns of temporal backscatter change across a gradient of increasing biomass from low to high biomass peat swamp forest?**

The radar signal was temporally stable over high biomass forest but showed considerable variation at lower biomass levels (<80 tonnes per hectare ) especially in the HH polarisation where backscatter varied from much lower to higher than that from high biomass forest.

Aim 2: **How do the levels of temporal backscatter change across the biomass gradient relate to the temporal radar signal across the whole landscape?**

Maps of temporal standard deviation showed high variability across the landscape, only a small proportion of which was related to biomass change

Aim 3: **Does the temporal variation of the radar signal need to be taken into account when producing maps of biomass from radar images?**

Different landscape unit shows different temporal patterns of backscatter change which could be used as the basis for land cover classification and biomass mapping.

These findings are important as they address knowledge gaps about the temporal behaviour of the radar signal over PSF and the validity of mapping biomass from single date radar images using empirically fitted biomass relationships. In the next chapter research the sources of radar signal variation in areas where no biomass change is occurring are investigated. Understanding the drivers of this variation in the radar signal and the areas in which various drivers dominate the radar signal variation is vital if radar is to be used to monitor forest carbon as in Balzter et al., (2003).

# 5. Non-disturbance related changes in radar backscatter

## 5.1 Introduction

From the data and analyses in Chapter 4 it was evident that much of the temporal variability in the radar stacks was not related to biomass change in forests. This chapter focuses on that part of the radar signal not related to forest loss and examines how changes in the peatland water table affect the radar signal.

### 5.1.1 Importance of peat water table for estimating carbon fluxes

The accumulation of organic matter in tropical peatland is a result of the anaerobic soil conditions in the waterlogged peat, a situation which is dictated by the climate and local hydrology and topography. Any alteration to this hydrology (e.g. as a result of drainage) can lower the water table and expose peat to aerobic conditions resulting in peat decomposition through microbial oxidation and an increased likelihood of fire, both processes resulting in significant fluxes of carbon dioxide from the peat to the atmosphere (Hooijer et al., 2012; Jauhiainen et al., 2012; Page et al., 2002). These losses of carbon from tropical peat soils can be large in magnitude, dwarfing those occurring as a result of the removal of above ground woody biomass. The water table in peatlands is naturally variable, depending on inputs from seasonal rainfall. Periods of low rainfall, usually occurring during the

short dry season but which may be extended during el Nino events, lower the water table and lead to increased rates of peat oxidation across a much deeper profile of the peat column (Hirano et al., 2007; Jauhiainen et al., 2005) as well as leading to an increased risk of fire (Lailan, 2002; Wösten et al., 2006). In peatlands that have been drained for agriculture, the water table will be maintained at a suitable level for crop production (e.g. 60 – 80 cm below the peat surface for oil palm (Jauhiainen et al., 2012)) which leads to a constant loss of peat carbon through oxidative decomposition. In Southeast Asia, however, there are also extensive areas of peatland that have been subject to unregulated drainage as a consequence of either logging activities (with canals constructed to float timber out of the forest) or failed agricultural schemes (e.g. the exMRP). Owing to the important influence that the peatland water table has in controlling the loss of carbon from long-term storage within the peat, assessing the position of the peatland water table and its variation through time forms an essential part of any monitoring system designed to estimate carbon losses from tropical peatlands (e.g. Jauhiainen et al., 2012).

There are two main techniques for monitoring water table and soil moisture in peatlands: using *in-situ* dipwells or remote sensing data. These two techniques measure different aspects of peatland hydrology which need to be clearly defined at the outset of this chapter: the first is the water table. The position of the ground water table is the depth at which the (peat) soil becomes completely saturated by water. By convention it is measured relative to the soil surface with negative values indicating that the water table is below the soil surface and positive numbers

indicating standing water above the soil surface (i.e. flooding). The second concept is soil moisture, typically measured as volumetric soil moisture content expressed as a percentage of dry soil weight. Soil moisture is measured at a defined soil depth for example surface soil moisture which is usually measured at a depth of 0-5 cm.

Most remote sensing methods cannot penetrate any distance into the soil (longer radar wavelengths such as P-Band and UHF frequencies), meaning remotely sensed measures of soil moisture are related to the volumetric soil moisture content of the top few centimetres of the soil, whereas dipwells directly measure the depth of the water table i.e. the position of the saturated soil layer, which is used as a proxy for soil moisture status. As the variable of interest in this study is estimating the water table it is important to have some understanding of the relationship between water table depth and surface soil moisture. The porous nature of tropical peats mean that they have the ability to draw water upwards from the saturated zone through capillary action. The implication of this is that peat above the saturated level of the water table will still contain moisture and that the percentage of soil moisture at any given point will decrease to zero as the water table falls. However little information is available on the exact nature of this relationship. (Price, 1997) studied drained lowland peat bogs in Canada and found that surface soil moisture content (as a percentage) and the depth of the water table (in cm) were positively correlated down to a water table limit of ~1 m at which point no further relationship was evident (Figure 5.1). Anecdotal evidence for tropical peatlands suggests that surface peat still holds a significant amount of

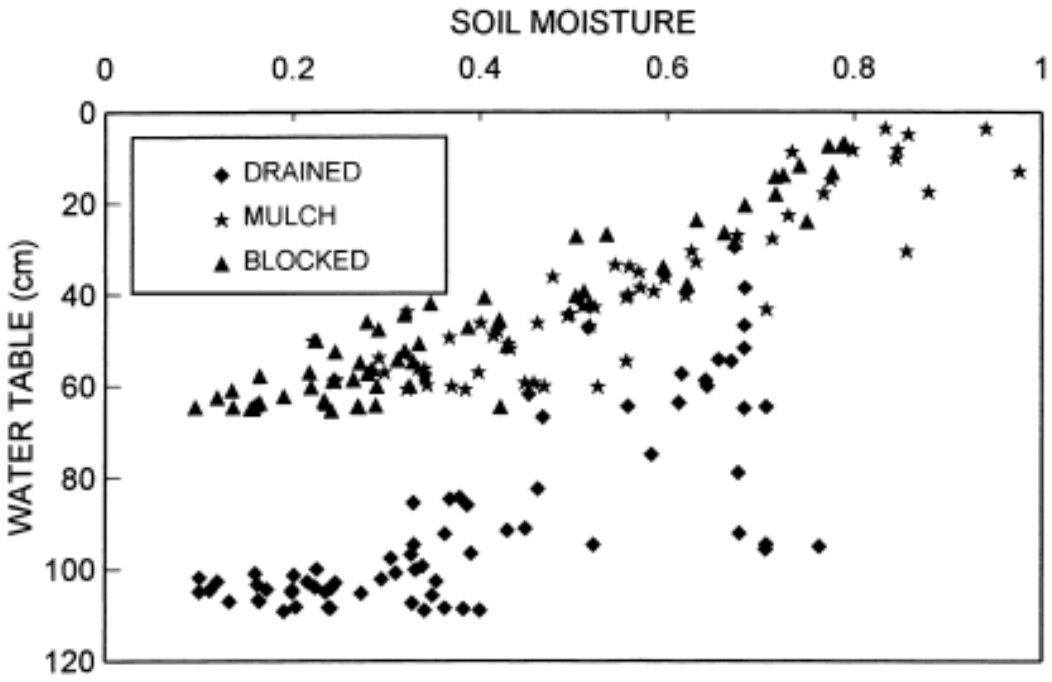


Figure 5.1. The relationship between water table depth and surface soil moisture. Figure taken from (Price, 1997, © Elsevier).

moisture at the surface when the water table is at ~40 cm depth owing to a capillary rise zone of 40 cm (Hooijer *pers comm*).

### 5.1.2 Methods of monitoring the peatland water table.

Dipwells are constructed from lengths of plastic drain pipe with holes drilled into them at regular intervals to allow the free entry and exit of water. These are inserted into holes augured vertically into the peat and the pipes should ideally be anchored in to the underlying substrate below the peat to prevent movement of the pipe relative to the peat surface. The water table in the peatland can then be measured using a float attached to a measured piece of line. A series of water table depth samples, usually taken from a number of dipwells located along transect lines that are sampled regularly (e.g. weekly or twice monthly), can form the basis of a water table monitoring program. Correctly installed dipwells provide

the most accurate data on variation in the water table of peatlands, although as dipwells can only provide data at single spatial locations, monitoring the water table over an entire peat dome usually involves the construction of a series of dipwell transects. Other drawbacks of this technique are that the installation, maintenance and monitoring of the dipwell networks is an expensive as well as a time and labour intensive process. The use of automatic dipwell logging devices can help to reduce labour costs, but the loggers are themselves expensive. Another drawback of the technique is that even networks of dipwells fail to provide a truly continuous spatial estimate of the peatland water table, although geospatial techniques such as kriging can be used to interpolate values for the water table occurring between the locations of individual dipwells.

The second major technique that can be used to provide information on soil moisture and could potentially be able to provide information on the peatland water table is remote sensing. Remote sensing of soil moisture is driven by the dielectric properties of saturated or unsaturated soil media that influence the microwave emissions (in the case of passive radar sensors) and backscatter (for active radars) of the soil. Several operational (e.g. SMOS and ASCAT, Brocca et al., 2010; Sinclair & Pegram, 2010) and proposed (e.g. SMAP, Entekhabi et al., 2010) orbiting radar satellites exploit this effect to produce spatial soil moisture estimates using algorithms to convert the radar data to estimated soil moisture values. These systems produce soil moisture estimates with a high temporal frequency (daily or less) and also produce spatially continuous datasets. However the spatial resolution is very coarse resolution with pixel sizes of many kilometres. At this scale, entire peatland domes can be covered by a single pixel and these data is of

little use in estimating soil moisture given the spatial scales of forest degradation which are of the order of tens of meters.

### 5.1.3 Relating peatland water table variation to PALSAR backscatter and coherence change

In Chapter 4 the temporal variability of the PALSAR dataset was analysed and it was evident that changes in the backscatter signal were not caused solely by changes in the amount of above ground forest biomass. The signatures of this change appeared, in some cases, to be quasi-seasonal indicating that the changes in the radar signal may be being driven by seasonal changes in the moisture content of the peatland. The fact that Central Kalimantan has relatively long and intense dry as well as monsoonal wet seasons mean that the peatland landscape regularly shows large changes in moisture conditions. In this chapter the relationship between the peatland water table and the radar data is examined and described and the possibility of using the PALSAR dataset to produce remotely sensed estimates of water table depth is investigated.

Previous efforts have been made to relate radar backscatter to soil moisture (e.g. Mattia et al., 2009; Pierdicca et al., 2010) but these have concentrated on low biomass environments such as croplands and have not correlated radar backscatter to water table depth. To understand how the radar signal might be affected by soil moisture it is important to consider how the mechanism of radar backscatter would be expected to change across a gradient of increasing above ground biomass. Soil moisture signals are most likely to be seen in areas with low above ground woody biomass where the dominant mode of radar backscatter is

from the soil surface. As the surface soil moisture content varies the changing dielectric properties of the soil will alter the backscattered signals with the literature suggesting that changes can be of the magnitude of 2-3dB (Kasischke et al., 2009). As biomass increases the amount of backscatter coming from the surface is likely to decrease as more of the incident radar signal is backscattered from tree trunks and the canopy, although there may some interaction between the two. If the water table is above the surface in degraded areas with standing tree trunks, as occurs after a fire, a very strong 'double bounce' signal can occur where the radar energy is scattered by both the water surface and the trunks. These two surfaces can act as corner reflectors returning a high proportion of the incoming radar signal back towards the satellite. Owing to the increasingly dominant role of volume scattering by tree biomass the moisture signal is likely to become reduced until it is swamped by the biomass signal. In areas of high biomass such as intact forest the radar signal will become saturated by the biomass and there is unlikely to be any soil moisture signal.

In previous studies examining how biomass and moisture influence the radar signal these two variables have been usually investigated separately. Studies of soil moisture and rainfall have been undertaken mainly by hydrologists and studies of land cover change and forest monitoring have been done by ecologists. Both communities see the effects of the other variable of interest as confounding and try to minimise or remove its effect on their variable of interest (Dubois et al., 1995; Joseph et al., 2010; Moran et al., 2004). The two variables are very rarely examined in a synergistic manner and studies of the interaction between moisture

and biomass effects are lacking. Hydrological studies on the effects of moisture on the returned radar signal have largely been carried out in low biomass systems, e.g. deserts (Stephen et al., , 2010), croplands (Joseph et al., 2010), and marshlands (Kasischke et al., 2009). Radar studies of forest biomass generally involve 'snapshots' of forest cover at a single instance (see Chapter 4 for examples) or time averaged values (Englhart et al., 2011) rather than multi-temporal monitoring and hence ignore effects of changing moisture values.

It is proven that soil moisture affects the radar signal most strongly in areas of low biomass, but the form of the relationship between soil moisture and radar backscatter is not proven and is highly dynamic and ecosystem dependent. Theory, mentioned previously, suggests that as the water table rises towards the soil surface, the surface soil moisture is expected to increase and because water has a high dielectric value increasing soil moisture would be expected to lead to increased backscattering from the soil. According to the literature these increases are likely to be in the range of 3dB (Bourgeau-Chavez et al., 2007; Wang et al., 1994). As the water table reaches the soil surface and standing water starts to form radar backscatter is expected to decrease surface scattering microwave energy away from the sensor. This relationship has been previously observed in Alaskan wetlands (Kasischke et al., 2009).

From the literature it is clear that the surface soil moisture interacts with the radar signal. In this chapter the analyses take this further: firstly by adding coherence data and secondly by attempting to link the radar signal to the depth of the peatland water table, with the literature suggesting that the latter is linked to surface soil moisture in peatlands.

## 5.2 Aims

The aim of this chapter is to investigate to what degree changes in the radar signal (HH and HV backscatter and coherence) is driven by changes in soil moisture and by proxy that this allows an estimate of the depth of the peatland water table to be derived from the radar data. Specific research questions are:

1. Do changes in water table alter the radar backscatter in a predictable way and does this conform with scattering mechanisms previously described in the literature?
2. What effect do changes in the water table have on interferometric coherence?
3. How are these relationships between the radar variables and the peatland water table affected by biomass of the overlying peat swamp forest and at what biomass value does the relationship break down?
4. Can a predictive model allow the estimation of water table depth from the PALSAR radar variables and over what biomass range is this effective?

## 5.3 Methods

Dipwell data from Block A of the exMRP had been collected by IAFCP project staff between May 2007 and December 2010 overlapping with the acquisition of PALSAR data. Dipwells were located along transects running between canals in both degraded and forested areas (Figure 5.2

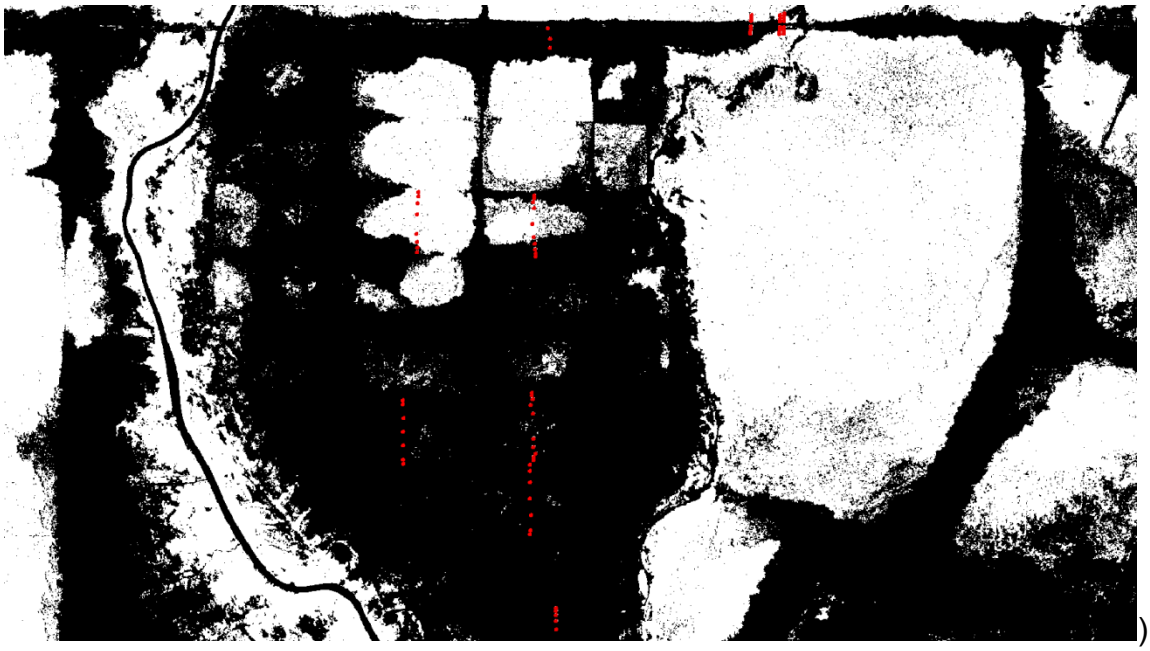
).

The depth of the water table relative to the peat surface was measured approximately every two weeks. As the dates when the water table was sampled and the dates on which PALSAR observations occurred were frequently not concurrent, water table records were temporally associated with the nearest available radar image up to a maximum of 7 days away. Water table data beyond 7 days of a radar image were discarded.

Mean backscatter in both the HH and HV polarisations and, where available, coherence data, were extracted for each dipwell using a circular buffer of radius 50 m around the GPS point. In order to examine what effect the vegetation type had upon the relationship between water table and the radar signal, the dipwells were classified as being located either in forest or in degraded areas based on the mean temporal HV backscatter calculated over the entire 4 year PALSAR dataset. The division between the two classes, -15.9dB, was chosen after visual inspection of the PALSAR images and the extracted data (Figure 5.3). The forest class

represents high biomass intact forest which had not previously burnt (although conceivably it could also include areas of significant regrowth), whilst the degraded class is exemplified by low biomass open areas which have burnt one or more times and are dominated by ferns. A map of the forest/degraded mask is shown in .

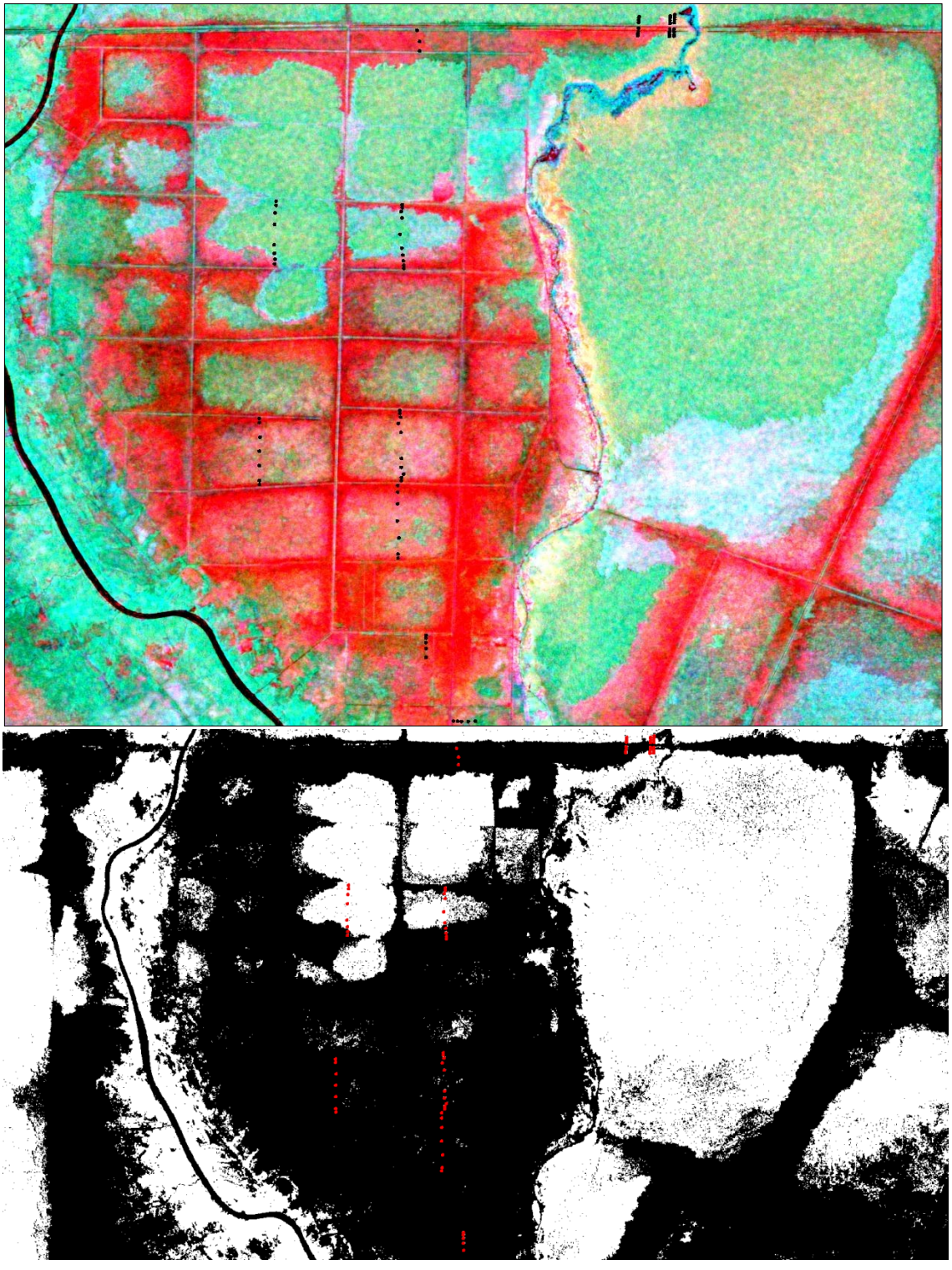

Figure 5.2 Top, PALSAR image of Block A of the exMRP acquired 20080809 (Red channel = coherence, Green = HV backscatter and Blue = HH backscatter). Dipwell transects for the monitoring of the peatland water table are shown as black dots. Bottom, location of dipwells overlaid on forest (white)/degraded (black) mask according to -15.9dB HV tMean threshold.

In order to examine the effect of water table on the radar signal (aim 1 & 2) values of water table depth were plotted against radar backscatter (Figure 5.4) and coherence (Figure 5.5). In order to examine what effect vegetation biomass had upon the water table signal (aim 3) data from forest and degraded classes were separated into two groups based on the vegetation classification.

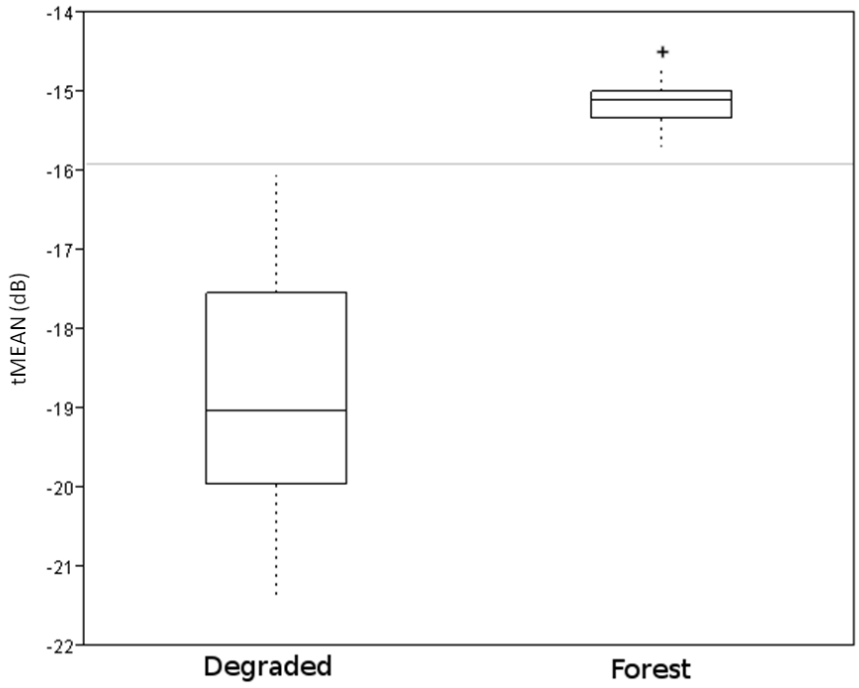


Figure 5.3. Classification of dipwells into forest and degraded classes based on the temporal mean HV backscatter. Horizontal line at -15.9 dB indicates division between vegetation classes

The same dataset was used to produce box plots (Figure 5.6) showing variation of the radar signal. As more potential water table signal was observed in the degraded areas, the high biomass forested areas were excluded from further investigations.

In order to move towards a predictive model of water table depth (aim 4) the strength of the correlation between radar variables and the water table was

assessed using scatter plots with separate linear fits for the backscatter data depending on whether the water table was below the ground <0cm or above the ground surface >=0cm ( Figure 5.7). Coherence data were fitted with a single line. Because the dipwell measurement data and radar image acquisition were not acquired simultaneously (with a maximum time lag of up to seven days) orthogonal regressions were chosen to fit regression lines as this assumes that there is uncertainty in the values of both axes. As both theory (Kasischke et al., 2009) and earlier results indicate that the radar water table relationship is fundamentally different, depending on whether the water table is above or below the surface, separate fit lines were plotted for water table values <0cm and >=0cm. Table 5.1 shows the correlation coefficient for each of the fitted lines shown in Figure 5.7.

For these reasons generalised additive models (GAMs) were used to generate predictive models of water table depth from the radar data. GAMs were chosen since instead of using linear fits to describe the relationship between independent and dependent variables they utilise splines to model curved response surfaces (Wood, 2006). Within GAMs the flexibility of the spline is controlled by the number of 'knots' (inflection points in the spline). Too many knots and the spline becomes overfitted and the predictive power of the model is lost, too few knots and the spline is not flexible enough to represent a true representation of the relationships present in the data. After examination of the data, five knots were chosen as being the most parsimonious solution (Wood, 2006), i.e. the maximum and minimum and three knots in between. Two GAMs were constructed; the first included HH and

HV backscatter intensity and coherence data as independent variables, the second used only the two backscatter variables.

A random sample comprising 17% of the full dipwell dataset was selected and assigned as a ‘control’ group with the remaining values assigned as a ‘test’ group. The control group were excluded from the water table modelling analyses described below and used only during the model validation section of this chapter. The results of fitting these two models are shown in Table 5.2.

## 5.4 Results

Data from 78 dipwells was selected over the period 19/06/2007 to 12/11/2010 giving a total of 616 dipwell data points which were matched to radar acquisition dates within 7 days of the dipwell measurement. From this total, 204 of the data points also had coherence data. Figure 5.4 shows how radar backscatter from forested and degraded areas varies with changing water table depth. In degraded areas backscatter values increase with rising water table before decreasing when the water table is above the ground surface. This trend is clear although a lot of scatter is present in the relationship. In forested areas the trend line is flat indicating that the relationship between the radar signal and the water table is insignificant. The difference in the water table radar relationship between the two vegetation types is likely a consequence of differences in vegetation biomass, which is very low in the former instance and very high in the latter. Coherence data (Figure 5.5) shows a linear trend of decrease with increasing water table depth, although there appears to be a much higher amount of scatter around the trend

lines and a suggestion of a small effect of the water table signal on coherence even in forested areas.

Figure 5.6 illustrates the differences in the variability of radar backscatter and coherence between degraded and forested areas. Much higher variability is seen in all the radar variables in degraded areas compared to forested areas.

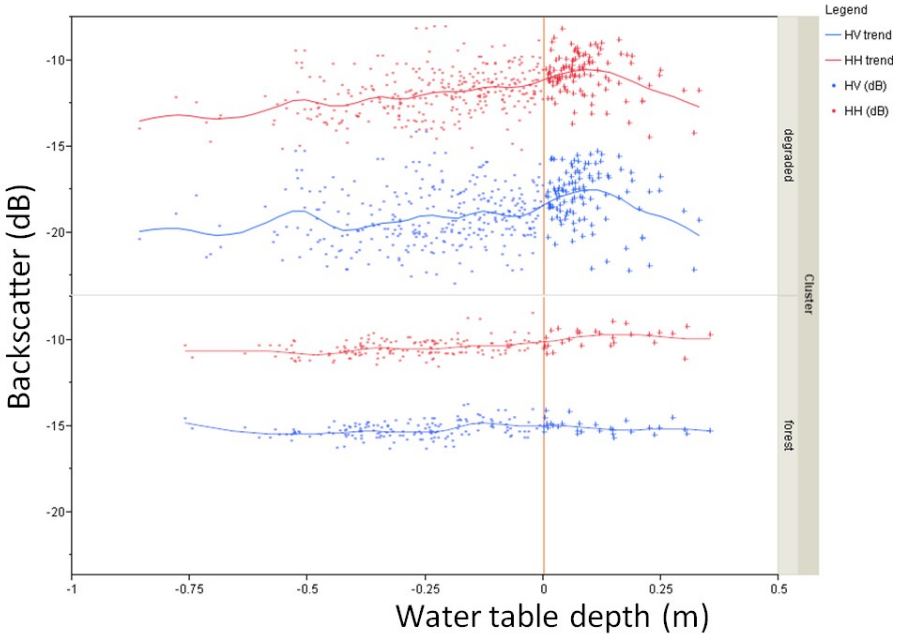


Figure 5.4. Water table depth plotted against radar backscatter in degraded and intact PSF, shown with smoothing line to indicate trend. Positive water table values indicate flooding.

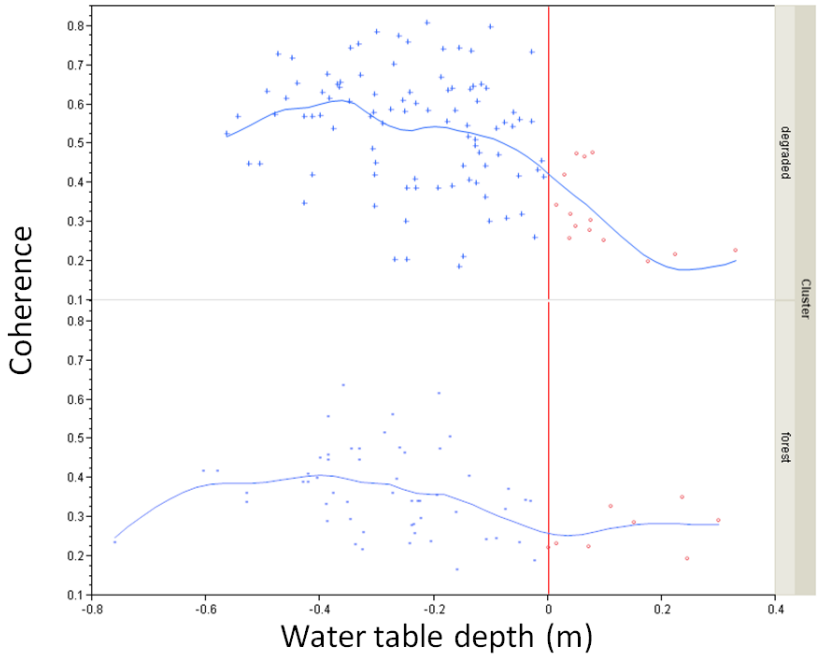


Figure 5.5. Coherence plotted against water table depth for degraded and intact PSF shown with a smoothing line to indicate trend. Positive water table values indicate flooding.

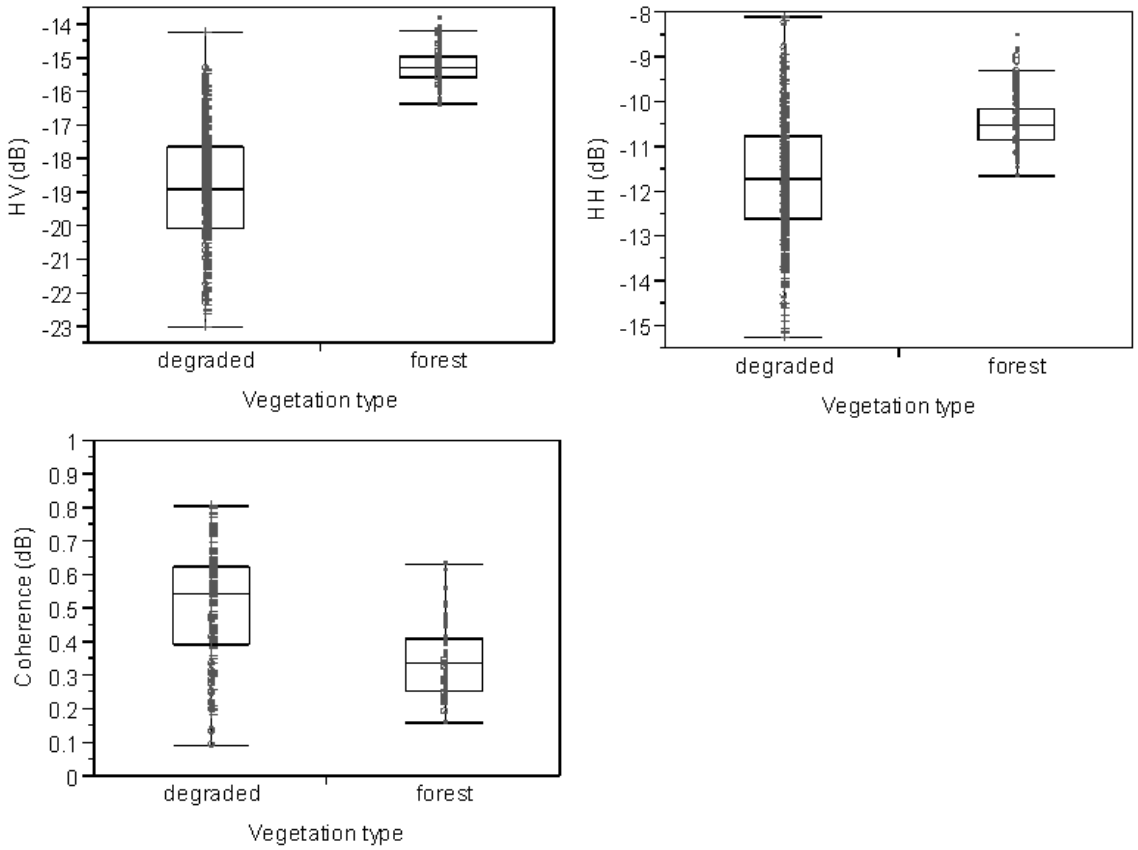


Figure 5.6. Box plots showing the variation radar backscatter and interferometric coherence over degraded and intact PSF. Top left HV backscatter, top right HH backscatter and bottom left coherence. Box plots show the median 25% & 75% quartiles and whiskers identify outliers.

Figure 5.7 show fitted linear relationships between the measured water depth table and radar backscatter and coherence and the water table level. Separate lines are fitted to the backscatter graphs depending on whether the surface is above or below the ground level. From these graphs it appears that different radar scattering mechanisms are occurring depending on whether the water table is above or below the ground surface. In contrast to the backscatter relationships, the coherence relationship with the water table can be modelled with a single regression line.

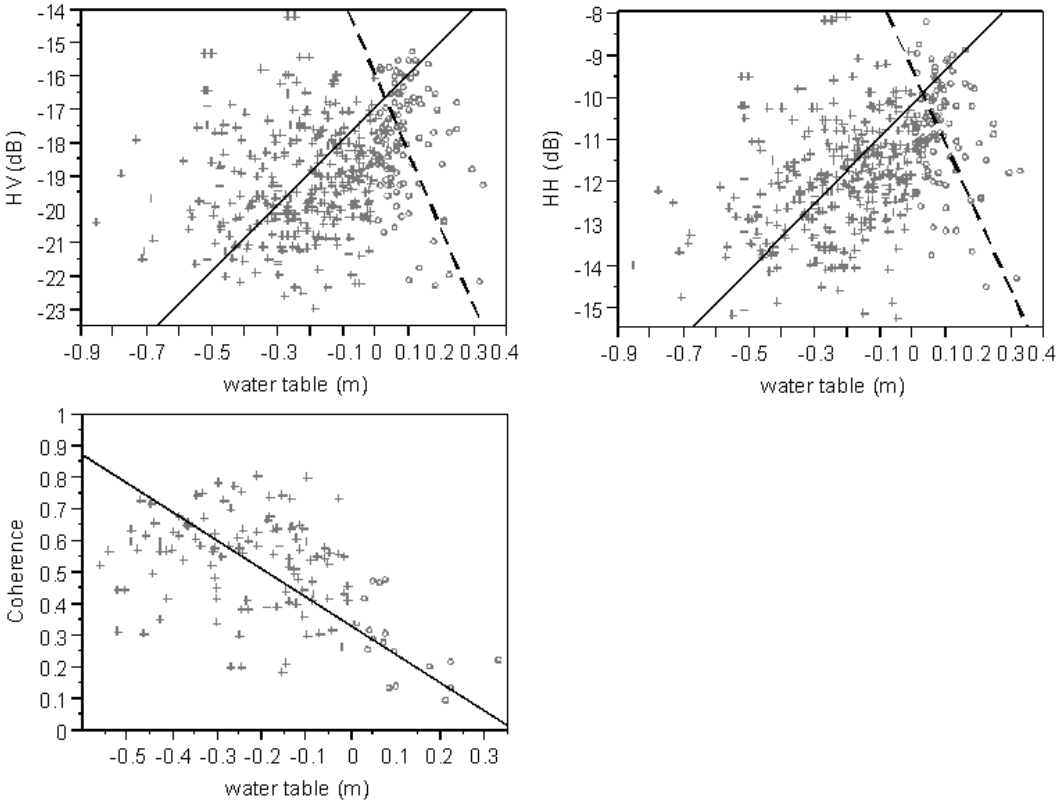


Figure 5.7 Scatter plots of radar backscatter and interferometric coherence plotted against the water table depth as measured in degraded peatlands. Top left HV backscatter, top right HH backscatter and bottom left coherence. Cross identify water table <0cm, circles water table >=0cm. Separate lines have been fitted to the backscatter data at <0 and >=0cm water table depth.

Table 5.1 Regression coefficients of the lines shown in Figure 5.7

| Data | < 0cm | >=0cm |
|---|---|---|
| HH | 0.32 | -0.23 |
| HV | 0.13 | -0.18 |
| Coherence | -0.47 | |

From Figure 5.7 it is clear that the relationship between water table depth and the radar variables is not linear and this rules out the use of any sort of linear fitting when constructing an accurate predictive model in order to accomplish aim 4. Table 5.2 shows the fitted formula structure and relevant statistics for both GAM models and Figure 5.8 shows a graphical representation of the response surface for the GAM model 1 (including coherence). The accuracy of the GAM including the coherence (model 1) model was evaluated from plots of the observed (i.e. measured) versus expected (calculated from radar variables) values using the data excluded at the start of the modelling process (Figure 5.9). Confidence intervals (+ and – 95% were also calculated for all values). The most accurate GAM model (model 1) was then applied to the PALSAR images over Block A of the study area for which all three radar variables were present on a pixel by pixel basis to give a map of estimated water table depth. Confidence intervals were also calculated. Maps of estimated water table depth are given in Figure 5.10.The logic behind the construction of the two models was to examine the predictive value gained by including the coherence data as an independent variable as the production of this data was computationally intensive and also unreliable in comparison to the backscatter data (many dates had missing data for coherence). Hence if there was little gain in predictive power from including coherence in the model the water table estimates would be easier to obtain and more frequently available if calculated solely from the backscatter data.

Table 5.2. Model statistics for the two GAM models. Model 1, HH and HV backscatter and coherence. Model 2, HH and HV backscatter only.

Model 1

| | DF | Sum of squares | F Ratio | Prob > F |
|---|---|---|---|---|
| HV Spline | 4 | 0.3637502 | 5.0617 | 0.001 |
| HH Spline | 4 | 0.1992221 | 2.7723 | 0.0314 |
| Coherence Spline | 4 | 1.0184276 | 14.1719 | <.0001 |
| | | | R Square | 0.504 |
| | | | Prob > F | <.0001 |

Model 2

| | DF | Sum of squares | F Ratio | Prob > F |
|---|---|---|---|---|
| HV Spline | 4 | 0.5813017 | 4.4434 | 0.0016 |
| HH Spline | 4 | 2.2236896 | 16.9976 | <.0001 |
| | | | R Square | 0.253 |
| | | | Prob > F | <.0001 |

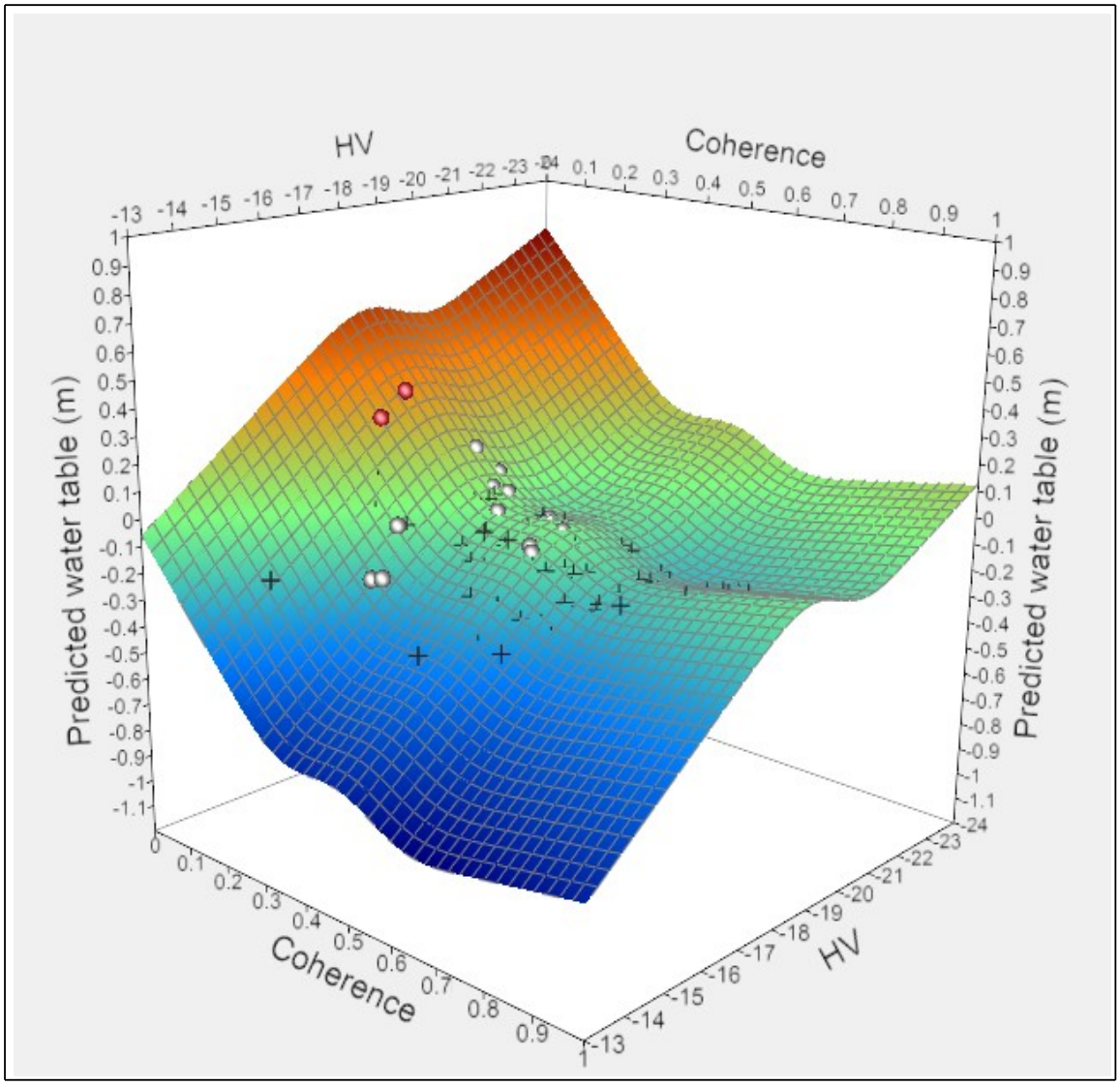


Figure 5.8. The response surface of the modelled GAM (model 1) including interferometric coherence. The X & Y values are the independent variables that account for the most variation in the measured water table depth. Real (measured) data points are shown around the surface

Table 5.3. The prediction formula from GAM model 1.

| |
|---|
| predicted water table = -2.7920 + (-0.0806 HV spline) + (-0.11048 HH spline) + (-2.0559 CC spline ) |

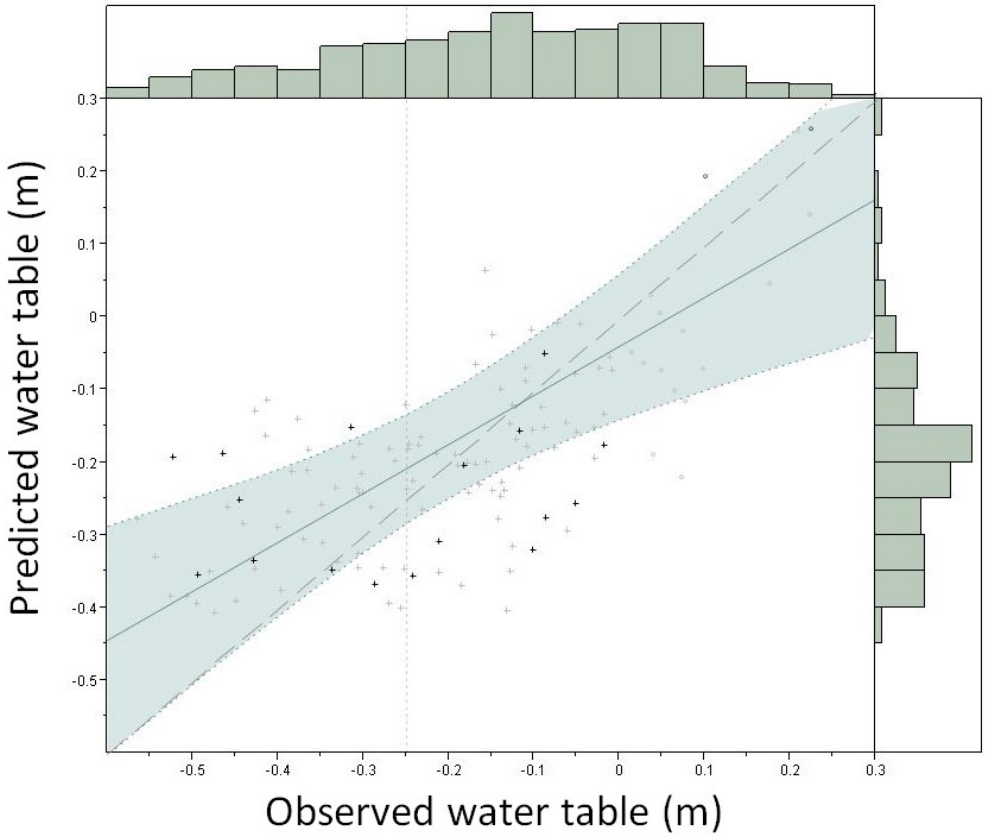


Figure 5.9. Observed vs. expected plots for the GAM model incorporating coherence (model 1). 1:1 (dashed) line is provided as an illustration of perfect fit. Solid line is the correlation between model outputs and control group measured values (black crosses). Light grey points are the test group and are for illustration only, they are not included in fit. Histograms at the side show the distribution of both observed and modelled values. R-square of correlation = 0.48, shaded area is the 95% confidence intervals of the fit.

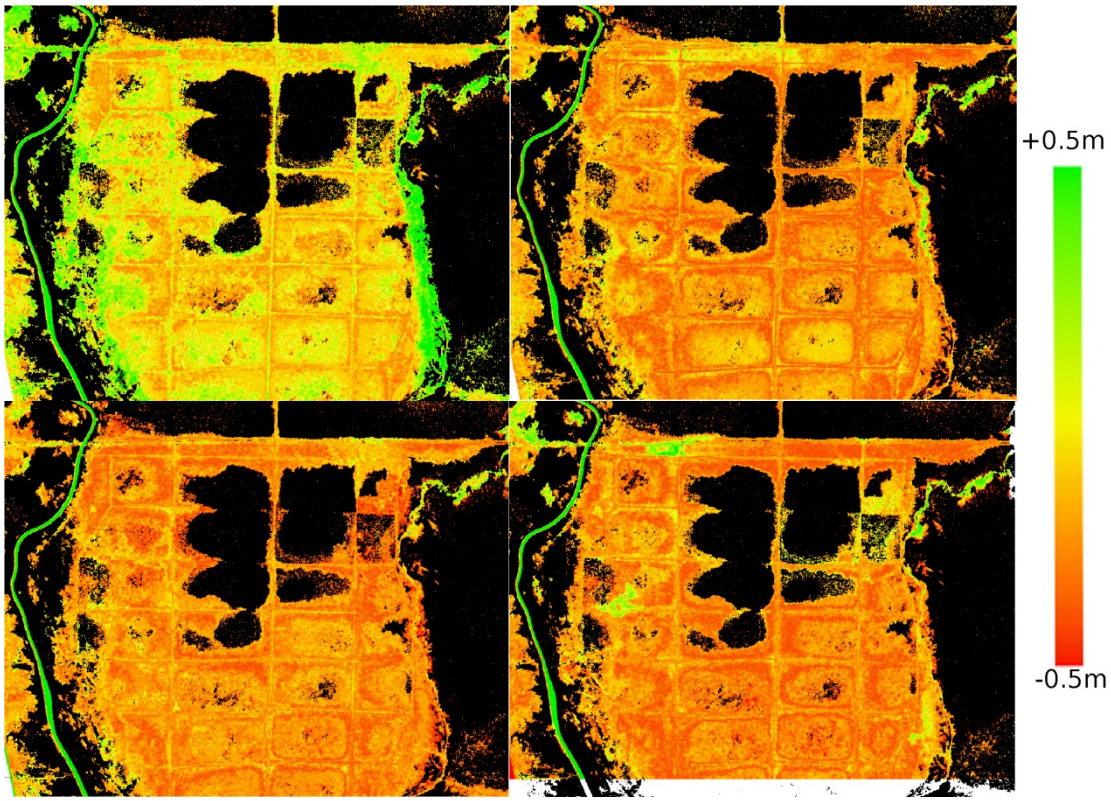


Figure 5.10. Maps of estimated water depth over block A of the exMRP. Top left 20070622, top right 20070807, bottom left 20080809, bottom right 20090627. Black areas masked using the forest/degraded area mask.

Table 5.2 The statistical details of the two predictive models (GAMs) are given in Table 5.2. Model 1 included all three radar variables and explained just over half of the variation seen in the training data set with coherence explaining the largest proportion of data variability, followed by HV backscatter. HH backscatter explains the least amount of data variation, even though all three model terms were statistically significant. The results were significant at the 0.0001 level. Model 2 did not include coherence as this would allow water table estimates to be made at every PALSAR observation date. Whilst this model was still significant it explained only 25% of the variation in the data

and for this reason subsequent analyses used only the full model as, in a trade off, accuracy was a more important factor than frequency.

A visual interpretation of the response surface given by model 1 is shown in Figure 5.8 with the two variables explaining the largest amount of variation (HV and coherence) on the x and y axes. The structure of the prediction expression is shown in table 3. The accuracy of model 1 was evaluated using the control group of data which had been excluded from the original analysis. Figure 5.9 shows the observed control group values plotted against the predicted (modelled) values. From this it can be seen that the fit is good; in the region <-0.25 cm water table depth, however, the predicted values become de-correlated from the observed values and the response appears to flatten out. This can also be seen by examining the histograms on the sides of the graphs in Figure 5.9. The distribution of the predicted data ends at -0.4 m whilst the observed data distribution continues down to -0.6 m. When the control group points in this region (<-0.25) are excluded the R-square between observed and expected values is 0.48 and the slope is 0.67 (1 is ideal in observed vs. expected plots). The lack of predicted values <-0.4 m indicates that this is the point at which the surface soil moisture becomes decoupled from the water table, i.e. the point where the surface soil moisture is zero.

Model 1 was then used to generate the images seen in Figure 5.10 where HH & HV backscatter and coherence are used on a pixel by pixel basis to generate estimated water table depth images for Block A of the exMRP.

## 5.5 Discussion

In this chapter it has been demonstrated that the water table depth can be correlated with radar backscatter. It has also been established that interferometric coherence correlates well with the position of the water table. No previous studies have shown such a link . The value of including coherence data in predictive models is high despite the difficulties involved with processing the data and the reduced temporal sample size that results. The radar signature of increasing levels of above ground biomass would be expected to lessen the influence of the water table on the radar signal until at very high levels of biomass (i.e. in undisturbed forest) the biomass saturates the radar signal and no water table signal can be detected. It is for this reason that most of the literature on the effects of soil moisture on radar signal comes from low biomass scenarios such as croplands, burn scars or wetlands. This mechanism is supported by the data presented in this chapter which demonstrates strong relationships between radar values and water table in low biomass, highly degraded peatland and very little relationship at higher biomass values, i.e. in intact forest. However it should be noted that at intermediate biomass levels ('lightly degraded') there was a relatively small sample size in particular for water table values >=0cm. Hence the most accurate radar estimates of water table depth will come from areas of low biomass. This attempt to model ground water depth, through soil moisture using orbital radars is novel and the spatial resolution of the resulting data is an order of magnitude higher than currently available soil moisture data products.

This chapter extends previous work relating backscatter intensity to soil moisture by linking the radar signal to water table depth. Coherence data have previously been shown to correlate with snow melt (Thiel & Schmullius, 2012) but this is the first time they have been shown to correlate with water table depth.

These results are broadly similar to those from previous studies examining the effect of soil moisture/water table depth on radar backscatter (Laura L. Bourgeau-Chavez et al., 2007; Kasischke et al., 2009; Pierdicca et al., 2010) in that an increasing soil moisture content leads to an increase in backscatter with standing water above the soil surface producing a decrease in radar backscatter (Bourgeau-Chavez et al., 2007). The former effect is likely due to the increasing dielectric constant of the soil with increasing wetness whilst the latter effect is likely due to an increase in specular reflection away from the sensor. Due to the roughness of the peat soil surface, as the above surface water table progressively increases in depth so less of the soil surface is visible to the radar, resulting in a gradual decrease in backscatter rather than a sharp decrease.

The successful retrieval of water table information from SAR data is likely mediated through a shared correlation with surface soil moisture. Previous research (Price, 1997) suggests that due to capillary action within the peat soil the water table and surface soil moisture are linearly related until the water table reaches a depth of between 1m (Canadian upland bogs, Price 1997) and 40 cm (Hoscilo, 2009 for tropical peat soils which have a lower bulk density and higher hydraulic conductivity). The results presented here confirm

this linear relationship down to a depth of ~0.30m in tropical peat soils at which point the relationship between water table depth and radar backscatter becomes decoupled. Despite this limitation in the technique of remotely monitoring the water table level, the amount of time that the water table is <0.3m is only 30% of the dipwell measurements used in this chapter, implying that PALSAR data could be used to calculate accurate water table estimates for ~70% of occasions in the exMRP and in other areas of degraded tropical peatland. The only previous study to investigate the effect of soil water table depth on the radar signal was the ESA INDREX 2 campaign which included some aerial P-band SAR data from the present study location (Hajnsek, 2006). However it occurred under unusually low water table conditions (<40cm) and unreported biomass levels and showed no relationship between L band backscatter and water table, although a relationship was observed for the P-band relationship down to a depth of~-65cm. This is in turn supported by the observation that peat fires only occur when the peat water table is below a critical threshold of <40cm (Hoscilo 2009).

## 5.6 Summary

The relationship between the depth of the peatland water table and the radar signal is examined and the following questions asked.

Aim 1: **Do changes in water table alter the radar backscatter in a predictable way and does this conform with scattering mechanisms previously described in the literature?**

Radar backscatter showed a non-linear relationship with water table depth. Backscatter increased as the water table rose to the surface and then decreased as flooding occurred, in line with relationships reported in the media.

Aim 2: **What effect do changes in the water table have on interferometric coherence?**

Interferometric coherence showed a linear relationship decreasing with water table depth

Aim 3: **How are these relationships between the radar variables and the peatland water table affected by biomass of the overlying peat swamp forest and at what biomass value does the relationship break down**?

The relationship with both radar backscatter and coherence was observed only in degraded low biomass areas.

Aim 4: **Can a predictive model allow the estimation of water table depth from the PALSAR radar variables and over what biomass range is this effective?**

The relationships between the radar variables and the water table depth allowed peatland water table depth to be estimated at high spatial resolution from the radar data using a generalised additive model. The method is only effective, however, in heavily degraded areas with low biomass and accurate estimates are only given within a restricted range of water table depths.

This chapter examined a source of the radar signal in areas where the amount of biomass is constant. In the next chapter the radar signal occurring as a result of changes in above ground biomass is examined

# 6. Effect of fire on radar backscatter change

## 6.1 Introduction

Chapter 5 examined what part of the temporal variation in the radar signal was driven by environmental factors, specifically rainfall and the position of the peatland water table. In trying to isolate these environmental factors, the Chapter focussed on areas and time periods in/over which there was no change in either the amount or the structure of the vegetation (biomass). This chapter focuses on characterising the temporal behaviour of the radar signal in areas undergoing a change in the amount or structure of the above ground vegetation and focuses on developing methods for differentiating this signal from the radar signal caused by environmentally driven variation in backscatter.

In the tropics there are a number of different ways in which forests cover can be lost (i.e. different 'modes' of deforestation). These include large scale mechanical clearing of forest (often for plantation agriculture) and small scale manual clearing of the forest for subsistence farming. Subsistence farmers often utilise fire to facilitate land clearance and in dry conditions these fires can spread out of control, making uncontrolled fire a third major mode of tropical deforestation (Cochrane et al., 1999). Each of these different modes of deforestation will result in a different pattern of change in the structure and

amount of vegetation remaining after the deforestation event and hence will likely have a different effect on the temporal behaviour of the radar signal over the time period in which deforestation is occurring. As discussed in the literature review, due to climatic conditions (long dry seasons exacerbated by el Nino episodes) and the regular use of fire as a traditional land clearance tool, the main mode of contemporary forest loss on the peatlands of Central Kalimantan is fire.

The temporal radar signal behaviour will likely vary according to the number of deforestation/degradation events (i.e. a fire in a primary forest is likely to produce a markedly different signal from a fire in a degraded forest that has already been burnt three times). The cause of these differences will be related to the amount of change seen in both the structure and the amount of vegetation before and after the fire. Changes caused by fire are likely to be much greater following the first fire where the prior vegetation was forest as opposed to the changes seen when an area that has already experienced multiple fires burns again; this difference will be reflected in the amount of carbon lost from above ground biomass following a fire. The time between fires during which regrowth of the forest can occur is also likely to affect the radar signal seen during deforestation events. However, recovery potential also reduces after multiple fires as the seed bank becomes reduced so the effect of regrowth on the radar signal during a degradation event is likely to vary depending on the number of fires experienced in any particular location. The power of the backscattered radar signal has been shown many times to be sensitive to the amount of biomass present (Austin, 2003; Rignot et al.,

1995) . The biomass range in these studies is a product of a study in a landscape including plantation forest stands of varying age. Radar remote sensing studies of deforestation events in natural forests are rarer, and usually take one of two forms: a time series of images during which a deforestation event occurs or a single date image comparing separate landscape units with different disturbance histories (i.e. fire/no fire or time since fire). There are few radar remote studies sensing observations of deforestation events (i.e. a time series of images including a deforestation event) occurring in tropical areas. What information there is on deforestation events is mostly related to fires in boreal and Mediterranean environments (Bourgeau-Chavez et al., 2002; Huang et al., 2006; Tanase et al. , 2011). Observations of tropical forests using L-band radar to give baseline information on backscatter intensity and variation are also lacking (though see Englhart et al., 2011). The majority of studies have been performed with C-band radar due to the larger number of radar satellites that have employed this wavelength. Observations have also been made using a variety of polarisations. These differences in methodology make it difficult to provide predictions from the literature for the behaviour of L-band PALSAR data in tropical PSF during deforestation events.

In Mediterranean pine and eucalypt plantations fire scars were found to have an 8db higher backscatter than surrounding unburnt areas (Gimeno et al., 2004) at C-band, VV polarisation. Also in C-band and using a time series approach Minchella (2009) showed an increased backscatter of 2db after fire in pine forests; subsequently the radar signal varied between being greater

than and less than that of unburnt forest. This variation was attributed to seasonal changes in soil moisture. Tanase (2010a) showed increases in backscatter following fire at both X and C band (HH &VV) but a decrease in backscatter at L-band. The HV polarisation showed a decrease in backscatter for all three radar frequencies.

In boreal forests recent burn scars were initially observed to be brighter than surrounding undisturbed forests before becoming darker than undisturbed forests at C-band (VV polarisation). This effect was attributed to the drying out of remaining dead tree trunks (Kasischke et al., 1992). A 3-6dB increase in backscatter following fire (relative to the surrounding unburnt forest) was observed by Borgeau-Chavez (2002) and related to increased ground moisture.

The variety of radar signal responses to fire in forests, as well as the number of variables (i.e. radar wavelength and polarisation and also forest type) which differ between studies, makes it hard to make any predictions as to what the radar signal response will be when PSF are affected by fire.

Many of the above studies were carried out in boreal areas and some discuss how changes in moisture (related to spring thaws) can modify the radar signal in burnt areas, although all of these observations are incidental. Although in a completely different climatic context  this thesis has already demonstrated how the peatland water table affects the backscattered radar signal and hence it is important to consider in this chapter whether there may be an interaction between how moisture affects the radar signal and how the change in forest

structure brought about by fire affects the radar signal. A methodological issue linked to this is that fire and the peatland water table are likely to be temporally auto-correlated: fires only burn out of control and affect PSF when the water table is low and similarly fires are often only extinguished when rains raise the water table towards the peat surface. Hence it is likely to be difficult if not impossible to separate the influence of these two factors on the radar signal.

## 6.2 Aims

In this chapter the radar signal resulting from the interaction of fire histories in tropical PSF and monthly rainfall is examined. Specifically, the following research questions are addressed:

1. What is the temporal signal of fire occurring in intact primary PSF and how does it differ from the signal observed in other areas of the image?
2. How does the temporal radar signal resulting from fire occurring in primary PSF differ from the radar signal resulting from fire in areas that have burnt two, three or more times?
3. Does the amount of time that has elapsed between consecutive fires alter the radar signal as might be expected to happen if secondary regrowth of the forest was occurring?
4. Is there an interaction between the radar signal change occurring as a result of fire and the rainfall signal described in Chapter 5? What form

does it take and can it be used to correct for biomass/disturbance classes?

## 6.3 Data & Methods

In the previous chapter it was shown that the position of the groundwater table significantly influenced the radar signal coming from degraded areas of PSF. However the labour intensive nature of collecting water table depth information from dipwells meant that the dataset was necessarily limited both spatially and temporally. For that reason in this chapter, monthly rainfall estimates derived remote sensing are used as an analogue for the water table position and general moisture conditions. A time series of monthly rainfall estimates from the Tropical Rainfall Measuring Mission (TRMM, Huffman et al., 2007) are employed which had been previously compared to ground station measurements of rainfall across insular South East Asia and corrected for dry season bias (Vernimmen et al., 2012). These data were obtained directly from the authors and have been shown to match ground measured rainfall with an $R^2$ of 0.93. The data covered the period of the radar dataset and had a ground resolution of $0.25^{o} * 0.25^{o}$ which at the latitude of the MRP is ~17$km^2$.

### 6.3.1 Identifying the fire signal in the temporal radar dataset

In order to understand the immediate effect of fire on radar backscatter temporal radar profiles were collected using ~1 hectare regions of interest (ROIs) located in primary forest burnt in October 2009 (Figure 6.2). Mean backscatter for each of these ROIs was plotted against time in order to give a

temporal profile of the radar signal during the transition from forest to burnt forest.

### 6.3.2 What is the long term backscatter behaviour following fire?

The analysis of fires that occurred during the four year PALSAR dataset is necessarily limited. This is because only one set of fires occurred during this period and they burnt only a limited number of landscape units. In order to build up a more comprehensive and longer term picture of temporal radar signal variation across the whole range of degradation scenarios from intact forest to multiple burns it was necessary to acquire an independent record of the long term fire history of the study area. To do this, a fire history dataset for Blocks A and E of the exMRP was obtained. The data were derived from Landsat satellite images covering the period 1991-2009 and were produced by RSS consulting Gmbh. This dataset covered a time period during which it had been shown that nearby peatland (Block C of exMRP) was undergoing profound changes in landcover caused by fire (Hoscilo et al., 2011) and visual inspection of the Landsat images showed that a similar change had also occurred in Block A over the same time period. These changes were from an almost entirely forested landscape to one heavily dominated by degraded peat forest and open fern communities (Figure 6.1). Yearly fire history maps were of $30m^2$ pixel size and maps were coded as being either unburnt (0) or burnt (1).

In order to use the maps to isolate the temporal behaviour of burnt PSF from riverine forests and forests on mineral based soils, burn maps were restricted to areas of peat >1m deep using the peat mask described in Chapter 4. Burn

scars with an area below a threshold of one hectare were deleted from the burn history datasets in order to eliminate age effects around small burn scars. This was done in order that extracted temporal radar profiles were not contaminated with radar data from unburnt pixels. Burn maps for specific years were converted in MATLAB to give maps of the number of fires each pixel had experienced over the 1991-2009 period and the time since the last fire had occurred (see Appendix 8.3.7-10 for relevant scripts). These maps were then converted to vector files and used to extract radar profiles from the 4 year PALSAR dataset. The resulting dataset contained data on the mean HH and HV backscatter for each burn scar over the 4 year period between 2007 and 2010 as well as the number of fires and time since most recent fire (in months).

### 6.3.3 What influence does fire history have on the radar signal change?

The burn map database was interrogated to answer a number of questions concerning how longer term landscape fire histories affect the temporal variation in the radar signal. Areas were selected from the database that had burnt on only a single occasion. This dataset included areas that had burnt in different fire years ranging from 1991 to 2009. By plotting the mean backscatter for each area against the time, in months since that fire had occurred, it was possible to construct similar backscatter profiles to those seen in Figure 6.2, but with the scale on the x-axis greatly enlarged. It is important to note that this longer term history has been synthesized from the

original 4 year PALSAR dataset, i.e. the x-axis scale has been lengthened simply by looking at burn scars of different ages.

Secondly the database was used to investigate the effect that the number of fires (over the period 1991-2009) has on the temporal backscatter profile. To do this the temporal backscatter profile was plotted separately for each fire frequency class (Figure 6.5). By looking at the time since the last fire it was possible to investigate if there were any signs in the radar signal of post fire vegetation regrowth. To do this the temporal radar profile was plotted with the dataset separated by the time since the last fire.

### 6.3.4 What causes variation of the radar signal in burnt areas?

The effect of rainfall on the radar signal from burn scars was examined by comparing the radar backscatter from burn scars and from intact forested areas against the TRMM derived corrected rainfall for Indonesia (Vernimmen et al., 2012). Figure 6.6 shows the temporal radar and rainfall profiles for areas of burnt and intact PSF in Block C. Figure 6.7 shows the same data displayed with the radar and rainfall data plotted against one another and with a regression line fitted. Similarly, Figure 6.8 shows radar signal plotted against monthly TRMM rainfall, however in this analysis the radar data were collected over co-located biomass plots (see previous chapter). Plots are grouped into low (<40 tonnes per hectare) and high (>200 tonnes per hectare) biomass groups in order to examine the effects of biomass on the moisture response. Separate regression lines are drawn for both groups.

## 6.4 Results

### 6.4.1 Identifying the fire signal

Figure 6.2 shows the mean backscatter profiles, in both HH and HV polarisations for a number of landscape units, extracted using ROIs from areas of approximately 1ha, as measured over the period 2007-2010. During this period fires burnt within the landscape in October 2009 (=band 9).

### 6.4.2 Long term radar response to fire

The database of temporal radar backscatter and fire history data over the IAFCP project area ran to ~280,800 spatially averaged backscatter values for both HH and HV backscatter. Figure 6.3 shows a long term record of backscatter variation for areas burnt only once over the period 1991-2009 synthesized from the long term Landsat fire history dataset. Note that the period of time covered by the x-axis is large (>20 years) and that because this data set has been synthesized by looking at burn scars of different ages there are some periods without observations.

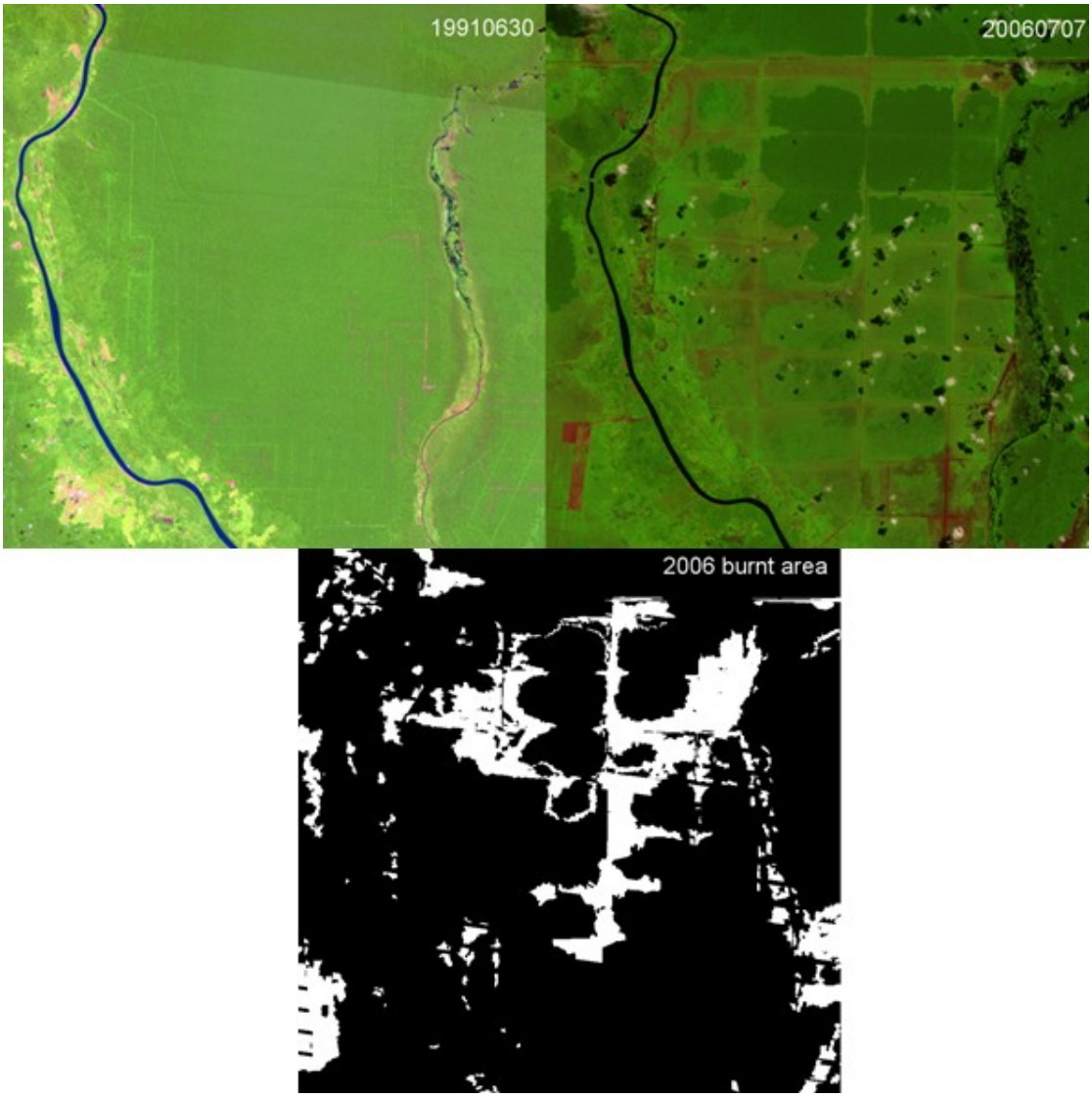


Figure 6.1. Landsat true colour mosaics (RGB= Bands 5,4,3) of Blocks A & E of exMRP). Top left image 30th June 1991, top right image 7th June 2006, bottom image burnt area map for 2006 (white areas are classified as burnt). Imagery courtesy of NASA/USGS Landsat

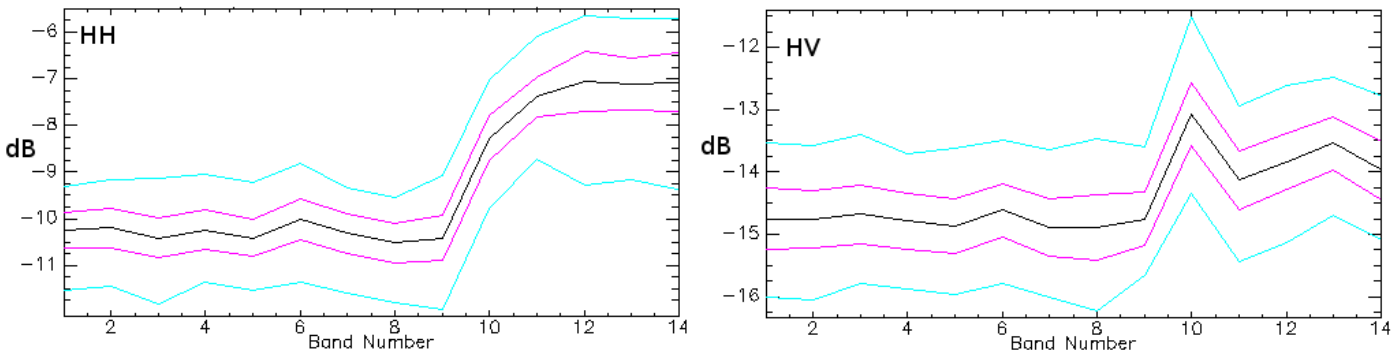


Figure 6.2.Temporal backscatter (dB) profiles from 2009 fire, left HH, right HV. Band 1= first data of radar stack, 20070709 and band 14 = last data of stack, 20101202. Fire occurred in October 2009 at a time corresponding to band number 9.

The effect of fire frequency (as number of fires) on backscatter variation across the four year PALSAR dataset is shown in Figure 6.4. Results for fire frequency are shown as separate trend lines on the graph This figure includes only data for burn scars that burnt in October 2009 (the timing of the fire is indicated by a red vertical line). The length of the fire free interval between fires is likely to have an effect on the radar signal as regrowth of above ground biomass can occur in this period. However the ability of the forest to regenerate is likely to be affected by the number of fires that have occurred. Figure 6.5 shows a series of graphs for different burn frequencies showing the variation in the radar signal across different groups of burn scars where the time since the last fire varies.

### 6.4.3 Understanding the causes of variation in the radar signal

Figure 6.6 & Figure 6.7 clearly show a link between the variation in the radar signal and monthly rainfall, with the HH signal being both more variable and more highly correlated with rainfall than the HV signal. Figure 6.8 shows how

the TRMM monthly rainfall estimate affects the radar backscatter from two groups of sample plots with high and low biomass.

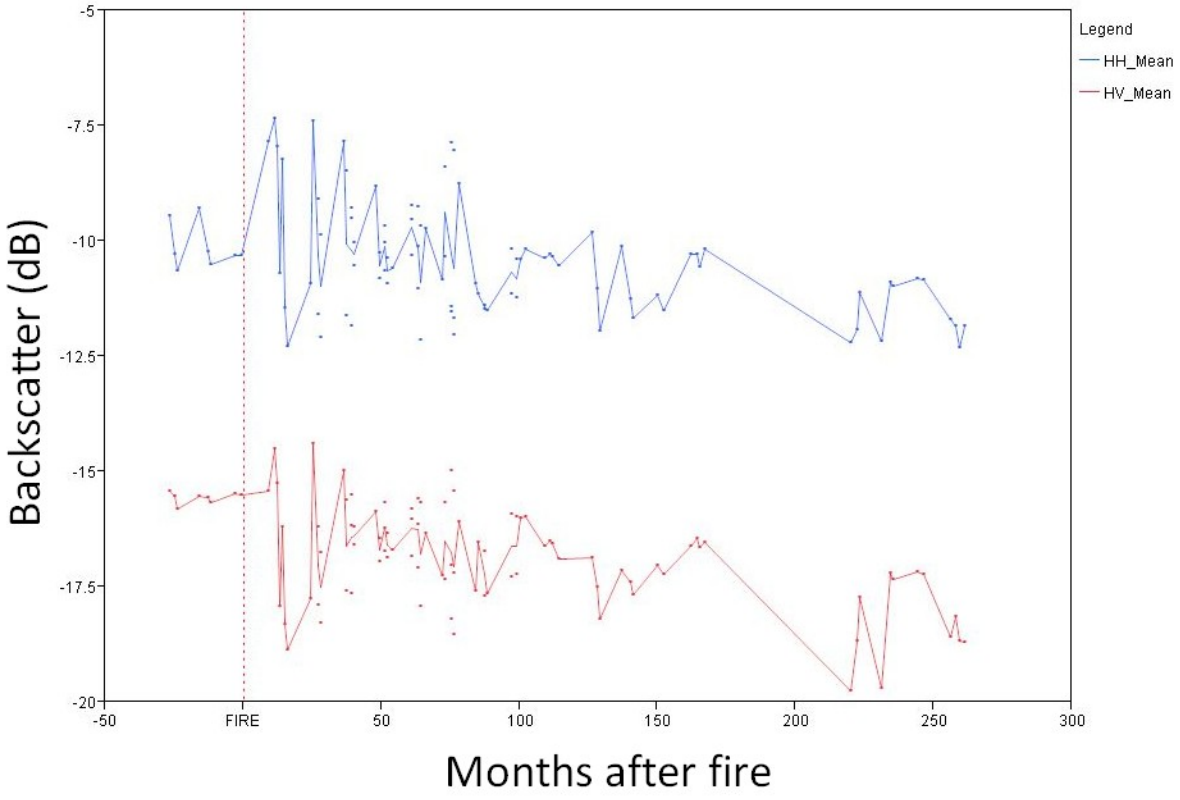


Figure 6.3. Synthesized long term record of backscatter variation following fire (fire occurs at time 0). Where more than one observation exists for any given month the line is drawn through the mean of points

.

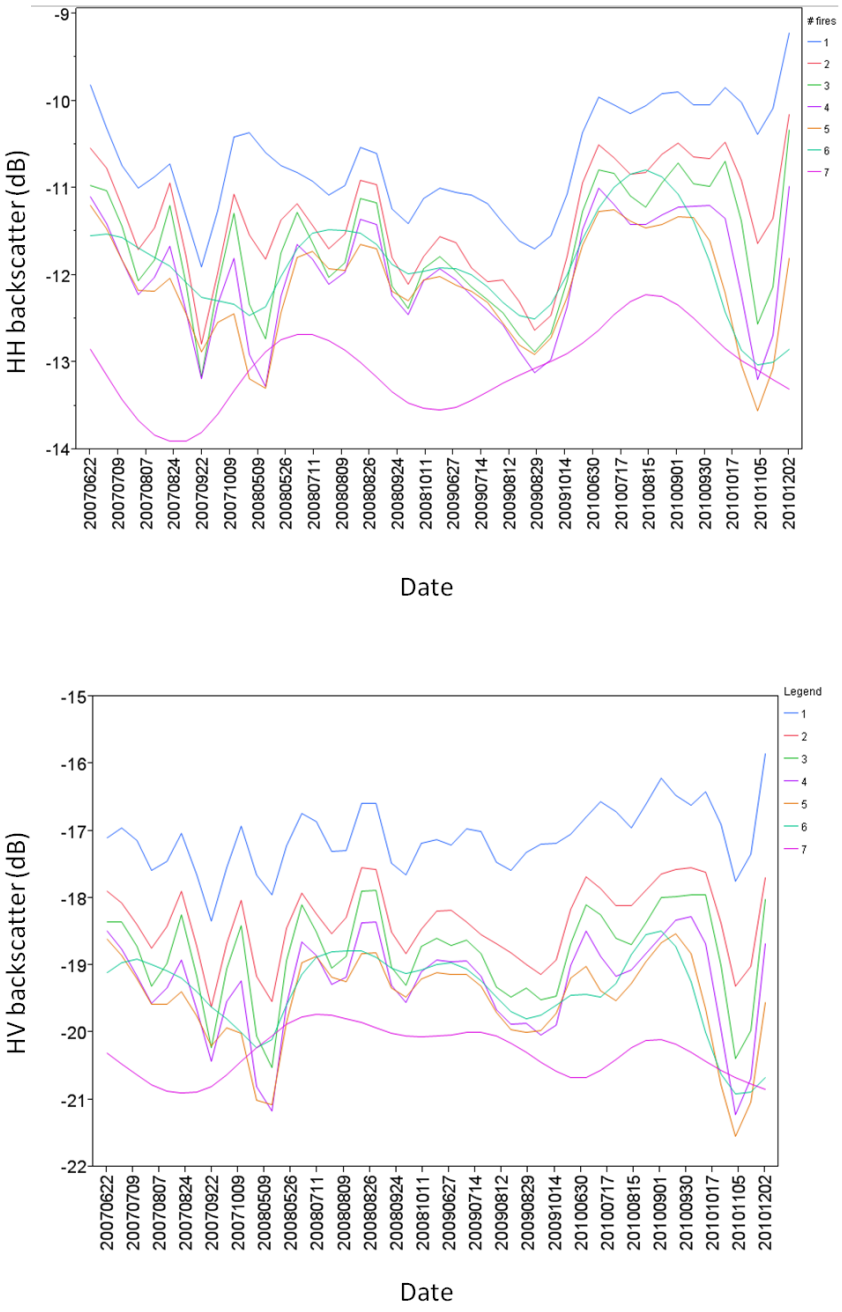


Figure 6.4. Effect of burn frequency (as number of fires) on the temporal radar profile. Top HH backscatter in dB, bottom HV backscatter in dB

.

## 6.5 Discussion

Despite the fact that fires in previously intact PSF clearly resulted in a significant reduction in biomass, both polarisations of L-band PALSAR data show an increase in backscatter of 4dB in HH and ~2dB in HV compared to the prefire i.e. intact forest signal (Figure 6.2). This observation clearly contradicts the assumptions behind empirically fitted biomass:radar relationships. The increased backscatter response persisted for at least 12 months, through to the end of the PALSAR dataset. In order to investigate how the radar backscatter varied as a result of fire over longer temporal scales a long term backscatter response was synthesized by using a fires history database to examine burn scars of different ages. This produced a large number of temporal backscatter profiles from individual burn scars. The post-fire high backscatter values do not persist for long after the fire (Figure 6.3) and there is a general downward trend in the radar post-fire radar signal. However superimposed upon this is a period of ~50 months during which the radar signal varies with an amplitude of ~4db from being higher than the prefire forest signal to being lower than the forest signal. The amplitude of this variation becomes less >50 months after the fire. This pattern is evident in both the HH and HV polarisations.

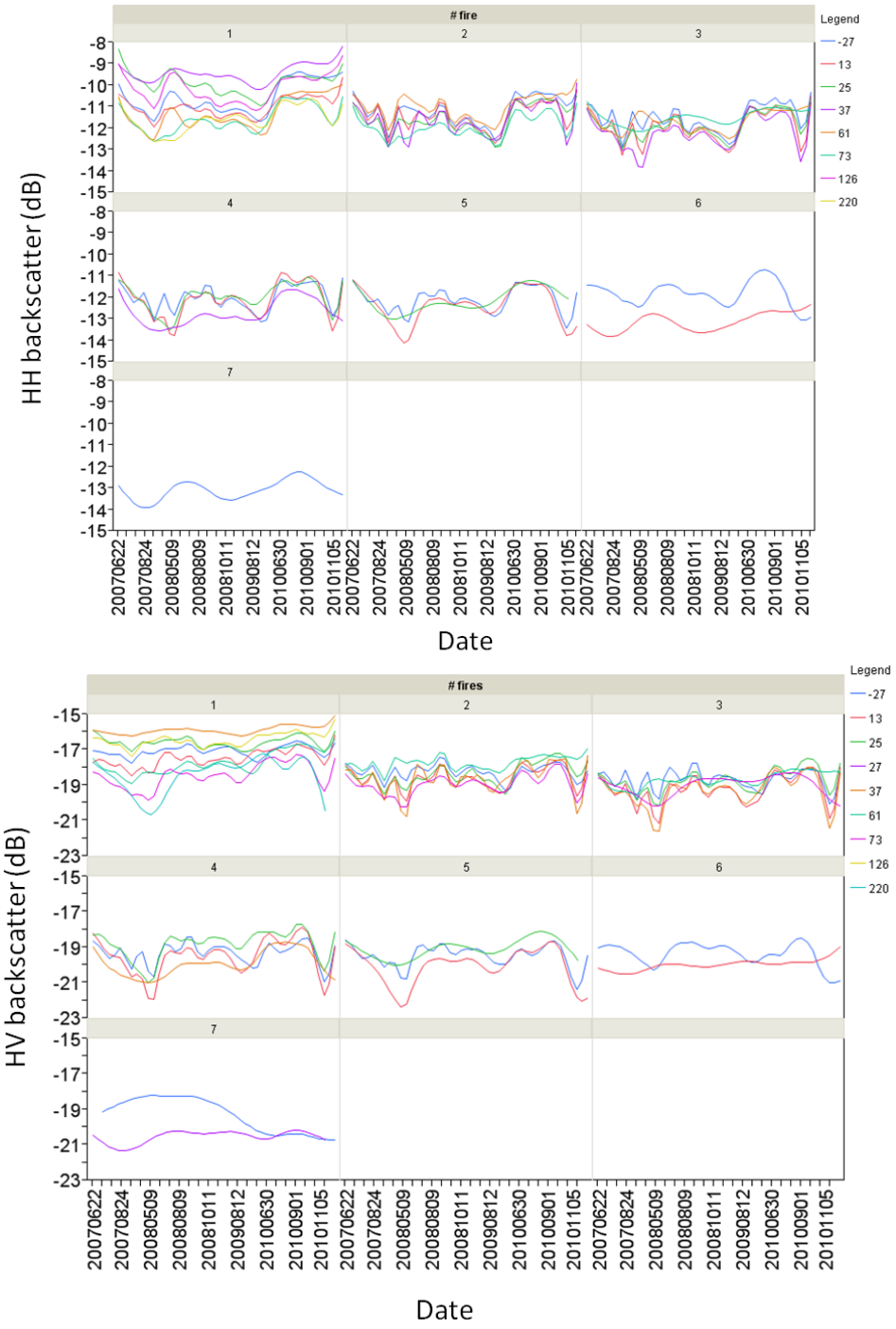


Figure 6.5. The effect of time since the last fire on the temporal radar profile for different fire frequency regimes. Fire frequency is shown separately in each panel Left HH, right HV

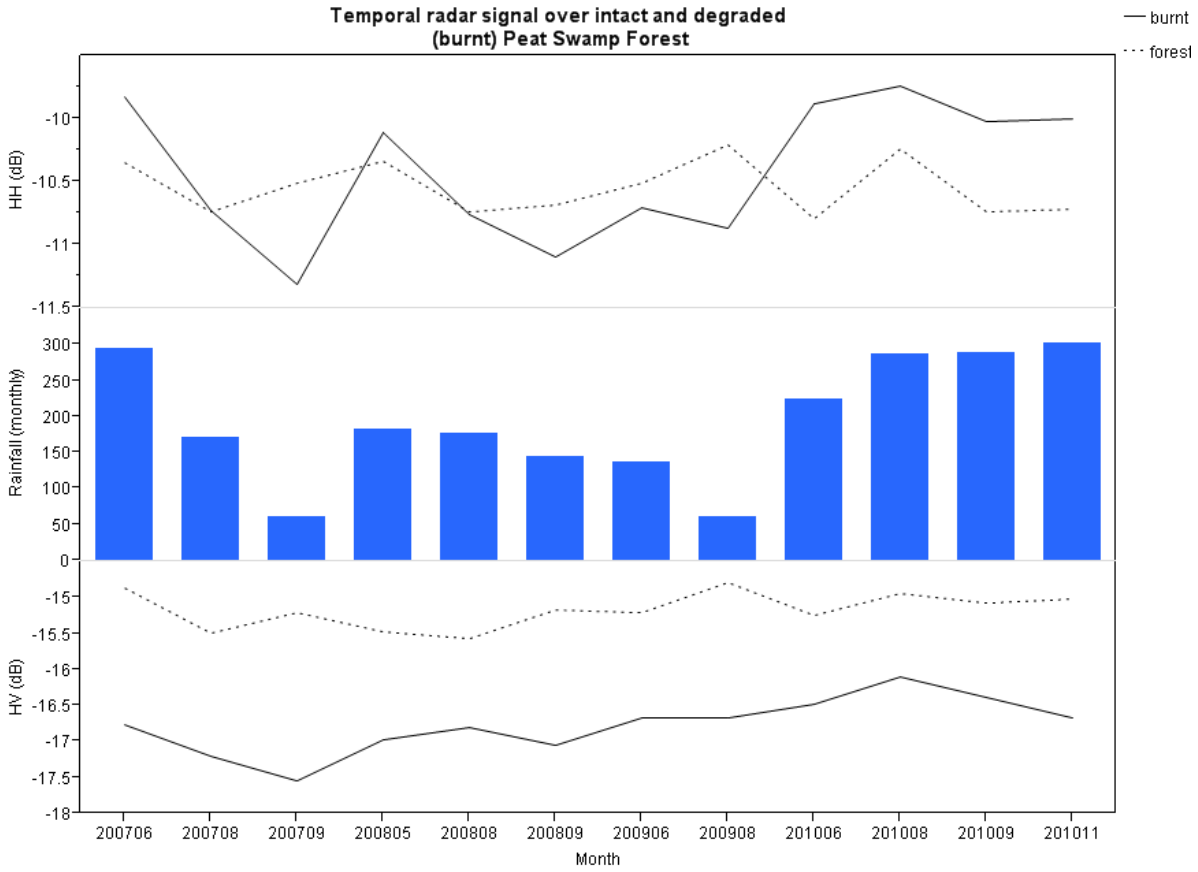


Figure 6.6. Variation in the radar signal over areas of burnt (single burn) and intact PSF. HH is shown own in the top graph, HV in the bottom. Monthly rainfall values (TRMM bias corrected data) are shown in the middle

In Figure 6.4 the effect of fire frequency (as number of fires) on the radar profiles is shown in both polarisations, with a general pattern of decreasing backscatter intensity with increasing number of fires, a trend that is most pronounced in the HV polarisation. It is also evident that there is some synchronisation of the variation in the backscatter profiles which would indicate a common outside influence such as moisture conditions becoming evident in burnt areas. . shows the temporal radar profiles for burn scars of different ages and different fire frequencies. These were examined for any

changes in the backscatter profiles. Distinct radar profiles for the different burn scar ages would indicate secondary regrowth and forest recovery occurring post fire. Evidence for this was only seen, however, for areas that had experienced a single fire. This agrees with field observations made by Hoscilo et al (2011) that no or little forest recovery occurs after a second fire due to the destruction of the soil seed bank and possibly also changes in chemical and physical characteristics of the peat surface (Leanne Milner pers. comm.).

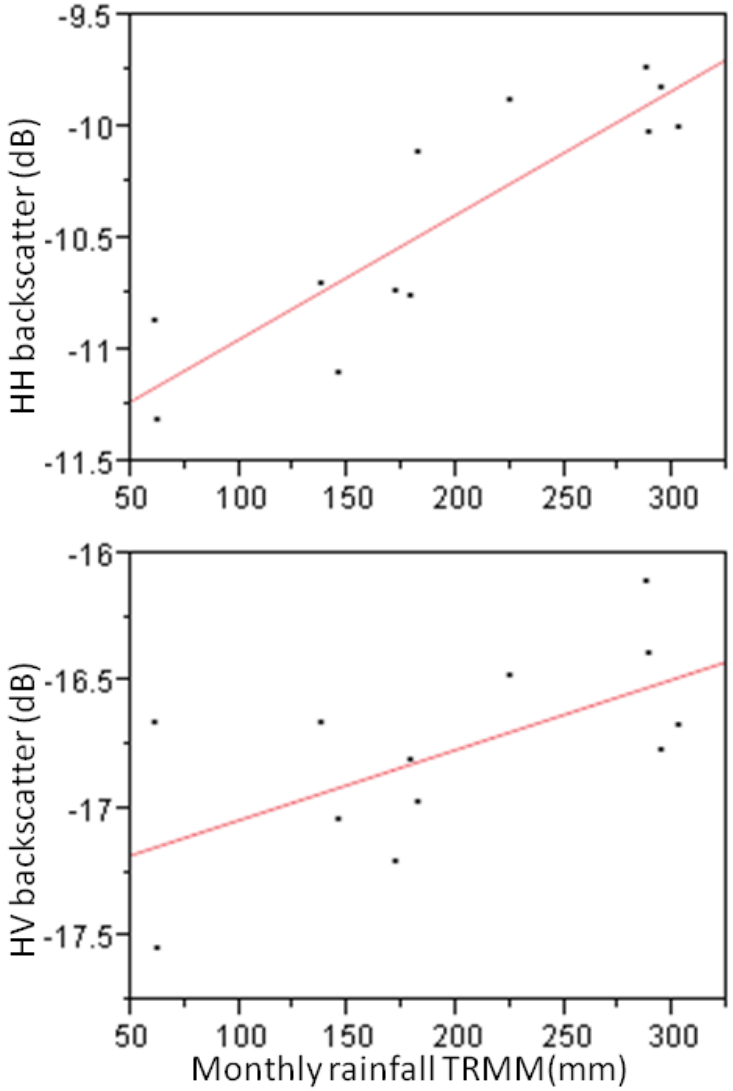


Figure 6.7. The correlation between monthly rainfall and the radar signal from burnt areas. Top HH ($R^2$=0.77), bottom HV ($R^2$=0.38). Data are the same as those shown in Figure 6.6.

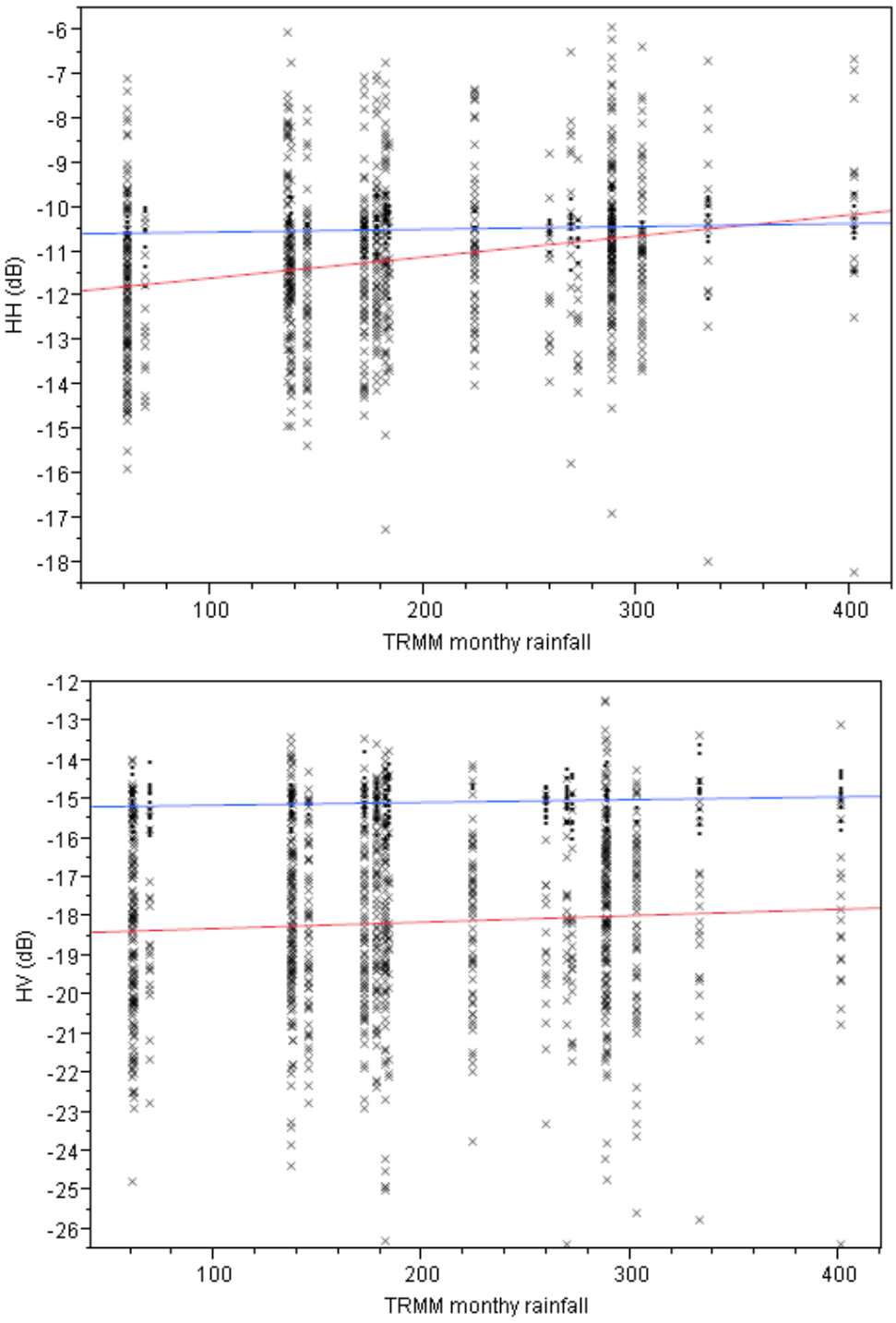


Figure 6.8. HH (top) and HV (bottom) radar signal plotted against monthly rainfall sum. Regression lines drawn for plots <40 tonnes per hectare biomass (red) and plots >200 tonnes per hectare biomass. (HH: low biomass $R^2$=0.003, high biomass $R^2$=0.017. HV: low biomass $R^2$=0.048, high biomass $R^2$=0.014).

The synthesized long term backscatter records have a number of potential drawbacks. Firstly some limited fires may have occurred in unmapped non-fire years. Secondly other modes of disturbance such as logging are not accounted for in this dataset. Also the number of burn scars sampled is large, much larger than the number of fires that have occurred. This is because the GIS maps of fire history contained many non-contiguous burns which were each regarded as separate burn scars despite all being formed during the same large fire. This does not limit the analysis, but provides a large sample size.

In Chapter 5 variation in the radar signal was successfully linked to in-situ measurements of the water table. As these data were only available for a small part of the study area, however, a more general technique was required to account for variation in the radar profile not linked to fire events. Thus TRMM derived estimated of monthly rainfall were employed (Figure 6.6). Figure 6.7 shows that backscatter variation can be correlated to monthly rainfall in degraded/burnt areas with the strongest relationship seen with the HH signal.

So far, this chapter has demonstrated variation in the radar profile and related differences in the temporal behaviour to various aspects of the fire regime. It is important, however, to understand the mechanisms controlling the variation of the radar signal in burnt areas as identifying the external sources of variation may allow easier differentiation of burnt areas using radar images in PSF landscapes. Figure 6.8, which includes data from a much larger sample of plots, shows that although there is a relationship between monthly rainfall and the radar signal, particularly for the HH polarisation, that this correlation is much weaker when examined across plots and that the rainfall correlation is

swamped by interplot variation in the radar signal. This result indicates that using rainfall data to correct for biomass values remains problematic.

## 6.6 Summary

Aim 1: **What is the temporal signal of fire occurring in intact primary PSF and how does it differ from the signal observed in other areas of the image?**

Fire in primary PSF produces and increase in backscatter intensity in both polarisations. The increase is largest (3dB) in the HH polarisation. The radar signal remains for ~12 months after fire and then shows large oscillations between greater and lesser backscatter in relation to intact forest.

Aim 2: **How does the temporal radar signal resulting from fire occurring in primary PSF differ from the radar signal resulting from fire in areas that have burnt two, three or more times?**

In the HH polarisations areas that had burnt once has higher backscatter ~0.5dB higher than areas that had experienced multiple fires. This difference was large in the HV polarisation. Areas that had experienced multiple fires did not show differences in backscatter.

Aim 3: **Does the amount of time that has elapsed between consecutive fires alter the radar signal as might be expected to happen if secondary regrowth of the forest was occurring?**

Some differences in the radar backscatter were seen with increasing time since fire were observed, indicating forest regrowth may be occurring, but only after a single fire

Aim 4: **Is there an interaction between the radar signal change occurring as a result of fire and the rainfall signal described in Chapter 5? What form does it take and can it be used to correct for biomass/disturbance classes?**

Variation in the radar signal from burnt areas was linked to monthly rainfall, but this correlation was not strong enough to allow identification of biomass classes.

Knowledge of how the radar signal responds during forest disturbance is key to the application of radar imaging to forest monitoring. In this instance the naive application of a radar:biomass calibration would lead to serious overestimation of biomass for burnt areas. Following fire the radar signal shows a high degree of variation; this behaviour appears to be linked with the rainfall and peatland hydrology.

# 7. Synthesis & Conclusions

## 7.1 Introduction

The aim of this thesis was to contribute knowledge towards a forest monitoring system able to better resolve the inaccuracies associated with estimating tropical forest carbon and of reliably detecting forest disturbance. In order to achieve this aim this study focussed on the use of radar remote sensing in the tropical peat swamp forests of Southeast Asia

In this Chapter, the answers to the questions posed in Chapters 4, 5 and 6 are discussed. This is followed by a discussion of the implications of the research findings within the wider context of the role that radar remote sensing plays in contributing towards a system for the monitoring of deforestation and forest degradation in tropical forests. The conclusions of this work and future avenues of research suggested by this work are then discussed.

## 7.2 Is the L-band backscatter coefficient related to biomass in a tropical peat swamp forest?

The results presented in Chapter 4 of this thesis indicate that radar:biomass calibration curves are not temporally stable, at least not in peat swamp forests. Simply adding more collocated radar/biomass data points in order to better characterise the curve and its associated uncertainties will not produce more accurate spatial estimates of forest biomass.

The assumption that, if the current paradigm relating radar and biomass was correct, was that temporal changes in the radar signal would be dominated by changes in biomass, which in this study area meant loss of forest through fire. This assumption was clearly not met. Whilst areas of forest loss could be observed in maps of the HH temporal mean and temporal standard deviation they were not sufficiently distinct from areas of low pole forest and riverine forest to be reliably separated based solely on these measures. The use of Empirical Orthogonal Functions (EOFs) allowed the separation of different temporal trends in the radar data and some of these trends were linked to forest loss from fire. Even in areas where many fires occurred, however, the EOF band most associated with fires accounted for less than 50 percent of the total variation in the dataset, indicating that factors other than biomass change were influencing the temporal changes in the radar signal.

To further confound the efficacy of empirically fitted radar:biomass relationships for estimating biomass from the radar signal the greatest temporal variation in the radar signal is observed at low biomass values where the gradient of the calibration curve is largest and hence might be expected to be the range in which the most accurate estimates of biomass would be produced. At low biomass values in the HH polarisation the higher portions of the radar signal range produce greater backscatter than high biomass forest (see Figure 7.1 for an example). The only parts of the calibration curve which show temporally stable behaviour are the high biomass areas where biomass estimation is most difficult due to saturation of the radar signal. Rather than being considered as static these calibrations should be deemed to be dynamic, changing according to seasonal rainfall patterns but also being affected by

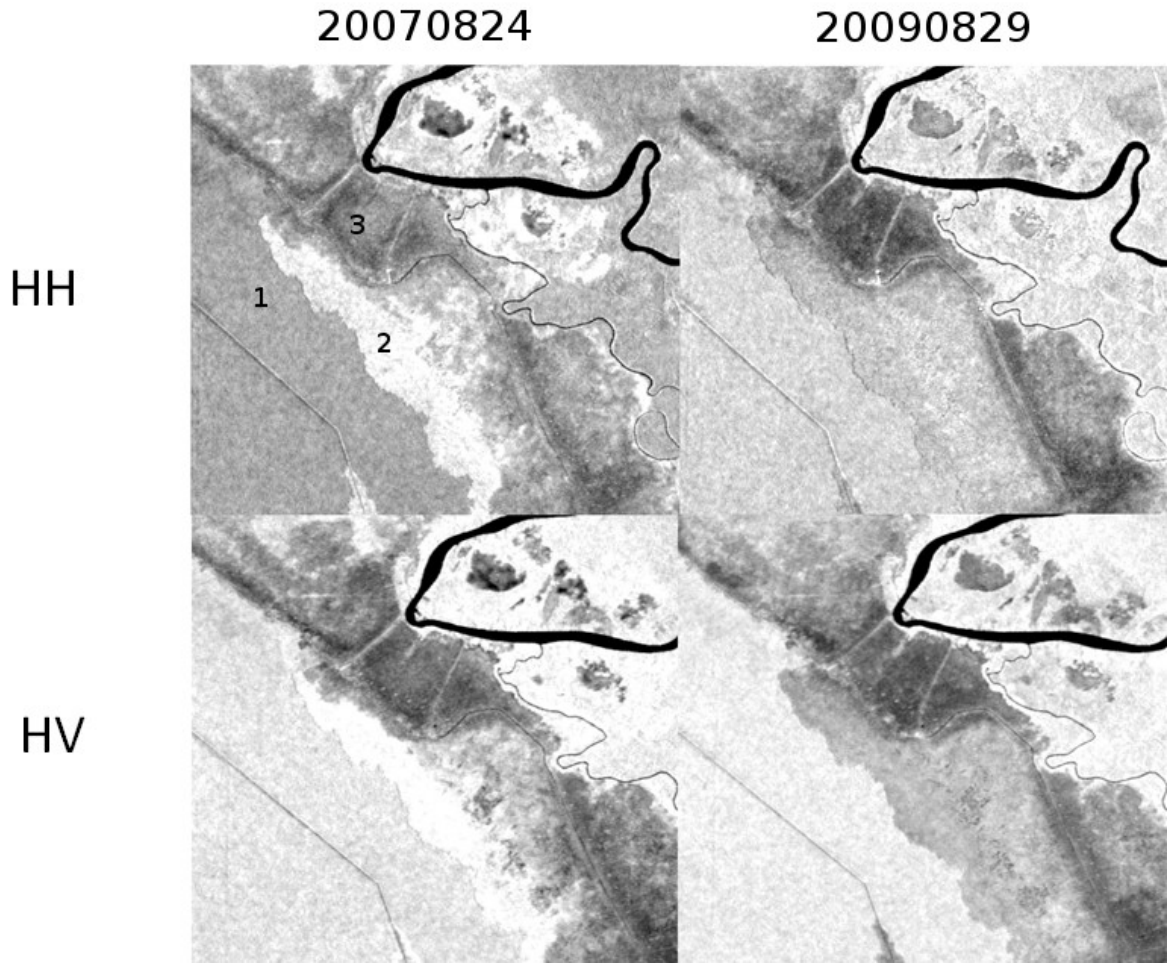


Figure 7.1 Examples of variable radar backscatter in burnt areas of peat swamp forest. On 20070824 low biomass burnt area centre is brighter than adjacent high biomass forest. On 20090824, the forest is brighter than the burnt area. No biomass change occurred in this period. Numbers refer to areas identified in Figure 7.2

periods of above and below average rainfall. These findings imply that any forest monitoring scheme reliant on a radar:biomass calibration curve that is implemented across a landscape of peat swamp forest will produce biomass estimates that vary hugely through time even when no actual change in the forest biomass has occurred. Such a large potential source of error would lead to inaccuracies in calculation of the forest carbon balance, while application of the methodology and

misclassification of landscape change in any future REDD style scenario could have major monetary consequences.

## 7.3 What is the source of changes in radar backscatter in undisturbed areas?

If changes in the radar signal were not only related to changes in above ground biomass ( as shown in Chapter 4) this raises the question of what is driving changes in the radar signal? As there is a strong rainfall seasonality across the peatlands of Central Kalimantan are the relationship between the radar signal and the peatland water was investigated. Field measurements of the peatland water table obtained using a network of dipwells were correlated with the radar signal in degraded areas with low above ground biomass. The relationship between the water table and the radar backscatter was non-linear, but broadly as expected from the literature, i.e. backscatter increased as the water table approached the soil surface, then decreased as the increasing water table resulted in standing water on the peat surface. The scope of this relationship was extended by including the correlation of the water table with interferometric coherence and statistical models of water table depth as estimated from radar backscatter and coherence. These showed that the position of the water table accounted for just over half of the variation observed in the radar data.

An understanding of the relationship between the three radar variables and the depth of the water table in peatlands is extremely valuable as inverting this relationship allows for the estimation of the water table depth. This is important as water table depth has an important influence on carbon emissions from peatlands due to an increase in the oxidative microbial degradation of the organic matter in peatland with lowering of the water table below the surface (Hirano et al., 2008; Hooijer et al., 2012; Page et al., 2011). In addition, this information can also be useful in predicting

risk of peat fires, since in the tropical peatlands of Southeast Asia, fires will only occur when the water table depth has fallen below 40 cm (Hoscilo, 2009). The spatial resolution of the water table depth estimates is the same as the radar data used in this thesis, i.e. 25$m^2$, which is several orders of magnitude greater than currently available estimates of soil moisture (e.g. soil moisture estimates from the TRMM, AMSR-E and SMOS satellites) and is at a scale that would allow for remote monitoring of peatland water table depth.

The linking of water table depth with radar signal is novel, as previous work has only correlated radar data with surface soil moisture (Joseph et al., 2010; Moran et al., 2004). It is likely that in this study changes in the radar signal are also a result of changes in surface soil moisture, which is a proxy for water table depth. This co-correlation also explains why the water table predictions are only accurate to a depth of ~40cm below the surface as this is the depth at which surface soil moisture is reduced to zero and surface soil moisture and water table depth hence become uncoupled. Despite this restriction on water table estimation, the natural range of the water table depth in undisturbed peat swamp forest is rarely beyond this limit under normal rainfall conditions (i.e. outside of El Nino-related droughts, see Jauhiainen et al., 2005). Hence, a remote sensing method that can indicate when the water table is at or approaching the critical depth of 40 cm could be of considerable utility in projects attempting to restore the hydrology of degraded peatlands in order to reduce carbon emissions and the risk of fire (e.g. the IAFCP REDD demonstration project in Block A of the exMRP, see http://www.iafcp.or.id/ ).

To this end, Interferometric coherence is a key variable for producing accurate estimates of the peatland water table. It should be noted, however, that remotely sensed estimates of water table can only be produced in areas of low biomass which

have been degraded by fire, as in this study area, or timber removal. In high biomass areas the radar signal is dominated by backscatter from the forest canopy and trunks, with none of the radar signal penetrating as far as the ground. Nevertheless, the extent of degraded peatland in Southeast Asia at the current time (30,000 $km^2$ in Borneo alone Miettinen & Liew, 2011) is such that this approach could have widespread application.

## 7.4 What are the changes in the radar backscatter signal associated with loss of forest?

Having understood the processes driving changes in the radar signal in undisturbed (i.e. no biomass change) areas the next question to address is what form the radar signal took over disturbed areas where changes in biomass were occurring. The sudden removal of biomass by fire between radar observations as occurred in October 2009 is precisely the type of event that should be clearly detectable by radar remote sensing systems. Reduction in forest biomass would be expected to produce an easily observable decrease in radar backscatter in the burned area. No such reduction in biomass was observed, however, with fire causing an immediate increase in HH backscatter of 2-3dB relative to unburnt forest, that remained evident until the end of the dataset a year later. A similar, though weaker signal, was also observed in the HV polarisation. As has been previously discussed changes in the radar signals over degraded areas of peat swamp forest is highly variable, thus the increase in backscatter associated with fire alone may not be distinctive enough to characterise forest loss due to fire. The feature of the fire signal in primary forest is that the increase in backscatter is preceded by a temporally stable signal.

Subsequent fire events (i.e. second, third burns, etc) also seem to be associated with increases in backscatter, although the magnitude of signal increase is smaller and the background non-fire variation is larger. There is no signal change following fire in highly degraded areas with virtually no above ground woody biomass as the radar signal change only arises due to changes in the structure of the vegetation. There was evidence in both radar polarisations for the detection of post-fire increases in biomass due to secondary regeneration of forest, but only after a single fire had occurred. Despite being unable to correlate these radar signal with biomass under these conditions (due to the rarity of areas with single fires, small sample size and the remote nature of these areas which precluded field data collection) this finding is encouraging as the low biomass range that would be expected in the areas of regrowth are precisely the regions where radar should be able to most easily discriminate biomass values. These findings also support the conclusion of Hoscilo et al., (2013) who observed that secondary regeneration of forest vegetation after a fire was possible after one fire but was absent after two fires, with, instead, regrowth of non-woody vegetation.

Although the amount of variability shown by the radar signal in areas with different burn histories was different, the pattern of variation (i.e. the timing of peaks and troughs) pointing to a common outside driver of the variation, likely to be related to the peatland water table. The radar signal in burnt areas was correlated with monthly rainfall, again most strongly in the HH polarisation. This was not in itself an unexpected result, since this study had already demonstrated a link between the radar signal and the water table which would be expected to correlate with rainfall. Instead this finding is important because it shows that in the absence of detailed

water table data remotely sensed monthly rainfall estimates can be used to examine variation in the radar data. In this case TRMM data were successfully used despite the mismatch in ground resolution.

Unfortunately although rainfall did correlate with the changes in the radar signal from burned areas  at any given site it was not possible to use the TRMM rainfall data in order to provide rainfall corrected estimates of biomass, as the variation in the radar signal between sites with similar levels of biomass was too large. This rainfall driven variation did not, however, explain the reason for the post fire increase in radar backscatter following fire in primary forest. One possible explanation for this increase is an interaction between the water table and the dead fuel load accumulated post fire either in the form of remaining standing dead timber or post fire debris on the ground.

## 7.5 Synthesis

The majority of radar work dealing with the estimation of above ground biomass utilises single or bi-temporal radar images (e.g. Carreiras et al., 2012; Mitchard et al., 2011). In such situations it is unlikely to be obvious how temporally stable the relationship between radar and biomass actually is. The research presented in this thesis has shown that the assumption that biomass scales with radar backscatter in a temporally stable manner is false for peat swamp forests. In this ecosystem any biomass estimates sourced from single date radar images are likely to be highly misleading if biomass is naively assumed to scale in a stable manner with radar backscatter. For example, Englhart et al (2011) provide unrealistically high woody biomass values for peat swamp forest of up to 400 tonnes per hectare in the same study area (above ground biomass values of peat swamp forest are rarely greater than 250 tonnes per hectare (IACFP project data, used in this thesis). Although

Englhart et al (2011) attempted to minimise the effects of rainfall by using only dry season images, the high biomass values could be the consequence of low biomass burnt areas with high intensity backscatter being misclassified as high biomass forest through the use of empirically fitted radar:biomass curves generated from single date radar images, with no consideration given to the temporal nature of the radar signal. The use of incorrectly fitted empirical radar:biomass relationships also has recently been criticised from a statistical point of view (Woodhouse, 2012).

This research demonstrates the need for multi-temporal radar datasets in order to correctly classify land cover and hence assign accurate biomass levels. Although calculating temporal averages is an improvement on single date data, algorithms which can classify land cover type based on temporal behaviours are needed. EOFs were successfully used in this thesis to investigate temporal patterns and could be used as the basis of a temporal classification, but there is an urgent need for simpler and more memory efficient algorithms. This need is only likely to grow as satellite data, in particular radar data, become more available.

Owing to the degradation history of the study area in which this research was conducted it was only possible to study in detail the effects of deforestation caused by fire on the behaviour of the radar signal. Forest, and in particular peat swamp forest, can, however, be lost in many different ways and these different modes

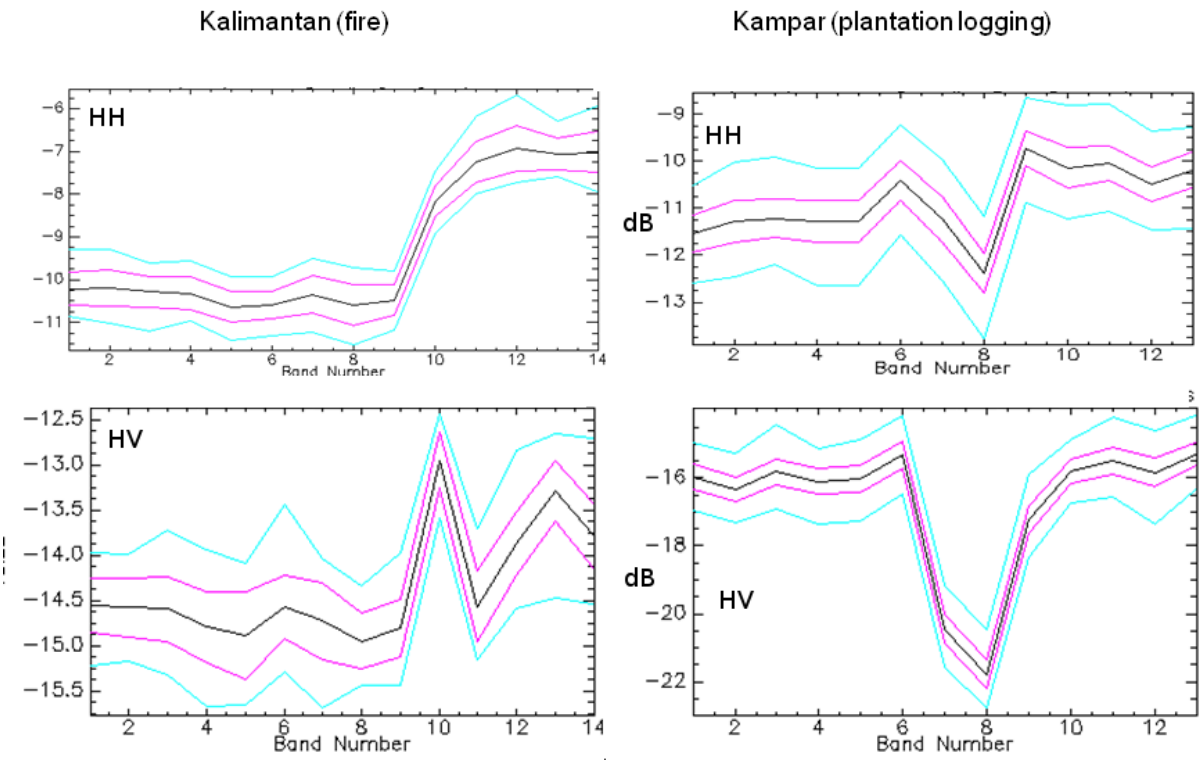


Figure 7.2 Temporal patterns of backscatter change (HH top and HV bottom) occurring as a result of different modes of deforestation in peat swamp forests (fire left and mechanical logging right). Band number refers to dates of images.

of deforestation have distinctly different radar signatures. Figure 7.2 contrasts the increased backscatter of the radar signal in burnt forest with the reduction in radar signal observed when peat swamp forest is the subject of mechanical clearing (data taken from a concurrent PALSAR dataset from the Kampar peninsula in Riau, Sumatra). These different radar signals both occur as result of a reduction in biomass and can help to explain the observations of Whittle et al (2012) who failed to find a unique radar signal indicative of forest disturbance using PALSAR data in Sumatra; instead the authors found 'diverse temporal characteristics'.

It is important to note some multi-temporal L-band radar studies (e.g. Ryan et al., 2011) have been carried out in areas where the radar signal does not appear to be as variable as in peat swamp forest and the relationship between radar and above ground biomass is much more stable. The question raised by this thesis is what areas of the globe can changes in the radar signal safely be assumed to be related to changes in biomass and in which areas is the situation more complex and require more caution when interpreting the radar signal? Although tropical peat swamp forest is globally quite a rare ecosystem, wetlands, including other types of forested wetland, are globally common. It might be expected that in areas of the globe that are predominantly either continuously dry or wet that the radar signal would remain temporally stable throughout the year and that most changes in the signal would be due to changes in biomass. In areas which have a strong seasonality in rainfall or moisture it is likely, however, that the behaviour of the radar signal will be more temporally dynamic and complex as has been observed in this study of peat swamp forest. A recommendation arising from this finding is that the radar images should be collected in conjunction with some estimate of moisture/rainfall anomaly.

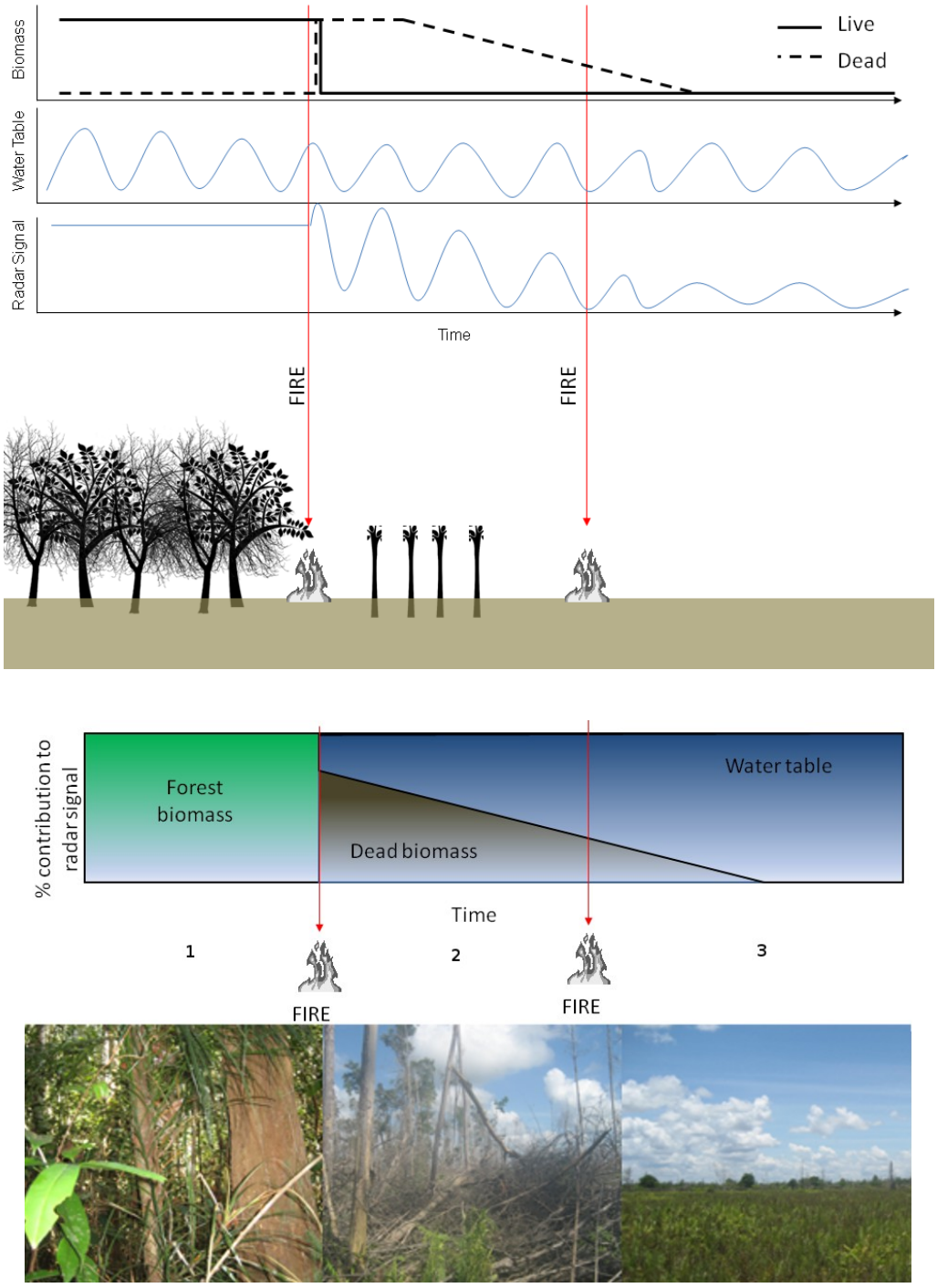


Figure 7.3. Hypothesized sources of radar backscatter in peat swamp forest. In intact forest (left) the radar signal is dominated by volume scattering from the forest canopy and trunks and the signal remains stable. Following first fire in primary forest live woody above ground biomass is lost to be replaced with dead wood. The removal of the canopy and most trees allows penetration of radar to the ground where it can interact with changing soil moisture levels to give a variable radar backscatter. Dead fuel decays or is consumed in subsequent fires. Numbers refer to areas in Fig 7.2.

Rather than trying to discount these variations in the radar signal, they can be used to provide estimates of water table which itself is of great value for estimating carbon fluxes from the tropical peatland system. For accurate estimates a measure of interferometric coherence is required, which can, however, be problematic as it is typically not supplied by space agencies and requires user intensive processing from a low level radar product. Inclusion of coherence data as an option when ordering data would facilitate the estimation of the peatland water table.

One of the conclusions that should be drawn from this thesis is the need for improved bottom up understanding of how radar describes the temporal changes in a particular vegetation type rather than the currently popular top down approach whereby entire continents or the global land mass are mapped using a single 'one size fits all' algorithm. In the long term a more accurate approach to mapping forest biomass over large areas would be to stratify understanding of individual empirically derived radar:biomass relationships by vegetation type, before creating final large scale maps from a mosaic of relationships.

Radar remote sensing is a key technology as part of a forest monitoring system capable of reducing the uncertainties in the location and amount of tropical biomass and in carbon fluxes due to land use change in the tropics. However in order for it to be fully utilised the exact temporal relationships between the radar signal and various land use processes occurring in different vegetation types and different areas of the globe need to be understood in much more detail. If temporal processes are not included it threatens to make any future radar based tracking of forest carbon less, rather than more, robust.

## 7.6 Conclusions

The research objectives of this thesis as introduced in Section 2.5 were:

1. To observe the temporal pattern of the radar signal change across a four year dataset and examine how these patterns are related to landscape processes such as.
2. To examine the effect that ecosystem processes other than changes in above ground biomass have on the radar.
3. To examine the radar signal occurring as a result of loss of peat swamp forest through fire.
4. To look at how these radar signals may be separated from each other in order to give accurate information on carbon emissions in peat swamp forests.

In answer to objective 1:

- Complex patterns of radar signal change were observed across the tropical peatland landscape.
- Large amounts of the backscatter change in peat swamp forest are unrelated to biomass change.
- The amount of temporal change in the radar signal is linked to forest biomass, with areas of biomass < 80 tonnes per hectare showing up to 6dB of variation.
- Empirically derived relationships between the radar signal with biomass are not useful tools in peat swamp forests due to the temporal variation in the radar signal.

In answer to objective 2:

- Changes in the radar signal in degraded areas related to changes in the depth of the peatland water table.
- Radar backscatter shows a non-linear relationship with water table depth.

- Interferometric coherence data is also related to the depth of the water table
- These relationships can be used to produce high spatial resolution estimates of water table depth in peatlands, though only in areas of low degraded forest where the amount of biomass is low.

In answer to objective 3:

- The radar signal related to loss of primary forest by fire is an increase in radar backscatter. This is counter to that which would be expected from empirically fitted radar:biomass relationships.
- Burnt areas show high amount of backscatter variation.
- This variation in the backscatter is linked to monthly rainfall.

In answer to objective 4:

- Temporal pattern of backscatter change was assessed using empirical orthogonal functions.
- These successfully grouped areas with similar patterns of backscatter change and could be used as the basis for landscape classifications.

## 7.7 Directions for future research

- In situations where empirically fitted biomass:radar relationships are to be utilised it should be appreciated that they are not necessarily static curves but can fluctuate. More effort should go into defining these relationships according to season, rainfall regime and vegetation type and further research is required to better understand the underlying mechanisms and factors influencing these relationships curves.

- What is the global distribution of variability in the radar signal?
  In this thesis high temporal radar backscatter variability has been demonstrated in peat swamp forest, but it remains to be established how this variability fits into the range of temporal backscatter variability over larger areas, e.g. the whole of Borneo or even globally? The generation of a global map of PALSAR temporal standard deviation and temporal mean backscatter would be a relatively simple if computationally intensive process. Such a map could help identify regions where the assumptions of using biomass:radar relationships are not broken and they can easily be applied.

- What variables would best predict global temporal standard deviation?
  Vegetation type, wetland distribution, rainfall and rainfall seasonality could all be hypothesized as influencing temporal behaviour and investigation of these variables could be a worthwhile direction for future research.

- Ultimately calculations of PALSAR temporal trends are limited as the archive covers a brief period of time (~4years) in comparison to the ~40 year Landsat archive which is now beginning to be fully exploited to examine temporal changes in land cover. Efforts should be made to extend the length of the radar image archive by using data from the ALOS 2 satellite when it is launched and by including JERS1 HH data in the temporal data stacks.

- What are the patterns of temporal backscatter change caused by different modes of forest disturbance (e.g. fire, logging, etc)?

  The temporal radar signal caused by a wide range of different types of forest disturbance should be characterised at various bands and polarisations. This could then be further extended to characterise patterns of disturbance in other vegetation types. One option to increase our understanding of temporal backscatter behaviour would be to use fully polarimetric SAR to identify the centres of backscattering and how these alter over time in both disturbed and undisturbed forest.

- How does the temporal radar signal vary when observed using alternative radar bands?

  Observations of temporal trends should be characterised at different bands, imaging modes and polarisations. Research questions could include: How different does a particular disturbance event look depending on, for example, imaging mode? Would these differences confound the identification of disturbance type from radar remote sensing or help to distinguish different disturbance types?

- There needs to be a continued development of algorithms for distinguishing and classifying temporal patterns in remote sensing data and an application of these techniques to the radar remote sensing domain.

# 8. Appendix: Computer processing scripts

## 8.1 Linux scripts

### 8.1.1 Radar processing scripts

**do_run_isp_palsar.csh** This script contain information on the scenes to be processed, location of data files, and processing parameters such as number of looks, polarisation and sources of geocoding data. A separate line is required for each scene processed, only example is given.

```
#./run_isp_palsar.csh region slc1_dir slc1 slc2_dir slc2 range_looks azimuth_looks image_width pol pixel_spacing
offset_meth flipping interp_mode year geocode_dem geocode_image

##################
##  Kalimantan  ##
##################
#421_7140#
#done#./run_isp_palsar_new.csh kalimantan 20070622_FBD_421_7140 IMG-HH-ALPSRP075057140-H1.1__A 20070807_FBD_421_7140
IMG-HH-ALPSRP081767140-H1.1__A 2 9 2320 HH 25 1 1 0 2007 srtm palsar

The following is an example of the do_run_isp_palsar.csh script for running the radar processing script on a cluster
computer
echo "module load gamma;cd /scratch/forest/msw13;./run_isp_palsar_ALICE.csh kampar 20090616_FBD_488_0000 IMG-HH-
ALPSRP180820000-H1.1__A 20090801_FBD_488_0000 IMG-HH-ALPSRP187530000-H1.1__A 2 9 2320 HH 25 1 1 0 2009 srtm palsar"
| qsub -N Gamma_Proc -M msw13@le.ac.uk -l walltime=00:25:00,nodes=1:ppn=1,pvmem=2Gb
```

**run_isp_palsar.csh** This is the main script for the processing of radar data. It has a modular design and various stages can be turned on or off. This script is the work of Kevin Tansey and Matthew Waldram with some contributions to the section on geocodinbg added by Emma Tebbs.

```
#!/bin/csh -fe
if ($#argv < 13) then
  echo " "
  echo "***  Process ALOS PALSAR DATA  ***"
  echo "***  Copyright 2004, Gamma Remote Sensing, v1.4 18-May-2004 ts/uw/clw  ***"
  echo "***  Emma Tebbs/MSW version  ***"
  echo " "
  echo "run_isp_palsar : To calibrate and run interferometric processing sequence for ALOS data"
  echo " "
  echo "usage: run_isp_palsar.csh"
  echo "       region_dir           Region directory e.g. kampar"
  echo "       slc1_dir             Data directory for slc1"
  echo "       slc1_IMG_file_name         PALSAR level 1.1 IMG file name e.g. IMG-HH-ALPSRP075937190-H1.1__A"
  echo "       slc2_dir             Data directory for slc2"
  echo "       slc2_IMG_file_name         PALSAR level 1.1 IMG file name e.g. IMG-HH-ALPSRP075937190-H1.1__A"
  echo "       mli_range_looks      Multi-look intensity range looks (FBS = 2; FBD, PLR = 1)"
  echo "       mli_azimuth_looks    Multi-look intensity azimuth looks (FBS, FBD = 6; PLR = 9)"
  echo "       image_width                Width (pixels) of the interferogram (mli and int)"
  echo "       polarisation               Polarisation (e.g. HH, HH_HV etc.)"
  echo "       grd_pixel_spacing          Ground pixel spacing in m for utm (e.g. 25, assume pixel is square)"
  echo "       create_offset_method       Offset_algorithm  1: intensity cross-correlation (default), 2: fringe
visibility"
  echo "       flipping             Left/right flipping flag, (default=1: normal, -1: mirror image)"
  echo "       interp_mode                Interpolation Mode (0: nn (default), 1: spline, 2: spline log)"
  echo "       year                 year of image aquisition"
  echo " "
  exit
  endif

set region        = $argv[1]
set slc1_dir            = $2
set slc2_dir            = $4
set insardir            = $2_$4
set slc1          = $3
```

```
set slc2          = $5
set range_looks   = $6
set azimuth_looks       = $7
set image_width   = $8
set pol           = $9
set grd_pixel_spacing   = $argv[10]
set create_offset_method = $argv[11]
set flipping            = $argv[12]
set interp_mode   = $argv[13]
set year          = $14
set dem_width           = $argv[15]
set dem_source    = $argv[15]
set img_source    = $argv[16]

set init_offset_corr_threshold_1 = 4.0
set init_offset_corr_threshold_2 = 4.0

set grd_rsp = $grd_pixel_spacing
set grd_azsp = $grd_pixel_spacing

if (1) then
  set do_prepare_slc    = 0
  set do_initial_offset = 0
  set do_create_offset  = 0
  set do_interferogram  = 0
  set do_base_est       = 0
  set do_flattening     = 0
  set do_coherence      = 0
  set do_ad_filtering   = 0
  set do_calibration    = 0
  set do_geocode1       = 1   #gecode a la kevin: srtm & landsat
  set do_geocode  = 0         #geocode from landsat
  set do_geo_fine_LS    = 0   #geocode from SRTM
  set do_header         = 1
  set do_kml            = 0
  set do_tidy_up  = 1
  endif
```

```
if (0) then
  set do_geo_fine_LS    = 0
  set do_geocode_LS     = 0
endif

if (0) then
  set do_prepare_slc    = 1
  set do_initial_offset = 0
  set do_create_offset  = 0
  set do_interferogram  = 0
  set do_base_est       = 0
  set do_flattening     = 0
  set do_coherence      = 0
  set do_ad_filtering   = 0
  set do_calibration    = 0
  set do_geocode1       = 0   #gecode a la kevin: srtm & landsat
  set do_geocode  = 0         #geocode from landsat
  set do_geo_fine_LS    = 0   #geocode from SRTM
  set do_header         = 1
  set do_kml            = 0
  set do_tidy_up  = 1
  endif

set do_unwrapping_bcut  = 0
set do_unwrapping_mcf   = 0

set hemisphere = 0
if ($region == "kalimantan") set hemisphere = "South"
if ($region == "jambi") set hemisphere = "South"
if ($region == "kampar") set hemisphere = "North"

cd $region/$year
if (! (-d $insardir\_$range_looks\x$azimuth_looks\_$pol) ) mkdir $insardir\_$range_looks\x$azimuth_looks\_$pol
cd $insardir\_$range_looks\x$azimuth_looks\_$pol

#Prepare slc data and processing parameter files#
```

```
if ($do_prepare_slc) then
  if (-e $slc1.slc) rm -f $slc1.slc
  if (-e $slc1.slc.par) rm -f $slc1.slc.par
  par_EORC_PALSAR /clusterhome/kjt7/$region/alos_palsar/$slc1_dir/l1data/LED* $slc1.slc.par
/clusterhome/kjt7/$region/alos_palsar/$slc1_dir/l1data/$slc1 $slc1.slc
  if (-e $slc2.slc) rm -f $slc2.slc
  if (-e $slc2.slc.par) rm -f $slc2.slc.par
  par_EORC_PALSAR /clusterhome/kjt7/$region/alos_palsar/$slc2_dir/l1data/LED* $slc2.slc.par
/clusterhome/kjt7/$region/alos_palsar/$slc2_dir/l1data/$slc2 $slc2.slc
  endif

###############################################################################
###   Offset estimation of the slc images                                   ###
###############################################################################

if ($do_initial_offset) then
  if (-e $slc1\_$slc2.off) rm -f $slc1\_$slc2.off
  if ($create_offset_method == 1) then
    create_offset $slc1.slc.par $slc2.slc.par $slc1\_$slc2.off $create_offset_method $range_looks $azimuth_looks <
../../../create_offset_input_ICC
    else
   endif
  if ($create_offset_method == 2) then
    create_offset $slc1.slc.par $slc2.slc.par $slc1\_$slc2.off $create_offset_method $range_looks $azimuth_looks <
../../../create_offset_input_FVI
   else
   endif
  init_offset $slc1.slc $slc2.slc $slc1.slc.par $slc2.slc.par $slc1\_$slc2.off $range_looks $azimuth_looks - - 0 0
$init_offset_corr_threshold_1
  init_offset $slc1.slc $slc2.slc $slc1.slc.par $slc2.slc.par $slc1\_$slc2.off 1 1 - - 0 0
$init_offset_corr_threshold_2
  endif

if ($do_create_offset) then
  if ($create_offset_method == 1) then
    if (-e $slc1\_$slc2.offs) rm -f $slc1\_$slc2.offs
    if (-e $slc1\_$slc2.snr) rm -f $slc1\_$slc2.snr
```

```
    if (-e $slc1\_$slc2.offsets) rm -f $slc1\_$slc2.offsets
    if (-e $slc1\_$slc2.coffs) rm -f $slc1\_$slc2.coffs
    if (-e $slc1\_$slc2.coffsets) rm -f $slc1\_$slc2.coffsets
    offset_pwr $slc1.slc $slc2.slc $slc1.slc.par $slc2.slc.par $slc1\_$slc2.off $slc1\_$slc2.offs $slc1\_$slc2.snr -
- $slc1\_$slc2.offsets 1 - - 7.0
    offset_fit $slc1\_$slc2.offs $slc1\_$slc2.snr $slc1\_$slc2.off $slc1\_$slc2.coff $slc1\_$slc2.coffsets - 4 0
    else
    endif

  if ($create_offset_method == 2) then
    if (-e $slc1\_$slc2.offs) rm -f $slc1\_$slc2.offs
    if (-e $slc1\_$slc2.snr) rm -f $slc1\_$slc2.snr
    if (-e $slc1\_$slc2.offsets) rm -f $slc1\_$slc2.offsets
    if (-e $slc1\_$slc2.coffs) rm -f $slc1\_$slc2.coffs
    if (-e $slc1\_$slc2.coffsets) rm -f $slc1\_$slc2.coffsets
    offset_SLC $slc1.slc $slc2.slc $slc1.slc.par $slc2.slc.par $slc1\_$slc2.off $slc1\_$slc2.offs $slc1\_$slc2.snr -
- $slc1\_$slc2.offsets 2 - - 3.0
    offset_fit $slc1\_$slc2.offs $slc1\_$slc2.snr $slc1\_$slc2.off $slc1\_$slc2.coff $slc1\_$slc2.coffsets - 4 0
    else
    endif
  endif


################################################################################
###   Compute interferogram                                                  ###
################################################################################

if ($do_interferogram) then
  if (-e $slc1\_$slc2.int) rm -f $slc1\_$slc2.int
  if (-e $slc2.rslc) rm -f $slc2.rslc
  if (-e $slc2.rslc.par) rm -f $slc2.rslc.par
  SLC_interp $slc2.slc $slc1.slc.par $slc2.slc.par $slc1\_$slc2.off $slc2.rslc $slc2.rslc.par
  SLC_intf $slc1.slc $slc2.rslc $slc1.slc.par $slc2.rslc.par $slc1\_$slc2.off $slc1\_$slc2.int $range_looks
$azimuth_looks
  if (-e $slc1.mli) rm -f $slc1.mli
  if (-e $slc1.mli.par) rm -f $slc1.mli.par
  if (-e $slc2.mli) rm -f $slc2.mli
```

```
  if (-e $slc2.mli.par) rm -f $slc2.mli.par
  if (-e $slc2.rmli) rm -f $slc2.rmli
  if (-e $slc2.rmli.par) rm -f $slc2.rmli.par
  multi_look $slc1.slc $slc1.slc.par $slc1.mli $slc1.mli.par $range_looks $azimuth_looks
  multi_look $slc2.slc $slc2.slc.par $slc2.mli $slc2.mli.par $range_looks $azimuth_looks
  multi_look $slc2.rslc $slc2.rslc.par $slc2.rmli $slc2.rmli.par $range_looks $azimuth_looks
  raspwr $slc1.mli $image_width 1 0 1 1 1.0 0.35 $flipping $slc1.mli.bmp
  raspwr $slc2.mli $image_width 1 0 1 1 1.0 0.35 $flipping $slc2.mli.bmp
  raspwr $slc2.rmli $image_width 1 0 1 1 1.0 0.35 $flipping $slc2.rmli.bmp
  if (-e $slc1.mli_flip.bmp) rm -f $slc1.mli_flip.bmp
  if (-e $slc2.mli_flip.bmp) rm -f $slc2.mli_flip.bmp
  if (-e $slc2.rmli_flip.bmp) rm -f $slc2.rmli_flip.bmp
  gm convert -flip $slc1.mli.bmp $slc1.mli_flip.bmp
  gm convert -flip $slc2.mli.bmp $slc2.mli_flip.bmp
  gm convert -flip $slc2.rmli.bmp $slc2.rmli_flip.bmp
  rm -f $slc1.mli.bmp $slc2.mli.bmp $slc2.rmli.bmp
  rasmph $slc1\_$slc2.int $image_width 1 0 1 1 1. 0.35 $flipping $slc1\_$slc2.mag_phase.bmp
  if (-e $slc1\_$slc2.mag_phase_flip.bmp) rm -f $slc1\_$slc2.mag_phase_flip.bmp
  gm convert -flip $slc1\_$slc2.mag_phase.bmp $slc1\_$slc2.mag_phase_flip.bmp
  rasmph_pwr $slc1\_$slc2.int $slc1.mli $image_width 1 1 0 1 1 1.0 0.35 $flipping $slc1\_$slc2.mag_phase_pwr.bmp
  if (-e $slc1\_$slc2.mag_phase_pwr_flip.bmp) rm -f $slc1\_$slc2.mag_phase_pwr_flip.bmp
  gm convert -flip $slc1\_$slc2.mag_phase_pwr.bmp $slc1\_$slc2.mag_phase_pwr_flip.bmp
  rm -f $slc1\_$slc2.mag_phase_pwr.bmp $slc1\_$slc2.mag_phase.bmp
  endif

###############################################################################
###   Generate baseline file (parallel component from the orbit parameters,   ###
###   perpendicular component from the fringe rate), remove the Earth phase trend,  ###
###   filter (running adf several times with a smaller coefficient and        ###
###   decreasing window size (e.g. 128,64,32) will lead to a better filtering but   ###
###   is time consuming) and estimate the phase noise (obs.: 05721_25394.smcc is    ###
###   not the degree of coherence but rather the phase noise because it is    ###
###   estimated from the filtered interferogram without use of the intensities).    ###
###############################################################################

if ($do_base_est) then   # generate baseline file (first remove an eventual first estimate)
  if (-e $slc1\_$slc2.base) rm -f $slc1\_$slc2.base
```

```
  if (-e $slc1\_$slc2.base.txt) rm -f $slc1\_$slc2.base.txt
  touch $slc1\_$slc2.base.txt
  base_init $slc1.slc.par $slc2.rslc.par $slc1\_$slc2.off $slc1\_$slc2.int $slc1\_$slc2.base 0 1024 1024 >
$slc1\_$slc2.base.txt
  endif

if ($do_flattening) then   # curved Earth phase trend removal (flattening) and filter
  if (-e $slc1\_$slc2.flt) rm -f $slc1\_$slc2.flt
  ph_slope_base $slc1\_$slc2.int $slc1.slc.par $slc1\_$slc2.off $slc1\_$slc2.base $slc1\_$slc2.flt
  if (-e $slc1\_$slc2.flt_mag_phase_flip.bmp) rm -f $slc1\_$slc2.flt_mag_phase_flip.bmp
  rasmph $slc1\_$slc2.flt $image_width 1 0 1 1 1. 0.35 $flipping $slc1\_$slc2.flt_mag_phase.bmp
  gm convert -flip $slc1\_$slc2.flt_mag_phase.bmp $slc1\_$slc2.flt_mag_phase_flip.bmp
  if (-e $slc1\_$slc2.flt_mag_phase_pwr_flip.bmp) rm -f $slc1\_$slc2.flt_mag_phase_pwr_flip.bmp
  rasmph_pwr $slc1\_$slc2.flt $slc1.mli $image_width 1 1 0 1 1 1.0 0.35 $flipping $slc1\_$slc2.flt_mag_phase_pwr.bmp
  gm convert -flip $slc1\_$slc2.flt_mag_phase_pwr.bmp $slc1\_$slc2.flt_mag_phase_pwr_flip.bmp
  rm -f $slc1\_$slc2.flt_mag_phase.bmp $slc1\_$slc2.flt_mag_phase_pwr.bmp
  endif


if ($do_coherence) then   # coherence estimation and generation of Bitmaps
  if (-e $slc1\_$slc2.cc) rm -f $slc1\_$slc2.cc
  cc_wave $slc1\_$slc2.flt $slc1.mli $slc2.rmli $slc1\_$slc2.cc $image_width
  if (-e $slc1\_$slc2.cc_flip.bmp) rm -f $slc1\_$slc2.cc_flip.bmp
  ras_linear $slc1\_$slc2.cc $image_width 1 0 1 1 0.0 1.0 $flipping $slc1\_$slc2.cc.bmp
  gm convert -flip $slc1\_$slc2.cc.bmp $slc1\_$slc2.cc_flip.bmp
  if (-e $slc1\_$slc2.cc_pwr_flip.bmp) rm -f $slc1\f
  endif

if ($do_ad_filtering) then   # adaptive interferogram filtering and generation of Bitmaps
  if (-e $slc1\_$slc2.cc_filt) rm -f $slc1\_$slc2.cc_filt
  if (-e $slc1\_$slc2.flt_filt) rm -f $slc1\_$slc2.flt_filt
  adf $slc1\_$slc2.flt  $slc1\_$slc2.flt_filt $slc1\_$slc2.cc_filt $image_width .5
  if (-e $slc1\_$slc2.flt_filt_mag_phase_pwr_flip.bmp) rm -f $slc1\_$slc2.flt_filt_mag_phase_pwr_flip.bmp
  rasmph_pwr $slc1\_$slc2.flt_filt $slc1.mli $image_width 1 1 0 1 1 1.0 0.35 $flipping
$slc1\_$slc2.flt_filt_mag_phase_pwr.bmp
  gm convert -flip $slc1\_$slc2.cc.bmp $slc1\_$slc2.cc_flip.bmp
  if (-e $slc1\_$slc2.cc_pwr_flip.bmp) rm -f $slc1\_$slc2.cc_pwr_flip.bmp
```

```
  rascc $slc1\_$slc2.cc $slc1.mli $image_width 1 1 0 1 1 0.1 0.9 1.0 0.35 $flipping $slc1\_$slc2.cc_pwr.bmp
  gm convert -flip $slc1\_$slc2.cc_pwr.bmp $slc1\_$slc2.cc_pwr_flip.bmp
  rm -f $slc1\_$slc2.cc.bmp $slc1\_$slc2.cc_pwr.bmp
  endif

##############################################################################################
###   Phase unwrapping                                                                     ###
##############################################################################################

if ($do_unwrapping_bcut) then   # phase unwrapping (first remove an eventual first estimate)
  if (-e $slc1\_$slc2.flag) rm -f $slc1\_$slc2.flag
  if (-e $slc1\_$slc2.unw) rm -f $slc1\_$slc2.unw
  corr_flag $slc1\_$slc2.cc_filt $slc1\_$slc2.flag $image_width 0.25
  neutron $slc1.mli $slc1\_$slc2.flag $image_width
  residue $slc1\_$slc2.flt_filt $slc1\_$slc2.flag $image_width
  tree_cc $slc1\_$slc2.flag $image_width 64
  grasses $slc1\_$slc2.flt_filt $slc1\_$slc2.flag $slc1\_$slc2.unw $image_width
  if (-e $slc1\_$slc2.unw.bmp) rm -f $slc1\_$slc2.unw.bmp
  if (-e $slc1\_$slc2.unw_flip.bmp) rm -f $slc1\_$slc2.unw_flip.bmp
  rasrmg $slc1\_$slc2.unw $slc1.mli $image_width 1 1 0 1 1 .5 1. .35 0.0 $flipping $slc1\_$slc2.unw.bmp
  gm convert -flip $slc1\_$slc2.unw.bmp $slc1\_$slc2.unw_flip.bmp
  endif

if ($do_unwrapping_mcf) then   # phase unwrapping (Minimum Cost Flow)
  if (-e $slc1\_$slc2.cc_mask.bmp) rm -f $slc1\_$slc2.cc_mask.bmp
  rascc_mask $slc1\_$slc2.cc $slc1.mli $image_width 1 1 0 1 1 0.2 - - - - - $slc1\_$slc2.cc_mask.bmp
  if (-e $slc1\_$slc2.unw_mcf0) rm -f $slc1\_$slc2.unw_mcf0
  mcf $slc1\_$slc2.flt_filt $slc1\_$slc2.cc $slc1\_$slc2.cc_mask.bmp $slc1\_$slc2.unw_mcf0 $image_width 1 0 0 - - 1
1 - - -
  rasrmg $slc1\_$slc2.unw_mcf0 $slc1.mli $image_width 1 1 0 1 1 .5 1. .35 0.0 $flipping $slc1\_$slc2.unw_mcf0.bmp
  gm convert -flip $slc1\_$slc2.unw_mcf0.bmp $slc1\_$slc2.unw_mcf0_flip.bmp
  if (-e $slc1\_$slc2.unw_mcf0_interp) rm -f $slc1\_$slc2.unw_mcf0_interp
  interp_ad $slc1\_$slc2.unw_mcf0 $slc1\_$slc2.unw_mcf0_interp $image_width
  rasrmg $slc1\_$slc2.unw_mcf0_interp $slc1.mli $image_width 1 1 0 1 1 .5 1. .35 0.0 $flipping
$slc1\_$slc2.unw_mcf0_interp.bmp
  gm convert -flip $slc1\_$slc2.unw_mcf0_interp.bmp $slc1\_$slc2.unw_mcf0_interp_flip.bmp
  if (-e $slc1\_$slc2.unw_mcf) rm -f $slc1\_$slc2.unw_mcf
```

```
  unw_model $slc1\_$slc2.flt_filt $slc1\_$slc2.unw_mcf0_interp $slc1\_$slc2.unw_mcf $image_width - - -
  if (-e $slc1\_$slc2.unw_mcf.bmp) rm -f $slc1\_$slc2.unw_mcf.bmp
  rasrmg $slc1\_$slc2.unw_mcf $slc1.mli $image_width 1 1 0 1 1 .5 1. .35 0.0 $flipping $slc1\_$slc2.unw_mcf.bmp
  gm convert -flip $slc1\_$slc2.unw_mcf.bmp $slc1\_$slc2.unw_mcf_flip.bmp
  rm -f $slc1\_$slc2.unw_mcf0_interp.bmp $slc1\_$slc2.unw_mcf0.bmp
  endif

if ($do_calibration) then     # Perform a calibration of the SLC data
  if (-e $slc1.cslc.par) rm -f $slc1.cslc.par
  if (-e $slc1.cslc) rm -f $slc1.cslc
  if (-e $slc2.cslc.par) rm -f $slc2.cslc.par
  if (-e $slc2.cslc) rm -f $slc2.cslc
  if (-e $slc1.cmli.par) rm -f $slc1.cmli.par
  if (-e $slc1.cmli) rm -f $slc1.cmli
  if (-e $slc2.cmli.par) rm -f $slc2.cmli.par
  if (-e $slc2.cmli) rm -f $slc2.cmli
  radcal_SLC $slc1.slc $slc1.slc.par $slc1.cslc $slc1.cslc.par 1 - 0 0 1 0 -115.0
  radcal_SLC $slc2.slc $slc2.slc.par $slc2.cslc $slc2.cslc.par 1 - 0 0 1 0 -115.0
  multi_look $slc1.cslc $slc1.cslc.par $slc1.cmli $slc1.cmli.par $range_looks $azimuth_looks
  multi_look $slc2.cslc $slc2.cslc.par $slc2.cmli $slc2.cmli.par $range_looks $azimuth_looks
  if (-e $slc1.cmli_flip.bmp) rm -f $slc1.cmli_flip.bmp
  if (-e $slc2.cmli_flip.bmp) rm -f $slc2.cmli_flip.bmp
  raspwr $slc1.cmli $image_width 1 0 1 1 1.0 0.35 $flipping $slc1.cmli.bmp
  gm convert -flip $slc1.cmli.bmp $slc1.cmli_flip.bmp
  raspwr $slc2.cmli $image_width 1 0 1 1 1.0 0.35 $flipping $slc2.cmli.bmp
  gm convert -flip $slc2.cmli.bmp $slc2.cmli_flip.bmp
  rm -f $slc1.cmli.bmp $slc2.cmli.bmp
  endif

#########################################################
#   Geocoding using SRTM & Landsat                      ##
#########################################################

if ($do_geocode1) then
  if (-e $slc1.dem_par) rm -f $slc1.dem_par
  if (-e $slc1.dem) rm -f $slc1.dem
  if (-e $slc1.dem_seg) rm -f $slc1.dem_segset
```

```
  if (-e $slc1.img) rm -f $slc1.img
  if (-e $slc1.rough.utm_to_rdc) rm -f $slc1.rough.utm_to_rdc
  if (-e $slc1.utm.sim_sar) rm -f $slc1.utm.sim_sar
  if (-e $slc1\_utm.dem_par) rm -f $slc1\_utm.dem_par
  if (-e $slc1\_utm.dem) rm -f $slc1\_utm.dem

  if ($dem_source == srtm) set dem_projection = eqa
  if ($img_source == landsat) set img_projection = utm
  if ($img_source == palsar) set img_projection = utm


  create_dem_par $slc1\_utm.dem_par $slc1.cmli.par - -$grd_rsp $grd_rsp <
/clusterhome/msw13/PALSAR_data/DEMs/landsat/create_dem_par_utm_$region
  dem_trans /clusterhome/msw13/PALSAR_data/DEMs/$dem_source/$region\_$dem_source\_$dem_projection.dem_par
/clusterhome/msw13/PALSAR_data/DEMs/$dem_source/$region\_$dem_source\_$dem_projection.dem $slc1\_utm.dem_par
$slc1\_utm.dem
  gc_map $slc1.cmli.par - $slc1\_utm.dem_par $slc1\_utm.dem $slc1.dem_par $slc1.dem_seg $slc1.rough.utm_to_rdc - -
$slc1.utm.sim_sar

  if ($img_source != -) then
    map_trans /clusterhome/msw13/PALSAR_data/DEMs/$img_source/$region\_$img_source\_$img_projection.dem_par
/clusterhome/msw13/PALSAR_data/DEMs/$img_source/$region\_$img_source\_$img_projection.img $slc1.dem_par $slc1.img
    endif

  set dem_width = `awk '{if($1 == "width:" ) printf("%d", $2)}' < $slc1.dem_par`

  if ($img_source != -) then
    geocode $slc1.rough.utm_to_rdc $slc1.img $dem_width $slc1.sim_sar $image_width - 1 0
    endif
  if ($img_source == -) then
    geocode $slc1.rough.utm_to_rdc $slc1.utm.sim_sar $dem_width $slc1.sim_sar $image_width - 1 0
    endif


  if (-e $slc1.diff_par) rm -f $slc1.diff_par
  if (-e geocode_info) rm -f
  create_diff_par $slc1.cmli.par - $slc1.diff_par 1 < /clusterhome/msw13/PALSAR_data/create_diff_par
```

```
  init_offsetm $slc1.cmli $slc1.sim_sar $slc1.diff_par - - - - - - 2.5 > geocode_info
  if (-e $slc1.gc_offs) rm -f $slc1.gc_offs
  if (-e $slc1.gc_snr) rm -f $slc1.gc_snr
  if (-e $slc1.gc_offsets) rm -f $slc1.gc_offsets
  if (-e $slc1.gc_coffs) rm -f $slc1.gc_coffs
  if (-e $slc1.gc_coffsets) rm -f $slc1.gc_coffsets
#put repeat steps here
  if ($img_source == -) then
    offset_pwrm $slc1.cmli $slc1.sim_sar $slc1.diff_par $slc1.gc_offs $slc1.gc_snr 256 256 $slc1.gc_offsets 1 8 8
7.0
    offset_fitm $slc1.gc_offs $slc1.gc_snr $slc1.diff_par $slc1.gc_coffs $slc1.gc_coffsets 7.0 3
    offset_pwrm $slc1.cmli $slc1.sim_sar $slc1.diff_par $slc1.gc_offs $slc1.gc_snr 128 128 $slc1.gc_offsets 2 24 24
7.0
    offset_fitm $slc1.gc_offs $slc1.gc_snr $slc1.diff_par $slc1.gc_coffs $slc1.gc_coffsets 7.0 3 >> geocode_info
    endif
  if ($img_source != -) then
    offset_pwrm $slc1.cmli $slc1.sim_sar $slc1.diff_par $slc1.gc_offs $slc1.gc_snr 128 128 - - 8 32
    offset_fitm $slc1.gc_offs $slc1.gc_snr $slc1.diff_par $slc1.gc_coffs $slc1.gc_coffsets - 1
    offset_pwrm $slc1.cmli $slc1.sim_sar $slc1.diff_par $slc1.gc_offs $slc1.gc_snr 128 128 - - 16 64
    offset_fitm $slc1.gc_offs $slc1.gc_snr $slc1.diff_par $slc1.gc_coffs $slc1.gc_coffsets - 1
    offset_pwrm $slc1.cmli $slc1.sim_sar $slc1.diff_par $slc1.gc_offs $slc1.gc_snr 128 128 - - 16 64
    offset_fitm $slc1.gc_offs $slc1.gc_snr $slc1.diff_par $slc1.gc_coffs $slc1.gc_coffsets - 3
    offset_pwrm $slc1.cmli $slc1.sim_sar $slc1.diff_par $slc1.gc_offs $slc1.gc_snr 128 128 - - 24 96
    offset_fitm $slc1.gc_offs $slc1.gc_snr $slc1.diff_par $slc1.gc_coffs $slc1.gc_coffsets - 4
    offset_pwrm $slc1.cmli $slc1.sim_sar $slc1.diff_par $slc1.gc_offs $slc1.gc_snr 96 96 - - 24 96
    offset_fitm $slc1.gc_offs $slc1.gc_snr $slc1.diff_par $slc1.gc_coffs $slc1.gc_coffsets - 4
    offset_pwrm $slc1.cmli $slc1.sim_sar $slc1.diff_par $slc1.gc_offs $slc1.gc_snr 96 96 - - 32 96
    offset_fitm $slc1.gc_offs $slc1.gc_snr $slc1.diff_par $slc1.gc_coffs $slc1.gc_coffsets - 4 >> geocode_info
    endif

#  offset_pwrm $slc1.cmli $slc1.sim_sar $slc1.diff_par $slc1.gc_offs $slc1.gc_snr 256 256 $slc1.gc_offsets 1 8 8 7.0
#  offset_fitm $slc1.gc_offs $slc1.gc_snr $slc1.diff_par $slc1.gc_coffs $slc1.gc_coffsets 7.0 3
#  offset_pwrm $slc1.cmli $slc1.sim_sar $slc1.diff_par $slc1.gc_offs $slc1.gc_snr 256 256 $slc1.gc_offsets 1 16 16
7.0
#  offset_fitm $slc1.gc_offs $slc1.gc_snr $slc1.diff_par $slc1.gc_coffs $slc1.gc_coffsets 7.0 3
#put repeat steps here
```

```
  if (-e $slc1.utm_to_rdc) rm -f $slc1.utm_to_rdc
  gc_map_fine $slc1.rough.utm_to_rdc $dem_width $slc1.diff_par $slc1.utm_to_rdc 0
  if (-e $slc1_dir.cmli.utm_$grd_rsp\m_$pol) rm -f $slc1_dir.cmli.utm_$grd_rsp\m_$pol
  if ($slc2_dir != -) then
    if (-e $slc2_dir.cmli.utm_$grd_rsp\m_$pol) rm -f $slc2_dir.cmli.utm_$grd_rsp\m_$pol
    if (-e $slc1_dir\_$slc2_dir.cc.utm_$grd_rsp\m_$pol) rm -f $slc1\_$slc2.cc.utm_$grd_rsp\m_$pol
    endif
  geocode_back $slc1.cmli $image_width $slc1.utm_to_rdc $slc1_dir.cmli.utm_$grd_rsp\m_$pol $dem_width 0 3 0
  cp $slc1.dem_par $slc1_dir.cmli.utm_$grd_rsp\m_$pol.par_file
  if ($slc2_dir != -) then
  if (-e $slc2_dir.cmli.utm_$grd_rsp\m_$pol.par_file) rm -f $slc2_dir.cmli.utm_$grd_rsp\m_$pol.par_file
    if (-e $slc1_dir\_$slc2_dir.cc.utm_$grd_rsp\m_$pol.par_file) rm -f
$slc1_dir\_$slc2_dir.cc.utm_$grd_rsp\m_$pol.par_file

    geocode_back $slc2.cmli $image_width $slc1.utm_to_rdc $slc2_dir.cmli.utm_$grd_rsp\m_$pol $dem_width 0 3 0
    geocode_back $slc1\_$slc2.cc $image_width $slc1.utm_to_rdc $slc1_dir\_$slc2_dir.cc.utm_$grd_rsp\m_$pol
$dem_width 0 1 0
    cp $slc1.dem_par $slc2_dir.cmli.utm_$grd_rsp\m_$pol.par_file
    cp $slc1.dem_par $slc1_dir\_$slc2_dir.cc.utm_$grd_rsp\m_$pol.par_file

    endif
  if (-e $slc1_dir.cmli.utm_$grd_rsp\m_$pol.bmp) rm -f $slc1_dir.cmli.utm_$grd_rsp\m_$pol.bmp
  raspwr $slc1_dir.cmli.utm_$grd_rsp\m_$pol $dem_width 1 0 1 1 1.0 0.35 1 $slc1_dir.cmli.utm_$grd_rsp\m_$pol.bmp
  if ($slc2_dir != -) then
    if (-e $slc2_dir.cmli.utm_$grd_rsp\m_$pol.bmp) rm -f $slc2_dir.cmli.utm_$grd_rsp\m.bmp_$pol
    if (-e $slc1_dir\_$slc2_dir.cc.utm_$grd_rsp\m_$pol.bmp) rm -f $slc1_dir\_$slc2_dir.cc.utm_$grd_rsp\m_$pol.bmp
    raspwr $slc2_dir.cmli.utm_$grd_rsp\m_$pol $dem_width 1 0 1 1 1.0 0.35 1 $slc2_dir.cmli.utm_$grd_rsp\m_$pol.bmp
    ras_linear $slc1_dir\_$slc2_dir.cc.utm_$grd_rsp\m_$pol $dem_width 1 0 1 1 0.0 1.0 1
$slc1_dir\_$slc2_dir.cc.utm_$grd_rsp\m_$pol.bmp
endif
    endif
 endif

#####################################
##   Geocode from landsat tile only ##
#####################################
```

```
if ($do_geocode) then
  if (-e $slc1\_utm_dem.par) rm -f $slc1\_utm_dem.par
  if (-e $slc1\dem) rm -f $slc1\dem
  if (-e $slc1.rough.utm_to_rdc) rm -f $slc1.rough.utm_to_rdc
  if (-e $slc1.utm.sim_sar) rm -f $slc1.utm.sim_sar
#  if (-e /clusterhome/kjt7/kalimantan/Landsat/$1\_l7_utm_dem.par) rm -f
/clusterhome/kjt7/kalimantan/Landsat/$1\_l7_utm_dem.par
#  if (-e /clusterhome/kjt7/kalimantan/Landsat/$1\_l7_utm_dem) rm -f
/clusterhome/kjt7/kalimantan/Landsat/$1\_l7_utm_dem

# Use for SRTM
#create_dem_par /clusterhome/kjt7/kalimantan/Landsat/$1\_l7_utm_dem.par $slc1.mli.par - -$grd_rsp $grd_azsp <
/clusterhome/msw13/PALSAR_data/DEMs/Landsat/create_dem_par_utm
#dem_trans /clusterhome/kjt7/kalimantan/Landsat/$1\_l7_eqa_dem.par
/clusterhome/kjt7/kalimantan/Landsat/$1\_l7_eqa_dem /clusterhome/kjt7/kalimantan/Landsat/$1\_l7_utm_dem.par
/clusterhome/kjt7/kalimantan/Landsat/$1\_l7_utm_dem

gc_map $slc1.mli.par - /clusterhome/kjt7/kalimantan/landsat/$1\_landsat_utm.dem_par
/clusterhome/kjt7/kalimantan/landsat/$1\_landsat_utm.img $slc1.dem_par $slc1.dem $slc1.rough.utm_to_rdc - -
$slc1.utm.sim_sar

set dem_width = `awk '{if($1 == "width:" ) printf("%d", $2)}' <
/clusterhome/kjt7/kalimantan/landsat/kalimantan_landsat_utm.dem_par` #gets dem width from dem_par file

  if (-e $slc1.sim_sar) rm -f $slc1.sim_sar
  geocode $slc1.rough.utm_to_rdc $slc1.utm.sim_sar $dem_width $slc1.sim_sar $image_width - 1 0
  if (-e $slc1.diff_par) rm -f $slc1.diff_par
  create_diff_par $slc1.mli.par - $slc1.diff_par 1 < /clusterhome/msw13/PALSAR_data/create_diff_par
  init_offsetm $slc1.mli $slc1.sim_sar $slc1.diff_par - - - - - - 2.0 > geocode_info
  if (-e $slc1.gc_offs) rm -f $slc1.gc_offs
  if (-e $slc1.gc_snr) rm -f $slc1.gc_snr
  if (-e $slc1.gc_offsets) rm -f $slc1.gc_offsets
  if (-e $slc1.gc_coffs) rm -f $slc1.gc_coffs
  if (-e $slc1.gc_coffsets) rm -f $slc1.gc_coffsets
  offset_pwrm $slc1.mli $slc1.sim_sar $slc1.diff_par $slc1.gc_offs $slc1.gc_snr 128 256 $slc1.gc_offsets 1 8 8 7.0
```

```
  offset_fitm $slc1.gc_offs $slc1.gc_snr $slc1.diff_par $slc1.gc_coffs $slc1.gc_coffsets 7.0 3
  if (-e $slc1.utm_to_rdcset) rm -f $slc1.utm_to_rdc
  gc_map_fine $slc1.rough.utm_to_rdc $dem_width $slc1.diff_par $slc1.utm_to_rdc 0
  if (-e $slc1_dir.cmli.utm_$grd_rsp\m_$pol) rm -f $slc1_dir.cmli.utm_$grd_rsp\m_$pol
  if ($slc2_dir != -) then
    if (-e $slc2_dir.cmli.utm_$grd_rsp\m_$pol) rm -f $slc2_dir.cmli.utm_$grd_rsp\m_$pol
    if (-e $slc1_dir\_$slc2_dir.cc.utm_$grd_rsp\m_$pol) rm -f $slc1\_$slc2.cc.utm_$grd_rsp\m_$pol
    endif
  geocode_back $slc1.cmli $image_width $slc1.utm_to_rdc $slc1_dir.cmli.utm_$grd_rsp\m_$pol $dem_width 0 3 0
  if ($slc2_dir != -) then
    geocode_back $slc2.cmli $image_width $slc1.utm_to_rdc $slc2_dir.cmli.utm_$grd_rsp\m_$pol $dem_width 0 3 0
    geocode_back $slc1\_$slc2.cc $image_width $slc1.utm_to_rdc $slc1_dir\_$slc2_dir.cc.utm_$grd_rsp\m_$pol
$dem_width 0 1 0
    endif
  if (-e $slc1_dir.cmli.utm_$grd_rsp\m_$pol.bmp) rm -f $slc1_dir.cmli.utm_$grd_rsp\m_$pol.bmp
  raspwr $slc1_dir.cmli.utm_$grd_rsp\m_$pol $dem_width 1 0 1 1 1.0 0.35 1 $slc1_dir.cmli.utm_$grd_rsp\m_$pol.bmp
  if ($slc2_dir != -) then
    if (-e $slc2_dir.cmli.utm_$grd_rsp\m_$pol.bmp) rm -f $slc2_dir.cmli.utm_$grd_rsp\m.bmp_$pol
    if (-e $slc1_dir\_$slc2_dir.cc.utm_$grd_rsp\m_$pol.bmp) rm -f $slc1_dir\_$slc2_dir.cc.utm_$grd_rsp\m_$pol.bmp
    raspwr $slc2_dir.cmli.utm_$grd_rsp\m_$pol $dem_width 1 0 1 1 1.0 0.35 1 $slc2_dir.cmli.utm_$grd_rsp\m_$pol.bmp
    ras_linear $slc1_dir\_$slc2_dir.cc.utm_$grd_rsp\m_$pol $dem_width 1 0 1 1 0.0 1.0 1
$slc1_dir\_$slc2_dir.cc.utm_$grd_rsp\m_$pol.bmp
    endif

#  if (-e $slc1.cmli.utm_$grd_rsp\m) rm -f $slc1.cmli.utm_$grd_rsp\m
#  if (-e $slc2.cmli.utmmv *.par processing_files_$grd_rsp\m) rm -f $slc2.cmli.utm_$grd_rsp\m
#  if (-e $slc1\_$slc2.cc.utm_$grd_rsp\m) rm -f $slc1\_$slc2.cc.utm_$grd_rsp\m
#  geocode_back $slc1.cmli $image_width $slc1.utm_to_rdc $slc1.cmli.utm_$grd_rsp\m $dem_width 0 3 0
#  geocode_back $slc2.cmli $image_width $slc1.utm_to_rdc $slc2.cmli.utm_$grd_rsp\m $dem_width 0 3 0
#  geocode_back $slc1\_$slc2.cc $image_width $slc1.utm_to_rdc $slc1\_$slc2.cc.utm_$grd_rsp\m $dem_width 0 1 0
#  if (-e $slc1.cmli.utm_$grd_rsp\m.bmp) rm -f $slc1.cmli.utm_$grd_rsp\m.bmp
#  if (-e $slc2.cmli.utm_$grd_rsp\m.bmp) rm -f $slc2.cmli.utm_$grd_rsp\m.bmp
#  if (-e $slc1\_$slc2.cc.utm_$grd_rsp\m.bmp) rm -f $slc1\_$slc2.cc.utm_$grd_rsp\m.bmp
#  raspwr $slc1.cmli.utm_$grd_rsp\m $dem_width 1 0 1 1 1.0 0.35 1 $slc1.cmli.utm_$grd_rsp\m.bmp
#  raspwr $slc2.cmli.utm_$grd_rsp\m $dem_width 1 0 1 1 1.0 0.35 1 $slc2.cmli.utm_$grd_rsp\m.bmp
#  ras_linear $slc1\_$slc2.cc.utm_$grd_rsp\m $dem_width 1 0 1 1 0.0 1.0 1 $slc1\_$slc2.cc.utm_$grd_rsp\m.bmp
```

```
  echo $dem_width
  endif

#########################################################
#   Geocoding using SRTM only                           ##
#########################################################

if ($do_geo_fine_LS) then
  if (-e $slc1\_utm.dem_par) rm -f $slc1\_utm.dem_par
  if (-e $slc1.dem) rm -f $slc1.dem
  if (-e $slc1.rough.utm_to_rdc) rm -f $slc1.rough.utm_to_rdc
  if (-e $slc1.utm.sim_sar) rm -f $slc1.utm.sim_sar
  if (-e /clusterhome/msw13/PALSAR_data/DEMs/SRTM/$1\_utm.dem_par) rm -f
/clusterhome/msw13/PALSAR_data/DEMs/Landsat/$1\_utm.dem_par
  if (-e /clusterhome/msw13/PALSAR_data/DEMs/SRTM/$1\_utm.dem) rm -f
/clusterhome/msw13/PALSAR_data/DEMs/Landsat/$1\_utm.dem

# Use for SRTM
create_dem_par /clusterhome/msw13/PALSAR_data/DEMs/SRTM/$1\_utm.dem_par $slc1.mli.par - -$grd_rsp $grd_azsp <
/clusterhome/msw13/PALSAR_data/DEMs/SRTM/create_dem_par_utm
dem_trans /clusterhome/msw13/PALSAR_data/DEMs/SRTM/$1\_srtm_eqa.dem_par
/clusterhome/msw13/PALSAR_data/DEMs/SRTM/$1\_srtm_eqa.dem /clusterhome/msw13/PALSAR_data/DEMs/SRTM/$1\_utm.dem_par
/clusterhome/msw13/PALSAR_data/DEMs/SRTM/$1\_utm.dem

gc_map $slc1.mli.par - /clusterhome/msw13/PALSAR_data/DEMs/SRTM/$1\_utm.dem_par
/clusterhome/msw13/PALSAR_data/DEMs/SRTM/$1\_utm.dem $slc1.dem_par $slc1.dem $slc1.rough.utm_to_rdc - -
$slc1.utm.sim_sar

set dem_width = `awk '{if($1 == "width:" ) printf("%d", $2)}' < $3.dem_par` #gets dem width from dem_par file

  if (-e $slc1.sim_sar) rm -f $slc1.sim_sar
  geocode $slc1.rough.utm_to_rdc $slc1.utm.sim_sar $dem_width $slc1.sim_sar $image_width - 1 0
  if (-e $slc1.diff_par) rm -f $slc1.diff_par
  create_diff_par $slc1.mli.par - $slc1.diff_par 1 < /clusterhome/msw13/PALSAR_data/create_diff_par
  init_offsetm $slc1.mli $slc1.sim_sar $slc1.diff_par - - - - - - 2.5 > geocode_info
  if (-e $slc1.gc_offs) rm -f $slc1.gc_offs
  if (-e $slc1.gc_snr) rm -f $slc1.gc_snr
```

```
  if (-e $slc1.gc_offsets) rm -f $slc1.gc_offsets
  if (-e $slc1.gc_coffs) rm -f $slc1.gc_coffs
  if (-e $slc1.gc_coffsets) rm -f $slc1.gc_coffsets
  offset_pwrm $slc1.mli $slc1.sim_sar $slc1.diff_par $slc1.gc_offs $slc1.gc_snr 128 256 $slc1.gc_offsets 1 8 8 7.0
  offset_fitm $slc1.gc_offs $slc1.gc_snr $slc1.diff_par $slc1.gc_coffs $slc1.gc_coffsets 7.0 3
  if (-e $slc1.utm_to_rdcset) rm -f $slc1.utm_to_rdc
  gc_map_fine $slc1.rough.utm_to_rdc $dem_width $slc1.diff_par $slc1.utm_to_rdc 0
  if (-e $slc1_dir.cmli.utm_$grd_rsp\m_$pol) rm -f $slc1_dir.cmli.utm_$grd_rsp\m_$pol
  if ($slc2_dir != -) then
    if (-e $slc2_dir.cmli.utm_$grd_rsp\m_$pol) rm -f $slc2_dir.cmli.utm_$grd_rsp\m_$pol
    if (-e $slc1_dir\_$slc2_dir.cc.utm_$grd_rsp\m_$pol) rm -f $slc1\_$slc2.cc.utm_$grd_rsp\m_$pol
    endif
  geocode_back $slc1.cmli $image_width $slc1.utm_to_rdc $slc1_dir.cmli.utm_$grd_rsp\m_$pol $dem_width 0 3 0
  if ($slc2_dir != -) then
    geocode_back $slc2.cmli $image_width $slc1.utm_to_rdc $slc2_dir.cmli.utm_$grd_rsp\m_$pol $dem_width 0 3 0
    geocode_back $slc1\_$slc2.cc $image_width $slc1.utm_to_rdc $slc1_dir\_$slc2_dir.cc.utm_$grd_rsp\m_$pol
$dem_width 0 1 0
    endif
  if (-e $slc1_dir.cmli.utm_$grd_rsp\m_$pol.bmp) rm -f $slc1_dir.cmli.utm_$grd_rsp\m_$pol.bmp
  raspwr $slc1_dir.cmli.utm_$grd_rsp\m_$pol $dem_width 1 0 1 1 1.0 0.35 1 $slc1_dir.cmli.utm_$grd_rsp\m_$pol.bmp
  if ($slc2_dir != -) then
    if (-e $slc2_dir.cmli.utm_$grd_rsp\m_$pol.bmp) rm -f $slc2_dir.cmli.utm_$grd_rsp\m.bmp_$pol
    if (-e $slc1_dir\_$slc2_dir.cc.utm_$grd_rsp\m_$pol.bmp) rm -f $slc1_dir\_$slc2_dir.cc.utm_$grd_rsp\m_$pol.bmp
    raspwr $slc2_dir.cmli.utm_$grd_rsp\m_$pol $dem_width 1 0 1 1 1.0 0.35 1 $slc2_dir.cmli.utm_$grd_rsp\m_$pol.bmp
    ras_linear $slc1_dir\_$slc2_dir.cc.utm_$grd_rsp\m_$pol $dem_width 1 0 1 1 0.0 1.0 1
$slc1_dir\_$slc2_dir.cc.utm_$grd_rsp\m_$pol.bmp
    endif

  echo $dem_width
  endif


################################
##   Create ENVI header file   ##
################################
```

```
if($do_header) then

  set pixels = `awk '{if($1 == "width:" ) printf("%d", $2)}' < $slc1.dem_par`
  set lines = `awk '{if($1 == "nlines:" ) printf("%d", $2)}' < $slc1.dem_par`
  set ul_easting = `awk '{if($1 == "corner_east:" ) printf("%.3f", $2)}' < $slc1.dem_par`
  set ul_northing = `awk '{if($1 == "corner_north:" ) printf("%.3f", $2)}' < $slc1.dem_par`
  set pixel_size = `awk '{if($1 == "post_east:" ) printf("%.10f", $2)}' < $slc1.dem_par`
  set projection = `awk '{if($1 == "projection_name:" ) printf("%s", $2)}' < $slc1.dem_par`
  set utm_zone = `awk '{if($1 == "projection_zone:" ) printf("%d", $2)}' < $slc1.dem_par`

  set envi_hdr_file = $slc1_dir.hdr
  echo "ENVI" > $envi_hdr_file
  echo "description = {" >> $envi_hdr_file
  echo "  File Imported into ENVI. }" >> $envi_hdr_file
  echo "samples = $pixels" >> $envi_hdr_file
  echo "lines   = $lines" >> $envi_hdr_file
  echo "bands   = 1" >> $envi_hdr_file
  echo "header offset = 0" >> $envi_hdr_file
  echo "file type = ENVI Standard" >> $envi_hdr_file
  echo "data type = 4" >> $envi_hdr_file
  echo "interleave = bsq" >> $envi_hdr_file
  echo "sensor type = UNKNOWN" >> $envi_hdr_file
  echo "byte order = 1" >> $envi_hdr_file
  echo "map info = {$projection, 1.0000, 1.0000, $ul_easting, $ul_northing, $pixel_size, $pixel_size, $utm_zone,
$hemisphere, WGS-84, units=Meters}"  >> $envi_hdr_file
  echo "wavelength units = Unknown" >> $envi_hdr_file
  echo "band names = {" >> $envi_hdr_file
  echo " }" >> $envi_hdr_file

  cp $slc1_dir.hdr $slc1_dir.cmli.utm_$grd_rsp\m_$pol.hdr
  if ($slc2_dir != -) then
    cp $slc1_dir.hdr $slc2_dir.cmli.utm_$grd_rsp\m_$pol.hdr
    cp $slc1_dir.hdr $slc1_dir\_$slc2_dir.cc.utm_$grd_rsp\m_$pol.hdr
    endif
  rm -f $slc1_dir.hdr
  endif
```

```
####################################
##  Create Google Earth KML file   ##
####################################

if ($do_kml) then
   if (-e $slc1\.eqa_par) rm -f $slc1\.eqa_par
   if (-e $slc2\.eqa_par) rm -f $slc2\.eqa_par
   if (-e $slc1_dir.cmli.eqa_$grd_rsp\m_$pol.bmp) rm -f $slc1_dir.cmli.eqa_$grd_rsp\m_$pol.bmp
   if (-e $slc2_dir.cmli.eqa_$grd_rsp\m_$pol.bmp) rm -f $slc2_dir.cmli.eqa_$grd_rsp\m_$pol.bmp
   if (-e $slc1_dir\_$slc2_dir.cc.eqa_$grd_rsp\m_$pol.bmp) rm -f $slc1_dir\_$slc2_dir.cc.eqa_$grd_rsp\m_$pol.bmp
   if (-e $slc1_dir.cmli.eqa_$grd_rsp\m_$pol.bmp.kml) rm -f $slc1_dir.cmli.eqa_$grd_rsp\m_$pol.bmp.kml
   if (-e $slc2_dir.cmli.eqa_$grd_rsp\m_$pol.bmp.kml) rm -f $slc2_dir.cmli.eqa_$grd_rsp\m_$pol.bmp.kml
   if (-e $slc1_dir\_$slc2_dir.cc.eqa_$grd_rsp\m_$pol.kml) rm -f $slc1_dir\_$slc2_dir.cc.eqa_$grd_rsp\m_$pol.kml

  create_dem_par $slc1\.eqa_par $slc1\.cmli.par - -$grd_rsp $grd_rsp < /clusterhome/msw13/PALSAR_data/create_kml
  create_dem_par $slc2\.eqa_par $slc2\.cmli.par - -$grd_rsp $grd_rsp < /clusterhome/msw13/PALSAR_data/create_kml

  map_trans $slc1\_utm.dem_par $slc1_dir.cmli.utm_$grd_rsp\m_$pol.bmp $slc1\.eqa_par
$slc1_dir.cmli.eqa_$grd_rsp\m_$pol.bmp - - 0 2
  map_trans $slc1\_utm.dem_par $slc2_dir.cmli.utm_$grd_rsp\m_$pol.bmp $slc2\.eqa_par
$slc2_dir.cmli.eqa_$grd_rsp\m_$pol.bmp - - 0 2
  map_trans $slc1\_utm.dem_par $slc1_dir\_$slc2_dir.cc.utm_$grd_rsp\m_$pol.bmp $slc1\.eqa_par
$slc1_dir\_$slc2_dir.cc.eqa_$grd_rsp\m_$pol.bmp - - 0 2

  kml_map $slc1_dir.cmli.eqa_$grd_rsp\m_$pol.bmp $slc1\.eqa_par $slc1_dir.cmli.eqa_$grd_rsp\m_$pol.kml
  kml_map $slc2_dir.cmli.eqa_$grd_rsp\m_$pol.bmp $slc2\.eqa_par $slc2_dir.cmli.eqa_$grd_rsp\m_$pol.kml
  kml_map $slc1_dir\_$slc2_dir.cc.eqa_$grd_rsp\m_$pol.bmp $slc1\.eqa_par
$slc1_dir\_$slc2_dir.cc.eqa_$grd_rsp\m_$pol.kml
  endif


####################################
#      tidy up                     ##
####################################


if ($do_tidy_up) then
```

```
  rm -f $slc1.slc $slc2.slc $slc2.rslc $slc1.cslc $slc2.cslc
  if (!(-e processing_files)) mkdir processing_files
  mv *.cmli processing_files
  mv *.par processing_files
  mv *.dem processing_files
  mv *.gc* processing_files
  mv *.mli processing_files
  mv *.utm_to_rdc processing_files
  mv *.sim_sar processing_files
  mv *.base processing_files
  mv *.txt processing_files
  mv *.cc_* processing_files
  mv *.cc processing_files
  mv *.flt* processing_files
  mv *.int processing_files
  mv *.snr processing_files
  mv *.rmli processing_files
  mv *.off* processing_files
  mv *_flip.* processing_files
  mv *.coff* processing_files
  mv *.dem_par processing_files
  mv *.dem_seg processing_files
  mv *.diff_par processing_files
  mv *.img processing_files
#  mv *.par_file* processing files

  endif

cd ..
cd ..
chmod -R 755 *
```

## 8.2 IDL scripts

The following scripts perform multichannel filtering of a stack of radar images according to the method of Quegan & Yu (2001) in an IDL environment. The process is performed by a series of 5 scripts and a data input file and were provided by Martin Whittle of the Department of Applied Mathematics, University of Sheffield.

### 8.2.1 **mcf.data** contains information on the names and locations of input files and other input parameters.

```
D:\IDL\
2 2
20090916_FBD_442_7190_HH.mli
20090916_FBD_442_7190_HV.mli
meanRI

Line 1 is the directory
Line 2 contains the number of bands for processing and the window size
Last line is the name of the "meanRI" file
```

### 8.2.2 **mcf_start.pro** runs the sequence of scripts needed to perform the calculation

```
pro mcf_start

;** script file to run multi-channel filtering

; Note: load .hdr files as well as .mli files to directory
; these compilation need to be done manually at present:
;.run D:\IDL\mcf_IDL\mcf_start.pro
;.run D:\IDL\mcf_IDL\checkfiles.pro
;.run D:\IDL\mcf_IDL\meanRI.pro
;.run D:\IDL\mcf_IDL\mcf.pro
```

```
;.run D:\IDL\mcf_IDL\dropout.pro

; then type mcf_start at idl prompt

      checkfiles
      print, '** starting meanRI **'
      meanRI
      print, '** starting mcf **'
      mcf
      print, '** mcf terminated OK**'

end
```

### 8.2.3 **checkfiles.pro** checks the dimensions of all input files are identical (required in order to proceed)

```
pro checkfiles

; ! USES dropout.pro

; Checks compatability of files


ENVI, /RESTORE_BASE_SAVE_FILES
ENVI_BATCH_INIT

FORWARD_FUNCTION ENVI_OPEN_FILE, ENVI_FILE_QUERY, ENVI_SETUP_HEAD, ENVI_GET_DATA, ENVI_FILE_MNG

 text=''
 datadir=''
 filename = ''

; ***** read the file containing filenames ******

OPENR,1,'D:\IDL\mcf_IDL\mcf.data'

; OPENR,1,'runfile2'      ; i.e. from /home/sm1mw
```

```
print, 'Opened run file '

readf,1, datadir
print, 'data directory is:  ', datadir

readf,1, temp1, temp2
nband = fix(temp1)
w = fix(temp2)

win = 1 + w*2      ;  total window width

    print, '   *******  Number of bands: ', nband

   print, ''
   print, '****   MeanRI  weighted mean ****'
   print, 'window range w:   ', w
   print, 'window width win: ', win
   print, ''

    print, 'Input files: '

for k=1, nband do begin

  readf,1, text
  filename = datadir + text

  print, 'Band: ',k, ':   filename:  ', filename

   ENVI_OPEN_FILE, filename, R_FID=fid1, NO_REALIZE=1

   ENVI_FILE_QUERY, fid1, ns=M, nl=N, nb=nb, data_type=data_type, descrip=descrip, bnames=bnames, $
                    sensor_type=sensor_type, wavelength_units=wavelength_units ;, dims=dims


    print, '   Number of rows: ', N ,' Number of columns ', M

if( k EQ 1 ) then begin
```

```
  N0 = N
  M0 = M
endif

if( N NE N0) then  begin
 print, ' WARNING row number incompatible '
 stop, N, N0
endif

if( M NE M0) then  begin
 print, ' WARNING column number incompatible '
 stop, M, M0
endif

endfor

descrip=descrip+ 'average of two files'

dims=[-1,0,M-1,0,N-1]

; *************    read output files ***********

  readf,1, text
  outfile = datadir + text

  print, ''
  print, k, ':   output file is:  ', outfile

ENVI_SETUP_HEAD, fname=outfile, ns=M, nl=N, nb=nb, data_type=data_type, offset=0, interleave=0, $
                 xstart=0, ystart=0, descrip=descrip, bnames=bnames, sensor_type=sensor_type, $
                 wavelength_units=wavelength_units, /write

openw, lun, outfile, /get_lun


close, 1
```

```
end
```

### 8.2.4 **meanRI.pro** calculates image isolating radar 'speckle'.

```
pro meanRI

; ! USES dropout.pro

; Computes the "meanRI" weighted mean central to multi channel filtering
; w is the window range and should be > 0


ENVI, /RESTORE_BASE_SAVE_FILES
ENVI_BATCH_INIT

FORWARD_FUNCTION ENVI_OPEN_FILE, ENVI_FILE_QUERY, ENVI_SETUP_HEAD, ENVI_GET_DATA, ENVI_FILE_MNG

 text=''
 datadir=''
 filename = ''

; ***** read the file containing filenames ******

OPENR,1,'D:\IDL\mcf_IDL\mcf.data'

; OPENR,1,'runfile2'      ; i.e. from /home/sm1mw

print, 'Opened run file '

readf,1, datadir
print, 'data directory is:  ', datadir

readf,1, temp1, temp2
nband = fix(temp1)
w = fix(temp2)

win = 1 + w*2      ;  total window width
```

```
    print, '   *******  Number of bands: ', nband

   print, ''
   print, '****   MeanRI  weighted mean ****'
   print, 'window range w:   ', w
   print, 'window width win: ', win
   print, ''

; *************    read input files ***********

for k=1, nband do begin

  readf,1, text
  filename = datadir + text

  print, k, ':   filename is:  ', filename

   ENVI_OPEN_FILE, filename, R_FID=fid1, NO_REALIZE=1

   ENVI_FILE_QUERY, fid1, ns=M, nl=N, nb=nb, data_type=data_type, descrip=descrip, bnames=bnames, $
                    sensor_type=sensor_type, wavelength_units=wavelength_units ;, dims=dims


if (k eq 1) then begin                ; definitions obtained from first band only: others assumed the same
   indata = FLTARR(M,N)
   meanRI = FLTARR(M,N)
   mask = FLTARR(M,N)
   dims=[-1,0,M-1,0,N-1]
   print, 'Number of samples: ', nb
                                  ; *** initialize mask
    for i=0,N-1 do begin          ; *** on rows
        for j=0,M-1 do begin       ; *** on columns
          mask(j,i) = 1.0
        endfor
    endfor
```

```
endif

    print, 'Progress meanRI - band number: ', k
    print, 'Number of rows: ', N ,' Number of columns ', M
   dropcount = 0

    indata=ENVI_GET_DATA(FID=fid1, POS=0, DIMS=dims)

                                        ; ******* Average over window ******
    dropcount = 0

    for i=0,N-1 do begin          ; *** on rows

         i1 = i - w
         i2 = i + w

            if(i1 LT 0) then begin          ; ****** Boundary conditions for rows ******
              i1 = 0
            endif

            if(i2 GT N-1) then begin
              i2 = N-1
            endif

           if ( (i mod 100) eq 0) then begin
              print, 'Progress meanRI- band ',k,' of ',nband,'  row number: ', i
           endif


        for j=0,M-1 do begin       ; *** on columns

if( indata(j, i) EQ 0.0 ) then begin       ;****** repair any dropouts *****

   dropout, indata, M, N, i, j, flag

   if( flag EQ 0) then begin               ;***** if it wasn't a dropout
     mask(j,i) = 0                         ;***** compile union mask from all images
```

```
   endif else begin
     dropcount = dropcount + flag
   endelse

endif

          j1 = j - w
          j2 = j + w

            if(j1 LT 0) then begin         ; ****** Boundary conditions for columns ******
              j1 = 0
            endif

            if(j2 GT M-1) then begin
              j2 = M-1
            endif

            s=0
            c=0

            for i0 = i1,i2 do begin ; on rows

                for j0 = j1,j2 do begin ; on columns

                    c = c + 1
                    s = s + indata(j0,i0)

                endfor

            endfor

            a=float(s)/float(c)        ; ****** normalised window average for pixel (j,i)

 ;           average(j,i)=a   ----- not needed
```

```
            if (a EQ 0.0) then begin

                tmpdata = indata(j,i)

            endif else begin

                tmpdata = indata(j,i)/a

            endelse

            meanRI(j,i) = meanRI(j,i) + tmpdata    ;*** Accumulate meanRI ****

         endfor

      endfor

     print, '** drop count =  ', dropcount

endfor


     print, '** Progress - union masking and normalising the result ** '

      for i=0, N-1 do begin

         if ( (i mod 1000) eq 0) then begin
            print, 'Progress - row number: ', i
         endif

         for j=0, M-1 do begin
            meanRI(j,i) = mask(j,i)*meanRI(j,i)/float(nband)
         endfor
      endfor


descrip=descrip+ 'meanRI'
```

```
; *************    read output files ***********

  readf,1, text
  outfile = datadir + text
  print, k, ':   output file is:  ', outfile

ENVI_SETUP_HEAD, fname=outfile, ns=M, nl=N, nb=nb, data_type=data_type, offset=0, interleave=0, $
                 xstart=0, ystart=0, descrip=descrip, bnames=bnames, sensor_type=sensor_type, $
                 wavelength_units=wavelength_units, /write

openw, lun, outfile, /get_lun

       writeu, lun, meanRI
       print, '** output data written **'

free_lun, lun
ENVI_FILE_MNG, id=fid1, /remove
close, 1

      print, '** meanRI terminated **'


end
```

### 8.2.5 **mcf.pro** removes isolated speckle from each of the input images.

```
pro mcf

; ! USES dropout.pro

; Multi-channel filtering using previously computed meanRI
; w is the window range and should be > 0 - this must be the same as used for meanRI

ENVI, /RESTORE_BASE_SAVE_FILES
ENVI_BATCH_INIT
```

```
FORWARD_FUNCTION ENVI_OPEN_FILE, ENVI_FILE_QUERY, ENVI_SETUP_HEAD, ENVI_GET_DATA, ENVI_FILE_MNG

 text=''
 datadir=''
 inpfile = ''
 outfile = ''

; ***** read the file containing filenames ******

OPENR,1,'D:\IDL\mcf_IDL\mcf.data'

; OPENR,1,'runfile2'      ; i.e. from /home/sm1mw

print, 'Opened data file '

readf,1, datadir
print, 'data directory is:  ', datadir

readf,1, temp1, temp2
nband = fix(temp1)
w = fix(temp2)
win = 1 + w*2      ;  total window width

    print, '   *******  Number of bands: ', nband

   print, ''
   print, '****   Multi-channel filtering ****'
   print, 'window range w:   ', w
   print, 'window width win: ', win
   print, ''

; ******* read the meanRI file **********

  inpfile = datadir + 'meanRI'
  print,' input filename is:  ', inpfile
```

```
   ENVI_OPEN_FILE, inpfile, R_FID=fid1, NO_REALIZE=1

   ENVI_FILE_QUERY, fid1, ns=M, nl=N, nb=nb, data_type=data_type, descrip=descrip, bnames=bnames, $
                       sensor_type=sensor_type, wavelength_units=wavelength_units

   indata = FLTARR(M,N)
   outdata = FLTARR(M,N)
   meanRI=FLTARR(M,N)
   dims=[-1,0,M-1,0,N-1]

   meanRI = ENVI_GET_DATA(FID=fid1, POS=0, DIMS=dims)

; *************    read input files ***********

for k=1, nband do begin

  readf,1, text
  inpfile = datadir + text

  print, k, ' input filename is:  ', inpfile

   ENVI_OPEN_FILE, inpfile, R_FID=fid1, NO_REALIZE=1

   ENVI_FILE_QUERY, fid1, ns=M, nl=N, nb=nb, data_type=data_type, descrip=descrip, bnames=bnames, $
                       sensor_type=sensor_type, wavelength_units=wavelength_units


if (k eq 1) then begin                ; definitions obtained from first band only: others assumed the same
   print, 'Number of samples: ', nb
endif

    print, 'Progress mcf- band number: ', k
    print, 'Number of rows: ', N ,' Number of columns ', M

    indata=ENVI_GET_DATA(FID=fid1, POS=0, DIMS=dims)

                                       ; ******* Average over window ******
```

```
    dropcount = 0

    for i=0,N-1 do begin          ; *** on rows

         i1 = i - w
         i2 = i + w

            if(i1 LT 0) then begin          ; ****** Boundary conditions for rows ******
              i1 = 0
            endif

            if(i2 GT N-1) then begin
              i2 = N-1
            endif

           if ( (i mod 100) eq 0) then begin
               print, 'Progress mcf- band ',k,' of ',nband,'  row number: ', i
           endif


        for j=0,M-1 do begin       ; *** on columns

if( indata(j, i) EQ 0.0 ) then begin       ;****** repair any dropouts *****

   dropout, indata, M, N, i, j, flag
   dropcount = dropcount + flag

endif

          j1 = j - w
          j2 = j + w

            if(j1 LT 0) then begin         ; ****** Boundary conditions for columns ******
              j1 = 0
            endif

            if(j2 GT M-1) then begin
```

```
              j2 = M-1
            endif

            s=0
            c=0

            for i0 = i1,i2 do begin ; on rows

                for j0 = j1,j2 do begin ; on columns

                    c = c + 1
                    s = s + indata(j0,i0)

                endfor

            endfor

            a=float(s)/float(c)        ; ****** normalised window average for pixel (j,i)

                outdata(j,i) = a*meanRI(j,i)            ; **** construct the mcf image ******

        endfor

      endfor

   print, '** drop count =  ', dropcount

; **** setup output file ******

  descrip=descrip+ 'mcf of files'
  outfile = inpfile + '.mcf'
  print, k, ':   output filename is:  ', outfile

  ENVI_SETUP_HEAD, fname=outfile, ns=M, nl=N, nb=nb, data_type=data_type, offset=0, interleave=0, $
                xstart=0, ystart=0, descrip=descrip, bnames=bnames, sensor_type=sensor_type, $
                wavelength_units=wavelength_units, /write
```

```
   openw, lun, outfile, /get_lun
   writeu, lun, outdata
   print, '** output data written **'
   free_lun, lun

endfor

  print, 'cycles ended OK '

ENVI_FILE_MNG, id=fid1, /remove
close, 1

end
```

### 8.2.6 **dropout.pro** is required by all the other IDL files for dealing with any missing values.

```
pro dropout, img, M, N, i, j, flag

; finds drop outs in the image file "img" and replaces them with
; a local average.  Also seta flag for counting


flag = 0

         i1 = i - 1
         i2 = i + 1

            if(i1 LT 0) then begin          ; ****** Boundary conditions for rows ******
              i1 = 0
            endif

            if(i2 GT N-1) then begin
              i2 = N-1
            endif
```

```
          j1 = j - 1
          j2 = j + 1

            if(j1 LT 0) then begin          ; ****** Boundary conditions for columns ******
              j1 = 0
            endif

            if(j2 GT M-1) then begin
              j2 = M-1
            endif


            c = 0
            s = 0

            for i0 = i1,i2 do begin ; on rows

              for j0 = j1,j2 do begin ; on columns

                if( img(j0, i0) GT 0.0 ) then begin
                   c = c + 1
                   s = s + img(j0,i0)
                endif

              endfor

            endfor

          if( c GT 6 ) then begin              ; if c is <= 6 img(j,i) is probably on the edge or out of the image
            img(j,i) = float(s) / float(c)     ; if c > 6 repair the drop
            flag = 1
          endif
end
```

## 8.3 MATLab scripts

The following files are used for the calculation of temporal mean standard deviation from a stack of input images and for the calculation Empirical Orthogonal functions.

### 8.3.1 **ENVIread.m** reads ENVI data files into MATLab. ENVIread and ENVIwrite were written by Ian Howat http://www.mathworks.co.uk/matlabcentral/fileexchange/15629-envi-file-reader-updated-292010 and modified by Martin Whittle.

```
function [varargout] = enviread(varargin)
% ENVIREAD Easily import ENVI raster files (BSQ,BIL,BIP) from header info.
%   Z = ENVIREAD(FILENAME); Reads an ENVI binary file (BSQ,BIL,BIP) into
%       an array using the information from the corresponding header
%       file FILENAME.hdr. The output array will be of dimensions
%       (m,n,b) where b is the number of bands.
%   Z = ENVIREAD(FILENAME,HEADERFILE); Uses the header information in
%       headerfile.
%   [Z,X,Y] = ENVIREAD(....); Returns the map coordinate vectors for geo-
%       registered data.
%   [Z,X,Y,info] = ENVIREAD(....); Returns the header information as a
%       structure.
%
%   NOTES:  -Requires READ_ENVIHDR to read header data.
%          -Geo-registration does not currently support rotated images.
%
%  Typical usage:
%  a(:,:,1) =
enviread('/data/sm1mw/SAR/Scene1_mcf/20070131.hh.R.mli.mcf','/data/sm1mw/SAR/Scene1_mcf/20070131.hh.R.mli.mcf.hdr');
%
% Ian M. Howat, Applied Physics Lab, University of Washington
% ihowat@apl.washington.edu
% Version 1: 11-Jul-2007 15:11:13
% Martin Whittle 2009 - minor modification added to recover original orientation
```

```
%
%  Typical usage:
%  a(:,:,1) =
enviread('F:\PALSAR_FBD_RECALIB\kalimantan_proc\FBD_421_utm50S_25m_HH_mcf_db','F:\PALSAR_FBD_RECALIB\kalimantan_proc
\FBD_421_utm50S_25m_HH_mcf_db.hdr');


%% check for header reader
if exist('read_envihdr.m','file') == 0
    error('This function requires READ_ENVIHDR.m')
end
%% READ HEADER INFO
% Read Filename
file = varargin{1};
hdrfile = [file,'.hdr'];
if nargin == 2
    hdrfile = varargin{2};
end
% Get image size and map data from header
info = read_envihdr(hdrfile);
%% Make geo-location vectors
if isfield(info.map_info,'mapx') && isfield(info.map_info,'mapy')
    xi = info.map_info.image_coords(1);
    yi = info.map_info.image_coords(2);
    xm = info.map_info.mapx;
    ym = info.map_info.mapy;
    %adjust points to corner (1.5,1.5)
    if yi > 1.5
       ym =  ym + ((yi*info.map_info.dy)-info.map_info.dy);
    end
    if xi > 1.5
        xm = xm - ((xi*info.map_info.dy)-info.map_info.dx)
    end

    varargout{2} = xm + ((0:info.samples-1).*info.map_info.dx);
    varargout{3} = fliplr(ym - ((0:info.lines-1).*info.map_info.dy));
end
```

```
%% Set binary format parameters
switch info.byte_order
    case {0}
        machine = 'ieee-le';
    case {1}
        machine = 'ieee-be';
    otherwise
        machine = 'n';
end
switch info.data_type
    case {1}
        format = 'int8';
    case {2}
        format= 'int16';
    case{3}
        format= 'int32';
    case {4}
        format= 'float';
    case {5}
        format= 'double';
    case {6}
        disp('>> Sorry, Complex (2x32 bits)data currently not supported');
        disp('>> Importing as double-precision instead');
        format= 'double';
case {9}
        error('Sorry, double-precision complex (2x64 bits) data currently not supported');
case {12}
        format= 'uint16';
case {13}
        format= 'uint32';
case {14}
         format= 'int64';
case {15}
        format= 'uint64';
    otherwise
        error(['File type number: ',num2str(dtype),' not supported']);
end
```

```
%% Read File
Z = fread(fopen(file),info.samples*info.lines*info.bands,format,0,machine); fclose all;
switch lower(info.interleave)
    case {'bsq'}
        Z = reshape(Z,[info.samples,info.lines,info.bands]);
        for k = 1:info.bands;
            tmp(:,:,k) = rot90(Z(:,:,k));
        end
    case {'bil'}
        Z = reshape(Z,[info.samples,info.lines*info.bands]);
        for k=1:info.bands
            tmp(:,:,k) = rot90(Z(:,k:info.bands:end));
        end
    case {'bip'}
        tmp = zeros(info.lines,info.samples);
        for k=1:info.bands
            tmp1 = Z(k:info.bands:end);
            tmp(:,:,k) = rot90(reshape(tmp1,[info.samples,info.lines]));
        end
end

[imax, jmax, kmax] = size(tmp);
Z = tmp;
for k = 1:kmax
  Z(:,:,k) = rot90(tmp(:,:,k)');        % modification to recover orientation of original (MW)
end

varargout{1} = Z;
varargout{4} = info;

read_envihdr.m  is required by envriread.m

function [varargout] = enviread(varargin)
% ENVIREAD Easily import ENVI raster files (BSQ,BIL,BIP) from header info.
%   Z = ENVIREAD(FILENAME); Reads an ENVI binary file (BSQ,BIL,BIP) into
%       an array using the information from the corresponding header
%       file FILENAME.hdr. The output array will be of dimensions
```

```
%       (m,n,b) where b is the number of bands.
%   Z = ENVIREAD(FILENAME,HEADERFILE); Uses the header information in
%       headerfile.
%   [Z,X,Y] = ENVIREAD(....); Returns the map coordinate vectors for geo-
%       registered data.
%   [Z,X,Y,info] = ENVIREAD(....); Returns the header information as a
%       structure.
%
%   NOTES:  -Requires READ_ENVIHDR to read header data.
%           -Geo-registration does not currently support rotated images.
%
%  Typical usage:
%  a(:,:,1) =
enviread('/data/sm1mw/SAR/Scene1_mcf/20070131.hh.R.mli.mcf','/data/sm1mw/SAR/Scene1_mcf/20070131.hh.R.mli.mcf.hdr');
%
% Ian M. Howat, Applied Physics Lab, University of Washington
% ihowat@apl.washington.edu
% Version 1: 11-Jul-2007 15:11:13
% Martin Whittle 2009 - minor modification added to recover original orientation
%
%  Typical usage:
%  a(:,:,1) =
enviread('F:\PALSAR_FBD_RECALIB\kalimantan_proc\FBD_421_utm50S_25m_HH_mcf_db','F:\PALSAR_FBD_RECALIB\kalimantan_proc
\FBD_421_utm50S_25m_HH_mcf_db.hdr');


%% check for header reader
if exist('read_envihdr.m','file') == 0
    error('This function requires READ_ENVIHDR.m')
end
%% READ HEADER INFO
% Read Filename
file = varargin{1};
hdrfile = [file,'.hdr'];
if nargin == 2
    hdrfile = varargin{2};
end
```

```
% Get image size and map data from header
info = read_envihdr(hdrfile);
%% Make geo-location vectors
if isfield(info.map_info,'mapx') && isfield(info.map_info,'mapy')
    xi = info.map_info.image_coords(1);
    yi = info.map_info.image_coords(2);
    xm = info.map_info.mapx;
    ym = info.map_info.mapy;
    %adjust points to corner (1.5,1.5)
    if yi > 1.5
       ym =  ym + ((yi*info.map_info.dy)-info.map_info.dy);
    end
    if xi > 1.5
        xm = xm - ((xi*info.map_info.dy)-info.map_info.dx)
    end

    varargout{2} = xm + ((0:info.samples-1).*info.map_info.dx);
    varargout{3} = fliplr(ym - ((0:info.lines-1).*info.map_info.dy));
end
%% Set binary format parameters
switch info.byte_order
    case {0}
        machine = 'ieee-le';
    case {1}
        machine = 'ieee-be';
    otherwise
        machine = 'n';
end
switch info.data_type
    case {1}
        format = 'int8';
    case {2}
        format= 'int16';
    case{3}
        format= 'int32';
    case {4}
        format= 'float';
```

```
    case {5}
        format= 'double';
    case {6}
        disp('>> Sorry, Complex (2x32 bits)data currently not supported');
        disp('>> Importing as double-precision instead');
        format= 'double';
case {9}
        error('Sorry, double-precision complex (2x64 bits) data currently not supported');
case {12}
        format= 'uint16';
case {13}
        format= 'uint32';
case {14}
         format= 'int64';
case {15}
        format= 'uint64';
    otherwise
        error(['File type number: ',num2str(dtype),' not supported']);
end
%% Read File
Z = fread(fopen(file),info.samples*info.lines*info.bands,format,0,machine); fclose all;
switch lower(info.interleave)
    case {'bsq'}
        Z = reshape(Z,[info.samples,info.lines,info.bands]);
        for k = 1:info.bands;
            tmp(:,:,k) = rot90(Z(:,:,k));
        end
    case {'bil'}
        Z = reshape(Z,[info.samples,info.lines*info.bands]);
        for k=1:info.bands
            tmp(:,:,k) = rot90(Z(:,k:info.bands:end));
        end
    case {'bip'}
        tmp = zeros(info.lines,info.samples);
        for k=1:info.bands
            tmp1 = Z(k:info.bands:end);
            tmp(:,:,k) = rot90(reshape(tmp1,[info.samples,info.lines]));
```

```
        end
end

[imax, jmax, kmax] = size(tmp);
Z = tmp;
for k = 1:kmax
  Z(:,:,k) = rot90(tmp(:,:,k)');        % modification to recover orientation of original (MW)
end

varargout{1} = Z;
varargout{4} = info;
```

### 8.3.2 **mean_SD_calc.m** calculated the temporal mean and temporal standard deviation of a stacked input image. Written by Matthew Waldram.

```
disp ('reading data from file')
tic;
a(:,:,:) = enviread('D:\Kali_subs\421_HH_sub','D:\Kali_subs\421_HH_sub.hdr');
disp('**files read**')
disp(toc)
[imax,jmax,kmax] = size (a);
M = zeros(imax,jmax,1);
S = zeros(imax,jmax,1);

disp ('calculating temporal StDev')
tic

for iy=1:imax
  for ix=1:jmax
       s = a(iy,ix,:);
       S(iy,ix) = std(s);
  end % for
end %for
```

```
disp(toc)
disp ('calculating temporal Mean')
tic

for iy=1:imax
  for ix=1:jmax
      m = a(iy,ix,:);
       M(iy,ix) = mean(m);
  end % for
end %for

disp(toc)

disp('writing temporal StDev ENVI file')
tic
enviwrite(S, 'D:\Kali_subs\sd');
disp(toc)

disp('writing temporal mean ENVI file')
tic
enviwrite(M, 'D:\Kali_subs\mean');
disp(toc)
disp ('Process finsished')
```

### 8.3.3 **map2mat.m** Converts data in map co-ordinates to data in columns. Written by Guillame Maze and available at http://www.mathworks.co.uk/matlabcentral/fileexchange/17915-pcatool

```
% D = MAP2MAT(F,C) Reshaping matrix
%
% => Conversion of a 'map' matrix C(TIME,LON,LAT) into a D(TIME,PT) matrix
% under the mask F(LON,LAT).
% F is a matrix contenaing 1 where you would like to keep the point and
%  0 elsewhere.
%
```

```
% Rq: No check is done about the input.
%
% See also: mat2map
%=============================================================

% March 2004
% gmaze@univ-brest.fr

function [D] = map2mat(F,C);

% Get dimensions
[tps nolon nolat] = size(C);

% So output matrix will be:
D = zeros(tps,nolon*nolat);

% point indice
ipt = 0;

% 'Un-mapping' :
for iy=1:nolat
  for ix=1:nolon
      if F(ix,iy)>0
         ipt = ipt + 1;
         D(:,ipt)=squeeze(C(:,ix,iy));
      end % if
  end % for
end %for

% OUTPUT:
D = squeeze(D(:,1:ipt));
```

### 8.3.4 **caleof.m** calculates Empirical Orthogonal Functions. Written by Guillaume Maze and available from http://www.mathworks.co.uk/matlabcentral/fileexchange/17915-pcatool

```
% [EOFs,PC,EXPVAR] = CALEOF(M,N,METHOD) Compute EOF
%
% => Compute the Nth first EOFs of matrix M(TIME,MAP).
% EOFs is a matrix of the form EOFs(N,MAP), PC is the principal
% components matrix ie it has the form PC(N,TIME) and EXPVAR is
% the fraction of total variance "explained" by each EOF ie it has
% the form EXPVAR(N).
% Differents method can be used:
% 1 - The "classic" one, ie we compute eigenvectors of the
%     temporal covariance matrix with the eig Matlab function.
% 2 - A faster "classic" one, same as method 1 but we use the
%     eigs Matlab function.
% 3 - We compute eigenvectors by the singular value decomposition,
%     by used of the svd Matlab function.
% 4 - Same as method 3 but faster by used of the svds Matlab function
%
% See also EIG, EIGS, SVD, SVDS
%
% Ref: L. Hartmann: "Objective Analysis" 2002
% Ref: H. Bjornson and S.A. Venegas: "A manual for EOF and SVD -
%      Analyses of climatic Data" 1997
%=================================================================

%  Guillaume MAZE - LPO/LMD - March 2004
%  Revised July 2006
%  gmaze@univ-brest.fr


function [e,pc,expvar,L] = caleof(M,N,method);

% Get dimensions
[n p]=size(M);
```

```
% Temporal covariance is p*p matrix, that why max EOF computable is p,
% so we perform a test on parameter N:
if(N>p)
 disp('Warning: N is larger than possible so it''s modified to perform')
 disp('         EOFs computing...');
 N = p;
end


% Eventualy time filtering of data
if 0==1
   disp('====> Time filtering...')
   Fc  = 1/20; Fc2 = 1/1;
   Fc  = 1/7 ; Fc2 = 1/3;
   SIGNAL = M(:,1);
   nj = fix(length(SIGNAL)/10); % Nombre de points du filtre
   for ipt = 1 : p
       SIGNAL = M(:,ipt);
       SIGNALF = lanczos(SIGNAL,Fc2,nj);
       SIGNALF = SIGNALF - lanczos(SIGNALF,Fc,nj);
       Y(:,ipt) = SIGNALF;
   end
   M = Y;
end


disp('====> Let''go for EOFs and pc computing...')
switch method
    case 1 % CLASSIC METHOD
%=================================================================
% Transform the data matrix in the correct form (map*time) for eig
M = M';

% Remove the time mean (ie the mean of each rows of M)
% Rq: detrend remove the mean of columns ie we take M'.
F = detrend(M','constant')';
```

```
% Covariance Matrix (inner product over space = covariance in time)
R = F * F';

% Eigenanalysis of the covariance matrix R
[E,L] = eig(R);

% Get PC by projecting eigenvectors on original data
Z = E'*F;

% Make them clear for output
for iN=1:N
    e(iN,:) = squeeze( E(:,p-(iN-1)) )';
   pc(iN,:) = squeeze( Z(p-(iN-1),:) );
end

% Amount of explained variance (at 0.1%)
dsum = diag(L)./trace(L);
for iN=1:N
   expvar(iN)=fix((dsum(p-(iN-1))*100/sum(dsum))*10)/10;
end

% Plots Original field and reconstructed one
if 0==1
figure;
subplot(1,2,1);imagesc(abs(M));title('ORIGINAL');cx=caxis;
%subplot(1,2,2);imagesc((E*Z));title('RECONSTRUCTED')
subplot(1,2,2);imagesc(abs(e'*pc));title('RECONSTRUCTED');caxis(cx);
end

    case 2 % RAPID CLASSIC METHOD
%=============================================================
% Remove the time mean of each column
F = detrend(M,'constant');

% Covariance Matrix
if n >= p
   R = F' * F;
```

```
else
   R = F * F';
end

% Eigen analysis of the square covariance matrix
[E,L] = eigs(R,N);
if n < p
  E = F' * E;
  sq = [sqrt(diag(L))+eps]';
  sq = sq(ones(1,p),:);
  E = E ./ sq;
end

% Get PC by projecting eigenvectors on original data
if n >= p
   Z = (F*E)';
else
   Z =  E'*F';
end


% Make them clear for output
for iN=1:N
    e(iN,:) = squeeze( E(:,iN) )';
   pc(iN,:) = squeeze( Z(iN,:) );
end

% Amount of variance explained a 0.1 pres et en %
dsum=diag(L)./trace(L);
for iN=1:N
   expvar(iN)=fix((dsum(iN)*100/sum(dsum))*10)/10;
end


    case 3 % SVD METHOD
%=================================================================
% Ref: H. Bjornson and S.A. Venegas: "A manual for EOF and SVD -
```

```
% Analyses of climatic Data" 1997 => p18

% Assume that M is (time*map) matrix
[n p]=size(M);

% Remove the mean of each column (ie the time mean in each station records)
F=detrend(M,'constant');

% Form the covariance matrix:
R = F'*F;

% Find eigenvectors and singular values
[C,L,CC] = svd(R);
% Eigenvectors are in CC and the squared diagonal values of L
% are the eigenvalues of the temporal covariance matrix R=F'*F

% find the PC corresponding to eigenvalue
PC = F*CC;

% Make them clear for output
for iN=1:N
    e(iN,:) = squeeze( CC(:,iN) )';
   pc(iN,:) = squeeze( PC(:,iN) )';
end

if 0
figure;
subplot(1,2,1);imagesc(F);title('ORIGINAL');cx=caxis;
subplot(1,2,2);imagesc(C*L*CC');title('RECONSTRUCTED');caxis(cx);
end

% Amount of variance explained at 0.1%
dsum=diag(L)./trace(L);
if length(dsum)<N % L was not squared
  dsum = [dsum ;zeros(N-length(dsum),1)];
end
for iN = 1 : N
```

```
   expvar(iN)=fix( ( dsum(iN)*100/sum(dsum) )*10 ) /10;
end


    case 4 % FAST SVD METHOD
%=================================================================
% Ref: H. Bjornson and S.A. Venegas: "A manual for EOF and SVD -
% Analyses of climatic Data" 1997 => p18

% Assume that M is (time*map) matrix
[n p]=size(M);

% Remove the mean of each column (ie the time mean in each station records)
F=detrend(M,'constant');

% Form the covariance matrix:
R = F' * F;

% Find eigenvectors and singular values
[C,L,CC,flag] = svds(R,N);
% Eigenvectors are in CC and the squared diagonal values of L
% are the eigenvalues of the temporal covariance matrix R=F'*F
% (Sometimes, CC stops for nul eigenvector, then we need to fill to reach N)
if size(CC,2)<N
  CC = [CC  zeros(size(CC,1),N-size(CC,2)+1)];
end

% find the PC corresponding to eigenvalue
PC = F*CC;
% Which is similar to: C*L

% Make them clear for output
for iN=1:N
    e(iN,:) = squeeze( CC(:,iN) )';
   pc(iN,:) = squeeze( PC(:,iN) )';
end
```

```
% Amount of variance explained a 0.1 pres et en %
dsum=diag(L)./trace(L);
if length(dsum)<N % L was not squared
  dsum = [dsum ;zeros(N-length(dsum),1)];
end
for iN=1:N
   expvar(iN)=fix( ( dsum(iN)*100/sum(dsum) )*10 ) /10;
end

%figure;
%subplot(1,2,1);imagesc(M);title('ORIGINAL');cx=caxis;
%subplot(1,2,2);imagesc((e'*pc)');title('RECONSTRUCTED');caxis(cx);


end % switch method
disp('====> Finished !')
```

### 8.3.5 **mat2map.m** converts data in columns (i.e. EOF output) to data in map co-ordinates. Written by Guillaume Maze and available from http://www.mathworks.co.uk/matlabcentral/fileexchange/17915-pcatool

```
% C = MAP2MAT(F,D) Reshaping matrix
%
% => Creation of a 'map' matrix C(TIME,LON,LAT) from D(TIME,PT)
% following mask F(LON,LAT).
% F is a matrix contenaing 1 where you would like to keep the point and
%  0 elsewhere (see mat2map).
%
% Rq: No check is done about the input.
%
% See also: map2mat
%=================================================================

% March 2004
```

```
% gmaze@univ-brest.fr

function [C] = mat2map(F,D);

% Get dimensions
[nolon nolat] = size(F);
[time npt] = size(D);

% So output 'map' matrix has the form:
C = zeros(time,nolon,nolat);

% Variables
nul = NaN.*ones(time,1);
ipt = 0 ;


% 'mapping' :
  for iy=1:nolat
      for ix=1:nolon
         if F(ix,iy)>0
            ipt = ipt + 1;
            C(:,ix,iy) = D(:,ipt);
         else
            C(:,ix,iy) = nul;
         end %if
      end %for ix
  end %for iy
```

8.3.6 **enviwrite.m** creates an ENVI file from an internal MATLab matrix. Written by Vincent Guissard and available at http://www.mathworks.co.uk/matlabcentral/fileexchange/4919-matlab-to-envi/content/enviwrite.m modified by Martin Whittle.

```
function i=enviwrite(image,fname)
```

```
% enviwrite             - write ENVI image from MATLAB array (V. Guissard, Apr 29 2004)
%       MODIFIED by M. Whittle.  Jan 2009 to rotate image and correct
%       orientation
%       and April 2009 to accept single bands
%
% *** NOTES : When diplaying in Envi some images (particularly masks) ****
% *** require the use of enhance/linear scaling to display properly   ****
% *** This may apply if only one channel is visible                   ****
% *** The .hdr is also generated and needs to be transferred to the   ****
% *** same directory as the .env file.   This will not contain        ****
% *** geographic information which need to be obtianed from another   ****
% *** file.  However, it is best to do this manually rather than      ****
% *** using "udating attributes" from anothe file                     ****
%
%                       Write a MATLAB array to a file in ENVI standard format
%                       from a [col x line x band] array
%
% SYNTAX:
%
%  i = enviwrite(temp, 'filename');
%  where temp(:,:,3) is a MATLAB array
%
% image=freadenvi(fname)
% [image,p]=freadenvi(fname)
% [image,p,t]=freadenvi(fname)
%
% INPUT :
%
%
% image     c by l by b name of the MATLAB variable containing the array to export
%                       to an ENVI image, with c = cols, l the lines and b the bands
% fname     string      full pathname of the ENVI image to write.
%
% OUTPUT :
%
% i         integer     i = -1 if process fail
%
```

```
%
%
%%%%%%%%%%%%

% Parameters initialization
i=0;

im_size=size(image);
im_size(3)=size(image,3);

Z = zeros(im_size(2), im_size(1), im_size(3));     %Transpose image
for(k = 1: im_size(3))
Z(:,:,k) = image(:,:,k)';
end

image=Z;

im_size=size(image);
im_size(3)=size(image,3);

elements={'samples =' 'lines   =' 'bands   =' 'data type ='};
d=[4 1 2 3 12 13];
% Check user input
if ~ischar(fname)
    error('fname should be a char string');
end

cl1=class(image);
if cl1 == 'double'
    img=single(image);
else
    img=image;
end

cl=class(img);
switch cl
```

```
    case 'single'
        t = d(1);
    case 'int8'
        t = d(2);
    case 'int16'
        t = d(3);
    case 'int32'
        t = d(4);
    case 'uint16'
        t = d(6);
    case 'uint32'
        t = d(7);
    otherwise
        error('Data type not recognized');
end
wfid = fopen(fname,'w');
if wfid == -1
    i=-1;
end
disp([('Writing ENVI image ...')]);
fwrite(wfid,img,cl);
fclose(wfid);

% Write header file

fid = fopen(strcat(fname,'.hdr'),'w');
if fid == -1
    i=-1;
end

fprintf(fid,'%s \n','ENVI');
fprintf(fid,'%s \n','description = {');
fprintf(fid,'%s \n','Exported from MATLAB}');
fprintf(fid,'%s %i \n',elements{1,1},im_size(1));
fprintf(fid,'%s %i \n',elements{1,2},im_size(2));
fprintf(fid,'%s %i \n',elements{1,3},im_size(3));
fprintf(fid,'%s %i \n',elements{1,4},t);
```

```
fprintf(fid,'%s \n','interleave = bsq');
fclose(fid);
```

### 8.3.7 **burn_map.m** Reclassifies input burn severity images (from RSS Gmbh )as burn/no burn images

```
a(:,:,:) =
enviread('F:\MSW\MATLAB\fire_maps\data\2009_season_20080519_TM7_20110512_TM7_merge_frost','F:\MSW\MATLAB\fire_maps\d
ata\2009_season_20080519_TM7_20110512_TM7_merge_frost.hdr');
[imax,jmax,kmax] = size (a);
h = zeros(imax,jmax);


for iy=1:imax
  for ix=1:jmax
      if a(iy,ix) >= 3;
           h(iy,ix)=1;
      else
          h(iy,ix)=0;
      end
   end % for
end %for


enviwrite(h,'F:\MSW\MATLAB\fire_maps\data\2009_season_20080519_TM7_20110512_TM7_burn_map');
```

### 8.3.8 **burn_count_map.m outputs** out puts a map of total number of fires from a stack of yearly burnt area input files

```
A(:,:,:) =
enviread('F:\MSW\MATLAB\fire_maps\data\burn_map_stack_sub','F:\MSW\MATLAB\fire_maps\data\burn_map_stack_sub.hdr');
[imax,jmax,kmax] = size (A);
h = zeros(imax,jmax);

for iy=1:imax
  for ix=1:jmax
```

```
      B = A(iy,ix,:);
      h(iy,ix)=sum(B);
  end % for
end %for

enviwrite(h,'F:\MSW\MATLAB\fire_maps\data\Burn_count_map');
```

### 8.3.9 **burn_map_select.m** outputs map of areas with selected fires frequency

```
a(:,:,:) = enviread('F:\MSW\MATLAB\fire_maps\data\fire_map_sum','F:\MSW\MATLAB\fire_maps\data\fire_map_sum.hdr');
[imax,jmax,kmax] = size (a);
h = zeros(imax,jmax);


for iy=1:imax
  for ix=1:jmax
      if a(iy,ix) == 1;
           h(iy,ix)=1;
      else
          h(iy,ix)=0;
      end
   end % for
end %for

enviwrite(h,'F:\MSW\MATLAB\fire_maps\data\burn_map_select_fire1');
```

### 8.3.10 **burn_history_map.m** produces maps of time of last fire for selected burn frequency from output of previous scripts

```
a(:,:,:) =
enviread('F:\MSW\MATLAB\fire_maps\data\burn_map_stack_sub','F:\MSW\MATLAB\fire_maps\data\burn_map_stack_sub.hdr');
b(:,:,:) =
enviread('F:\MSW\MATLAB\fire_maps\data\burn_map_select_fire1_sub','F:\MSW\MATLAB\fire_maps\data\burn_map_select_fire
1_sub.hdr');
[imax,jmax,kmax] = size (a);
```

```
h = zeros(imax,jmax);

for iy=1:imax
  for ix=1:jmax
      if b(iy,ix) == 1;
            if a(iy,ix,1)==1
            h(iy,ix)=126;
            end
            if a(iy,ix,2)==1
            h(iy,ix)=73;
            end
            if a(iy,ix,3)==1
            h(iy,ix)=61;
            end
            if a(iy,ix,4)==1
            h(iy,ix)=37;
            end
            if a(iy,ix,5)==1
            h(iy,ix)=25;
            end
            if a(iy,ix,6)==1
            h(iy,ix)=13;
            end
            if a(iy,ix,7)==1
            h(iy,ix)=-2;
            end
      else
            h(iy,ix)=0;
      end
   end % for
end %for

enviwrite(h,'F:\MSW\MATLAB\fire_maps\data\burn_map_year');
```

# 9. Bibliography

Abdoellah, O. S. (1987). 10: Transmigration Policies in Indonesia: Government Aims and Popular Response. *Center for Migration Studies special issues*, *5*(2), 180–196.

Achard, F., Eva, H. D., Stibig, H.-J., Mayaux, P., Gallego, J., Richards, T., & Malingreau, J.-P. (2002). Determination of deforestation rates of the world's humid tropical forests. *Science (New York, N.Y.)*, *297*(5583), 999–1002.

Asner, G. P., Keller, M., Pereira Jr., R., & Zweede, J. C. (2002). Remote sensing of selective logging in AmazoniaAssessing limitations based on detailed field observations, Landsat ETM+, and textural analysis. *Remote Sensing of Environment*, *80*(3), 483–496.

Asner, G. P., Keller, M., Pereria, R., Zweede, J. C., & Silva, J. N. M. (2004). Canopy damage and recovery after selective logging in Amazonia: field and satellite studies. *Ecol. Appl.*, *14*(4), s280–s298.

Asner, G. P., Knapp, D. E., Broadbent, E. N., Oliveira, P. J. C., Keller, M., & Silva, J. N. (2005). Selective logging in the Brazilian Amazon. *Science*, *310*, 480.

Asner, G. P., Powell, G. V. N., Mascaro, J., Knapp, D. E., Clark, J. K., Jacobson, J., Hughes, R. F. (2010). High-resolution forest carbon stocks and emissions in the Amazon. *Proceedings of the National Academy of Sciences of the United States of America*, *107*(38), 1–5.

Austin, J. (2003). Estimating forest biomass using satellite radar: an exploratory study in a temperate Australian Eucalyptus forest. *Forest Ecology and Management*, *176*(1-3), 575–583.

Ballhorn, U., Jubanski, J., & Siegert, F. (2011). ICESat/GLAS Data as a Measurement Tool for Peatland Topography and Peat Swamp Forest Biomass in Kalimantan, Indonesia. *Remote Sensing*, *3*(9), 1957–1982.

Balzter, H., Skinner, L., Luckman, A., & Brooke, R. (2003). Estimation of tree growth in a conifer plantation over 19 years from multi-satellite L-band SAR. *Remote Sensing of Environment*, *84*(2), 184–191. doi:10.1016/S0034-4257(02)00106-2

Bourgeau-Chavez, L. L., Kasischke, E. S., Brunzell, S., Mudd, J. P., & Tukman, M. (2002). Mapping fire scars in global boreal forests using imaging radar data. *International Journal of Remote Sensing*, *23*(20), 4211–4234.

Bourgeau-Chavez, Laura L., Kasischke, E. S., Riordan, K., Brunzell, S., Nolan, M., Hyer, E., Ames, S. (2007). Remote monitoring of spatial and temporal surface soil moisture in fire disturbed boreal forest ecosystems with ERS SAR imagery. *International Journal of Remote Sensing*, *28*(10), 2133–2162.

Brocca, L., Melone, F., Moramarco, T., Wagner, W., & Hasenauer, S. (2010). ASCAT soil wetness index validation through in situ and modeled soil moisture data in central Italy. *Remote Sensing of Environment*, *114*(11), 2745–2755.

Busch, J., Lubowski, R. N., Godoy, F., Steininger, M., Yusuf, A. A., Austin, K., Boltz, F. (2012). Structuring economic incentives to reduce emissions from deforestation within Indonesia. *Proceedings of the National Academy of Sciences*.

Canadell, J. G., Kirschbaum, M., Kurz, W., Sanz, M., Schlamadinger, B., & Yamagata, Y. (2007). Factoring out natural and indirect human effects on terrestrial carbon sources and sinks. *Environmental Science & Policy*, *10*(4), 370–384.

Carreiras, J. M. B., Vasconcelos, M. J., & Lucas, R. M. (2012). Understanding the relationship between aboveground biomass and ALOS PALSAR data in the forests of Guinea-Bissau (West Africa). *Remote Sensing of Environment*, *121*, 426–442.

Cartus, O., Santoro, M., & Kellndorfer, J. M. (2012). Mapping forest aboveground biomass in the Northeastern United States with ALOS PALSAR dual-polarization L-band. *Remote Sensing of Environment*, *124*, 466–478.

Chave, J, Andalo, C., Brown, S., Cairns, M. A., Chambers, J. Q., Eamus, D., Yamakura, T. (2005). Tree allometry and improved estimation of carbon stocks and balance in tropical forests. *Oecologia*, *145*(1), 87–99.

Chave, Jérôme. (2005). Measuring wood density for tropical forest trees. *A field manual for the CTFS sites*, 1–7.

Clements, G. R., Sayer, J., Boedhihartono, A. K. Venter, O., Love- joy, T., Koh, L. P., & Laurance, W. F. (2010). Cautious Optimism over Norway-Indonesia REDD Pact. *Conservation Biology*, *24*, 1437–1438.

Cochrane, M. A., Alencar, A., Schulze, M. D., Souza, C. M., Nepstad, D. C., Lefebvre, P., & Davidson, E. A. (1999). Positive feedbacks in the fire dynamic of closed canopy tropical forests. *Science*, *284*(5421), 1832–1835.

Cohen, W. B., Yang, Z., & Kennedy, R. E. (2010). Detecting trends in forest disturbance and recovery using yearly Landsat time series: 2. TimeSync — Tools for calibration and validation. *Remote Sensing of Environment*, *114*(12), 2911–2924.

Coops, N. C., Wulder, M. a., & Iwanicka, D. (2009). Large area monitoring with a MODIS-based Disturbance Index (DI) sensitive to annual and seasonal variations. *Remote Sensing of Environment*, *113*(6), 1250–1261.

De Grandi, G., Bouvet, A., Lucas, R. M., Shimada, M., Monaco, S., & Rosenqvist, A. (2011). The K&C PALSAR mosaic of the African continent: processing issues and first thematic results. *IEEE Transactions on Geoscience and Remote Sensing*, *49*(10), 3593–3610.

DeFries, R. (2002). Carbon emissions from tropical deforestation and regrowth based on satellite observations for the 1980s and 1990s. *Proceedings of the National Academy of Sciences*, *99*, 14256–14261.

Dennis, R. a., & Colfer, C. P. (2006). Impacts of land use and fire on the loss and degradation of lowland forest in 1983-2000 in East Kutai District, East Kalimantan, Indonesia. *Singapore Journal of Tropical Geography*, *27*(1), 30–48.

Dubois, P. C., Van Zyl, J., & Engman, T. (1995). Measuring soil moisture with imaging radars. *IEEE Transactions on Geoscience and Remote Sensing*, *33*(4), 915–926.

Eliasch, J. (2008). *Climate Change: Financing Global Forests.* London.

Englhart, S., Keuck, V., & Siegert, F. (2011). Aboveground biomass retrieval in tropical forests — The potential of combined X- and L-band SAR data use. *Remote Sensing of Environment*, *115*(5), 1260–1271.

Entekhabi, D., Njoku, E. G., O'Neill, P. E., Kellogg, K. H., Crow, W. T., Edelstein, W. N., Van Zyl, J. (2010). The Soil Moisture Active Passive (SMAP) Mission. *Proceedings of the IEEE*, *98*(5), 704–716.

Evans, T. L., Costa, M., Telmer, K., & Silva, T. S. F. (2010). Using ALOS/PALSAR and RADARSAT-2 to Map Land Cover and Seasonal Inundation in the Brazilian Pantanal. *IEEE Journal of Selected Topics in Applied Earth Observations and Remote Sensing*, *3*(4), 560–575.

Field, R. D., Van der Werf, G. R., & Shen, S. S. P. (2009). Human amplification of drought-induced biomass burning in Indonesia since 1960. *Nature Geoscience*, *2*(3), 185–188.

Foley, J., DeFries, R., Asner, G., & Barford, C. (2005). Global consequences of land use. *Science*, *309*, 570-4.

Gibbs, H. K., Brown, S., Niles, J. O., & Foley, J. A. (2007). Monitoring and estimating tropical forest carbon stocks: making REDD a reality. *Environmental Research Letters*, *213.*

Gimeno, M., San-Miguel-Ayanz, J., & Schmuck, G. (2004). Identification of burnt areas in Mediterranean forest environments from ERS-2 SAR time series. *International Journal of Remote Sensing*, *25*(22), 4873–4888.

Grainger, A. (2008). Difficulties in tracking the long-term global trend in tropical forest area. *Proceedings of the National Academy of Sciences of the United States of America*, *105*(2), 818–23.

Hajnsek, I. (2006). INDREX-II–Indonesian Radar Experiment Campaign over Tropical Forest in L-and P-band. *ESA Final Report*, 142.

Hannachi, A. (2004). A Primer for EOF Analysis of Climate Data. *Reading*, 1–33.

Hannachi, A., Jolliffe, I., & Stephenson, D. (2007). Empirical orthogonal functions and related techniques in atmospheric science: A review. *International Journal of Climatology*, *27*(9), 1119–1152.

Hansen, M. C., Stehman, S. V, & Potapov, P. V. (2010). Quantification of global gross forest cover loss. *Proceedings of the National Academy of Sciences of the United States of America*, *107*(19), 8650–5.

Hansen, M. C., Stehman, S. V, Potapov, P. V, Loveland, T. R., Townshend, J. R. G., DeFries, R. S., Dimiceli, C. (2008). Humid tropical forest clearing from 2000 to 2005 quantified by using multitemporal and multiresolution remotely sensed data. *Proceedings of the National Academy of Sciences of the United States of America*, *105*(27), 9439–44.

Harris, N. L., Brown, S., Hagen, S. C., Saatchi, S. S., Petrova, S., Salas, W., Lotsch, A. (2012). Baseline Map of Carbon Emissions from Deforestation in Tropical Regions. *Science*, *336*(6088), 1573–1576.

Herold, M., & Johns, T. (2007). Linking requirements with capabilities for deforestation monitoring in the context of the UNFCCC-REDD process. *Environmental Research Letters*, *2*(4), 045025.

Herold, M., & Skutsch, M. (2011). Monitoring, reporting and verification for national REDD + programmes: two proposals. *Environmental Research Letters*, *6*(1), 014002.

Hirano, T., Jauhiainen, J., Inoue, T., & Takahashi, H. (2008). Controls on the Carbon Balance of Tropical Peatlands. *Ecosystems*, *12*(6), 873–887.

Hirano, T., Segah, H., Harada, T., Limin, S., June, T., Hirata, R., & Osaki, M. (2007). Carbon dioxide balance of a tropical peat swamp forest in Kalimantan, Indonesia. *Global Change Biology*, *13*(2), 412–425. x

Hooijer, A., Page, S., Jauhiainen, J., Lee, W. A., Lu, X. X., Idris, A., & Anshari, G. (2012). Subsidence and carbon loss in drained tropical peatlands. *Biogeosciences*, *9*(1), 1–11.

Hooijer, Al, Vat, M. van der, Prinsen, G., Vernimmen, R., Brinkman, J., & Zijl, F. (2008). *Master Plan for the Rehabilitation and Revitalisation of the Ex-Mega Rice Project Area in Central Kalimantan: HYDROLOGY OF THE EMRP AREA: WATER MANAGEMENT IMPLICATIONS FOR PEATLANDS Technical Report No. 2* (p. 131). Wageningen.

Hooijer, Aljosja, Page, S., Canadell, J. G., Silvius, M., Kwadijk, J., Wösten, H., & Jauhiainen, J. (2010). Current and future CO2 emissions from drained peatlands in Southeast Asia. *Biogeosciences*, *7*(5), 1505–1514.

Hoscilo, A. (2009). *Fire regime, vegetation dynamics and land cover change in tropical peatland, Indonesia*. Phd thesis, University of Leicester.

Hoscilo, A., Page, S. E., Tansey, K. J., & Rieley, J. O. (2011). Effect of repeated fires on land-cover change on peatland in southern Central Kalimantan, Indonesia, from 1973 to 2005. *International Journal of Wildland Fire*, *20*(4), 578.

Hoscilo, A., Tansey, K., & Page, S. E. (2013). Post-fire vegetation response as a proxy to quantify the magnitude of burn severity in tropical peatland. *International Journal of Remote Sensing*, *34*(2), 412–433.

Houghton, R. A. (2005). Aboveground Forest Biomass and the Global Carbon Balance. *Global Change Biology*, *11*(6), 945–958.

Houghton, R., & Lawrence, K. (2001). The spatial distribution of forest biomass in the Brazilian Amazon: a comparison of estimates. *Global Change*, *7*, 731–746.

Huang, C., Goward, S. N., Masek, J. G., Thomas, N., Zhu, Z., & Vogelmann, J. E. (2010). An automated approach for reconstructing recent forest disturbance history using dense Landsat time series stacks. *Remote Sensing of Environment*, *114*(1), 183–198.

Huang, S., Member, S., & Siegert, F. (2006). Backscatter Change on Fire Scars in Siberian Boreal. *IEEE Geoscience and Remote Sensing Letters*, *3*(1), 154–158.

Huffman, G. J., Adler, R. F., Bolvin, D. T., Gu, G., Nelkin, E. J., Bowman, K. P., Wolff, D. B. (2007). The TRMM Multisatellite Precipitation Analysis (TMPA): Quasi-Global, Multiyear, Combined-Sensor Precipitation Estimates at Fine Scales. *Journal of Hydrometeorology*, *8*(1), 38.

IPCC. (2007). *Climate Change 2007: Working Group III: Mitigation of Climate Change*. (B. Metz, O. Davidson, P. Bosch, R. Dave, & L. Meyer, Eds.)*IPCC Third Assessment* (p. 851). Cambridge University Press.

Jaenicke, J., Rieley, J., Mott, C., Kimman, P., & Siegert, F. (2008). Determination of the amount of carbon stored in Indonesian peatlands. *Geoderma*, *147*(3-4), 151–158.

Jauhiainen, J., Hooijer, A., & Page, S. E. (2012). Carbon dioxide emissions from an Acacia plantation on peatland in Sumatra, Indonesia. *Biogeosciences*, *9*(2), 617–630.

Jauhiainen, J., Silvennoinen, H., Hämäläinen, R., Kusin, K., Limin, S., Raison, R. J., & Vasander, H. (2012). Nitrous oxide fluxes from tropical peat with different disturbance history and management. *Biogeosciences*, *9*(4), 1337–1350.

Jauhiainen, J., Takahashi, H., Heikkinen, J. E. P., Martikainen, P. J., Vasander, H., (2005). Carbon fluxes from a tropical peat swamp forest floor. *Global Change Biology*, *11*(10), 1788–1797.

Joseph, a. T., Van der Velde, R., O'Neill, P. E., Lang, R., & Gish, T. (2010). Effects of corn on C- and L-band radar backscatter: A correction method for soil moisture retrieval. *Remote Sensing of Environment*, *114*(11), 2417–2430.

Kasischke, E. S. (2003). Effects of seasonal hydrologic patterns in south Florida wetlands on radar backscatter measured from ERS-2 SAR imagery. *Remote Sensing of Environment*, *88*(4), 423–441.

Kasischke, E. S., Bourgeau-Chavez, L. L., French, N. H. F., Harrell, P., & Christensen, N. L. (1992). Initial observations on using SAR to monitor wildfire scars in boreal forests. *International Journal of Remote Sensing*, *13*(18), 3495–3501.

Kasischke, E. S., Bourgeau-Chavez, L. L., Rober, A. R., Wyatt, K. H., Waddington, J. M., & Turetsky, M. R. (2009). Effects of soil moisture and water depth on ERS SAR backscatter measurements from an Alaskan wetland complex. *Remote Sensing of Environment*, *113*(9), 1868–1873.

Kennedy, R. E., Yang, Z., & Cohen, W. B. (2010). Detecting trends in forest disturbance and recovery using yearly Landsat time series: 1. LandTrendr — Temporal segmentation algorithms. *Remote Sensing of Environment*, *114*(12), 2897–2910.

Kronseder, K., Ballhorn, U., Böhm, V., & Siegert, F. (2012). Above ground biomass estimation across forest types at different degradation levels in Central Kalimantan using LiDAR data. *International Journal of Applied Earth Observation and Geoinformation*, *18*, 37–48.

Lailan, S. (2002). The Effects of Climatic Variations on Peat Swamp Forest Condition and Peat Combustibility, *X*(1), 1–14.

Le Quéré, C. (2010). Trends in the land and ocean carbon uptake. *Current Opinion in Environmental Sustainability*, *2*(4), 219–224.

Le Toan, T., Quegan, S., Davidson, M. W. J., Balzter, H., Paillou, P., Papathanassiou, K., … Ulander, L. (2011). The BIOMASS mission: Mapping global forest biomass to better understand the terrestrial carbon cycle. *Remote Sensing of Environment*, *115*(11), 2850–2860.

Le Toan, T., Beaudoin, A., Riom, J., & Guyon, D. (1992). Relating forest biomass to SAR data. *IEEE Transactions on Geoscience and Remote*

*Sensing*, *30*(2), 403–411. doi:10.1109/36.134089Lee, J.-S. (1986). Speckle Suppression And Analysis For Synthetic Aperture Radar Images. *Optical Engineering*, *25*(5), 255636.

Lindquist, E. J., D'Annunzio, R., Gerrand, A., MacDicken, K., Achard, F., Beuchle, R., Stibig, H.-J. (2012). *Global forest land-use change 1990–2005*. FAO, Rome.

Luckman, A., Baker, J., & Honza, M. (1997). Tropical Forest Biomass Density Estimation Using JERS-1 SAR : Seasonal Variation , Confidence Limits , and Application to Image Mosaics, *4257*(97), 126–139.

Lähteenoja, O., Reátegui, Y. R., Räsänen, M., Torres, D. D. C., Oinonen, M., & Page, S. (2012). The large Amazonian peatland carbon sink in the subsiding Pastaza-Marañón foreland basin, Peru. *Global Change Biology*, *18*(1), 164–178.

Macdonald, G. M., Beilman, D. W., Kremenetski, K. V, Sheng, Y., Smith, L. C., & Velichko, A. A. (2006). Rapid early development of circumarctic peatlands and atmospheric CH4 and CO2 variations. *Science (New York, N.Y.)*, *314*(5797), 285–8.

Malhi, Y., Wood, D., Baker, T. R., Wright, J., Phillips, O. L., Cochrane, T., … Vinceti, B. (2006). The regional variation of aboveground live biomass in old-growth Amazonian forests. *Global Change Biology*, *12*, 1107–1138.

Martinez, J., & Le Toan, T. (2007). Mapping of flood dynamics and spatial distribution of vegetation in the Amazon floodplain using multitemporal SAR data. *Remote Sensing of Environment*, *108*(3), 209–223.

Mattia, F., Satalino, G., Pauwels, V. R. N., & Loew, A. (2009). Soil moisture retrieval through a merging of multi-temporal L-band SAR data and hydrologic modelling. *Hydrology and Earth System Sciences*, *13*(3), 343–356.

Meir, P., Cox, P., & Grace, J. (2006). The influence of terrestrial ecosystems on climate. *Trends in ecology & evolution (Personal edition)*, *21*(5), 254–60.

Miettinen, J., & Liew, S. C. (2011). Separability of insular Southeast Asian woody plantation species in the 50 m resolution ALOS PALSAR mosaic product. *Remote Sensing Letters*, *2*(4), 299–307.

Miettinen, Jukka, Hooijer, A., Shi, C., Tollenaar, D., Vernimmen, R., Liew, S. C., Page, S. E. (2012). Extent of industrial plantations on Southeast Asian peatlands in 2010 with analysis of historical expansion and future projections. *GCB Bioenergy*,

Miettinen, Jukka, Hooijer, A., Wang, J., Shi, C., & Liew, S. C. (2012). Peatland degradation and conversion sequences and interrelations in Sumatra. *Regional Environmental Change*.

Minchella, A., Del Frate, F., Capogna, F., Anselmi, S., & Manes, F. (2009). Use of multitemporal SAR data for monitoring vegetation recovery of

Mediterranean burned areas. *Remote Sensing of Environment*, *113*(3), 588–597.

Mitchard, E. T. a., Saatchi, S. S., Gerard, F. F., Lewis, S. L., & Meir, P. (2009). Measuring Woody Encroachment along a Forest–Savanna Boundary in Central Africa. *Earth Interactions*, *13*(8), 1.

Mitchard, E. T. a., Saatchi, S. S., White, L. J. T., Abernethy, K. a., Jeffery, K. J., Lewis, S. L., Meir, P. (2012). Mapping tropical forest biomass with radar and spaceborne LiDAR in Lopé National Park, Gabon: overcoming problems of high biomass and persistent cloud. *Biogeosciences*, *9*(1), 179–191.

Mitchard, E. T. a., Saatchi, S. S., Woodhouse, I. H., Nangendo, G., Ribeiro, N. S., Williams, M., Meir, P. (2009). Using satellite radar backscatter to predict above-ground woody biomass: A consistent relationship across four different African landscapes. *Geophysical Research Letters*, *36*(23).

Mitchard, E. T., Saatchi, S. S., Lewis, S. L., Feldpausch, T. R., Gerard, F. F., Woodhouse, I. H., & Meir, P. (2011). Comment on “A first map of tropical Africa”s above-ground biomass derived from satellite imagery’. *Environmental Research Letters*, *6*(4), 049001.

Mitchard, E.T.a., Saatchi, S. S., Lewis, S. L., Feldpausch, T. R., Woodhouse, I. H., Sonké, B., Meir, P. (2011). Measuring biomass changes due to woody encroachment and deforestation/degradation in a forest–savanna boundary region of central Africa using multi-temporal L-band radar backscatter. *Remote Sensing of Environment*, *115*(11), 2861–2873.

Moore, S., Gauci, V., Evans, C. D., & Page, S. E. (2011). Fluvial organic carbon losses from a Bornean blackwater river. *Biogeosciences*, *8*(4), 901–909.

Moran, M. S., Peters-Lidard, C. D., Watts, J. M., & McElroy, S. (2004). Estimating soil moisture at the watershed scale with satellite-based radar and land surface models. *Canadian Journal of Remote Sensing*, *30*(5), 805–826.

Muhamad, N. Z., & Rieley, J. O. (2002). Management of tropical peatlands in Indonesia: mega reclamation project in Central Kalimantan. . In: J. In S. Page & J. Rieley (Eds.), *Proceedings of the International Symposium on tropical peatland, Jakarta, 22-23 August 2001* (pp. 155–162).

Murdiyarso, D., Dewi, S., Lawrence, D., & Seymour, F. (2011). Indonesia ' s forest moratorium A stepping stone to better forest governance ? CIFOR

Page, S. E., Hoscilo, A., Wösten, H., Jauhiainen, J., Silvius, M., Rieley, J., … Limin, S. (2009). Restoration Ecology of Lowland Tropical Peatlands in Southeast Asia: Current Knowledge and Future Research Directions. *Ecosystems*.

Page, S. E., Morrison, R., Malins, C., & Hooijer, A. (2011). Review of peat surface greenhouse gas emissions from oil palm plantations in Southeast Asia. *Transportation*, (15).

Page, S. E., Rieley, J. O., & Banks, C. J. (2011). Global and regional importance of the tropical peatland carbon pool. *Global Change Biology*, *17*(2), 798–818.

Page, S. E., Rieley, J. O., Shotyk, W., & Weiss, D. (1999). Interdependence of peat and vegetation in a tropical peat swamp forest. *Philosophical transactions of the Royal Society of London. Series B, Biological sciences*, *354*(1391), 1885–97.

Page, S., Siegert, F., Rieley, J., & Boehm, H. (2002). The amount of carbon released from peat and forest fires in Indonesia during 1997. *Nature*, *1999*(1), 61–65.

Peres, C. a, Barlow, J., & Laurance, W. F. (2006). Detecting anthropogenic disturbance in tropical forests. *Trends in ecology & evolution (Personal edition)*, *21*(5), 227–9.

Pierdicca, N., Pulvirenti, L., & Bignami, C. (2010). Soil moisture estimation over vegetated terrains using multitemporal remote sensing data. *Remote Sensing of Environment*, *114*(2), 440–448.

Price, J. (1997). Soil moisture, water tension, and water table relationships in a managed cutover bog. *Journal of Hydrology*, *202*(1-4), 21–32.

Quegan, S., & Yu, J. J. (2001). Filtering of multichannel SAR images. *IEEE Transactions on Geoscience and Remote Sensing*, *39*(11), 2373–2379.

Rajeev, K., Parameswaran, K., Nair, S. K., & Meenu, S. (2008). Observational evidence for the radiative impact of Indonesian smoke in modulating the sea surface temperature of the equatorial Indian Ocean. *Journal of Geophysical Research-Atmospheres*, *113*(D17), 0.

Rignot, E. J., Zimmermann, R., & Van Zyl, J. J. (1995). Spaceborne applications of P band imaging radars for measuring forest biomass. *IEEE Transactions on Geoscience and Remote Sensing*, *33*(5), 1162–1169.

Rogers, N. C., Quegan, S., Kim, J. S., & Papathanassiou, K. P. (2013). Impacts of Ionospheric Scintillation on the BIOMASS P-Band Satellite SAR. IEEE Transactions on Geoscience and Remote Sensing, 1–1. doi:10.1109/TGRS.2013.2255880

Romshoo, S. A. (2003). Radar remote sensing for monitoring of dynamic ecosystem processes related to biogeochemical exchanges in tropical peatlands. *Visual Geosciences*, *9*(1), 9–28.

Rosenqvist, a., Shimada, M., Chapman, B., Freeman, A., De Grandi, G., Saatchi, S., & Rauste, Y. (2000). The Global Rain Forest Mapping project - A review. *International Journal of Remote Sensing*, *21*(6), 1375–1387. doi:10.1080/014311600210227

Roy, D. P., Ju, J., Kline, K., Scaramuzza, P. L., Kovalskyy, V., Hansen, M., … Zhang, C. (2010). Web-enabled Landsat Data (WELD): Landsat ETM+ composited mosaics of the conterminous United States. *Remote Sensing of Environment*, *114*(1), 35–49.

Ryan, C. M., Hill, T., Woollen, E., Ghee, C., Mitchard, E., Cassells, G., … Williams, M. (2012). Quantifying small-scale deforestation and forest degradation in African woodlands using radar imagery. *Global Change Biology*, *18*(1), 243–257.

Saatchi, S S, Halligan, K., Despain, D. G., & Crabtree, R. L. (2007). Estimation of forest fuel load from radar remote sensing. *IEEE Trans. Geosci. Remote Sens.*, *45*, 10.

Saatchi, S. S., Houghton, R. A., Dos Santos Alvala, R. C., Soares, J. V., & Yu, Y. (2007). Distribution of aboveground live biomass in the Amazon basin. *Global Change Biology*, *13*(4), 816–837.

Saatchi, Sassan S, Harris, N. L., Brown, S., Lefsky, M., Mitchard, E. T. A., Salas, W., … Morel, A. (2011). Benchmark map of forest carbon stocks in tropical regions across three continents. *Proceedings of the National Academy of Sciences of the United States of America*, *108*(24), 9899–904.

Salas, W. A., Ducey, M. J., Rignot, E., & Skole, D. (2002). Assessment of JERS-1 SAR for monitoring secondary vegetation in Amazonia: I. Spatial and temporal variability in backscatter across a chrono-sequence of secondary vegetation stands in Rondonia. *International Journal of Remote Sensing*, *23*(7), 1357–1379.

Sandberg, G., Ulander, L. M. H., Fransson, J. E. S., Holmgren, J., & Le Toan, T. (2011). L- and P-band backscatter intensity for biomass retrieval in hemiboreal forest. *Remote Sensing of Environment*, *115*(11), 2874–2886.

Shearman, P. L., Ash, J., MacKey, B., Bryan, J. E., & Lokes, B. (2009). Forest conversion and degradation in Papua New Guinea 1972-2002. *Biotropica*, *41*(3), 379–390.

Sheldon, S., Xiao, X., & Biradar, C. (2012). Mapping evergreen forests in the Brazilian Amazon using MODIS and PALSAR 500-m mosaic imagery. *ISPRS Journal of Photogrammetry and Remote Sensing*, *74*, 34–40.

Siegert, F., & Ruecker, G. (2000). Use of multitemporal ERS-2 SAR images for identification of burned scars in south-east Asian tropical rainforest. *International Journal of Remote Sensing*, *21*(4), 831–837.

Siegert, F., Ruecker, G., Hinrichs, A., & Hoffmann, A. A. (2001). Increased damage from fires in logged forests during droughts caused by el Niño. *Nature*, *414*, 437–440.

Sinclair, S., & Pegram, G. G. S. (2010). A comparison of ASCAT and modelled soil moisture over South Africa, using TOPKAPI in land surface mode. *Hydrology and Earth System Sciences*, *14*(4), 613–626.

Small, C., & Elvidge, C. D. (2011). Mapping Decadal Change in Anthropogenic Night Light. *Procedia Environmental Sciences*, *7*, 353–358.

Smith-Jonforsen, G., Folkesson, K., Hallberg, B., & Ulander, L. M. H. (2007). Effects of Forest Biomass and Stand Consolidation on P-Band Backscatter. *IEEE Geoscience and Remote Sensing Letters*, *4*(4), 669–673.

Stephen, H., Ahmad, S., Piechota, T. C., & Tang, C. (2010). Relating surface backscatter response from TRMM precipitation radar to soil moisture: results over a semi-arid region. *Hydrology and Earth System Sciences*, *14*(2), 193–204.

Stibig, H.-J., Achard, F., & Fritz, S. (2009). A new forest cover map of continental southeast Asia derived from SPOT-VEGETATION satellite imagery. *Applied Vegetation Science*, *7*(2), 153–162.

Tanase, M. a., Santoro, M., De la Riva, J., Prez-Cabello, F., & Le Toan, T. (2010a). Sensitivity of X-, C-, and L-Band SAR Backscatter to Burn Severity in Mediterranean Pine Forests. *IEEE Transactions on Geoscience and Remote Sensing*, *48*(10), 3663–3675.

Tanase, M. a., Santoro, M., Wegmüller, U., De la Riva, J., & Pérez-Cabello, F. (2010b). Properties of X-, C- and L-band repeat-pass interferometric SAR coherence in Mediterranean pine forests affected by fires. *Remote Sensing of Environment*, *114*(10), 2182–2194.

Tanase, M., De la Riva, J., Santoro, M., Pérez-Cabello, F., & Kasischke, E. S. (2011). Sensitivity of SAR data to post-fire forest regrowth in Mediterranean and boreal forests. *Remote Sensing of Environment*, *115*(8), 2075–2085.

Thiel, C., & Schmullius, C. (2012). Effect of tree species on PALSAR INSAR coherence over Siberian forest at frozen and unfrozen conditions. In *2012 IEEE International Geoscience and Remote Sensing Symposium* (pp. 190–193).

Toan, T. Le, Quegan, S., & Woodward, I. (2004). Relating radar remote sensing of biomass to modelling of forest carbon budgets. *Climatic Change*, 379–402.

Trouve, E., Chambenoit, Y., Classeau, N., & Bolon, P. (2003). Statistical and operational performance assessment of multitemporal sar image filtering. *IEEE Transactions on Geoscience and Remote Sensing*, *41*(11), 2519–2530.

Ulaby, F. T., & Dobson, M. C. (1989). *Handbook of Radar Scattering Statistics for Terrain*. *Data Base* (Vol. 1, p. 357).Vasander, H., & Kettunen, A. (2006). Carbon in boreal peatlands. *Boreal Peatland Ecosystems*, *188*(Lappalainen 1996), 165–194.

Venter, O., Meijaard, E., Possingham, H., Dennis, R., Sheil, D., Wich, S., … Wilson, K. (2009). Carbon payments as a safeguard for threatened tropical mammals. *Conservation Letters*, *2*(3), 123–129.

Verbesselt, J., Hyndman, R., Newnham, G., & Culvenor, D. (2010). Detecting trend and seasonal changes in satellite image time series. *Remote Sensing of Environment*, *114*(1), 106–115.

Vernimmen, R. R. E., Hooijer, A., Aldrian, E., & Van Dijk, I. J. M. (2012). Evaluation and bias correction of satellite rainfall data for drought monitoring in Indonesia. *Hydrology and Earth System Sciences*, *16*(1), 133–146.

Wang, Y., Davis, F., Melack, J., Kasischke, E. S., & Christensen Jr, N. (1995). The effects of changes in forest biomass on radar backscatter from tree canopies. *International Journal of Remote Sensing*, *16*(3), 503–514.

Wang, Yong, Kasischke, E. S., Melack, J. M., Davis, F. W., & Christensen Jr., N. L. (1994). The effects of changes in loblolly pine biomass and soil moisture on ERS-1 SAR backscatter. *Remote Sensing of Environment*, *49*(1), 25–31.

Whittle, M., Quegan, S., Uryu, Y., Stüewe, M., & Yulianto, K. (2012). Detection of tropical deforestation using ALOS-PALSAR: A Sumatran case study. *Remote Sensing of Environment*, *124*, 83–98.

Wood, S. N. (2006). *Generalized additive models: an introduction with R* (p. 410). Chapman and Hall.

Woodhouse, I. H., Mitchard, E. T. A., Brolly, M., Maniatis, D., & Ryan, C. M. (2012). Radar backscatter is not a “direct measure” of forest biomass. *Nature Clim. Change*, *2*(8), 556–557

Wooster, M. J., Perry, G. L. W., & Zoumas, A. (2011). Fire, drought and El Niño relationships on Borneo during the pre-MODIS era (1980–2000). *Biogeosciences Discussions*, *8*(1), 975–1013

Wright, E. L., Black, C. R., Chessman, A. W., Drage, T., Large, D., Turner, B. L., & Sjorgersten, S. (2011). Contribution of subsurface peat to CO2 and CH4 fluxes in a neotropical peatland. *Global Change Biology*, *17*(9), 2867–2881

Wösten, J. H. M., Van Den Berg, J., Van Eijk, P., Gevers, G. J. M., Giesen, W. B. J. T., Hooijer, A., Wibisono, I. T. (2006). Interrelationships between

Hydrology and Ecology in Fire Degraded Tropical Peat Swamp Forests. *International Journal of Water Resources Development*, *22*(1), 157–174.

Zhu, Z., & Woodcock, C. E. (2012). Object-based cloud and cloud shadow detection in Landsat imagery. *Remote Sensing of Environment*, *118*, 83–94.

Zhu, Z., Woodcock, C. E., & Olofsson, P. (2012). Continuous monitoring of forest disturbance using all available Landsat imagery. *Remote Sensing of Environment*, *122*, 75–91.